MODELING OF X-RAY PHOTOCONDUCTORS FOR X-RAY IMAGE DETECTORS

A Thesis

Submitted to the College of Graduate Studies and Research

in Partial Fulfillment of the Requirements

for the degree of

Doctor of Philosophy

in the Department of Electrical Engineering

University of Saskatchewan

Saskatoon

by

MOHAMMAD ZAHANGIR KABIR

Saskatoon, Saskatchewan

COPYRIGHT

ABSTRACT

Direct conversion flat panel x-ray image sensors based on using a photoconductor with an active matrix array provide excellent images. These image sensors are suitable for replacing the present day x-ray film/screen cassette to capture an x-ray image electronically, and hence enable a clinical transition to digital radiography. The performance of these sensors depends critically on the selection and design of the photoconductor. This work quantitatively studies the combined effects of the detector geometry (pixel size and detector thickness), operating conditions (x-ray energy and applied electric field) and charge transport properties (e.g., carrier trapping and recombination) of the photoconductor on the detector performance by developing appropriate detector models. In this thesis, the models for calculating the x-ray sensitivity, resolution in terms of the modulation transfer function (MTF), detective quantum efficiency (DQE), and ghosting of x-ray image detectors have been developed. The modeling works are based on the physics of the individual phenomena and the systematic solution of the fundamental physical equations in the photoconductor layer: (1) semiconductor continuity equation (2) Poisson's equation (3) trapping rate equations. The general approach of this work is to develop models in normalized coordinates to describe the results of different photoconductive x-ray image detectors. These models are applied to a-Se, polycrystalline HgI_2 and polycrystalline CdZnTe photoconductive detectors for diagnostic medical x-ray imaging applications (e,g., mammography, chest radiography and fluoroscopy). The models show a very good agreement with the experimental results.

The research presented in this thesis shows that the imaging performances (e.g., sensitivity, MTF, DQE and ghosting) can be improved by insuring that the carrier with higher mobility-lifetime product is drifted towards the pixel electrodes. The carrier schubwegs have to be several times greater, and the absorption depth has to be at least two times smaller than the photoconductor thickness for achieving sufficient sensitivity. Having smaller pixels is advantageous in terms of higher sensitivity by ensuring that the carrier with the higher mobility-lifetime product is drifted towards the pixel electrodes.

A model for calculating zero spatial frequency detective quantum efficiency, DQE (0), has been developed by including incomplete charge collection and x-ray interaction depth dependent conversion gain. The DQE(0) analyses of *a*-Se detectors for fluoroscopic applications show that there is an optimum photoconductor thickness, which maximizes the DQE(0) under a constant voltage operation. The application of DQE(0) model to different potential photoconductive detectors for fluoroscopic applications show that, in addition to high quantum efficiency, both high conversion gain and high charge collection efficiency are required to improve the DQE performance of an x-ray image detector.

An analytical expression of MTF due to distributed carrier trapping in the bulk of the photoconductor has been derived using the trapped charge distribution across the photoconductor. Trapping of the carriers that move towards the pixel electrodes

degrades the MTF performance, whereas trapping of the other type of carriers improves the sharpness of the x-ray image.

The large signal model calculations in this thesis show an upper limit of small signal models of x-ray image detectors. The bimolecular recombination between drifting carriers plays practically no role on charge collection in a-Se detectors up to the total carrier generation rate q_0 of 10^{18} EHPs/m^2-s. The bimolecular recombination has practically no effect on charge collection in a-Se detectors for diagnostic medical x-ray imaging applications.

A model for examining the sensitivity fluctuation mechanisms in a-Se detectors has been developed. The comparison of the model with the experimental data reveals that the recombination between trapped and the oppositely charged drifting carriers, electric field dependent charge carrier generation and x-ray induced new deep trap centers are mainly responsible for the sensitivity fluctuation in biased a-Se x-ray detectors.

The modeling works in this thesis identify the important factors that limit the detector performance, which can ultimately lead to the reduction of patient exposure/dose consistent with better diagnosis for different diagnostic medical x-ray imaging modalities. The quantitative analyses presented in this thesis show that the detector structure is just as important to the overall performance of the detector as the material properties of the photoconductor itself.

ACKNOWLEDGEMENTS

I would like to extend my sincere gratitude to my supervisor, Professor S. O. Kasap, for his continued guidance, encouragement, help, friendship, and financial support during the course of this project. I am grateful to Dr. Oliver Tousignant from ANRAD Corporation for providing me experimental data and for many fruitful discussions. Many thanks go to Professor John Rowlands from the University of Toronto for his insightful discussions and for reviewing numerous manuscripts expeditiously. I would like to thank Dylan Hunt, Andreas Rau, James Mainprize and Dr. Winston Ji from the Sunnybrook Health Science Center, University of Toronto, for many discussions we have had. My thanks are extended to George Belev for his spontaneous efforts to fix various computer problems. I would also like to thank Mohammad Yunus for many discussions. I would like to express my appreciation to NSERC and the University of Saskatchewan for the financial support I have received. Finally, not least, I am deeply indebted to my wife Anjuman for her unfailing support, encouragement, and especially her patience.

TABLE OF CONTENTS

LIST OF FIGURES

LIST OF TABLES

LIST OF ABBREVIATIONS

a-Se	Amorphous selenium
a-Si:H	Hydrogenated amorphous silicon
AB	Anti-bonding
ADC	Analog to digital conversion
AMA	Active matrix array
AMFPI	Active matrix flat panel imager
CZT	Cadmium zinc telluride
DQE	Detective quantum efficiency
DR	Dynamic range
EHP	Electron-hole pair
ITO	Indium-tin-oxide
IVAP	Intimate valence alternation pair
keV	kilo electron volt
kVp	kilo volt peak
LP	Lone pair
LSF	Line spread function
MC	Monte Carlo
MeV	Mega electron volt
MTF	Modulation transfer function
NB	Nonbonding
NPS	Noise power spectrum
PC	Personal computer
PVD	Physical vapor deposition
PSF	Point spread function
SNR	Signal to noise ratio
SP	Screen printing
TFT	Thin film transistor
VAP	Valence alternation pair
WSS	Wide-sense-stationary

1. INTRODUCTION

1.1 Radiographic Imaging

The discovery of x rays approximately 100 years ago by Wilhelm Roentgen lead very quickly to the development of radiology and medical imaging. Radiographic imaging still remains as one of the most useful tools to aid physicians in making a patient diagnosis. Radiographic imaging systems rely on the differential attenuation of ionizing radiation through different structures and tissues in the body to produce a radiological image. Although radiography is one of the most common medical diagnostic tools, it remains largely a film based, analog technology. Recently, there has been much interest in developing solid-state, digital x-ray systems [1]. Making the transition from analog to digital could bring several advantages to x-ray imaging: Contrast, resolution and other aspect of image quality could be improved which permits a reduction in x-ray exposure or dose; storage and transmission of x-ray images could be done conveniently by the use of computer; and the x-ray image would be available immediately for use in real-time imaging.

The x rays that pass through a patient undergo differential attenuation and this modulates the radiation intensity that reaches the detector. The conventional detector consists of a cassette of photographic film held in position just behind a light emitting phosphor screen. X rays impinging on the screen give off light that exposes the film creating a latent image that is subsequently amplified and made permanent by the chemical development process.

Extensive research in recent years has shown that the flat panel x-ray image detectors based on a large area thin-film transistor (TFT) or switching diode self-

scanned active matrix array (AMA) is the most promising digital radiographic technique and suitable to replace the conventional x-ray film/screen cassettes for diagnostic medical digital x-ray imaging applications (e.g., mammography, chest radiography and fluoroscopy) [2, 3]. Such large area integrated circuits or active matrix arrays have been developed as the basis for large area displays. Flat panel imagers incorporating active matrix arrays are called active matrix flat panel imagers or AMFPI. The physical form of the x-ray AMFPI is similar to a film/screen cassette and thus it will easily fit into current medical x-ray systems. The x-ray image is stored and displayed on the computer almost immediately after the x-ray exposure. The stored image can be transmitted instantaneously to remote locations for consultation and analysis. The dynamic range of recently developed AMFPI systems is much higher than the film/screen imaging systems [4]. AMFPIs are currently able to read out an entire image in 1/30 seconds, sufficient to perform fluoroscopy (real-time imaging) [5].

1.2 Flat-panel Detectors

The AMFPI concept is illustrated in Figure 1.1 where x-rays passing through an object (a hand in the figure) are incident on a large area flat panel sensor that replaces the normal film. The AMFPI consists of millions of pixels each of which acts as an individual detector. Each pixel converts the radiation it receives to an amount of charge that is proportional to the amount of radiation received by that pixel. To generate this signal charge, either a phosphor is used to convert the x rays to visible light which in turn is detected with a *pin* photodiode at the pixel (*indirect approach*) or an x-ray photoconductor converts the incident x rays to charge (*direct approach*) in one step [3]. For both indirect and direct conversion approaches the latent image is a charge distribution residing on the panel's pixels. The charges are simply read out by scanning the arrays row by row using the peripheral electronics and multiplexing the parallel columns to a serial digital signal. This signal is then transmitted to a computer system for storage and display.

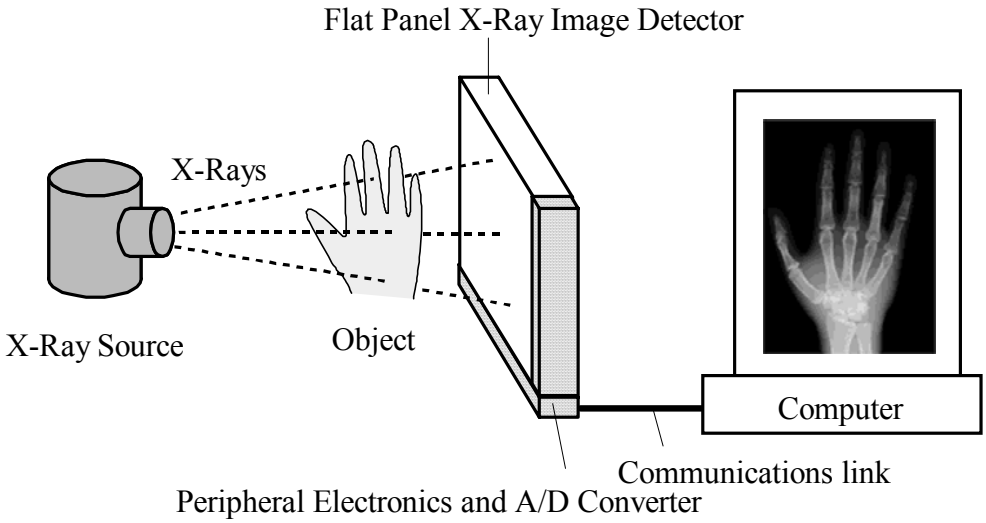

Figure 1.1 Schematic illustration of a flat panel x-ray image detector [6].

Several manufactures and academic researchers have used the indirect approach [7, 8]. In the indirect detection, phosphor screen absorbs x rays and creates visible lights. These visible lights are detected by a large area photodiode array read out with active matrix. The photodiode in each pixel generates an electrical charge whose magnitude is proportional to the light intensity emitted from the phosphor in the region close to the pixel. This charge is stored in the pixel capacitor until the active matrix is read out. The structure of an indirect conversion x-ray image sensor is illustrated in Figure 1.2. The bottom metallic contact is chromium. This is followed by a ~10 to 50 nm thick n^+ blocking layer, an 1.5 μm thick intrinsic hydrogenated amorphous silicon (a-Si:H) layer, a ~10 to 20 nm thick p^+ μc-$Si_{1-x}C_x$:H blocking layer, a ~50 nm layer of transparent indium tin oxide (ITO), and finally a surface passivation layer of oxy-nitride (a mixture of silicon oxide and silicon nitride phase; SiO_xN_y). *Passivation* refers to the process of chemically or physically (encapsulating a semiconductor surface with a protective layer) protecting a semiconductor surface from degradation. An externally applied reverse bias voltage of ~ –5 V applied to the ITO.

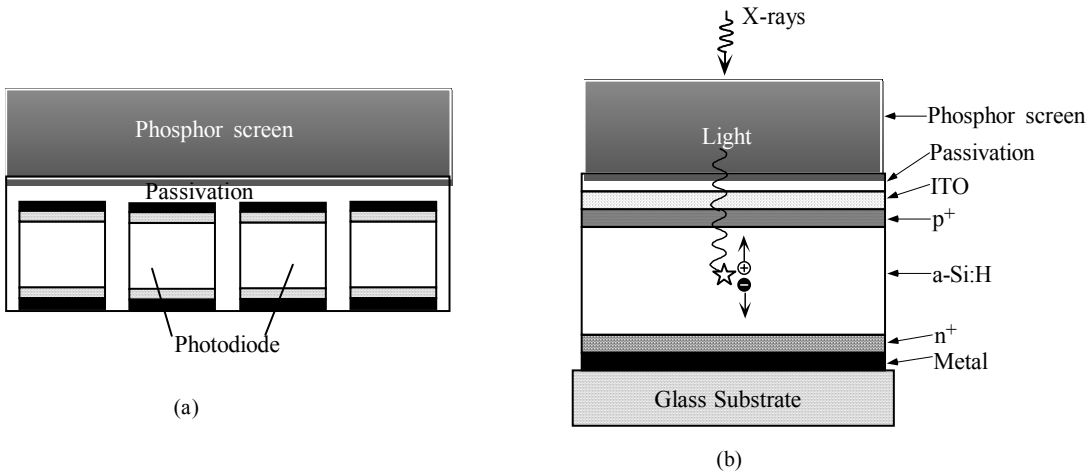

Figure 1.2 (a) A simplified cross-section of an indirect conversion x-ray image detector. Photodiodes are arranged in a two-dimensional array. (b) A cross-section of an individual hydrogenated amorphous silicon (a-Si:H) P-I-N photodiode. Phosphor screen absorbs x-ray and creates visible lights. These visible lights create electron-hole pairs in s-Si:H layer and the charge carriers are subsequently collected [3]. ITO stands for indium tin oxide.

It has been found that the direct approach produces systems that are superior in image quality to indirect conversion sensors and are also easier and cheaper to manufacture due to their simpler structure [9, 10]. The system is simple, compact, inherently digital and has so many advantages that it has now become a major contending choice in digital radiography [3, 11]. A photograph of a direct conversion flat panel x-ray image sensor and an x-ray image of a hand obtained by the sensor are shown in figure 1.3. This thesis considers only direct conversion x-ray imagers and how its charge collection efficiency, sensitivity, resolution, detective quantum efficiency (DQE) and ghosting depend on the photoconductor and detector structure. A detailed description of the direct conversion detector is given in the following section.

Figure 1.3 Left: A flat panel active matrix direct conversion x-ray image sensor using stabilized a-Se as a photoconductor. Active area is 14 inch × 17 inch and active matrix array size 2480 × 3072. The pixel size is 139 μm × 139 μm. Right: Scaled x-ray image of a hand obtained by the sensor on the left (Courtesy of Direct Radiography Corp.).

1.2.1 Direct conversion detector

A simplified schematic diagram of the cross sectional structure of two pixels and a simplified physical structure of a single pixel with TFT of the self-scanned direct conversion x-ray image detector are shown in figure 1.4. Each TFT has three electrical connections as shown in figure 1.4 (b): the gate is for the control of the "on" or "off" state of the TFT; the drain (D) is connected to a pixel electrode and a pixel storage capacitor, which is made by overlapping the pixel electrode with either the adjacent gate line or a separate ground line; the source (S) is connected to a common data line. A large bandgap (> 2 eV), high atomic number semiconductor or x-ray photoconductor (e.g., stabilized amorphous selenium, *a*-Se) layer is coated onto the active matrix array to serve as a *photoconductor layer*. An electrode (labeled *A*) is subsequently deposited

on the photoconductor layer to enable the application of a biasing potential and, hence, an electric field F in the photoconductor layer.

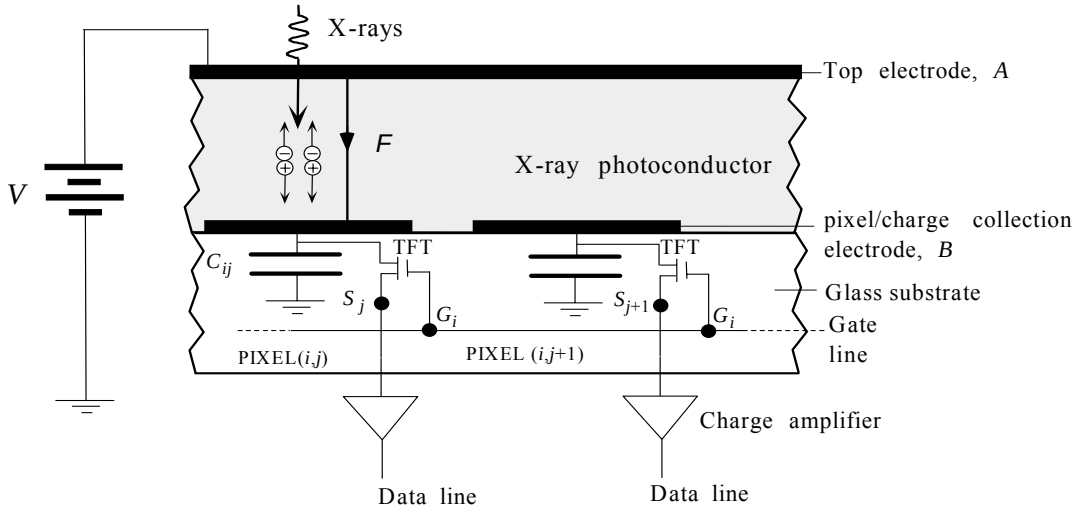

(a)

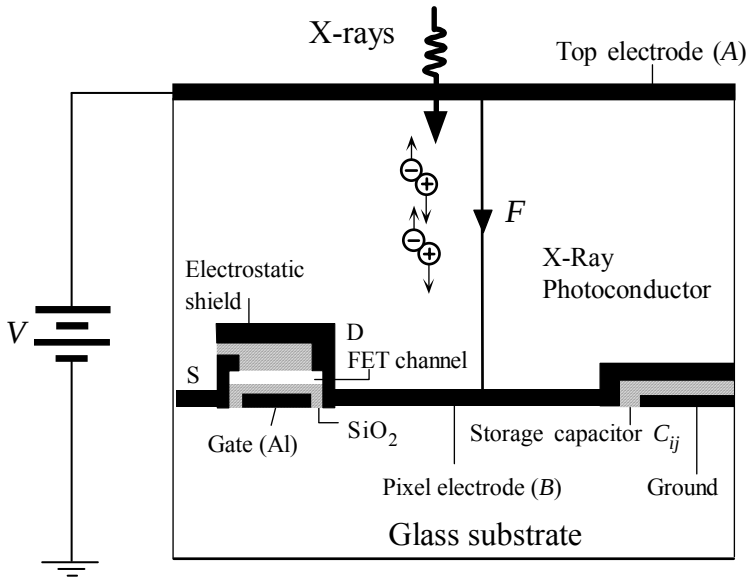

(b)

Figure 1.4 (a) A simplified schematic diagram of the cross sectional structure of two pixels of the photoconductive self-scanned x-ray image detector. (b) Simplified physical cross section of a single pixel (i, j) with a TFT switch. The top electrode (A) on the photoconductor is a vacuum coated metal (e.g., Al). The bottom electrode (B) is the pixel electrode that is one of the plates of the storage capacitance (C_{ij}). (Not to scale and the TFT height is highly exaggerated) [1, 6].

The applied bias voltage to the radiation receiving electrode *A* may be positive or negative, the selection of which depends on many factors and is discussed in later chapters of this thesis. The applied bias varies from few hundred to several thousand Volts. The capacitance C_{pc} of the photoconductor layer over the pixel is much smaller than the pixel capacitance C_{ij} so that most of the applied voltage drops across the photoconductor.

The electron-hole pairs (EHPs) that are generated in the photoconductor by the absorption of x-ray photons travel *along* the field lines and are collected by the electrodes. If the applied bias voltage is positive, then electrons collect at the positive bias electrode and holes accumulate on the storage capacitor C_{ij} attached to the pixel electrode, and thereby providing a charge-signal Q_{ij} that can be read during self-scanning. Each pixel electrode carries an amount of charge Q_{ij} that is proportional to the amount of incident x-ray radiation in photoconductor layer over that pixel. To readout the latent image charge, Q_{ij}, the appropriate TFT is turned on every Δt seconds and the charge signal is transferred to the data line and hence to the charge amplifier. These signals are then multiplexed into serial data, digitized, and fed into a computer for imaging. A snapshot of the physical structure of direct conversion flat panel detector is shown in Figure 1.5.

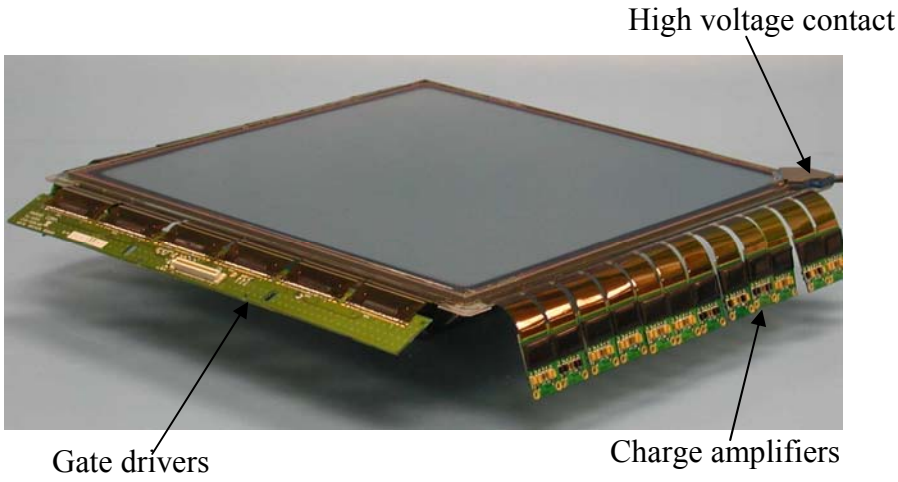

Figure 1.5 The physical structure of a direct conversion flat panel detector (Courtesy of ANRAD Corp.).

1.2.2 Active matrix readout

Large area integrated circuits or active matrix arrays have been developed as the basis for large area displays. Active matrix arrays based on hydrogenated amorphous silicon (a-Si:H) TFTs have been shown to be practical pixel addressing system. Active matrix arrays allow monolithic imaging system of large areas (*e.g.* 40 cm x 40 cm) to be constructed. As for conventional integrated circuits, planar processing of the array through deposition and doping of lithographically masked individual layers of metals, insulators and semiconductors implement the design of active matrix arrays. In the future, even larger areas should become feasible if required. Millions of individual pixel electrodes in the matrix are connected, as in Figure 1.6. Each pixel has its own thin film transistor (TFT) switch and storage capacitor to store image charges. The TFT switches control the image charge so that one line of pixels is activated electronically at a time. Normally, all the TFTs are turned off permitting the latent image charge to accumulate on the array. The readout is achieved by external electronics and software controlling the state of the TFT switches. The active matrix array consists of $M \times N$ (*e.g.* 2480 × 3072) storage capacitor C_{ij} whose charge can be read through properly addressing the TFT (i,j) via the gate (i) and source (j) lines. The charges read on each C_{ij} are converted to a digital image as described below. The readout is essentially self-scanning in that no external means such as a laser is used. The scanning is part of the AMFPI electronics and software, and thus permitting a truly compact device.

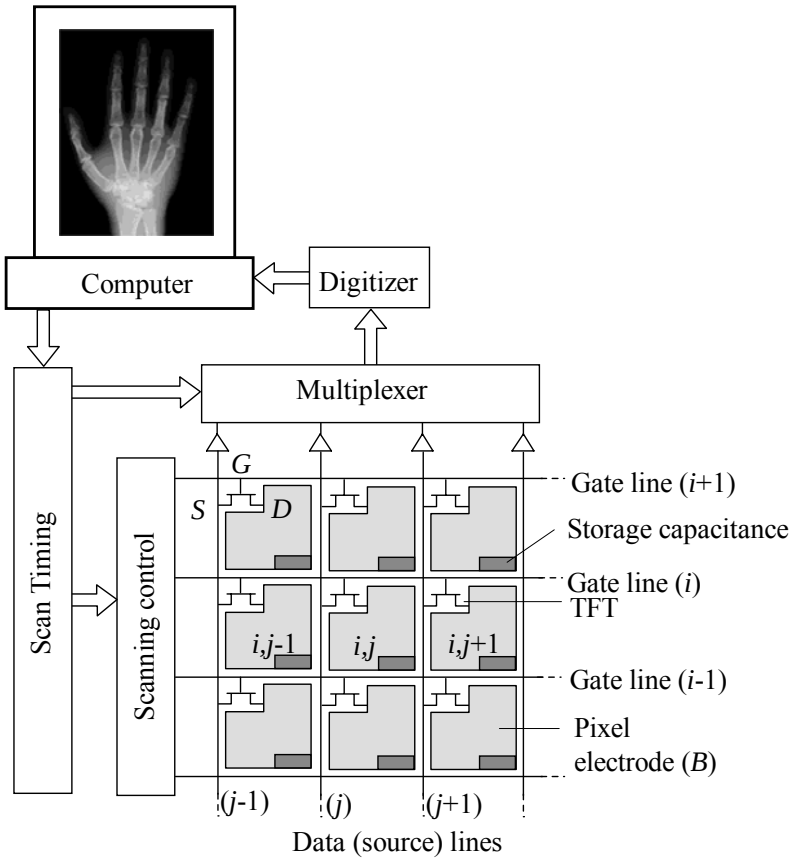

Figure 1.6 Schematic diagram that shows few pixels of active matrix array (AMA) for use in x-ray image detectors with self-scanned electronic readout. The charge distribution residing on the panel's pixels are simply read out by scanning the arrays row by row using the peripheral electronics and multiplexing the parallel columns to a serial digital signal [6].

The gates of all the TFTs in each row are connected to the same gate control line. The TFTs in each column are connected by their source to a common readout or *data* line. If gate *i* is activated, all TFTs in that particular row are turned 'on' and *N* data lines (from *j* =1 to *N*) will transfer the charges on the pixel electrodes in row *i* to the individual amplifier on each column. From this beginning, the parallel data are either digitized and then multiplexed into serial digital data, or multiplexed in analog forma and then digitized before being transferred to a computer usually through specialized image correction hardware for storage and further processing. Then the next row, *i*+1, is activated by the scanning control and the process is repeated until all rows have been

activated and processed. Thus, the system is ready for the next exposure by the time the previous image is read out.

The flat-panel imaging system is completed with active matrix array, peripheral circuitry that amplifies, digitizes, and synchronizes the readout of the image and a computer that manipulates and distributes the final image to the appropriate soft- or hard-copy device. A schematic diagram of a complete flat-panel x-ray imaging system is shown in Figure 1.7.

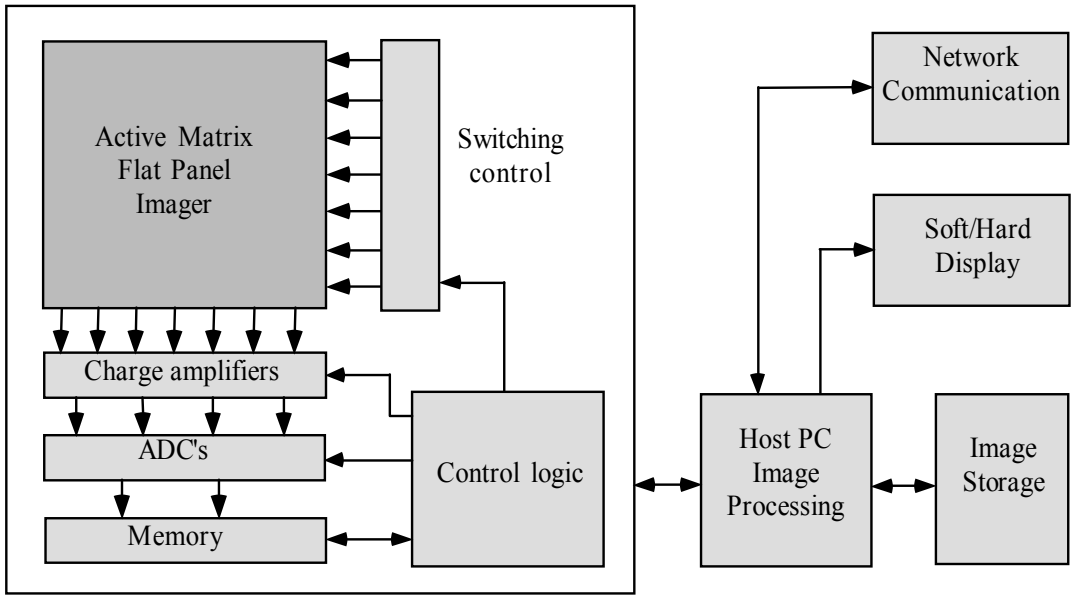

Figure 1.7 Diagram illustrating the configuration of a complete flat-panel x-ray imaging system [3].

1.2.3 General requirements of x-ray imaging systems

Any flat panel x-ray image detector design must first consider the required specifications based on the clinical need of the particular imaging modality, e.g., mammography, chest radiology, and fluoroscopy. Table 1.1 summarizes the specifications for flat panel detectors for chest radiology, mammography and fluoroscopy.

Table 1.1 Parameters for digital x-ray imaging systems. kVp is the maximum kV value applied across the x-ray tube during the time duration of the exposure, and the maximum energy of emitted x-ray photons is equal to the kVp value. (data are taken from Rowlands and Yorkston [3]).

Clinical Task	Chest radiology	Mammography	Fluoroscopy
Detector size	35 cm × 43 cm	18 cm × 24 cm	25 cm × 25 cm
Pixel size	200 μm × 200 μm	50 μm × 50 μm	250 μm × 250 μm
Number of pixels	1750 × 2150	3600 × 4800	1000 × 1000
Readout time	~ 1 s	~ 1 s	1/30 s
X-ray spectrum	120 kVp	30 kVp	70 kVp
Mean exposure	300 μR	12 mR	1 μR
Exposure range	30 - 3000 μR	0.6 – 240 mR	0.1 - 10 μR

1.3 Ideal X-ray Photoconductors

The performance of direct conversion x-ray detectors depends critically on the selection and design of the photoconductor. It is therefore instructive to identify what constitutes a nearly ideal x-ray photoconductor to guide a search for improved performance or better materials. Ideally, the photoconductive layer should possess the following material properties:

(a) Most of the incident x-ray radiation should be absorbed within a practical photoconductor thickness to avoid unnecessary patient exposure. This means that over the energy range of interest, the absorption depth δ of the x-rays must be substantially less than the device layer thickness L.

(b) The photoconductor should have high intrinsic x-ray sensitivity, *i.e.*, it must be able to generate as many collectable (free) electron hole pairs (EHPs) as possible per unit of incident radiation. This means the amount of radiation energy required,

denoted as $W_{\pm}$, to create a single *free* electron and hole pair must be as low as possible. Typically, $W_{\pm}$ increases with the bandgap E_g of the photoconductor [12].

(c) There should be no bulk recombination of electrons and holes as they drift to the collection electrodes; EHPs are generated in the bulk of the photoconductor. Bulk recombination is proportional to the product of the concentrations of holes and electrons, and typically it is negligible for clinical exposure rates (i.e. provided the instantaneous x-ray exposure is not too high).

(d) There should be negligible deep trapping of EHPs which means that, for both electrons and holes, the *schubweg* defined as $\mu\tau F >> L$ where μ is the drift mobility, τ' is the deep trapping time (lifetime), F is the electric field and L is the photoconductor layer thickness. The schubweg ($\mu\tau F$) is the distance a carrier drifts before it is trapped and unavailable for conduction. The temporal responses of the x-ray image detector, such as lag and ghosting depend on the rate of carrier trapping.

(e) The diffusion of carriers should be negligible compared with their drift. This property ensures less time for lateral carrier diffusion and leads to better spatial resolution.

(f) The dark current should be as small as possible, because it is a source of noise. This means the contacts to the photoconductor should be non-injecting and the rate of thermal generation of carriers from various defects or states in the bandgap should be negligibly small (*i.e.*, dark conductivity is practically zero). Small dark conductivity generally requires a wide bandgap semiconductor that conflicts with condition (b) above. The dark current should preferably not exceed ~10-1000 pA/cm^2, depending on the clinical application [6].

(g) The longest carrier transit time, which depends on the smallest drift mobility, must be shorter than the image readout time and inter-frame time in fluoroscopy.

(h) The properties of the photoconductor should not change or deteriorate with time because of repeated exposure to x-rays, i.e. *x-ray fatigue* and *x-ray damage* should be negligible.

(i) The photoconductor should be easily coated onto the AMA panel (typically 30 × 30 cm and larger), for example, by conventional vacuum techniques without raising the temperature of the AMA to damaging levels (e.g., ~ 300°C for a-Si panels). This eliminates the possibility of using single crystal materials that would require extended exposure to much higher temperature if they were to be grown directly onto the panel.

(j) The photoconductor should have uniform characteristics over its entire area.

(k) The temporal artifacts such as image *lag* and *ghosting* should be as small as possible (image lag and ghosting are defined in Chapter 2).

The large area coating requirement in (i) over areas typically 30 cm × 30 cm or greater, rules out the use of x-ray sensitive crystalline semiconductors, which are difficult to grow in such large areas. Thus, only amorphous or polycrystalline (poly) photoconductors are currently practical for use in large area x-ray image detectors. Amorphous selenium (a-Se) is one of the most highly developed photoconductors for large area detectors due to its commercial use as an electrophotographic photoreceptor [13]. In fact, the direct conversion flat panel imaging technology has been made possible by the use of two key elemental amorphous semiconductors: a-Si:H (used for TFTs) and a-Se (used for photoconductor layer). Although their properties are different, both can be readily prepared in large areas, which is essential for an x-ray image sensor. Amorphous selenium can be easily coated as thick films (e.g., 100-1000 μm) onto suitable substrates by conventional vacuum deposition techniques without the need to raise the substrate temperature beyond 60-70°C (well below the damaging temperature of the AMA, e.g., ~300°C for a-Si:H panels). Its amorphous state maintains uniform

characteristics to very fine scales over large areas. Thus currently stabilized a-Se (a-Se alloyed with 0.2–0.5%As and doped with 10–40 ppm Cl) is still the preferred choice for x-ray image sensors because it has an acceptable x-ray absorption coefficient, good charge transport properties for both holes and electrons and dark current in a-Se is much smaller than many competing polycrystalline layers [6, 12]. The flat panel x-ray image detectors with an *a*-Se photoconductor have been demonstrated to provide excellent images as shown in Figure 1.3.

Although, stabilized a-Se is still the preferred choice for the photoconductor, there has been an active research to find potential x-ray photoconductors to replace a-Se in flat panel image detectors because of the substantially high $W_{\pm}$ of a-Se compared to other potential x-ray photoconductors [6, 14]. For example, the typical value of the electric field used in a-Se devices is ~ 10 V/μm where the value of $W_{\pm}$ is about 45 eV; the value of $W_{\pm}$ is typically 5-6 eV for polycrystalline mercuric iodide (poly-HgI_2) and polycrystalline Cadmium Zinc Telluride (poly-CdZnTe). The main drawback of polycrystalline materials is the adverse effects of grain boundaries in limiting charge transport and nonuniform response of the sensor due to large grain sizes. Another disadvantage of these polycrystalline detectors is the higher dark current compared to a-Se detectors. However, there has been active research to improve the material properties and reduce the dark currents of polycrystalline HgI_2 and CdZnTe based image detectors [15, 16]. Recent experiments on large area HgI_2, PbI_2, CdZnTe (< 10 % Zn), and PbO polycrystalline x-ray photoconductive layers on AMAs have shown encouraging results [17, 18, 19]. A more detailed description of these potential photoconductors for direct conversion AMFPIs will be presented in Chapter 3.

1.4 Research Objectives

The general objective of this thesis work is the modeling of x-ray photoconductors for direct conversion flat panel x-ray image detector applications based on how charge transport properties (e.g., carrier trapping and recombination) of the photoconductor, operating conditions (e.g., bias voltage and polarity), and the detector geometry

(detector thickness and pixel size) affect the detector performances. Performance studies include x-ray sensitivity, detective quantum efficiency (DQE), resolution in terms of modulation transfer function, and temporal response (ghosting). Some of the x-ray generated carriers (electrons and holes) are trapped in deep trap centers (from which there is no escape over the time scale of charge read out) during their travel towards the electrodes. Carrier trapping reduces collected charge and hence reduces the sensitivity. Trapped charges induce charges at different nearby pixels and reduces resolution. Again, carrier trapping is a random process, creates fluctuation in collected charge and hence creates additional noise. Thus carrier trapping deteriorates signal to noise performance of the image signal and thus reduces DQE. The temporal response caused by charge carrier trapping, recombination and release gives rise to the imaging problems associated with lag and ghosting. The modeling works in this thesis are based on the physics of the individual phenomenon and the systematic solution of the physical equations (e.g., semiconductor continuity equations, Poisson's equation, trapping rate equations etc.) in the photoconductor layer. The general approach of this project is to develop models in normalized coordinates to probe the results to different photoconductive x-ray image detectors. The following subsections will provide a brief outline of the research objectives for this work.

1.4.1 X-ray sensitivity of a photoconductive detector

The x-ray sensitivity of a photoconductive detector is defined as the collected charge per unit area per unit exposure of radiation. High sensitivity increases the dynamic range of the image detector and also permits low patient exposure of radiation or dose. The x-ray sensitivity of a photoconductive detector can be addressed in terms of three controlling factors. The first factor is how much radiation is actually absorbed from the incident radiation that is useful for EHPs generation. This factor is characterized by the quantum efficiency of the detector and depends on the linear attenuation coefficient (α) of the photoconductor and the photoconductor thickness (L). The attenuation coefficient of the photoconductor is x-ray photon energy (E) dependent. The second factor is the generation of EHPs by x-ray interactions which is characterized

by the ionization energy or by the EHP creation energy ($W_{\pm}$) of the photoconductor and the average absorbed energy (E_{ab}) per attenuated x-ray photon of energy E. $W_{\pm}$ depends on the material properties of the photoconductor. E_{ab} depends on the incident x-ray photon energy [20] and the material properties. In some photoconductors (e.g., *a*-Se) $W_{\pm}$ depends on the applied electric field and the incident x-ray photon energy [21, 22]. The third factor is how much of the x-ray generated charge is actually collected in the external circuit. This factor is characterized by the charge carrier drift mobilities (μ) and lifetimes, the applied electric field, and the photoconductor thickness.

The combined effects of x-ray absorption (first factor) and charge transport properties (third factor) on the x-ray sensitivity of a photoconductive detector have been studied in this thesis. An analytical expression for the calculation of charge transport and absorption-limited sensitivity (this sensitivity is called as *normalized sensitivity*) has been developed by considering the drift of electrons and holes in the presence of deep traps under the situation of exponentially decaying distribution of electron hole pair generation across the thickness of the photoconductor. The sensitivity expression can be used to examine the sensitivity of various photoconductor materials as a function of operating conditions (*e.g.* electric field and incident x-ray photon energy), detector thickness, or material properties; carrier ranges ($\mu\tau$') and attenuation coefficients. The sensitivity model is applied to different potential photoconductive detectors.

1.4.2 Detective quantum efficiency of a photoconductive detector

Detective quantum efficiency (DQE) measures the ability of the detector to transfer signal relative to noise from its input to its output. The random nature of image quanta gives rise to random fluctuations in image signals contributing to image formation and hence creates random noises. Images are partially degraded by various sources of statistical fluctuations which arise along the imaging chain. The relative increase in image noise due to an imaging system as a function of *spatial frequency*, *f*', is expressed

quantitatively by the spatial-frequency-dependent detective quantum efficiency, DQE(f'). The DQE(f') of an imaging detector is defined as

$$\mathrm{DQE}(f') = \frac{\mathrm{SNR}_{\mathrm{out}}^2(f')}{\mathrm{SNR}_{\mathrm{in}}^2(f')}, \tag{1.1}$$

where $\mathrm{SNR}_{\mathrm{in}}$ and $\mathrm{SNR}_{\mathrm{out}}$ are the signal to noise ratio at the input and output stages of an x-ray image detector, respectively. DQE(f') is considered as the appropriate metric of system performance and unity for an ideal detector. For simplicity, we are often interested to measure the zero spatial frequency detective quantum efficiency DQE (f' = 0) of an imaging detector. DQE(0) represents signal quality degradation due to the signal and noise transfer characteristics of the system without considering signal spreading.

The random nature of charge carrier trapping in the photoconductor layer creates fluctuation in collected charge and hence creates additional noise. Thus carrier trapping deteriorates signal to noise performance of the image signal and thus reduces DQE. The effects of charge carrier trapping (i.e. incomplete charge collection) on the DQE(0) of a photoconductive detector are examined by considering x-ray interaction depth dependent conversion gain and depth dependent charge collection efficiency. The x-ray image in fluoroscopy is highly sensitive to added noise because of its low exposure rate. The DQE(0) of a photoconductive detector for a fluoroscopic application is analyzed as a function of charge transport parameters and photoconductor thickness with varying amounts of electronic noise and exposure under (a) constant field, and (b) constant voltage operating conditions. The optimum detector thickness for maximum possible DQE(0) is investigated as a function of x-ray exposure, electronic noise and bias voltage. The DQE of an *a*-Se x-ray image detector for actual broad x-ray spectrum emitted from a typical x-ray tube is calculated. This DQE of a polyenergetic x-ray beam is also compared with the DQE of a monoenergetic x-ray beam having the same average photon energy and the validity of using average energy concept in x-ray detector modeling is examined.

1.4.3 Resolution of a direct conversion flat panel detector

The study of spatial resolution characteristics of an imaging detector is an important measure of examining the quality of images that it produces. Resolution or resolving power is the ability to record separate images of small objects that are placed very closely together. The spatial resolution of an imaging device or a system is described in terms of the modulation transfer function (MTF), which is the relative response of the system as a function of spatial frequency.

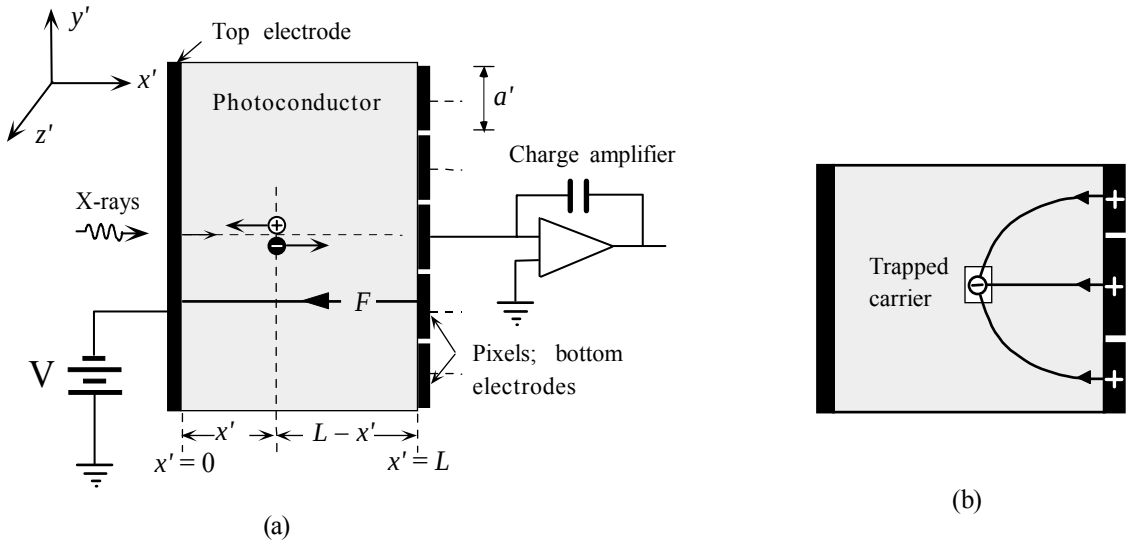

Figure 1.8 (a) A cross section of a direct conversion pixellated x-ray image detector. (b) Trapped carriers in the photoconductor induce charges not only on the central pixel electrode but also on neighboring pixel electrodes, spread the information and hence reduce spatial resolution [14].

The direct conversion flat-panel detector geometry consists of a photoconductor layer sandwiched between two electrodes; the electrode at one side is a continuous metal plate and the electrode on the other side of the photoconductor is segmented into an array of individual square pixels of size $a' \times a'$ as shown in figure 1.8(a). There is a gap of negligible dimension between the pixel electrodes. Suppose that a carrier is trapped in the photoconductor above a particular (central) pixel electrode of a pixellated image sensor. This trapped carrier induces charges not only on the central pixel

electrode but also on neighboring pixel electrodes as shown in figure 1.8(b), and consequently there is a lateral spread of information and hence a loss of image resolution. An analytical expression of MTF due to distributed carrier trapping, MTF_{trap}, in the bulk of the photoconductor is derived using the trapped charge distribution across the photoconductor. The analytical expressions of trapped charge distributions (for both electrons and holes) are also derived. The MTF_{trap} of photoconductive x-ray detectors is studied for (a) different levels of carrier trapping of both carrier types (electrons and holes) and (b) different values of x-ray absorption depths.

1.4.4 X-ray sensitivity of a pixellated x-ray image detector

If x rays are incident over a particular pixel volume of a pixellated detector, the radiation-receiving pixel and also the neighboring pixels collect charges due to carrier trapping effects. The collected charge at the radiation-receiving pixel is the desired signal and contributes to sensitivity. The x-ray sensitivity of a pixellated detector is defined as the collected charge per unit area per unit exposure of radiation for a pixel that is assumed to receive the radiation. Therefore, we need to calculate the collected charge at a particular pixel by considering x-ray radiation over its entire area. The X-ray sensitivity is influenced by the pixel size in addition to the photoconductor properties, operating conditions and the detector thickness. The charge collection and absorption-limited x-ray sensitivity of a pixellated detector (e.g. flat panel detector) is modeled by incorporating charge carrier trapping and small pixel effects. The sensitivity of a direct conversion pixellated x-ray detector is studied as a function of pixel size for various levels of both types of carrier trappings (electrons and holes).

1.4.5 Effects of repeated x-ray exposure on x-ray sensitivity of an a-Se detector

Recently, it is experimentally found that the x-sensitivity of an a-Se x-ray image detector deceases in subsequent exposures [23, 24]. Several simplifying assumptions can be made for a single and low exposure case; (i) the electric field is relatively uniform, (ii) the loss of carriers by deep trapping is more significant than carrier

recombination, and (iii) there is no trapped charge in the photoconductor before x-ray exposure. While these are valid assumptions for a single and low x-ray exposure case, for the repeated x-ray exposure case one must also consider the trapped charges from previous exposures, the recombination between drifting and trapped charge carriers, space charge effects on the electric field and hence field dependent charge carrier generation (ionization) in the photoconductor.

The bulk carrier trapping has the following effects. (i) A trapped charge in the photoconductor due to previous exposure may act as a charge capture center for oppositely charged carriers. The trapped charge may recombine with subsequently generated opposite charge carriers and thus reduces the charge collection efficiency. (ii) The trapped carrier concentrations may become relatively large after a few consecutive x-ray exposures. These trapped charges modify the electric field distribution across the photoconductor, change the conversion gain and hence modify the new carrier generation in subsequent exposures. Therefore, the x-ray sensitivity in subsequent exposures is modified which has been found to be the dominant source for ghosting in a-Se x-ray image detectors [23, 24]. It is also reported in the literature that x-ray exposure can create meta-stable deep trap centers in the bulk of a-Se [25, 26, 27], which further reduces the sensitivity. The dependence of the sensitivity of x-ray image detectors on x-ray exposure and exposure history is studied in this thesis incorporating all the effects mentioned above. The comparison of the model against the experimental data allows a quantitative explanation of the mechanisms that cause ghosting.

1.4.6 Effects of large signals on charge collection

The bulk recombination between drifting holes and electrons is proportional to the product of the concentrations of holes and electrons, and typically it is very small provided the carrier generation rate is not too high. However, this bimolecular recombination has very adverse effect on charge collection at very high carrier generation regime; because the collected charge exhibits a square root dependence on the x-ray intensity in the recombination-limited regime of detector operation. The study

of the effects of bimolecular recombination on the charge collection efficiency shows an upper limit of the small signal operation (up to a level of the photogeneration rate the recombination practically plays no role) and how the bimolecular recombination affects the charge collection (or the x-ray sensitivity). The carrier generation rate can be related to x-ray exposure depending on the material properties of the photoconductor used in the x-ray detector. The recombination coefficient/rate is different in different photoconductors. The effects of carrier generation rate (or the x-ray exposure rate) on the charge collection efficiency are examined by considering bimolecular recombination and x-ray induced new trap center generation. The numerical results are also compared with experimental data. The comparison of the model against the experimental data reveals a quantitative explanation of the mechanisms that cause signal nonlinearity as a function of exposure rate.

1.5 Thesis Outline

This thesis is divided into nine chapters. Following this introductory chapter, a review of useful theories, definitions and explanations of important terms for image detectors is given in Chapter 2. A discussion of the properties of the potential photoconductors for x-ray image detectors is presented in Chapter 3. The model and results on x-ray sensitivity and DQE of a photoconductive detector are presented in Chapter 4 and 5, respectively. Chapter 6 describes the MTF model and results due to distributed carrier trapping in the bulk of the photoconductor. The x-ray sensitivity of a pixellated x-ray image detector is presented in Chapter 7. The effect of large signals on charge collection efficiency and the reduction in x-ray sensitivity due to previous exposure and exposure history are studied in Chapter 8. The conclusions drawn from the theoretical calculations are presented in Chapter 9, along with some recommendations for future works.

2. BACKGROUND THEORY

2.1 Introduction

Thermally generated charge carriers in the bulk of x-ray photoconductors are negligibly small and the photoconductors act as insulators in the dark (without illumination). The charge collection in the external circuit follows certain mechanism. Some theories and concepts necessary to understand the charge collection mechanism and imaging characteristics of x-ray image detectors are discussed in this chapter.

2.2 Shockley-Ramo Theorem

When x rays are absorbed in a detector material, a cloud of many electron-hole pairs is created. If the detector material is a doped semiconductor, or ionic material, free charges move to surround mobile charges, effectively screening their fields from being sensed at macroscopic distances. Since charge neutrality is maintained at all points in these detectors, no electrode currents are observed until moving carriers actually reach the electrodes. However, there is no reservoir of free carriers available in photoconductor materials to surround drifting carriers and maintain local charge neutrality, at least not on the time scale of interest. The characteristic relaxation time of a medium is given by $\tau_R = \varepsilon\rho$, where ρ is the resistivity, and $\varepsilon = \varepsilon_0\varepsilon_r$ is the dielectric constant of the material. For a-Se having a resistivity of 10^{14} Ω cm, and a relative dielectric constant of 6.7, the relaxation time is ~ 1 min, which is very long compared to typical carrier transit times of few microseconds. Therefore, currents resulting from introduction of mobile carriers into the photoconductive detector are due entirely to induction.

The Shockley-Ramo's theorem provides a convenient way to calculate the induced current flowing through an electrode of multi-electrode detectors (e.g. pixellated image detector) due to the motion of charge carriers in the detector. The induced current I_j and charge Φ_j on an electrode j by a moving point charge e at x', as shown in figure 2.1 (a), are given by [28, 29, 30],

$$I_j = e\mathbf{v} \cdot \mathbf{F}_{wj}(x') \tag{2.1}$$

$$\Phi_j = -eV_{wj}(x') \tag{2.2}$$

where v is the instantaneous velocity of charge e, $F_{wj}(x')$ and $V_{wj}(x')$ are the weighting field and potential of electrode j. $F_{wj}(x')$ and $V_{wj}(x')$ are the electric field and potential that would exist at charge e's instantaneous position x' if the electrode of interest (j) is raised to unit potential and all other electrodes kept at zero potential and all charges removed. V_{wj} is unitless and the unit of F_{wj} is m^{-1}.

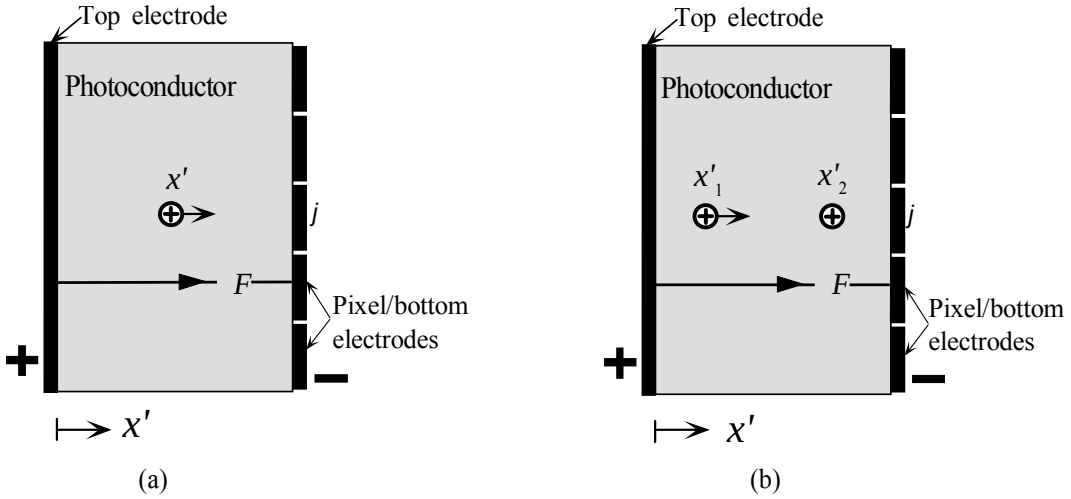

Figure 2.1 A cross section of a multi-electrode detector. (a) A positive point charge at x' is drifting by an applied field. (b) A point charge is moved from point x'_1 to x'_2.

Let a positive point charge be moving from x'_1 to x'_2. Φ_{j1} and Φ_{j2} are the induced charges at electrode j when the charge is at x'_1 and x'_2, respectively. The induced

charges, $\Phi_{j1} = -eV_{wj}(x'_1)$ and $\Phi_{j2} = -eV_{wj}(x'_2)$. The collected charge at electrode j for moving a positive point charge from x'_1 to x'_2 is given by,

$$Q_j = -\left(\Phi_{j2} - \Phi_{j1}\right) = e\left[V_{wj}\left(x'_2\right) - V_{wj}\left(x'_1\right)\right] \tag{2.3}$$

For a large area single-element detector, as shown in figure 2.2 (a), $F_w(x) = 1/L$, $V_w(x') = x'/L$, and thus current, $i = ev/L$ [31], where L is the photoconductor thickness. In this case, the collected charge at the electrode for moving a positive point charge from x_1 to x_2 is simply,

$$Q_j = -\left(\Phi_{j2} - \Phi_{j1}\right) = e\frac{\left(x'_2 - x'_1\right)}{L} \tag{2.4}$$

If there is carrier trapping, only a fraction of photogenerated charge is collected in the external circuit. Consider an electron and a hole (an EHP) are generated at x' and drift under the influence of the electric field as shown in Figure 2.2 (b). The average electron and hole photocurrents are $i_e(t') = (ev_e/L)\exp(-t'/\tau'_e)$ and $i_h(t') = (ev_h/L)\exp(-t'/\tau'_h)$, respectively; where $v_e = \mu_e F$, $v_h = \mu_h F$, e is the elementary charge, μ is the carrier mobility and τ' is the carrier lifetime. The subscripts e and h refer to electrons and holes respectively. Both types of carrier drifts produce currents of the same polarity at any electrode. Therefore, the collected charge at any electrode is the sum of the contributions of both types of carrier transports. The average collected charge is,

$$\begin{aligned} Q(x') &= \int_0^{t_e} i_e(t')dt' + \int_0^{t_h} i_h(t')dt' \\ &= \frac{e\mu_e\tau'_e F}{L}\left[1 - e^{-x'/\mu_e\tau'_e F}\right] + \frac{e\mu_h\tau'_h F}{L}\left[1 - e^{-(L-x')/\mu_h\tau'_h F}\right], \end{aligned} \tag{2.5}$$

where $t_e = x'/\mu_e F$ and $t_h = (L - x')/\mu_h F$ are the electron and hole transit times, respectively. Equation (2.5) is the well-known ***Hecht equation*** for calculating the average collected charge.

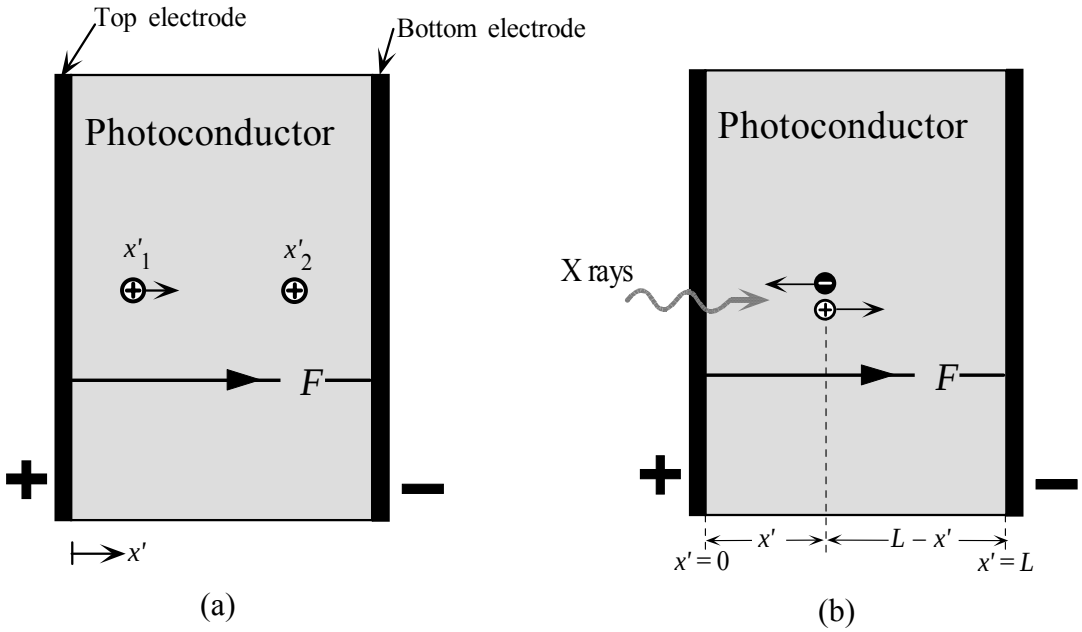

Figure 2.2 A cross section of a large area single detector. (a) A point charge is moved from point x'_1 to x'_2. (b) An electron and a hole are generated at x' and drift under the influence of the electric field.

2.3 X-ray Interactions in Photoconductor

A portion of the incident x rays is attenuated in the photoconductor layer of the detector. Attenuation is the removal of x-ray photons from the x-ray beam by either absorption or scattering events in the photoconductor layer. The fraction of the x-ray photons that are attenuated in the photoconductor layer is called the quantum efficiency η of the detector, and η is determined by the linear attenuation coefficient α and the photoconductor thickness L as $\eta = 1 - e^{-\alpha L}$.

The range of x-ray energies for diagnostic medical x-ray imaging is from 10 keV to 120 keV. These x rays interact with matter by three different mechanisms. The types of interactions are the photoelectric effect, Rayleigh scattering and Compton scattering. The incident x rays can be completely absorbed in the medium (photoelectric effect) or scattered (Rayleigh or Compton scattering).

Rayleigh scattering involves the elastic (coherent) scattering of x rays by atomic electrons. The energy of the scattered x ray is identical to that of the incident x ray. There is no exchange of energy from the x ray to the medium. However, the scattered x ray experiences a change in its trajectory relative to that of the incident x ray, and this has a bad effect in medical imaging, where the detection of scattered x rays is undesirable. *Compton* scattering involves the inelastic (incoherent) scattering of an x-ray photon by an atomic electron. Compton scattering typically occurs when the energy of the x-ray photon is much greater than the binding energy of the atomic electron. Therefore, the Compton effect occurs with outer-shell of the atom, essentially free electrons in the medium. This interaction includes an electron of kinetic energy E'', an ionized atom, and a scattered x-ray photon of energy E' that is lower than the incident photon energy E. Thus some energy is imparted to the medium in Compton scatting event. The imparted energy depends on the scattering angle which is random. *Rayleigh* and Compton scattering processes are illustrated in Figure 2.3.

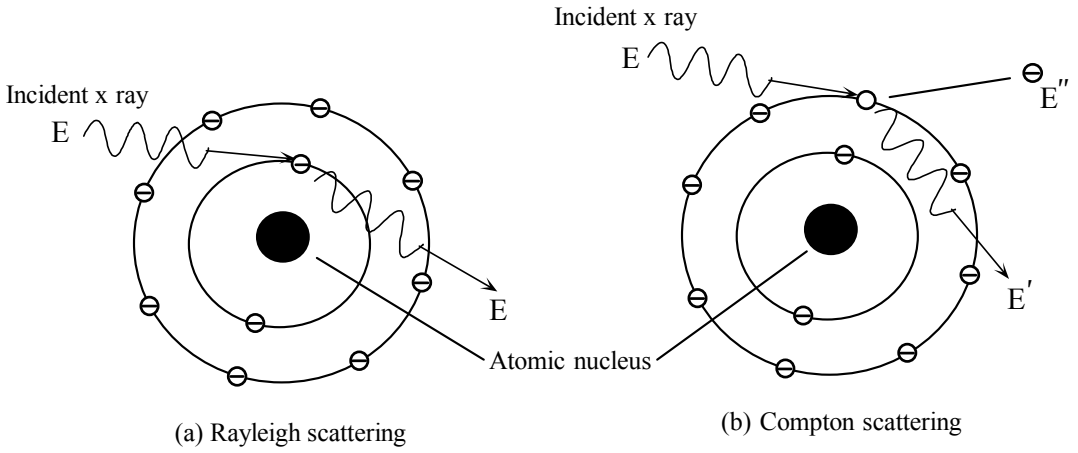

Figure 2.3 (a) The incident x ray interacts with the electric field of an orbiting electron and is scattered in Rayleigh scattering process. (b) In Compton scattering, an incident x ray interacts with an outer-shell electron, and creates an electron of kinetic energy E'', an ionized atom, and a scattered x-ray photon of energy E' [20].

In the photoelectric interaction, the incident x ray interacts with an electron in the medium, and all its energy is transferred to the electron. Part of this energy is used to overcome the binding energy of the electron, and the remaining fraction becomes the

kinetic energy of the photoelectron. The atom becomes ionized. If the energy of the incident x ray is less than the binding energy of the electron, photoelectric interaction with that electron is energetically unfeasible and will not occur. K-shell (inner most shell) electrons are bound more tightly to the atom (higher binding energy) than outer-shell (L shell, M shell and so on) electrons. Thus, if photoelectric interaction is energetically unfeasible with K-shell electrons, interaction may still occur with an outer-shell electron. The binding energy associated with the K shell is called the K *edge* and so on. If an electron is liberated from an inner core shell, then there exists a vacancy in its parent atom. A cascade of electron transitions can take place, which can produce one or more *characteristics* x rays (also called *fluorescent* x rays) or alternately a series of nonradiative transitions involving *Auger* electrons will take place, resulting in the complete local deposition of energy through charged particles. The *characteristics* x rays are named as K-fluorescent, L-fluorescent etc. based on the electron receiving shell. The photoelectric process is illustrated in Figure 2.4.

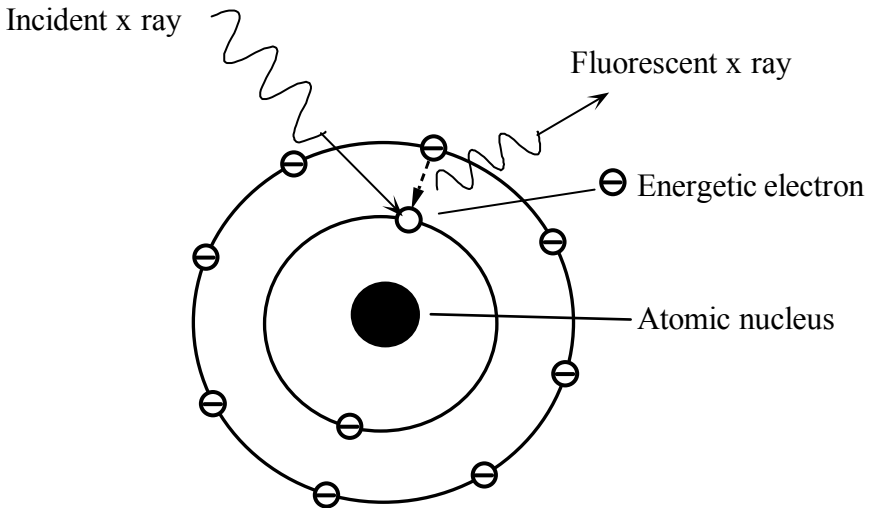

Figure 2.4 In the photoelectric effect, the energy of an incident x ray is fully absorbed by an electron, which is ejected from the atom causing ionization. An electron from the outer shell fills the vacancy in the inner shell, which creates a fluorescent x ray.

Energetic primary electrons created by photoelectric effect or Compton scattering travel in the solid, can cause ionization along its track and create many electron-hole

pairs (EHPs). They can also interact with matter and produce bremsstrahlung radiation. When energetic electrons approach very close to the nucleus of the atom, they interact with the Coulomb field of the nucleus and orbit partially around the nucleus, and hence decelerate with the reduced energy. The loss in energy will appear as *bremsstrahlung* (breaking) radiation as illustrated in Figure 2.5.

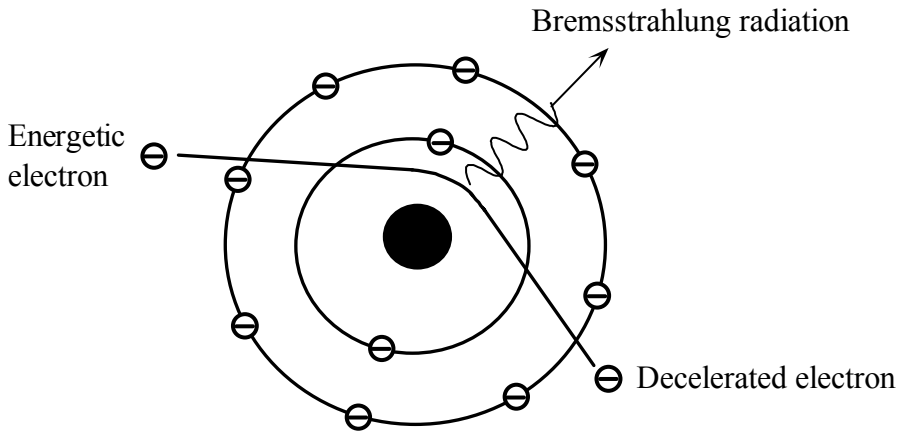

Figure 2.5 Bremsstrahlung radiation is produced when energetic electrons are decelerated by the electric field of target nuclei.

The whole x-ray interaction processes in the absorbing medium (e.g., photoconductor) are shown in the Figure 2.6. Primary interaction of x-rays with the medium can be divided into two main categories. First the creation of scattered photons which include scattered x rays through Compton and Rayliegh scattering events, and the characteristics x-rays from photoelectric effect. Second the creation of high energy photoelectrons by the photoelectric effect and the Compton scattering event. The high energy photoelectron imparts energy to the medium and hence creates EHPs, and also some of its energy can be lost by bremsstrahlung radiation. The entire process is random. However, the average energy absorbed in the medium by the primary x-ray interaction can be determined and is described by the energy absorption coefficient α_{en}. Thus $(\alpha_{en}/\alpha)E$ is the average absorbed energy E_{ab} by primary x-ray interaction per attenuated x-ray photon of energy E. For sufficiently thick medium, the escaped radiations from the primary interaction site can interact with atomic electrons of the

medium like primary x rays (events A & B in Figure 2.6) but at different points. Thus the actual average absorbed energy per attenuated x-ray photon of energy E in a very thick detector is higher than $(\alpha_{en}/\alpha)E$ (see section 5.2.1 for further details).

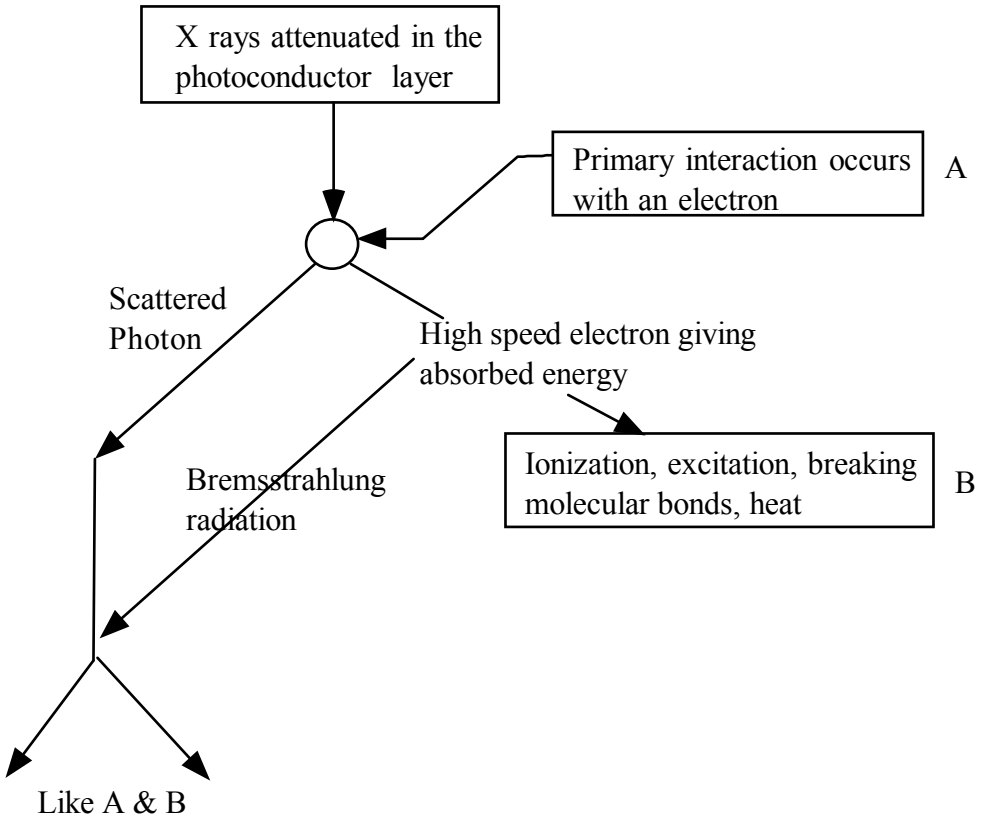

Figure 2.6 A number of different interactions are possible when an x-ray photon enters a material [32].

The total mass attenuation and energy absorption coefficients of a-Se as a function of photon energy for diagnostics medical x rays are shown in Figure 2.7. Figure 2.7 also shows the individual contribution of photoelectric effect, Rayleigh scattering and Compton scattering to the total attenuation. The mass attenuation (or energy absorption) coefficient of a material is the attenuation (or energy absorption) coefficient divided by its density. The photoelectric effect is the dominant interaction process in a-Se for diagnostics medical x rays as shown in Figure 2.7. There is an abrupt jump in the total attenuation or energy absorption coefficient of a-Se at the photon energy of 12.66 keV

(K-edge energy in a-Se) because of the onset of photoelectric interaction of x rays with K-shell electrons.

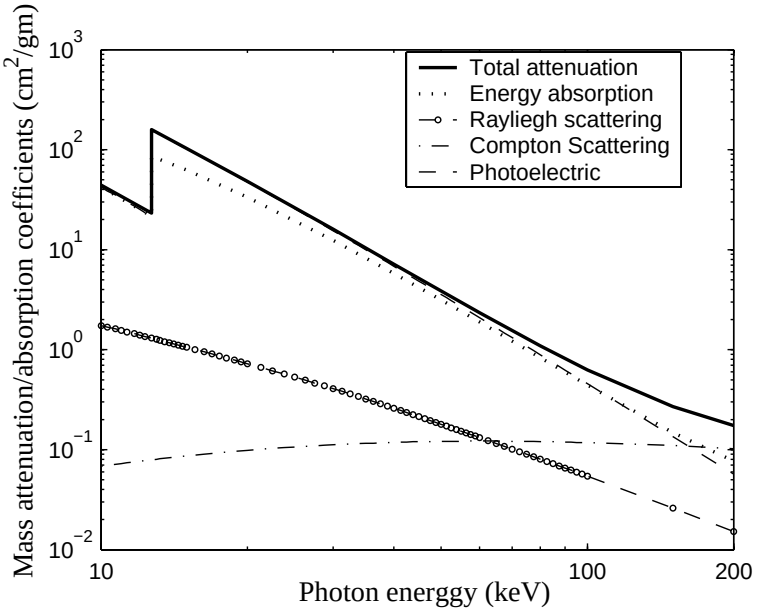

Figure 2.7 The total mass attenuation and energy absorption coefficients in a-Se versus photon energy. This figure also shows the individual contribution of photoelectric effect, Rayleigh scattering and Compton scattering to the total attenuation [33].

2.4 Ionization Energy (EHP Creation Energy) $W_{\pm}$

The amount of radiation energy $W_{\pm}$ absorbed by a medium to create a single *free* electron hole pair (EHP) is called the ionization energy or the EHP creation energy. This must be as low as possible because the free (or collectable) charge generated from an absorbed radiation of energy E_{ab} is simply $eE_{ab}/W_{\pm}$. The x-ray sensitivity of a photoconductive detector largely depends on $W_{\pm}$.

The creation of EHPs by an incident energetic particle or an x-ray photon first involves the generation of an energetic primary electron. As this energetic photoelectron travels in the solid, it causes ionization along its track and creates many EHPs. In this way, one x-ray photon can create hundreds or thousands of EHPs. The ionization

energy $W_{\pm}$ is the average absorbed energy required to create a single EHP. For many semiconductors the energy $W_{\pm}$ required to create an EHP has been shown to depend on the energy bandgap E_g via *Klein's rule* [34],

$$W_{\pm} \approx 2.8E_g + E_{phonon} \tag{2.6}$$

The phonon energy term E_{phonon} is small < 0.5 eV) so that typically $W_{\pm}$ is close to $2.8E_g$. Further in many crystalline semiconductors, $W_{\pm}$ is field independent and well defined. This $W_{\pm}$ is so well defined in crystalline semiconductors, such as high purity Si and Ge crystals, that they are used in spectrometers to measure the energy of x-rays [35]. $W_{\pm}$ can be easily calculated for various crystalline solids, but there are also a number of solids such as a-Si:H, HgI_2 and PbI_2 that have $W_{\pm}$ values less than that predicted by Klein's rule.

Recently, Que and Rowlands argued that if the conservation of **k** rule is relaxed, then instead of Klein's rule, the value of $W_{\pm}$ should be about $2.2E_g + E_{\text{phonon}}$ [36]. Since amorphous material is inherently disordered, crystal momentum (**k** rule) is not conserved in these materials and the value of $W_{\pm}$ should be $2.2E_g + E_{\text{phonon}}$. The photoconductor requirement of negligible dark currents implies that the semiconductor should have a wide bandgap which, however, leads to a higher $W_{\pm}$ and lower x-ray sensitivity. In some photoconductors (e.g., *a*-Se) $W_{\pm}$ depends on the applied electric field and the incident x-ray photon energy [21, 22], whose origin has not been conclusively identified and is currently a topical research area [37].

2.5 X-ray Sensitivity

The x-ray sensitivity of an image detector is defined as the collected charge per unit area per unit exposure of radiation,

$$S = \frac{Q}{AX}, \tag{2.7}$$

where Q is the collected charge in Coulomb (C), A is the radiation-receiving area in cm^2, and X is the radiation exposure in Roentgen (R), as shown Figure 2.8. The unit of sensitivity is C cm^{-2} R^{-1}. One *Roentgen* is the quantity of radiation that creates ions carrying a total charge of 2.58 x 10^{-4} Coulombs per kg of air. It has been found that on average, it takes 33.97 eV to produce an ion pair in air, and this is equal to 33.97 J/C. Thus the energy absorbed in air by a 1 R exposure is, 2.58 x 10^{-4} C/kg × 33.97 J/C = 0.00876 J/kg. The schematic diagram representing the equivalent circuit of a photoconductive detector is shown in Figure 2.8. A photoconductor layer is sandwiched between two large area parallel plate electrodes. A current integrating amplifier is connected to the pixel electrode (bottom electrode) and measures the collected charge by integrating the induced x-ray photocurrent through the pixel electrode (the integration time is longer than the exposure time). The radiation-receiving electrode (top electrode) is biased with a voltage V to establish an electric field F in the photoconductor. The biasing voltage can be positive or negative. The x-ray generated electrons and holes are drifted in opposite directions by the applied field and give rise to a transient x-ray photocurrent and the integration of the photocurrent is the collected charge.

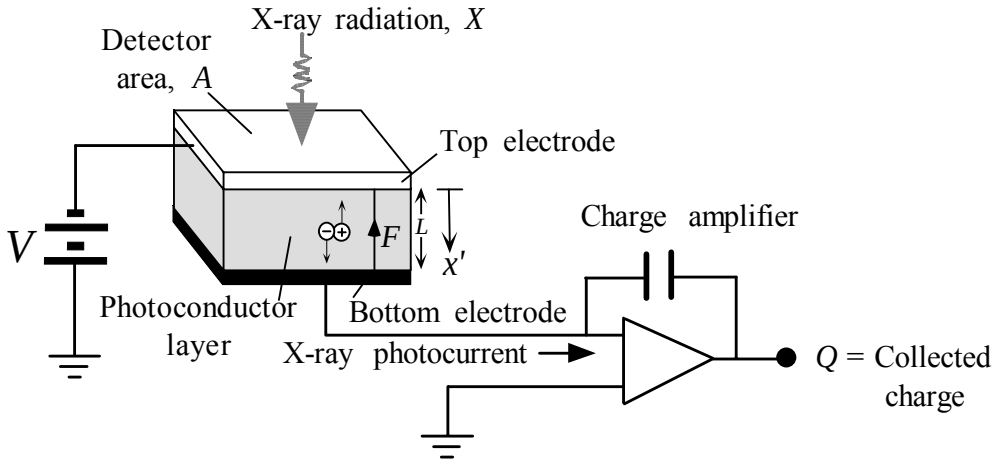

Figure 2.8 Schematic diagram represents the equivalent circuit of a photoconductive x-ray image detector. The x-ray radiation is incident over an area A and the electric field F is established by applied bias voltage V.

2.6 Resolution/Modulation Transfer Function

Modulation transfer function (MTF) measures the efficiency of an imaging system such as a detector to resolve (transfer) different spatial frequencies of information in an image. In other words, MTF is the relative signal response of the system as a function *spatial frequency f'*. Consider an image that is made up of a periodic array of black lines separated by white spaces as shown as A in Figure 2.9. Then, each cycle becomes a line pair-the bright stripe and its neighboring dark stripe. The distance of a dark stripe and its neighboring bright stripe in A is 1 mm. The spatial frequency of this periodic image is therefore 1 line pairs per millimeter, 1 lp/mm. Thus, the units of spatial frequency are usually expressed as line pairs/mm (lp/mm), instead of cycles/mm. The spatial frequencies of images in B and C are 2 lp/mm and 4 lp/mm, respectively. The ability of the detector to resolve the image is shown below the image. The detector is able to 100% resolve in A, to good extent in B, but the information in C is totally lost which represents 0% resolving ability.

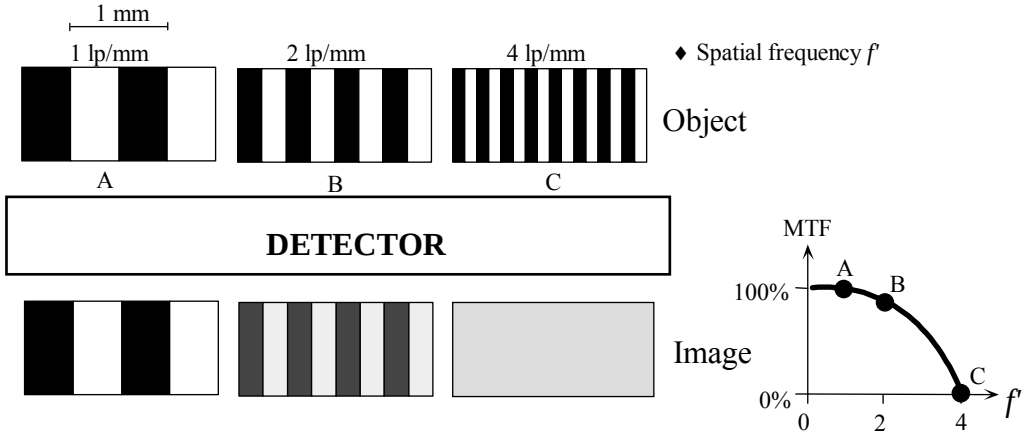

Figure 2.9 Modulation transfer function (MTF) measures the efficiency of a detector to resolve (transfer) different spatial frequencies of information. The detector is able to 100% resolve A, to good extent B, but the information in C is totally lost which represents 0% resolving ability.

Resolution or resolving power is the ability to record separate images of small objects that are placed very closely together. The overall resolution of a system can be expressed as a convolution of the component resolutions. However, the spatial

resolution of an imaging device or a system can also be described in terms of the MTF. The MTF of an imaging system can be described as a cascade of several stages where the overall MTF is simply the product of the MTF of all the individual stages. The MTF(*f*) is a much more convenient descriptor of spatial response since the resolving power as a multiplication is much more easily comprehended than convolution. The response of the system to a delta function is called the *point spread function* (PSF). It contains all of the deterministic spatial-transfer information of the system. The MTF is just the two-dimensional Fourier-Transform amplitude of the PSF as a function of spatial frequency. In practice, a one-dimensional MTF plot is usually used because it is almost impossible to measure a true two-dimensional MTF. In that case, one-dimensional MTF is the one-dimensional Fourier transform of *line spread function* (LSF). The LSF is the response of a system to a "line" delta function as shown in Figure 2.10. The overall MTF (or presampling MTF) of an image detector can be expressed as,

$$\mathrm{MTF}(f') = \mathrm{MTF}_{\mathrm{m}}(f') \times \mathrm{MTF}_{\mathrm{a}}(f'), \tag{2.8}$$

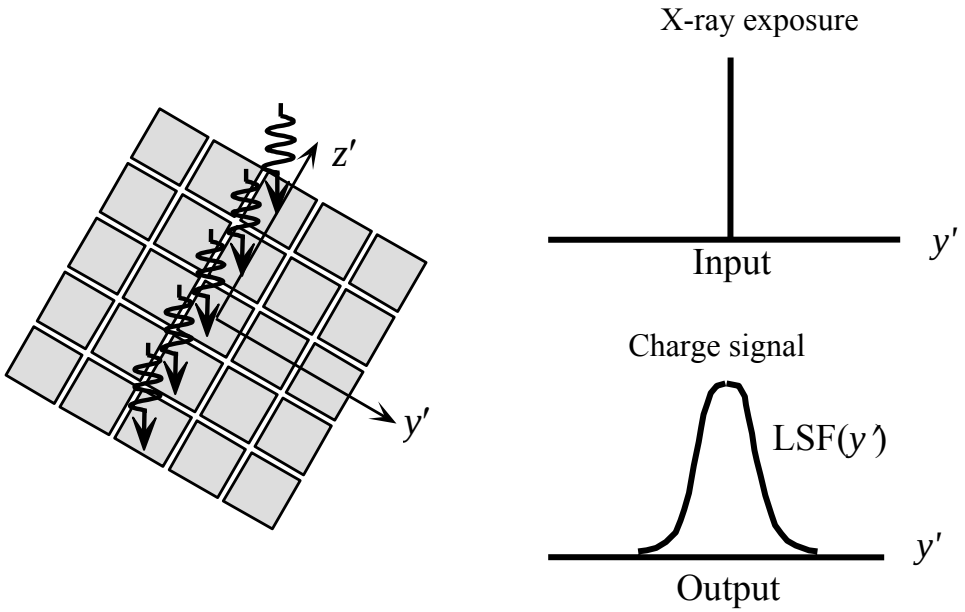

Figure 2.10 X-rays are incident along a line (along z' in the figure) over an x-ray image detector, where $y'z'$ plane represents the plane of the detector. The x-ray incidence along y' is a delta function. The output charge signal along y is spread out which presents the LSF.

where $MTF_m(f')$ is the modulation transfer function of the detector material and $MTF_a(f')$ is the modulation transfer function associated with the aperture function of the pixel electrodes. $MTF_a(f')$ arises due to averaging the signal over the pixel aperture area. The aperture MTF describes how spatial frequencies are passed through the detector elements. Active portion of detector element determines the spatial frequency response.

The *geometric* pixel aperture width in a flat panel detector is smaller than the pixel pitch as shown in Figure 2.11 (for simplicity, a square pixel aperture is assumed). The center-to-center spacing between two pixels is called *pixel pitch*. If the aperture is square with dimension a', then, $MTF_a(f')$ will be of the form $\text{sinc}(a'f')$, where $\text{sinc}(a'f')$ is

$$MTF_a(f') = \left|\text{sinc}(a'f')\right| = \left|\frac{\sin(\pi a'f')}{\pi a'f'}\right| \tag{2.9}$$

The $MTF_a(f')$ as a function of f' is shown in Figure 2.11 (b). Note that the first zero of $MTF_a(f')$ occurs at the spatial frequency $f' = 1/a'$.

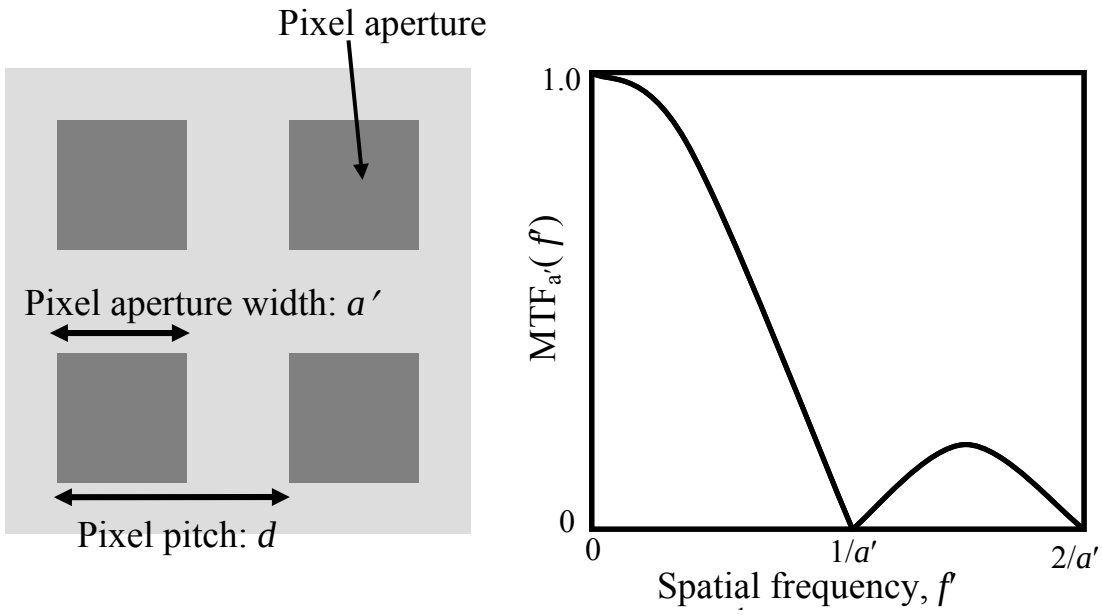

Figure 2.11 (a) Pixel aperture width and pixel pitch. (b) $MTF_a(f')$ as a function of f'. First zero of $MTF_a(f')$ occurs at the spatial frequency $f' = 1/a'$ [38].

The spacing between the samples (pixel pitch) on a digital image determines the highest frequency (*Nyquist frequency*, f_{ny}) that can be imaged. If the spacing between the samples is d, then $f_{ny} = 1/(2d)$ and aliasing will occur for frequencies between $1/(2d)$ and $1/a'$.

2.7 Noise Power Spectrum

Noise Power Spectrum (NPS) is the Fourier transform of the covariance function of a random process. The autocovariance describes the correlation of a random variable $g(x')$ with itself at a location displaced by x' about the expected values. If the process is wide-sense-stationary (WSS), then the NPS is commonly called Wiener spectrum, which is the Fourier transform of the auto covariance function. The $NPS(f')$ describes the spectral decomposition of the noise variance, i.e., the noise variance between spatial frequencies f' and $(f' + df')$. If a one-dimensional random variable $g(x')$ is real, $NPS_g(f')$ is also real. X rays transmitted through a patient and incident on an imaging detector

form an x-ray quantum image. The quantum image must be interpreted as distributions in the mathematical sense, having dimension area^{-1} for a two dimension image. If the two-dimensional image quanta are uncorrelated, the NPS is flat and simply equal to the expected number of quanta per unit area. For example, a uniform distribution of x rays coming from a medical x-ray tube are uncorrelated and the NPS = $\overline{\Phi}_0$, where $\overline{\Phi}_0$ is the mean incident x-ray fluence (photons per unit area) on a detector. But the distribution of secondary quanta (x rays to charge carriers or light) always have an uncorrelated component, they may also have a correlated component. Therefore, the NPS of a distribution of secondary quanta may have a frequency-dependent component extending to essentially infinite frequencies.

2.8 Detective Quantum Efficiency

Detective quantum efficiency (DQE) measures the ability of the detector to transfer signal relative to noise from its input to its output. The random nature of image quanta gives rise to random fluctuations in image signals contributing to image formation and hence creates random noises. The scattering of image quanta gives rise to image blurring which is quantified by modulation transfer function MTF(f'). Images are partially degraded by various sources of statistical fluctuations which arise along the imaging chain. The relative increase in image noise due to an imaging system as a function of *spatial frequency*, f', is expressed quantitatively by the spatial-frequency-dependent detective quantum efficiency, DQE(f'). The DQE(f') represents signal to noise transfer efficiency for different frequencies of information in an image. The DQE(f') of an imaging detector is defined as

$$\mathrm{DQE}(f') = \frac{\mathrm{SNR}_{\mathrm{out}}^2(f')}{\mathrm{SNR}_{\mathrm{in}}^2(f')}, \tag{2.9}$$

where $\mathrm{SNR}_{\mathrm{in}}$ and $\mathrm{SNR}_{\mathrm{out}}$ are the signal to noise ratio at the input and output stages of an image detector, respectively. DQE(f') is considered as the appropriate metric of system performance and unity for an ideal detector. For simplicity, we are often interested to measure the zero spatial frequency detective quantum efficiency DQE (f' = 0) of an

imaging detector. DQE(0) represents signal quality degradation due to the signal and noise transfer characteristics of the system without considering signal spreading. The relation between DQE(0) and DQE(f') is given by

$$\mathrm{DQE}(f') = \frac{\mathrm{DQE}(0)\mathrm{MTF}^2(f')}{\mathrm{NPS}_0(f')} \tag{2.10}$$

where MTF(f') is the overall system modulation transfer function and $\mathrm{NPS}_0(f')$ is the noise power spectrum of the system normalized to unity as f' approaches 0.

2.9 Dynamic Range of an Imaging System

Dynamic Range of an Imaging System describes the maximum variation in signal over which the detector output represents the photon fluence without losing significant amounts of information. The dynamic range is defined by

$$DR = \frac{X_{\max}}{X_{noise}}, \tag{2.11}$$

where $X_{\max}$ is the x-ray fluence corresponding to the maximum signal that the detector can accommodate and X_{noise} is the fluence that provides a signal equivalent to the quadrature sum of the detector noise and the x-ray quantum noise. A system with low dynamic range has high contrast but only over a limited portion of the image. The larger the dynamic range, the more gradual the contrast representing the range from maximal to minimal x-ray intensity. Therefore, the greater the dynamic range the better the contrast resolution. High dynamic range detectors have the potential to switch its use between low exposure fluoroscopic imaging and higher exposure radiographic imaging modes. The dynamic range requirements differ among different imaging tasks. But there are some general principles for determining the requirements of each modality. If we have mean exposure X_{mean} for a system, a multiplicative factor is necessary to get a range of exposure values above and below X_{mean}. For example, a dynamic range of 100:1 is acceptable; then, the range of exposures should be between $X_{\mathrm{mean}}/10$ and 10 X_{mean}. Therefore, X_{mean} is the geometric mean of the acceptable highest and lowest exposures. The dynamic ranges of 400:1 and 100:1 are generally acceptable for mammographic and chest radiographic digital x-ray imaging systems respectively.

2.10 Image Lag and Ghosting

Lag is the carry-over of image charge generated by previous x-ray exposures into subsequent image frames. The residual signal fractions following a pulsed x-ray irradiation are referred to as "image lag". It is revealed as changes in dark images, i.e., readout of the detector without an x-ray exposure. Lag is manifested as an increase in pixel values in previously exposed areas as shown in Figure 2.12 (a).

Ghosting is the change of x-ray sensitivity of the x-ray image detector as a result of previous exposure to radiation. In the presence of ghosting, a shadow impression of a previously acquired image is visible in subsequent uniform exposure as shown in Figure 2.12 (b). Ghosting is manifested as a reduction in pixel sensitivity in previously exposed areas and can only be seen with subsequent x-ray images. Ghosting can affect the diagnostic value of x-ray images in particular when images are acquired in a fast sequence, e.g., in fluoroscopy.

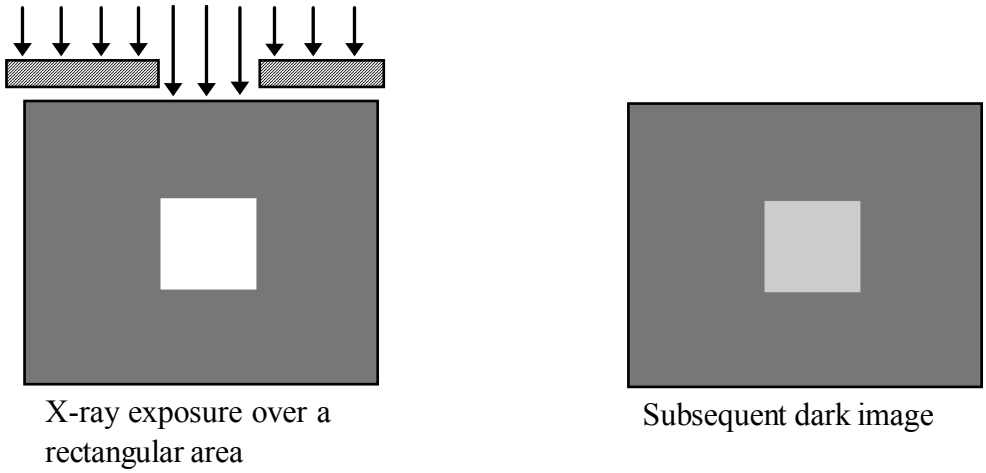

(a) Lag

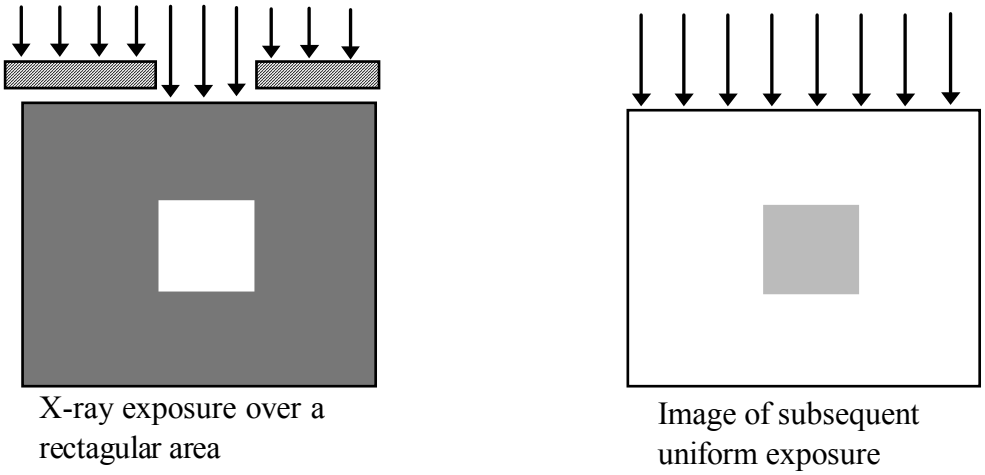

(b) Ghosting

Figure 2.12 Typical images demonstrating the characteristics of lag and ghosting by considering x-ray exposure over a rectangular area: (a) A dark image acquired immediately after the x-ray exposure, lag is manifested as an increase in pixel values in previously exposed areas; (b) A shadow impression of a previously acquired image is visible in subsequent uniform exposure. Ghosting is revealed as a reduction in pixel sensitivity in previously exposed areas and can only be seen with subsequent x-ray images.

2.11 Summary

The signal generation mechanism in x-ray image detectors is described using Shockley-Ramo theorem. Different x-ray interaction mechanisms in absorbing medium are described in this chapter. The imaging characteristics such as x-ray sensitivity,

resolution in terms of modulation transfer function and detective quantum efficiency are defined and explained in this chapter. The temporal response of x-ray imaging detectors is characterized by lag and ghosting. The concepts of the imaging properties of lag and ghosting are also described.

3. X-RAY PHOTOCONDUCTORS

3.1 Introduction

The performance of direct conversion x-ray detectors mostly depends on the design and properties of the photoconductor layer used in flat-panel detectors. The properties of an ideal photoconductor for x-ray image detectors are discussed in Section 1.3 of Chapter 1. Only amorphous or polycrystalline (poly) photoconductors are currently practical for use in large area x-ray image detectors. In this chapter, some important properties of several potential photoconductors for x-ray image detectors are discussed and compared with the ideal case.

3.2 Amorphous and Polycrystalline Solids

A perfect elemental crystal consists of a regular spatial arrangement of atoms, with precisely defined distances (the interatomic spacing) separating adjacent atoms. Every atom has a strict number of bonds to its immediate neighbors (the coordination) with a well defined bond length and the bonds of each atom are also arranged at identical angular intervals (bond angle). This perfect ordering maintains a long range order and hence a periodic structure. A hypothetical two-dimensional crystal structure is shown in Figure 3.1(a), where the coordination of bonding is three.

Amorphous solid exhibits no crystalline structure or long range order and it only posses a short range orders because the atoms of amorphous solid must satisfy their individual valence bonding requirements, which leads to a little deviation in the bonding angle and length. Thus, the bonding geometry around each atom is not

necessarily identical to that of other atoms, which leads to the loss of long-range order as illustrated in Figure 3.1(b) for the same material in Figure 3.1 (a). The short range order and long range disorder in amorphous semiconductor lead to the model of the continuous random network. The specific structural feature of a random network is the coordination of an atom to its neighbor. Thus the elementary defect of an amorphous semiconductor is the coordination defect, when an atom has either over- or under-coordination from their normal structure bonding. As a consequence of the lack of long-range order, amorphous materials do not possess such crystalline imperfections as grain boundaries and dislocations, which is a distinct advantage in certain engineering applications.

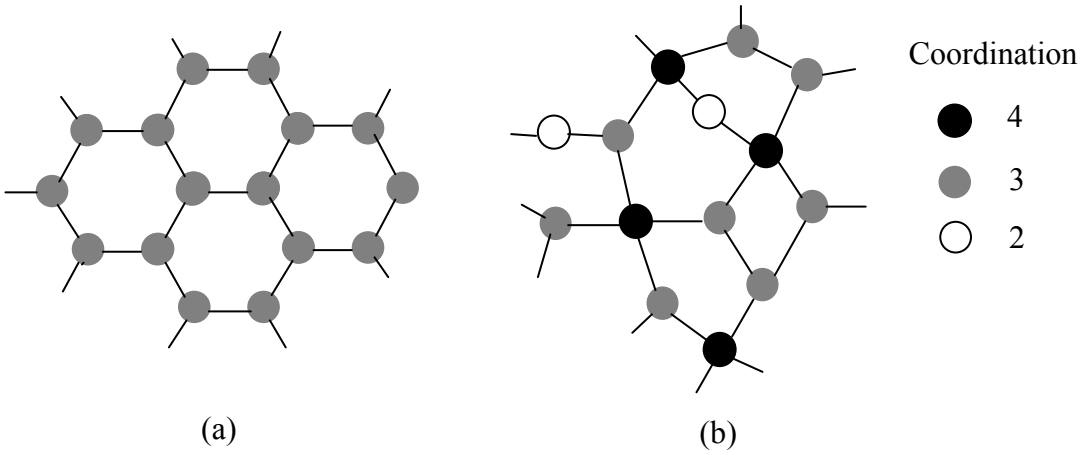

Figure 3.1 Two dimensional representation of the structure of (a) a crystalline semiconductor; (b) an amorphous solid.

Polycrystalline material is not a single crystal as a whole, but composed of many small crystals randomly oriented in different directions. The small crystals in polycrystalline solids are called grain**.** Theses grains have irregular shapes and orientations as shown in Figure 3.2. A polycrystalline material has grain boundaries where differently oriented crystals meet. The atoms at the grain boundaries obviously cannot follow their normal bonding tendency because the crystal orientation suddenly changes across the boundary. Therefore, there are voids, and stretched and broken bonds at the grain boundary. In addition, there are misplaced atoms in grain boundary,

which cannot follow the crystalline pattern on either side of the boundary. In many polycrystalline materials, impurities tend to congregate in the grain boundary region. The atomic arrangement in the grain boundary region is considered as *disorder*.

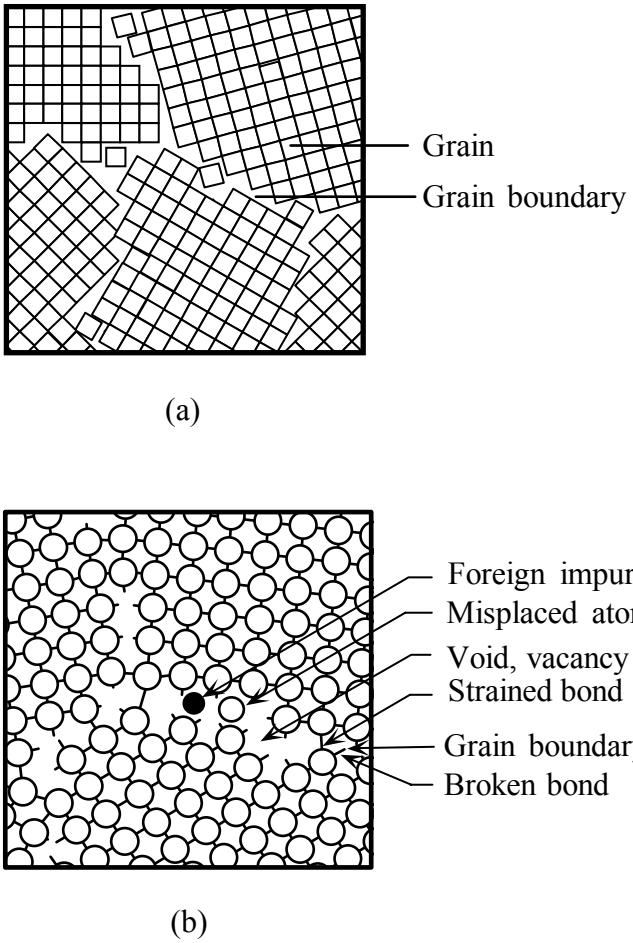

Figure 3.2 (a) The grain structure of polycrystalline solids. (b) The grain boundaries have impurity atoms, voids, misplaced atoms, and broken and strained bonds [39].

3.3 Amorphous Selenium (*a*-Se)

As mentioned in Chapter 1, stabilized a-Se (a-Se alloyed with 0.3% As and doped with ppm-level Cl) is currently the preferred photoconductor for clinical x-ray image sensors because it can be quickly and easily deposited as a uniform film over large areas (e.g., 40 cm × 40 cm or larger). Amorphous selenium can be easily coated as thick films (e.g., 100-1000 μm) onto suitable substrates by conventional vacuum deposition

techniques and without the need to raise the substrate temperature beyond 60-70°C. Stabilized a-Se, not pure a-Se, is used in the x-ray sensors, because pure a-Se is thermally unstable and crystallizes over time. Crystalline Se is unsuitable as an x-ray photoconductor because it has a much lower dark resistivity and hence orders of magnitude larger dark current than a-Se. Alloying pure a-Se with As (0.2 – 0.5% As) greatly improves the stability of the composite film and helps to prevent crystallization. However, it is found that arsenic addition has adverse effect on the hole lifetime because the arsenic introduces deep hole traps. If the alloy is doped with 10 – 20 parts per million (ppm) of a halogen (such as Cl), the hole lifetime is restored to its initial value. Thus, a-Se film that has been alloyed with 0.2 – 0.5% As (nominal 0.3% As) and doped with 10 – 20 ppm Cl is called *stabilized a-Se*. The density of a-Se is 4.3 gm/cm^3, relative permittivity $\varepsilon_r = 6.7$, and energy gap $E_g = 2.22$ eV.

Selenium is a member of the group VI column of the periodic table; the family name of the elements of this group is *chalcogens*. The atomic number (Z) of selenium is 34, and it has six valence electrons. It's electronic structure is $[Ar]3d^{10}4s^2p^4$. The s state and one of the p states are filled with electron pairs, forming nonbonding states known as lone pairs (LP). The remaining two singly occupied p states form covalent bonds, splitting into bonding (B) and anti-bonding (AB) orbitals. Lone-pair orbitals form the top of the valence band; bonding states are much deeper and antibonding states form the conduction band. The atomic coordination is 2 and the bond angle is 105°. The bonding of chalcogens is therefore divalent and they form chain-like structures. The bonding within the chain is covalent and between two chains is van der Waals. The addition of trigonally bonded atoms, such as those from Groups IV or V in the periodic table, cross-link the divalent chains. This provides three-dimensional stability in the amorphous solid. The bonding configuration of selenium atoms is shown in Figure 3.3.

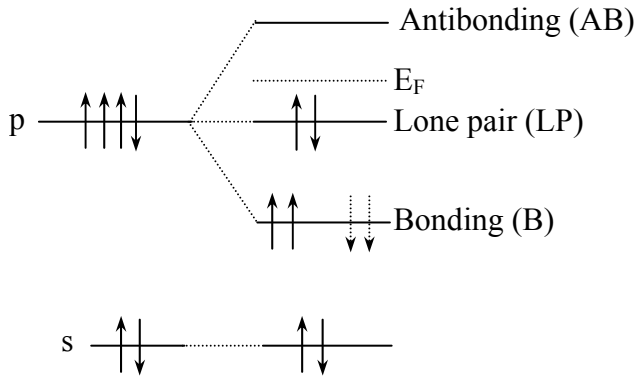

Figure 3.3 The bonding configuration of selenium atoms.

Although the two-fold coordinated neutral structure, Se_2^0, represents the lowest energetically favorable configuration for the Se atom, structural defects also exists in the amorphous state. All the atoms cannot satisfy their individual valency requirement due to the lack of periodicity in the structure. Consequently, some of the atoms become over- or under-coordinated. An interaction with valence electrons on neighboring atoms is responsible for the local lattice distortion, creation of unusual bonding configurations and creation of localized defect states in the energy gap of a-Se. The important bonding configurations for a-Se are shown in Figure 3.4. The energy of a nonbonding orbital is taken to be zero. As a first approximation, the energy per electron of any B orbital to be $-E_b$. Since AB orbitals are always pushed up in energy more than B orbitals are pushed down, the energy of a AB orbital is $E_b + \Delta$, where $\Delta > 0$. If an additional electron is placed on an atom, there is an increase in energy due to the coulombic repulsion between electrons on the same site called electronic correlation. The correlation energy is smaller if the electron is placed in an antibonding orbital (U_{AB}) than if it is placed in a LP orbital (U_{LP}). The energy E_b is significantly larger than Δ, U_{AB} and U_{LP}.

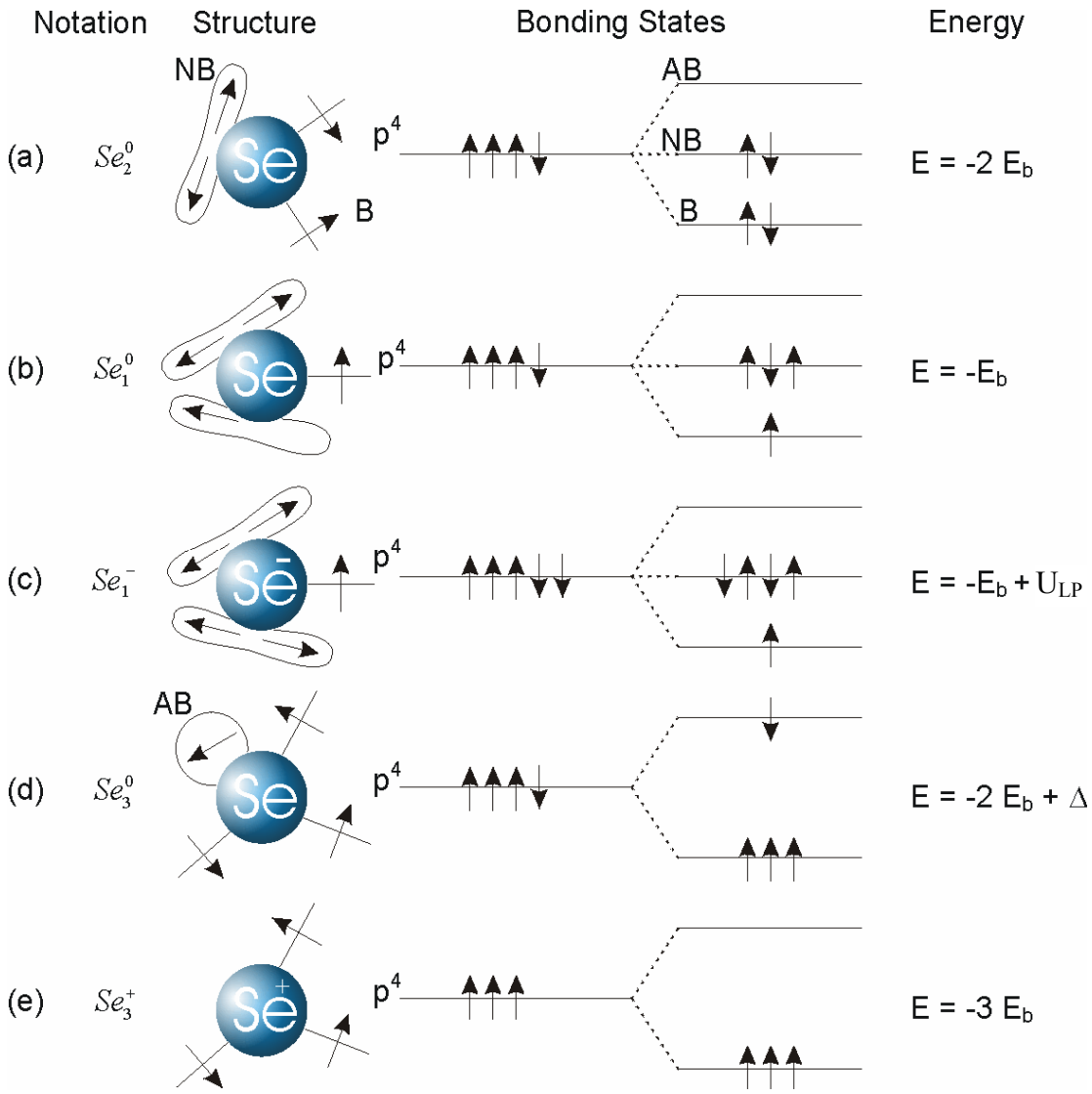

Figure 3.4 Structure and energy of simple bonding configurations for selenium atoms. Straight lines represent bonding (B) orbitals, lobes represent lone-pair (NB) orbitals, and circles represent anti-bonding (AB) orbitals. The energy of a lone-pair is taken as the zero energy (courtesy of Nesdoly [40]).

The energy of Se_2^0 is $-2E_b$. The neutral dangling bond (chain end) configuration, Se_1^0, has an energy of $-E_b$ and thus is not energetically favourable. A chain end atom, Se_1^0, can lower its energy by interacting with neighbouring Se_2^0 atom and create an Se_3^0 configuration. The lowest-energy neutral defect is rather Se_3^0 since its energy is

$-2E_b + \Delta$; almost the same as $-2E_b$. However, the Se_3^0 configuration is unstable [41]. The reaction $2Se_3^0$ (total energy, $-4E_b + 2\Delta$) $\rightarrow$ $Se_1^- + Se_3^+$ (total energy, $-4E_b + U_{LP}$) is energetically favourable since the correlation energy, U_{LP}, is less than 2Δ. Most of the defect centers are therefore either positively or negatively charged. A pair charged defects of type Se_1^- and Se_3^+ is called valence alternation pair (VAP). If the atoms of the pair (Se_3^+ and Se_1^-) are in close proximity (which is the case in a-Se), they are termed an intimate valence alternation pair (IVAP). An important feature of this structure is that, because of close proximity of positive and negative defects, the IVAP centers and overall structure of material would appear neutral. These VAPs or IVAPs are thermodynamically derived structural defects (the defect concentrations are thermal equilibrium with ambient) and are believed to be responsible for deep carrier trapping in a-Se photoconductor films. Another feature of the IVAP is that all of the electrons are paired. The addition of impurities into a-Se provides additional sources of structural VAP defects (Se_3^+ or Se_1^-) or neutral defects (Se_1^0 or Se_3^0), and thereby shifts the balance between Se_3^+ and Se_1^-. Therefore, it is possible to control the charge transport parameters of a-Se by suitably alloying a-Se with other elements. Further, irradiation can generate defects in a-Se and the defects can also interconvert [27, 42].

There are many localized states in the so-called *forbidden gap* of a-Se. Some of them are located near the band edges (*shallow traps*) and some are located deep in the energy band (*deep traps*). Localized states are simply *traps* and are not extended throughout the material, but are localized in space. The localized states (both shallow and deep) are due to various structural defects that are stable at room temperature. Drift of both electrons and holes involves interactions with shallow and deep traps as shown in Figure 3.5. Shallow traps reduce the drift mobility and deep traps prevent the carriers from crossing the photoconductor. The effective drift mobility μ of carriers is the mobility μ_0 in the extended states reduced by the trapping and release events due to the presence of shallow traps,

$$\mu = \frac{\tau_c}{\tau_c + \tau_r} \mu_0 \,, \tag{3.1}$$

where τ_c and τ_r are the average capture and release times in the shallow trap centers. The capture time represents the mean time that a mobile carrier drifts in the extended states before becoming trapped in a shallow trap center. The release time is the mean time that a carrier remains in a trap before being released back into the extended states. Re-emission from a shallow trap is mostly dominated by thermally activated processes. The shallow trap release time is very short and a typical carrier may experience many shallow capture and release events while traversing across the detector thickness. The drift mobilities in the extended states; the hole mobility $\mu_{0h} \approx 0.3$ cm^2/V-s and the electron mobility $\mu_{0e} \approx 0.1$ cm^2/V-s at room temperature [43, 44].

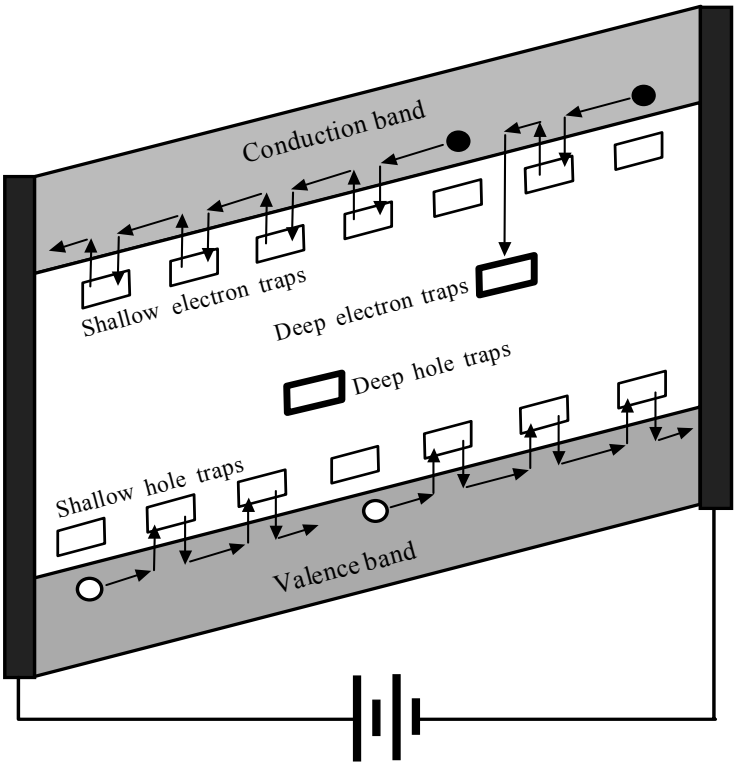

Figure 3.5 Diagram illustrating the band gap of a photoconductor with an applied electric field which tilts the bands encouraging drift of holes in the direction of the field and electrons counter to the field. Drift of both electrons and holes involves interactions with shallow and deep traps. Shallow traps reduce the drift mobility and deep traps prevent the carriers from crossing the photoconductor.

Although the exact nature of the shallow traps in a-Se has not been fully established, the drift mobilities of both holes and electrons are quite reproducible. The room-temperature effective hole mobility μ_h is independent of the preparation of the sample and has a value of ~ 0.12 cm^2/V-s whereas the effective electron mobility μ_e is in the range 0.003–0.006 cm^2/V-s [14]. The hole drift mobility does not change with addition of As or Cl. The value of μ_e decreases with As addition to a-Se (e.g., in stabilized a-Se) but Cl doping does not affect it.

Shallow traps reduce the drift mobility, whereas deep traps prevent the carriers from crossing the photoconductor. Once a carrier is caught in a deep trap, it will remain immobile until a lattice vibration imparts enough energy to the carrier to excite it back into the extended states, where it can drift once again. The deep trap release time is very long, and a deeply trapped carrier is essentially permanently removed from conduction when considering the transit time of carrier across a specimen under high electric field. Therefore, the carrier life-time depends on the concentration of deep rather than shallow traps. The charge carrier lifetimes vary substantially between different samples and depend on various factors such as the source of a-Se material, impurities, and the preparation method. The electron lifetime is particularly sensitive to impurities in the a-Se source material. The hole lifetime drops rapidly with decreasing substrate temperature (temperature of the a-Se substrate during the evaporation process) whereas the electron lifetime does not seem to depend on the substrate temperature. Increasing As concentration to a-Se decreases hole lifetime τ'_h and increases electron life time τ'_e [45]. On the other hand, Cl doping increases hole lifetime and decreases electron lifetime. The typical ranges of lifetimes in stabilized a-Se are 10 – 500 μs for holes and 100 –1500 μs for electrons [14]. Taking deep trapping capture coefficient $C_t \approx 10^{-8}$ cm^3s^{-1} [46] and τ'_h = 50 μs, then the integral concentration of deep hole traps, $N_{0h} = \mu_{0h}/ C_t \mu_h \tau'_h \approx 5 \times 10^{12}$ cm^{-3} [47].

The increase in the electron lifetime with the As addition is greater than the drop in its drift mobility and thus the electron range increases with As content. The effect of Cl doping on carrier ranges is more pronounced than that of As doping. Most importantly,

we can control both electron and hole ranges ($\mu\tau'$ product) by appropriately choosing the relative amounts of As and Cl in a-Se.

The deep electron traps are about ~1.0 eV below conduction band edge in the mobility gap and the hole trapping states centered about ~ 0.85 eV above the valence band [46, 48]. The release time is related to the trap depth E_t by $\nu_0^{-1} \exp(E_t/kT)$, where k is the Boltzmann constant, T is the absolute temperature and ν_0 is the phonon frequency, typically 10^{12} s^{-1}. Thus at room temperature, the release time constant for deeply trapped holes and electrons are less than 10 minutes and few hours or longer, respectively. The peak in the shallow traps for electrons is ~ 0.3 eV [46], which implies the release time constant from shallow trap is ~ 100 ns. The release time constant for shallow trapped holes is even less than 100 ns.

The electron-hole-pair creation energy $W_{\pm}$ in *a*-Se has a strong dependence on the electric field F but only a weak dependence on the incident x-ray photon energy E [21, 22]. The quantity $W_{\pm}$ decreases with increasing electric field and photon energy. $W_{\pm}$ at a given E follows an empirical relation in a-Se given by [49],

$$W_{\pm} \approx W_{\pm}^{0} + \frac{B(E)}{F^{n}} \tag{3.2}$$

where $B(E)$ is a constant that depends on the energy, $W_{\pm}^{0}$ is the saturated EHP creation energy (at infinity F), and n is typically 0.7–1 [50]. The value of $W_{\pm}^{0}$ should be $2.2E_g + E_{\text{phonon}}$. With $E_g \approx 2.22$ eV and $E_{phonon} < 0.5$ eV, we would expect that $W_{\pm}^{0} \approx 5$–6 eV. The energetic primary electron generates many EHPs but only a certain fraction of theses are free to drift and the rest of the EHPs quickly recombine before they can contribute to the photocurrent. There are various possible explanations for the electric field dependence of the EHP creation energy. First, the simultaneously generated electron and its hole twin are attracted to each other by their mutual Coulombic force and may eventually recombine. This type of recombination is called *geminate recombination* (Gemini – the twins). Another possible mechanism is *columnar*

recombination that involves the recombination of nongeminate electrons and holes generated close to each other in the columnar track of the single high energy electron (*primary*) created by the absorption of an x-ray. In both cases, the number of carriers escaping recombination should increase with increasing electric field that acts to separate the oppositely charged carriers. Whether the field dependence of $W_{\pm}$ in a-Se is dominated by geminate or columnar recombination has not been fully resolved and is currently a topical area of research [36, 51]. However, the energy dependence of $W_{\pm}$ is better understood. It decreases slowly with increasing photon energy in the diagnostic [21] and megavoltage range [52]. The total change in $W_{\pm}$ from 20 keV to 6 MeV is of the factor of three. This appears to be due to a reduction of recombination with increase in energy. The rate of deposition of energy per unit distance travelled by a primary electron decreases as a function of energy, decreasing the density of EHPs in the column around it. This is expected to reduce columnar recombination – as is seen. Thus it appears that at low energies the contribution from columnar recombination is approximately twice that from geminate, but at high enough energy the columnar effect is reduced to zero. The typical value of the electric field used in a-Se devices is 10 V/μm where the value $W_{\pm}$ is 35−55 eV over the diagnostic beam energy (12 to 120 keV) and ~ 20 eV at megavoltage energies.

The dark resistivity of a-Se is $\sim 10^{14}$ Ω-cm. The dark current in a-Se detectors is less than the acceptable level (1 nA/cm^2) for an electric field as high as 20 V/μm. For p-i-n diode-like a-Se detector structure, dark current is less than 100 pA/cm^2 at fields as high as 20 V/μm [11]. The image lag in a-Se detectors is under 2% after 33 ms and less than 1% after 0.5 s in the fluoroscopic mode of operation [53].Therefore, image lag in a-Se detectors is considered as negligible. The pixel to pixel sensitivity variation is also negligible in a-Se detectors. The presampling MTF of these detectors is almost close to the theoretical MTF (*sinc* function) determined by the pixel aperture [5].

3.4 Polycrystalline Mercuric Iodide (poly-HgI_2)

Polycrystalline Mercuric Iodide (Poly-HgI_2) has been used as a photoconductor layer in x-ray image detectors. Poly-HgI_2 layers have been prepared by both physical vapor deposition (PVD) and also by screen printing (SP) from a slurry of HgI_2 crystal using a wet particle-in-binder process [17]. There appears to be no technological barrier to preparing large area layers, and direct conversion X-ray AMFPI of 20 × 25 cm^2 (1536 × 1920 pixels) and 5×5 cm^2 (512 × 512 pixels) size have been demonstrated using PVD and SP poly-HgI_2 layer, respectively [17, 54]. The prototype HgI_2 sensors can potentially be used for fluoroscopic or radiographic imaging. The main drawback of polycrystalline materials is the adverse effects of grain boundaries in limiting charge transport and nonuniform response of the sensor due to large grain sizes. However, there has been active research to improve the material properties of poly-HgI_2 based image detectors including the efforts of improving the nonuniformity by reducing the grain size [54]. The band gap energy E_g = 2.1 eV, the ionization energy $W_{\pm}$ ~ 5 eV and the density of poly-HgI_2 is 6.3 gm/cm^3. The resistivity of this material is ~4×10^{13} Ω-cm [55] and the relative permittivity ε_r = 8.3.

HgI_2 tends to chemically react with various metals; hence a thin blocking layer (typically, ~1 μm layer of insulating polymer) is used between the HgI_2 layer and the pixel electrodes to prevent the reaction and also to reduce the dark current. The HgI_2 layer is deposited onto either conductive (ITO or gold coated) glass plates or a-Si TFT arrays. The HgI_2 layer thickness varies from 100-400 μm, grain size varies from 20-60 μm. A deposition of several hundred angstroms of palladium (Pd) or gold is used to form a bias (top) electrode.

The dark current of HgI_2 imagers increases superlinearly with the applied bias voltage. Dark current of a PVD HgI_2 detector strongly depends on the operating temperature; it increases by a factor of approximately two for each 6°C of temperature rise. It is reported [54] that the dark current varies from ~ 2 pA/mm^2 at the 10°C to ~

180 pA/mm^2 at the 35°C at an applied electric field of 0.95 V/μm, which is not desirable for medical imagers (the desirable dark current for medical imaging should be less than 10 pA/mm^2). Therefore, the PVD HgI_2 imagers should be operated at relatively low bias (preferably less than ~ 0.5 V/μm) and relatively low temperature (< 25°C). The dark current in the SP sample is an order of magnitude smaller than in PVD sample and more stable against temperature variation. The only disadvantage of SP detectors is that they show ~2–4 times less sensitivity compared to PVD detectors. This is probably a charge collection efficiency limited sensitivity difference since μτ′ values are higher for PVD layers.

Electrons have much longer ranges than holes in HgI_2 and thus the receiving electrode is negatively biased to obtain a higher sensitivity. The $\mu\tau'$ for electrons in the SP HgI_2 is in the range 10^{-6} to 10^{-5} cm^2/V, and the μτ′ in the PVD sample is about an order of magnitude greater. Recently it is reported that the μτ′ for electrons in PVD HgI_2 is in the range 10^{-5} to 10^{-4} cm^2/V, which is almost equal to that of single crystal HgI_2 [15, 56]. The reason is that the PVD HgI_2 layer grows in a columnar structure perpendicular to the substrate. Thus a charge carrier may drift along a column without having to pass through grain boundaries where it will encounter excess trapping and/or recombination. Samples with larger grain sizes may have fewer grain boundary defects and hence there is a trend of increasing electron $\mu\tau'$ with grain size in the PVD sample. But this trend is not observed in the SP sample, which indicates another mechanism is responsible for its low electron $\mu\tau'$. Larger grain sizes may cause nonuniform response of the sensor. The grain sizes must be much smaller than the pixel size to get uniform response. The $\mu\tau'$ for holes in poly-HgI_2 is in the order of ~10^{-7} cm^2/V.

Two important drawbacks of polycrystalline sensors are the image lag and the pixel to pixel sensitivity variation or nonuniform response. The lowest image lag characteristics reported are ~7% first frame lag, ~0.8 % after 1s and ~0.1 % at 3s in fluoroscopic mode (15 frame/ see) [54]. The pixel to pixel sensitivity variation reduces the dynamic range of the imagers. The relative standard deviation of the sensitivity

(standard deviation/average value) in the latest HgI_2 AMFPI is ~10% [54]. It is reported that HgI_2 image detectors with smaller grain sizes show good sensitivity and also an acceptable uniform response. The presampling MTF of these detectors is almost close to the theoretical MTF (sinc function) determined by the pixel aperture.

As reported in the literature, ploy-HgI_2 imagers show excellent sensitivity, good resolution, and acceptable dark current, homogeneity and lag characteristics, which make this material a good candidate for diagnostic x-ray image detectors.

3.5 Polycrystalline Cadmium Zinc Telluride (poly-CZT)

CdZnTe (< 10 % Zn) polycrystalline film has been used as a photoconductor layer in x-ray AMFPI. CdZnTe is commonly called CZT. Although CZT can be deposited on large areas, direct conversion AMFPI of only 7.7×7.7 cm^2 (512 × 512 pixels) from a polycrystalline CZT (poly-CZT) has been demonstrated. The CZT layer thickness varies from 200-500 μm. Temporal lag and nonuniform response were noticeable in early CZT sensors. Large and nonuniform grain sizes are believed to be responsible for temporal lag and nonuniform response of the sensor. Recent studies show that clorine doping into CZT photoconductive layer makes a finer and more uniform grain structure. The ionization energy $W_{\pm}$ ~ 5 eV and the density of $Cd_{.95}Zn_{.05}Te$ is 5.8 gm/cm^3. The band gap energy, E_g, of $Cd_{.95}Zn_{.05}Te$ is 1.7 eV, the relative permittivity ε_r = 10.7, and the resistivity of this material is ~10^{11} Ω-cm [57].

Introduction of Zn into the CdTe lattice increases the bandgap, decreases conductivity and hence largely reduces dark current. Hole mobility in CZT decreases with increasing Zn concentration whereas electron mobility remains nearly constant. Again, addition of Zn into CdTe increases lattice defects and hence reduces carrier lifetimes. The poly-CZT has a lower crystal density resulting in a lower x-ray sensitivity than its single crystal counterpart. Although (for a detector of given thickness) x-ray sensitivity in CZT detectors is lower than in CdTe detectors, the CZT detectors show a

better signal to noise ratio and hence give a better DQE. The measured sensitivities are higher than other direct conversion sensors (e.g. a-Se) and the results are encouraging.

The dark current of $Cd_{.95}Zn_{.05}Te$ imagers increases almost linearly with the applied field and is ~ 70 pA/mm^2 at an applied electric field of 0.25 V/μm [18], which makes it unsuitable for long exposure time applications. The dark current would be expected to decrease with increasing Zn concentration due to the increased E_g. The dark current in $Cd_{.92}Zn_{.08}Te$ sensors is 40 pA/mm^2 at an applied electric field of 0.4 V/μm [16].

The mobility-lifetime products of both electrons and holes in poly-CZT are less than in single crystal CZT. The $\mu\tau$ for electrons and holes in single crystal $Cd_{.9}Zn_{.1}Te$ are in the range 10^{-4} to 10^{-3} cm^2/V and 10^{-6} to 10^{-5} cm^2/V, respectively [58]. But the $\mu\tau$ for electrons and holes in poly-$Cd_{.95}Zn_{.05}Te$ are ~ 2×10^{-4} cm^2/V and ~3×10^{-6} cm^2/V, respectively [59, 60]. Since $\mu\tau$ product of electrons is much greater than holes in CZT, negative bias to the radiation receiving electrode is the preferred choice for better sensitivity and temporal response.

The relative standard deviation of the sensitivity (standard deviation/average value) in the latest CZT AMFPI is ~20% [16]. The image lag characteristics reported, ~70% first frame lag, ~20 % after 3 frames and 10% in fluoroscopic mode (30 frames/ sec). In single pulse radiographic mode the first frame lag is less than 10% [16]. The longer image lag characteristics of CZT sensors at fluoroscopic mode imply that it not suitable for fluoroscopic applications. The presampling MTF of CZT detector is ~0.3 (150 μm pixel size) at the Nyquist frequency f_{ny}(theoretical MTF, sinc function, is ~0.64 at the f_{ny} = 3.3 lp/mm), where the MTF of CsI imagers is less than 0.2 [18].

3.6 Polycrystalline Lead Iodide (poly-PbI_2)

PbI_2 photoconductive polycrystalline layers have been prepared by physical vapor deposition (PVD) at a substrate temperature of 200 to 230°C. A deposition of several

hundred angstroms of palladium (Pd) is used to form a top electrode. Grains are described as hexagonal platelets with the longest dimensions being 10 μm or less. The platelets grow perpendicular to the substrate, thus producing films less dense (3 to 5 gm/cm^3) than bulk crystalline material (6.2 gm/cm^3). There appears to be no technological barrier to preparing large area layers, and direct conversion AMFPI of 20×25 cm^2 size (1536 × 1920 pixels) have been demonstrated using PVD polycrystalline PbI_2 (poly- PbI_2) layer [61]. Lead iodide coating thickness varies from 60-250 μm and PbI_2 imagers are used for radiographic imaging [61]. The band gap energy E_g = 2.3 eV, and the ionization energy $W_{\pm}$ ~ 5 eV. The resistivity of this material is in the range 10^{11}–10^{12} Ω-cm.

Lead iodide detectors have a very long image lag decay time. The image lag depends on the exposure history. The image lag characteristics reported, ~75% first frame lag, ~15 % after 3s in fluoroscopic mode (15 frame/ sec.), whereas in single pulse radiographic mode the first frame lag is less than 50% and it drops below 1% within 1s [61]. The longer image lag characteristics of PbI_2 at fluoroscopic mode imply that it is unsuitable for fluoroscopic applications.

The dark current of PbI_2 imagers increases sublinearly with the applied bias voltage. The dark current is in the range 10-50 pA/mm^2 at F = 0.5 V/μm. The dark current of PbI_2 imagers is much higher than PVD HgI_2 detectors, making it unsuitable for long exposure time applications. The presampling MTF of PbI_2 detector is ~0.35 (127 μm pixel size) at f_{ny} (theoretical MTF, sinc function, is ~0.64 at f_{ny} = 3.93 lp/mm), where the MTF of CsI imagers is less than 0.2 [61]. The resolution of PbI_2 imagers is acceptable but slightly less than that of HgI_2 imagers. Also, the x-ray sensitivity of PbI_2 imagers is lower than that of HgI_2 imagers. The pixel to pixel sensitivity variation in PbI_2 imagers is substantially low.

The $\mu\tau'$ product of holes and electrons in PVD PbI_2 are 1.8×10^{-6} cm^2/V and 7×10^{-8} cm^2/V, respectively [61]. The μ_h in poly-PbI_2 is in the range 0.02–0.15 cm^2/V-s

whereas the μ_h in single crystal PbI_2 is 2 cm^2/V-s [62]. This indicates that μ_h in poly-PbI_2 is controlled by shallow-traps.

3.7 Polycrystalline Lead Oxide (poly-PbO)

The large area deposition requirement complies with the use of polycrystalline PbO (poly-PbO) film as a photoconductor layer in AMFPI. Direct conversion flat panel X-ray imagers of 18 × 20 cm^2 (1080 × 960 pixels) from a poly-PbO with film thickness of ~300 μm have been demonstrated [19]. One advantage of PbO over other x-ray photoconductors is the absence of heavy element K-edges for the entire diagnostic energy range up to 88 keV, which suppresses additional noise and blurring due to the K-fluorescence. The ionization energy $W_{\pm}$ ~ 8 eV and the density of poly-PbO is 4.8 gm/cm^3. The band gap energy, E_g, of PbO is 1.9 eV and the resistivity of this material is in the range 7-10 $\times 10^{12}$ Ω-cm [19].

Lead oxide PbO photoconductive polycrystalline layers have been prepared by thermal evaporation in a vacuum chamber at a substrate temperature of ~100°C. A deposition of Al, Au or Pd is used to form a top electrode. The metal top electrode layer thickness is preferably between 100 nm to 200 nm [63]. PbO layer consists of very thin platelets of a few microns thickness and have a density of ~50% of the single crystal density. PbO slowly degrades under normal ambient temperature. PbO does not noticeably degrade if it is exposed to air for a few hours. However, in the long term PbO reacts with water and CO_2 causing an increase in dark current and a decrease in x-ray sensitivity. Therefore, a polymer or a semiconductor (e.g., doped a-Se) passivation layer is used between the photoconductor layer and the metal electrode. The passivation layer avoids degradation of the PbO layer and reduces the dark current [63]. The dark current in PbO sensors is ~40 pA/mm^2 at F = 3 V/μm [19]. The $\mu_e \tau'_e$ in poly-PbO is ~5×10^{-7} cm^2/V [19]. The lag signal in fluoroscopic mode is in the range 3-8% after 1s. The presampling MTF of PbO detector is ~0.5 (184 μm pixel size) at f_{ny} (theoretical MTF, sinc function, is ~0.64 at f_{ny} =2.72 lp/mm) [19].

The material properties of these potential photoconductors for x-ray image detectors are given in table 3.1. A detailed description of transport and imaging properties of different potential photoconductors can be found in Ref. [64].

Table 3.1 Material properties of some potential x-ray photoconductors for x-ray image detectors

Photoconductor /state /preparation	E_g (eV)	$W_{\pm}$ (eV)	Density (g/cm^3)	Resistivity (Ω cm)	Electron $\mu_e(cm^2/Vs)$ $\mu_e\tau'_e(cm^2/V)$	Hole $\mu_h(cm^2/Vs)$ $\mu_h\tau'_h(cm^2/V)$
Stabilized a-Se Vacuum deposition	2.22	~45 at 10V/μm	4.3	10^{14} - 10^{15}	μ_e = 0.003 - 0.006 $\mu_e\tau'_e = 0.3\times10^{-6}$ - 10^{-5}	μ_h = 0.12 $\mu_h\tau'_h = 10^{-6}$ - 6×10^{-5}
HgI_2, Polycrystalline, PVD	2.1	5	6.3	$\sim4\times10^{13}$	μ_e = 88 $\mu_e\tau'_e \sim 10^{-5}$-$10^{-4}$	μ_h=3~4 $\mu_h\tau'_h \sim 10^{-6}$
HgI_2, Polycrystalline, SP	2.1	5	6.3	$\sim4\times10^{13}$	$\mu_e\tau'_e \sim 10^{-6}$-$10^{-5}$	$\mu_h\tau'_h \sim 10^{-7}$
$Cd_{.95}Zn_{.05}Te$ Polycrystalline, Vacuum deposition	1.7	5	5.8	$\sim10^{11}$	$\mu_e\tau'_e \sim 2\times10^{-4}$	$\mu_h\tau'_h \sim 3\times10^{-6}$
PbI_2, Polycrystalline, PVD	2.3	5	3-5	10^{11}–10^{12}	$\mu_e\tau'_e = 7\times10^{-8}$	μ_h=0.02 -0.15 $\mu_h\tau'_h \sim 2\times10^{-6}$
PbO, Polycrystalline, Vacuum deposition	1.9	8-20	4.8	7-10 $\times10^{12}$	$\mu_e\tau'_e \sim 5\times10^{-7}$	?

3.8 Summary

The x-ray imaging properties of several potential photoconductors for x-ray image detectors have been discussed and compared with the ideal case. Stabilized a-Se is currently the best choice of photoconductor for clinical x-ray image detectors. The next competitor is the ploy-HgI_2 imagers, which show excellent sensitivity, good resolution, and acceptable dark current, homogeneity and lag characteristics. However, the long

term stability of HgI_2 imagers has not been as thoroughly studied as stabilized a-Se sensors. Both the dark current and the image lag characteristics of CZT, PbI_2 and PbO detectors are worse than those of HgI_2 sensors. However, the x-ray detectors made of CZT photoconductive layer should be mechanically and chemically more stable compared to HgI_2 based detectors. Current research on poly-CZT sensors shows that CZT is also a potential competitor of a-Se. The main drawback of a-Se detectors is its low conversion gain, which specially affects the imaging sensor performance at low exposure. The main drawbacks of polycrystalline sensors are the image lag and the non-uniform response. Making smaller, finer and more uniform grain size in polycrystalline sensors may overcome these drawbacks.

4. X-RAY SENSITIVITY OF PHOTOCONDUCTORS

4.1 Introduction

The x-ray sensitivity *S* of a detector is considered as one of the important performance measures for a superior image. High sensitivity increases the dynamic range of the image detector and also permits low patient exposure of radiation or dose. The x-ray sensitivity of a direct conversion image detector depends on the x-ray sensitivity of the photoconductor that converts the absorbed radiation to collected charge. The selection of the x-ray photoconductor is highly influenced by the *sensitivity* of the photoconductor. Recently there has been an increased interest to improve the x-ray sensitivity of the image detectors based on different potential photoconductors such as amorphous selenium (a-Se) [65], polycrystalline HgI_2 [17] and polycrystalline CdZnTe [18].

Nemirovsky *et al.* [66] have calculated charge collection efficiency for exponential absorption of radiation (e.g., x rays) with application to CZT radiation detectors. Recently, Kasap [50] has developed a model for calculating x-ray sensitivity of *a*-Se detectors by considering exponentially decaying distribution of electron and hole pair (EHP) generation and distributed charge trapping effects across the photoconductor thickness. Kasap calculated the amount of collected charge in the external circuit for a monoenergetic x-ray beam by integrating the Hecht charge collection equation combined with x-ray attenuation profile. In this thesis, the continuity equations for both holes and electrons are analytically solved by considering the drift of electrons and holes in the presence of deep traps under the situation of exponentially decaying

distribution of electron hole pair generation across the photoconductor thickness. An expression is derived for the amount of collected charge in terms of $W_{\pm}$, x-ray exposure X, linear attenuation coefficient α and energy absorption coefficient α_{en} of the photoconductor, transport properties of the photoconductor (i.e., carrier mobility μ, and carrier lifetime τ'), the operating conditions (i.e., electric field F and x-ray photon energy E) and photoconductor thickness L. A generalized expression for charge carrier transport and absorption-limited *normalized sensitivity* is also derived in terms of the following normalized parameters,

Δ = normalized attenuation depth (attenuation depth/thickness) = $1/(\alpha L)$,

τ_e = normalized electron schubweg (electron schubweg per unit thickness)

$= \mu_e \tau'_e F/L$ and,

τ_h = normalized hole schubweg (hole schubweg per unit thickness) = $\mu_h \tau'_h F/L$.

where, $\mu_{e(h)}$ and $\tau'_{e(h)}$ are the mobility and deep trapping time (lifetime) of electrons (holes), respectively. The schubweg ($\mu\tau F$) is the distance a carrier drifts before it is deeply trapped and unavailable for conduction. Equivalently, τ_e and τ_h are the normalized carrier lifetimes (carrier lifetimes per unit transit time) for electrons and holes, respectively. When we divide the charge collection and absorption-limited x-ray sensitivity by the maximum sensitivity we get the normalized sensitivity. Maximum sensitivity is the total collected charge if all the radiation is absorbed, then converted to charges which are all collected by the external circuit. The normalized sensitivity is determined by the x-ray absorption profile, photoconductor thickness and the charge collection efficiency, and closely controlled by Δ, τ_e and τ_h. The ranges of these normalized parameters for *a*-Se, poly-HgI_2 and poly-CZT detectors are given in Table 4.1.

Table 4.1 The values of Δ, τ_e and τ_h for *a*-Se, poly-HgI_2 and poly-CZT detectors. *E* is the average energy of incident x rays to the detector, *F* and *L* are the normal operating electric field and photoconductor thickness respectively.

Photoconductor	$\mu_e\tau'_e$(cm^2/V) $\mu_h\tau'_h$(cm^2/V)	*F* (V/μm)	*E* (keV)	*L* (mm)	τ_e	τ_h	$\Delta = 1/\alpha L$
Stabilized a-Se	$\mu_e\tau'_e = 0.3\times10^{-6}$ - 10^{-5} $\mu_h\tau'_h = 10^{-6}$ - 6×10^{-5}	~10	20	0.2	1.5 -50	5 -300	0.24
			60	1.0	0.3 -10	1 - 60	0.98
Poly-HgI_2	$\mu_e\tau'_e \sim 10^{-6}$-$10^{-5}$ $\mu_h\tau'_h \sim 10^{-7}$	0.5 -1	20	0.15	0.7 - 7	~0.1	0.21
			60	0.3	0.35-3.5	~0.05	0.85
Poly-$Cd_{.95}Zn_{.05}Te$	$\mu_e\tau'_e \sim 2\times10^{-4}$ $\mu_h\tau'_h \sim 3\times10^{-6}$	~0.25	20	0.3	~17	~0.25	0.26
			60	0.3	~17	~0.25	0.89

The normalized sensitivity of an x-ray image detector is examined as a function of normalized parameters τ_e, τ_h and Δ. The three-dimensional universal sensitivity curves are obtained which allow x-ray sensitivity of any potential photoconductive detector to be determined from τ_t, τ_b and Δ. The normalized sensitivity equation is applied to stabilized *a*-Se, poly-CZT and poly-HgI_2 detectors. The sensitivity model is fitted to experimental data on HgI_2 photoconductive detector to obtain the carrier ranges ($\mu\tau'$) in poly-HgI_2.

4.2 X-ray Sensitivity Model

The schematic diagram representing the equivalent circuit of a photoconductive detector is shown in Figure 4.1. A photoconductor layer is sandwiched between two large area parallel plate electrodes. A current integrating amplifier is connected to the bottom electrode and measures the collected charge by integrating the induced x-ray photocurrent (the integration time is longer than the exposure time). The lateral dimension of the photoconductor slab is much greater than the photoconductor thickness *L*. The radiation-receiving electrode (top electrode) is biased with a voltage *V* to establish an electric field *F* in the photoconductor. The biasing voltage can be

positive or negative. It is assumed in Figure 4.1 that the x-ray receiving electrode is biased positively. The x-ray generated electrons and holes are drifted in opposite directions by the applied field and give rise to a transient x-ray photocurrent and the integration of the photocurrent is the collected charge.

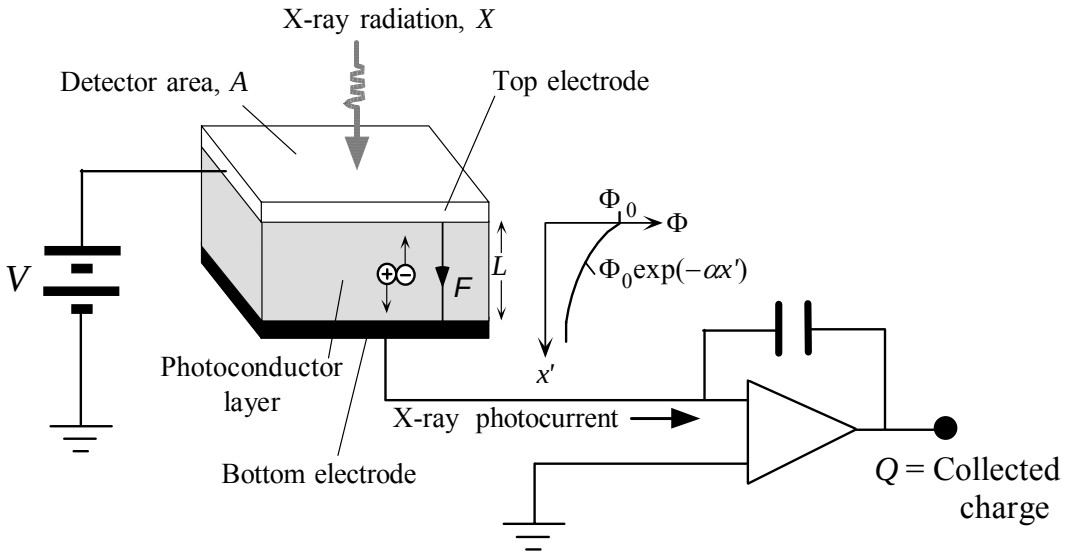

Figure 4.1 Schematic diagram represents the equivalent circuit of a photoconductive x-ray image detector. A photoconductor layer is sandwiched between two large area parallel plate electrodes. The x-ray radiation is incident over an area A and the electric field F is established by applied bias voltage V. The x-ray photocurrent is integrated to obtain the collected charge.

The following assumptions are made to allow the problem to be analytically tractable. (1) The thermal equilibrium concentration of charge carriers is negligibly small. (2) The diffusion of carriers is negligible compared with their drift because of high applied field across the photoconductor. (3) A constant drift mobility μ and a single deep trapping time (lifetime) τ' are assigned to each type of carriers (holes and electrons) since the interrupted field time-of-flight measurements indicate a single deep trapping time for both types of carriers [17, 50]; the drifting carrier concentration falls exponentially as $\exp(-t'/\tau')$, where t' is the time. (4) The field remains relatively uniform. (5) The loss of carriers by deep trapping is more significant than bulk recombination. (6) The trapped charge concentrations are very small compared to the trap center concentrations and thus trap saturation effect is negligible. (7) The

photoconductor is exposed to a monoenergetic pulse of x-ray radiation that has a very short duration compare to the charge carrier transit times across the sample thickness. The assumptions (1) to (3) are the valid general assumptions for the photoconductors used in x-ray image detector for diagnostic medical applications. The assumptions (4) – (6) are valid for small signal operation (e.g. low carrier densities). That means, there is no interaction between drifting carriers. Since the detector system is linear by the assumptions (1) to (6), the assumption (7) can also be conveniently made to calculate x-ray sensitivity for small signal case.

The x rays are attenuated exponentially as $\exp(-\alpha x')$ along the photoconductor thickness and generate electron hole pair (EHP) concentration that follows the x-ray photon attenuation profile as shown in Figure 4.2. The x-ray generated carriers follow the straight electric field lines and either reach the electrodes or become trapped in the photoconductor. Figure 4.2 shows the hole and electron concentrations at the instant of carrier generation and also at a later time when the two distributions have drifted apart. It is assumed that the x-ray receiving electrode is biased positively. If the x-ray receiving electrode is negatively biased, then the electron and hole drifts have to be reversed. Neglecting the secondary photon interaction and taking Φ_0 as the number of x-ray photons per unit area incident on the photoconductor area A, then, $\alpha_{en}\Phi_0 E\exp(-\alpha x')/W_{\pm}$ is the initial collectable hole or electron concentration at location x'. Note that the absorbed energy in the medium due to the secondary photon interaction is much less than the primary photon interaction. The secondary photon interaction is neglected in obtaining normalized sensitivity calculation because it does not have any significant influence on the normalized sensitivity. However, this effect is included in DQE calculation (Chapter 5) where it has a significant effect on DQE at low exposure. Therefore, the initial hole or electron distribution across the photoconductor is [67],

$$p'(x',0) = n'(x',0) = \frac{\alpha_{en} E\Phi_0}{W_{\pm}} \exp(-\alpha x') = B\exp(-\alpha x'), \tag{4.1}$$

where, B ($=\alpha_{en}E\Phi_0/W_{\pm}$) is the electron or hole concentration at location $x'= 0$ and time, $t' =0$.

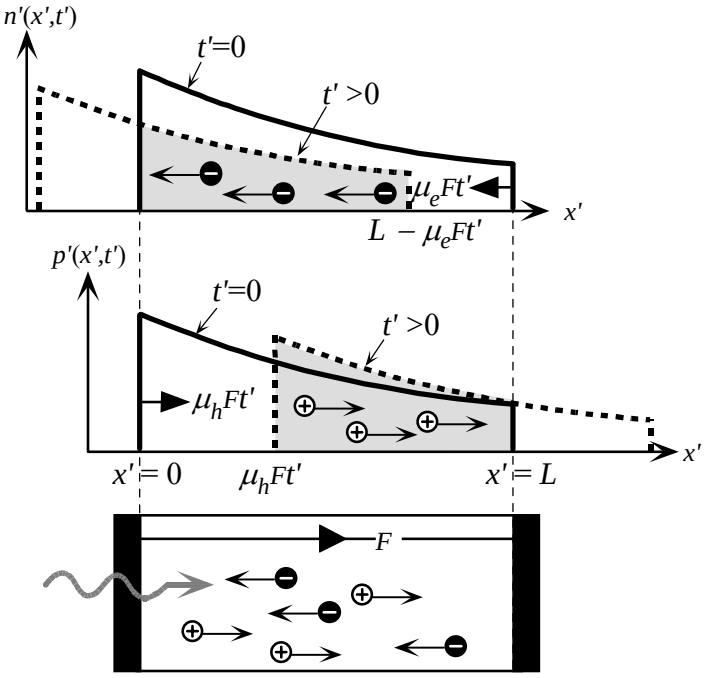

Figure 4.2 Electron and hole concentration profiles, $n'(x', t')$ and $p'(x', t')$ respectively, due to bulk photogeneration and subsequent drift of injected carriers.

The incident x-ray photons per cm^2 is related to x-ray exposure X by [20]

$$\Phi_0 = \frac{5.45\times10^{13}\,X}{(\alpha_{air}/\rho_{air})E}, \tag{4.2}$$

Where X is in roentgens, E is in eV, α_{air} and ρ_{air} are the energy absorption coefficient and the density of air respectively (α_{air}/ρ_{air} is in cm^2 g^{-1}). (See Appendix A for the derivation and plot of equation 4.2).

Considering the assumptions mentioned above, the continuity equation for holes under positive bias is given by

$$\frac{\partial p'(x',t')}{\partial t'} = -\mu_h F \frac{\partial p'(x',t')}{\partial x'} - \frac{p'(x',t')}{\tau_h'} \tag{4.3}$$

where $p'(x',t')$ is the concentration of holes at location x' at time t', and F is the applied field V/L.

We introduce the following normalized parameters for holes,

$$x = x'/L,\ t = t'/t_h,\ \tau_h = \tau'_h/t_h\ ,\ \Delta = 1/\alpha L \text{ and } p = p'/p_0. \tag{4.4}$$

Where $t_h = L/\mu_h F$ = transit time of the holes across the semiconductor. Thus, τ_h is the normalized hole lifetime (hole lifetime per unit transit time). Charge carrier concentrations are normalized with respect to the total collectable EHP generation in the photoconductor as if the total EHP is uniformly distributed over the sample volume. Therefore, the normalized parameter for hole concentration,

$$p_0 = \frac{1}{L}\int_0^L B\, e^{-\alpha x'} dx' = B\Delta\left(1 - e^{-1/\Delta}\right) = B\Delta\eta \tag{4.5}$$

where, $\eta = 1 - \exp(-1/\Delta)$; quantum efficiency of the detector. The quantum efficiency represents the fraction of incident x-rays that interact with the detector.

Considering the assumptions mentioned above and using the normalized coordinates, the continuity equation for holes under positive bias is given by

$$\frac{\partial p}{\partial t} = -\frac{\partial p}{\partial x} - \frac{p}{\tau_h}\ , \tag{4.6}$$

The solution of equation (4.6) is a drifting hole distribution that is given by [68],

$$\begin{aligned} &p(x,t) = \frac{1}{\Delta\eta}\exp[-(x-t)/\Delta]\exp(-t/\tau_h)\ ;\ t < x < 1 \\ &p(x,t) = 0\ ;\ x < t \text{ and } x > 1 \end{aligned} \tag{4.7}$$

The normalized collected charge in the external circuit due to hole drift is,

$$Q_h = \int_0^1\int_t^1 p(x,t)dxdt = \frac{\tau_h}{\eta}\left[\left(1 - e^{-\frac{1}{\Delta}}\right) + \frac{1}{\Delta/\tau_h - 1}\left(e^{-\frac{1}{\tau_h}} - e^{-\frac{1}{\Delta}}\right)\right] \tag{4.8}$$

Similarly, the normalized collected charge due to electron drift is,

$$Q_e = \frac{\tau_e}{\eta}\left[\left(1-\mathrm{e}^{-\frac{1}{\Delta}}\right)-\frac{1}{\Delta/\tau_e+1}\left(1-\mathrm{e}^{-\frac{1}{\Delta}-\frac{1}{\tau_e}}\right)\right] \tag{4.9}$$

The total collected charge is the sum of the collected charges due to holes and electrons. The total normalized collected charge, $Q = Q_h + Q_e$, which represents the *charge collection efficiency* since the collected charge is normalized by the maximum collected charge per unit area that would arise if all the liberated carriers are collected. Therefore, the normalized sensitivity *s* is the product of the normalized collected charge *Q* and the quantum efficiency η. Thus,

$$\begin{aligned} S/S_0 &= \tau_h\left[\left(1-\mathrm{e}^{-\frac{1}{\Delta}}\right)+\frac{1}{\Delta/\tau_h-1}\left(\mathrm{e}^{-\frac{1}{\tau_h}}-\mathrm{e}^{-\frac{1}{\Delta}}\right)\right]+\tau_e\left[\left(1-\mathrm{e}^{-\frac{1}{\Delta}}\right)-\frac{1}{\Delta/\tau_e+1}\left(1-\mathrm{e}^{-\frac{1}{\Delta}-\frac{1}{\tau_e}}\right)\right] \\ &= s_{\text{hole}}(\tau_h,\Delta)+s_{\text{electron}}(\tau_e,\Delta)=s(\tau_h,\tau_e,\Delta) \end{aligned} \tag{4.10}$$

Where S_0 is the maximum sensitivity that would arise if all the incident radiation were absorbed and all the liberated carriers were collected. Thus combining equations (4.1), (4.2) and (4.5), we get [68],

$$S_0 = \frac{ep_0L/\eta}{X} = \frac{eE\Phi_0}{XW_\pm}\left(\frac{\alpha_{en}}{\alpha}\right) = \left[\frac{5.45\times10^{13}e}{(\alpha_{air}/\rho_{air})W_\pm}\right]\left(\frac{\alpha_{en}}{\alpha}\right) \tag{4.11}$$

Where *e* is the elementary charge. If $W_\pm$ is in eV, α_{air}/ρ_{air} is in $\mathrm{cm^2\ g^{-1}}$ and exposure is in roentgens as in equation (4.2), then sensitivity is in $\mathrm{C\ cm^{-2}\ R^{-1}}$. S_0 is a constant that depends on the x-ray photon energy and the material properties of the photoconductor since $W_\pm$ is a material property and can be taken as constant for a given material [34]. For those materials (e.g., *a*-Se) that have a field dependent $W_\pm$, then S_0 depends on the field [21, 50]. The sensitivity *S* for a detector of finite thickness in which carrier collection is not perfect is always less than S_0.

The two square brackets on the right hand side of the normalized sensitivity s expression (equation 4.10) represent the relative contributions of hole and electron transport to the overall sensitivity for a given Δ. It is assumed that the radiation receiving side of the detector is biased positively. If the bias polarity is reversed, then τ_e and τ_h must be interchanged. The normalized sensitivity expression (4.10) takes into account only the charge transport and absorption effects. Note that $s(\tau_h, \tau_e, \Delta) = s_{\text{hole}} + s_{\text{electron}} = 1$ when all the incident radiation is absorbed and all the charges are collected, that is $\tau_h, \tau_e >> 1$ and $\Delta << 1$. The sensitivity then is simply S_0 and controlled by $W_{\pm}$.

Equation (4.10) applies for incident radiation that is monoenergetic and has to be appropriately integrated over the radiation spectrum of the x-ray source considering the x-ray photon energy dependent terms $W_{\pm}$, α and α_{en}. It should be emphasized that equation (4.10) applies to an isolated photoconductor sandwiched between two large area parallel plate electrodes (small pixel effects are excluded) and operating under a constant field, which means that the injected charge concentration should be small (small signal case).

4.3 Results and Discussions

The normalized sensitivity (equation 4.10) can be used to examine the sensitivity of various photoconductive planar detectors as a function of operating conditions (*e.g.*, electric field and incident x-ray photon energy), photoconductor thickness or material properties; carrier ranges ($\mu\tau$'s) and attenuation coefficients. The sensitivity is closely controlled by τ_h and τ_e as well as Δ. The relative importance of the polarity of the carrier depends on the bias applied to the radiation receiving electrode, the magnitudes of τ_h, τ_e and Δ.

Figures 4.3(a) and 4.3(b) show three-dimensional plots of the hole and electron contributions to the sensitivity, $s_{\text{hole}}(\tau_h, \Delta)$ and $s_{\text{electron}}(\tau_e, \Delta)$ in equation (4.10) for

positively biased radiation receiving electrode. Notice that the hole contribution is much higher than the electron contribution provided that Δ is not too large (that is, absorption is not uniform). The reverse will be true if the bias voltage is negative. The hole contribution to the sensitivity, $s_{\text{hole}}(\tau_h, \Delta)$, increases with increasing τ_h and decreasing Δ. At very high Δ, a large amount of incident radiation is obviously not absorbed in the photoconductor, which results in a low x-ray sensitivity. The electron contribution to the sensitivity, $s_{\text{electron}}(\tau_e, \Delta)$, increases with increasing τ_e and has a critical dependence on Δ as shown in Fig. 4.3(b). At very low Δ, the electron and hole generation occurs mainly near the radiation receiving electrode and falls very rapidly with the thickness of the photoconductor. Therefore, the electron current exists for a short period which gives low charge collection due to the electron drift and makes $s_{\text{electron}}(\tau_e, \Delta)$ small. Notice that $s_{\text{electron}}(\tau_e, \Delta)$ versus Δ has a maximum at around $\Delta \approx 0.5$. We cannot however conclude that the sensitivity of the photoconductor is the maximum at $\Delta \approx 0.5$. The sensitivity of the photoconductor is the sum of both electron and hole contributions. We therefore have to examine the effects of Δ on the total sensitivity, which will be discussed below.

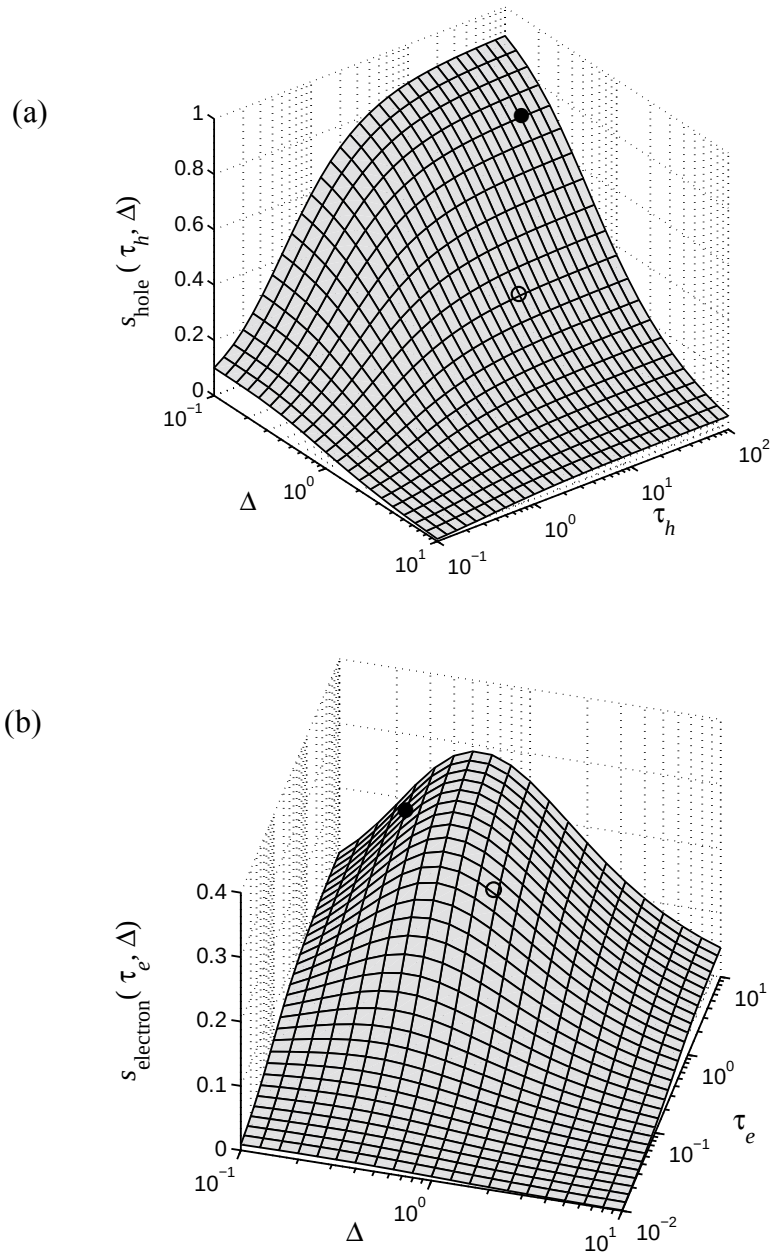

Figure 4.3 (a) Normalized sensitivity due to hole transport, $s_{\text{hole}}(\tau_h, \Delta)$, versus normalized hole schubweg (τ_h) and normalized attenuation depth (Δ). (b) Normalized sensitivity due to electron transport, $s_{\text{electron}}(\tau_e, \Delta)$,versus normalized electron schubweg (τ_e) and normalized attenuation depth (Δ). The normalized sensitivity contributions of holes and electrons for a 1000 μm thick *a*-Se detector with E = 60 keV, F = 10 V/μm, are marked with open circles and for a 200 μm thick *a*-Se detector with E = 20 keV, F = 10 V/μm, are marked with filled in circles, respectively.

The usefulness of Figs. 4.3(a) and 4.3(b) is that we can estimate the sensitivity of any photoconductive planar detector from these two figures. We can estimate individual carrier contributions to the sensitivity, $s_{hole}(\tau_h, \Delta)$ and $s_{electron}(\tau_e, \Delta)$, from material properties (carrier ranges), operating conditions (*e.g.* F and energy spectrum) and detector thickness. The sensitivity of the photoconductor will be the simple sum of $s_{hole}(\tau_h, \Delta)$ and $s_{electron}(\tau_e, \Delta)$. For example, taking a 1000 μm *a*-Se detector, E = 60 keV, F = 10 V/μm, $\mu_e\tau_e' \approx 10^{-6}$ cm^2/V, $\mu_h\tau_h' \approx 10^{-5}$ cm^2/V, $\Delta \approx 1$, $\tau_e = 1$ and $\tau_h = 10$. From Fig. 4.3(a), s_{hole} = 0.36 and from Fig. 4.3(b), $s_{electron}$ = 0.20 that give the total normalized sensitivity, $s = s_{hole} + s_{electron}$= 0.56. On the other hand, for E = 20 keV and L = 200 μm as in mamographic detectors, s_{hole} = 0.76, $s_{electron}$ = 0.21 and $s = s_{hole} + s_{electron}$ = 0.97. Similarly, the charge transport and absorption limited sensitivity of a-Se, poly-HgI_2 and poly-CZT can be estimated using the normalized parameters listed in table 4.1 and figure 4.3.

Figures 4.4(a) and 4.4(b) show the dependence of the normalized sensitivity s on the normalized hole and electron schubwegs as a function of Δ for positively biased radiation receiving electrode. For sufficiently long schubwegs, the sensitivity is nearly saturated but strongly depends on Δ. It is apparent that the carrier schubwegs have to be several times greater, and the attenuation depth δ (=1/α) has to be at least two times smaller than the device thickness L for achieving sufficient sensitivity. It can be seen from Figs. 4.4(a) and 4.4(b) that the sensitivity is mainly controlled by the charges that have the same polarity as the bias on the radiation receiving electrode; holes for positive bias and electrons for negative bias. The extent of disparity between s_{hole} and $s_{electron}$ depends on Δ. The disparity is stronger for lower Δ and can be understood by noting that the electron and hole generation does not occur uniformly throughout the thickness of the sample but rather closer to the radiation receiving electrode. Full hole trapping, τ_h = 0 in Fig. 4.4(a), reduces the sensitivity by about 66% at Δ= 0.5 and 77% at Δ= 0.25 whereas full electron trapping, τ_e = 0 in Fig. 4.4(b), reduces the sensitivity by about 34% at Δ= 0.5 and 23% at Δ= 0.25. An interesting feature is that s versus Δ has a maximum that moves to higher Δ as τ_h gets shorter.

(a)

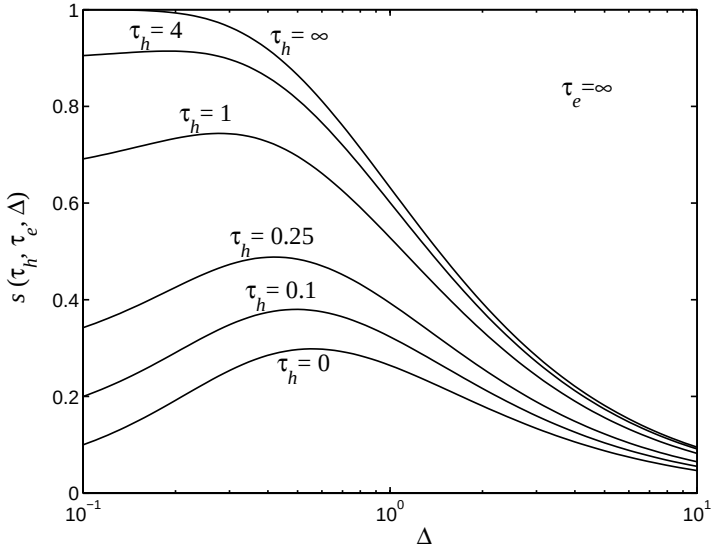

(b)

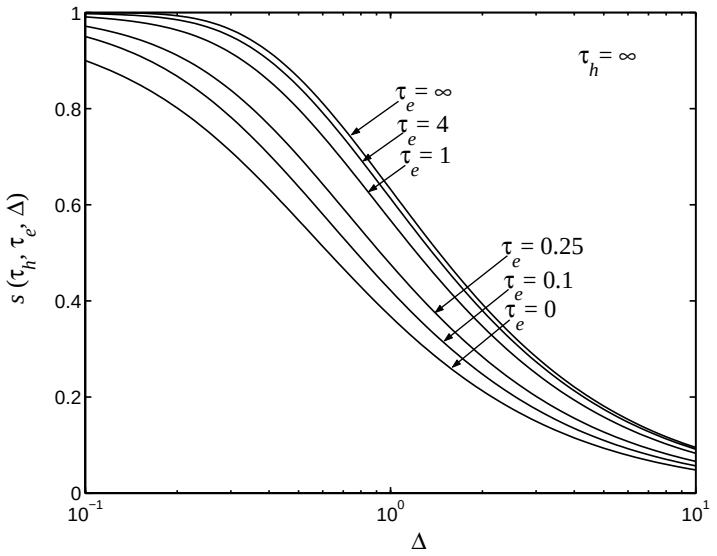

Figure 4.4 (a) Normalized x-ray sensitivity (*s*) versus normalized attenuation depth (Δ) with no electron trapping ($\tau_e = \infty$) for various levels of hole trapping (normalized hole schubweg per unit thickness τ_h). (b) Normalized x-ray sensitivity (*s*) versus normalized attenuation depth (Δ) with no hole trapping ($\tau_h = \infty$) for various levels of electron trapping (electron schubweg per unit thickness, τ_e).

(a)

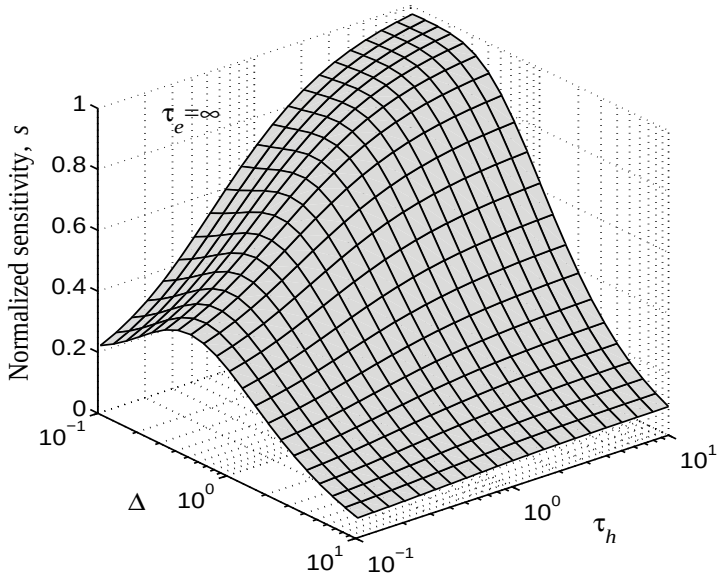

(b)

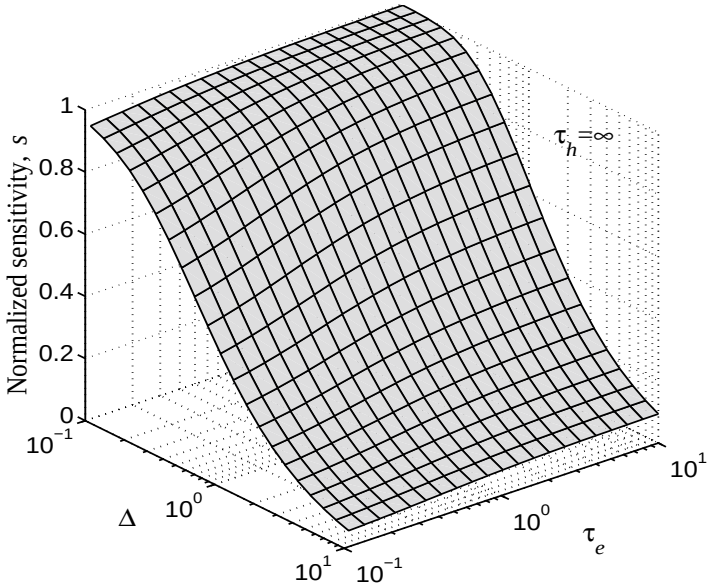

Figure 4.5 (a) Normalized sensitivity s with no electron trapping ($\tau_e = \infty$) as a function of τ_h and Δ for positive bias. (b) Normalized sensitivity s with no hole trapping ($\tau_h = \infty$) as a function of τ_e and Δ for positive bias.

The two-dimensional plots of Figures 4.4(a) and 4.4(b) are essentially cuts from more general three-dimensional plots of Figures 4.5(a) and 4.5(b), respectively. Figure 4.5(a) shows a three-dimensional plot of the normalized sensitivity s with no electron trapping ($\tau_e = \infty$) as a function of τ_h and Δ for negative bias. The normalized sensitivity increases with increasing τ_h and has a critical dependence on Δ. The sensitivity versus Δ

has a maximum that moves to higher Δ as τ_h gets shorter. For very large Δ, a large amount of incident radiation is obviously not absorbed in the photoconductor, which results in a low x-ray sensitivity. For very small Δ, the carrier generation occurs mainly near the radiation receiving electrode. If these carriers are trapped, the sensitivity is reduced as apparent in Fig. 4.5(a). Thus, there is an optimum thickness that compromises between higher absorption (higher L) and less trapping (smaller L). Figure 4.5(b) shows a three-dimensional plot of the normalized sensitivity s with no hole trapping ($\tau_h = \infty$) as a function of τ_e and Δ for negative bias. The normalized sensitivity increases with decreasing Δ and has weak dependence on τ_e.

One of the advantages of a-Se detectors is that both τ_e and τ_h are much greater than one, which is not the case for other photoconductors as shown in table 4.1. Therefore, charge collection efficiency in a-Se detectors is close to unity and the normalized sensitivity is controlled by the quantum efficiency of the detector. The x-ray sensitivity of different photoconductive detectors using the normalized parameters from table 4.1 is given in table 4.2. The values of $W_{\pm}$ for a-Se were taken from the work of Blevis, Hunt and Rowlands [21]. At applied electric field, F = 10 V/μm, $W_{\pm}$ = 42.5 and 46 eV for the x-ray photon energy of 60 and 20 keV, respectively. The maximum x-ray sensitivity S_0 of chest radiographic detectors (E = 60 keV) is much higher than of mammographic detectors (E = 20 keV) because of lower α_{air}/ρ_{air} values at higher x-ray photon energies (equation 4.11) [20]. The value of S_0 in a-Se detectors is much lower than in poly-HgI_2 and poly-CZT detectors because of higher $W_{\pm}$ in a-Se. Although this is a disadvantage in a-Se detectors, the overall x-ray sensitivity S of a-Se detectors is still acceptable. A bar chart representing the sensitivity range of different competitive photoconductors is shown in Figure 4.6. The x-ray sensitivity of a-Se detectors has less dependency on the bias polarity compared to HgI_2 and CZT detectors. Because both τ_e and τ_h in a-Se are much greater than one and hence charge collection efficiency is close to unity under both the positive and negative biases. But the x-ray sensitivity of HgI_2 and CZT detectors significantly depends on the bias polarity because of highly asymmetric transport properties ($\mu\tau$ products) for electrons and holes.

Table 4.2 X-ray sensitivity of *a*-Se, poly-HgI_2 and poly-CZT detectors using the normalized parameters from table 4.1.

Photoconductor	*E* (keV)	S_0 ($\mu Ccm^{-2}R^{-1}$)	$s = S/S_0$		S ($\mu Ccm^{-2}R^{-1}$)	
			Positive bias	Negative bias	Positive bias	Negative bias
Stabilized a-Se	20	0.244	0.9 – 0.98	0.8 – 0.98	0.22 – 0.24	0.2 – 0.24
	60	5.37	0.39 – 0.64	0.35 – 0.62	2.1 – 3.38	1.88 – 3.35
Poly-HgI_2	20	2.75	0.25 – 0.29	0.53 – 0.81	0.7 – 0.81	1.46 – 2.24
	60	38.54	0.15 – 0.3	0.21 – 0.4	6.76 – 11.21	8.18 – 15.6
Poly-$Cd_{.95}Zn_{.05}Te$	20	3	~ 0.456	~ 0.85	~ 1.37	~ 2.55
	60	35.87	~ 0.41	~ 0.51	~ 14.69	~ 18.12

(a)

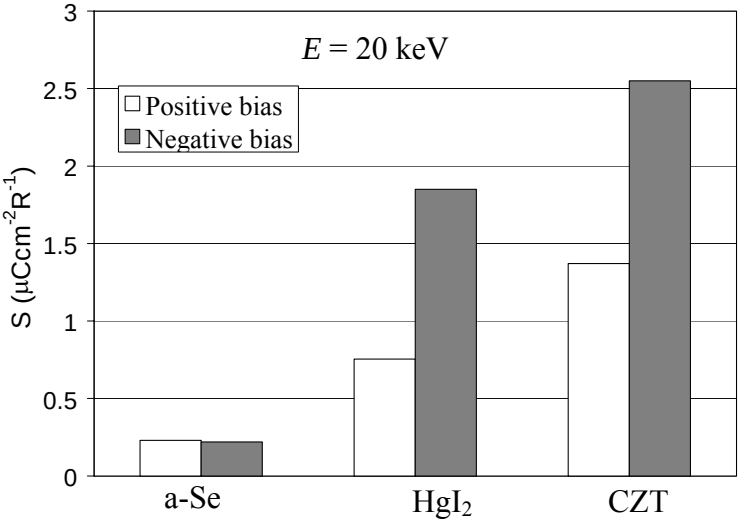

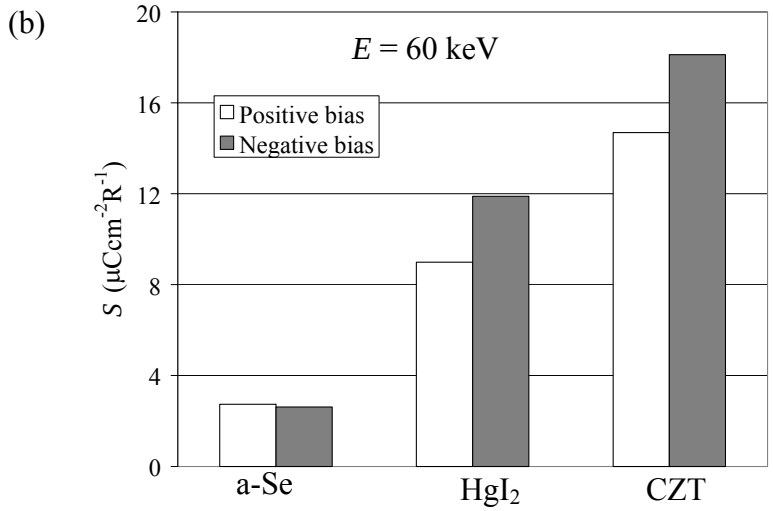

Figure 4.6 Sensitivity S of a-Se, HgI_2 and CZT detectors under normal operating conditions. (a) E = 20 keV (mammographic applications) (b) E = 60 keV (chest radiographic applications).

The charge transport and absorption limited sensitivity equation (4.10) is applied to screen-printed (SP) poly-HgI_2. The electron and hole pair creation energy $W_{\pm}$ for HgI_2 photoconductors does not depend on electric field F. Therefore the collected charge (or sensitivity) is constant for a fixed x-ray exposure. Figure 4.7 shows the collected charge as a function of electric field for both positive and negative bias in a SP polycrystalline HgI_2 photoconductor sample of thickness 250 μm at 100 kVp x-ray exposure. The experimental data have been extracted from Fig. 8 of reference [69] and replotted as collected charge (arbitrary unit) versus electric field. As apparent from Fig. 4.7, there is a very good fit of the experimental data to equation (4.9). From the curve fittings in Fig. 4.7, the electron and hole ranges have been found to be 6.4×10^{-6} cm^2/V and 7×10^{-8} cm^2/V, respectively [68]. According to published data, electron and hole ranges in single crystal HgI_2 are 10^{-5} to 10^{-4} cm^2/V and ~10^{-6} cm^2/V, respectively (i.e. $\mu_e\tau'_e >> \mu_h\tau'_h$) [55]. However, grain boundaries in polycrystalline samples can substantially reduce carrier lifetimes and hence $\mu\tau'$ products compared to single crystals (the mobility for both electrons and holes may also decrease but large changes in the $\mu\tau'$ are primarily due to changes in the carrier lifetimes). The extent of reduction in $\mu\tau'$ depends on the purity and stoichiometry of the starting material and the preparation process for the

polycrystalline layer. Samples with larger grain sizes may have fewer grain boundary defects and hence have larger $\mu\tau'$. Therefore, $\mu\tau'$ may vary significantly from sample to sample. Recently, Street *et al* have reported $\mu_e\tau'_e$ of 6×10^{-5} cm^2/V for a physical vapour deposited (PVD) sample [69]. They have also mentioned that $\mu_e\tau'_e$ in SP sample is about an order of magnitude smaller which agrees with the present results. In their earlier publication, $\mu_e\tau'_e$ is estimated as 10^{-7} cm^2/V for their first SP HgI_2 sample [55]. The average grain sizes in SP HgI_2 sample may vary widely (10-300 μm) [70]. Therefore, sample quality, grain sizes, the calculation technique and assumptions may be responsible for the discrepancy in $\mu_e\tau'_e$ between this work and Ref. 55. However, the present result shows a remarkable improvement in the SP polycrystalline HgI_2 sample quality, which makes SP polycrystalline HgI_2 a potential photoconductor for flat-panel image detectors.

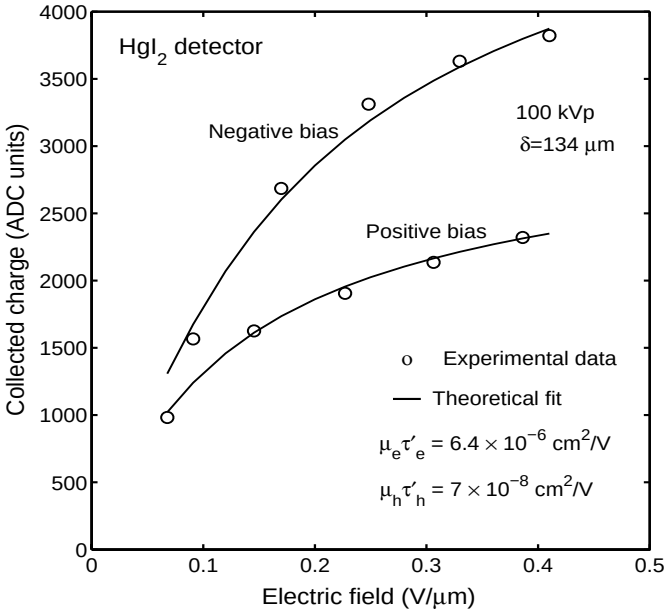

Figure 4.7 Collected charge as a function of electric field for positive and negative bias in a polycrystalline HgI_2 photoconductor sample of thickness 250 μm at 100 kVp exposure. Here, absorption depth, $\delta = 1/\alpha$ and ADC is the abbreviation for 'analog to digital conversion'. [Experimental data are extracted from Fig. 8 of reference [69] and replotted as collected charge versus electric field].

4.4 Summary

A normalized model of the x-ray sensitivity of a photoconductor sandwiched between two parallel plate electrodes (a detector) operating under a constant electric field has been developed by analytically solving the *continuity equation* for both holes and electrons considering the drift of electrons and holes in the presence of deep traps. A generalized expression for charge carrier transport and absorption-limited sensitivity of an x-ray detector has been derived in terms of material properties $W_{\pm}$, α, α_{en} and normalized parameters Δ, τ_e and τ_h. The three-dimensional universal sensitivity curves have been obtained which allow x-ray sensitivity of any potential photoconductive detector to be determined from τ_t, τ_b and Δ. It has been shown that the carrier schubwegs have to be several times greater, and the absorption depth $\delta (=1/\alpha)$ has to be at least two times smaller than the device thickness L for achieving sufficient sensitivity. The normalized sensitivity equation is applied to stabilized *a*-Se, poly-CZT and poly-HgI_2 detectors. It is found that the sensitivity is mainly controlled by the transport properties of the charges that have the same polarity as the bias on the radiation receiving electrode; holes for positive bias and electrons for negative bias. Therefore, positive bias is the preferred choice for a-Se detectors and negative bias is for poly-HgI_2 and poly-CZT detectors as shown in table 4.1. The x-ray sensitivity is also strongly influenced by Δ. The sensitivity model is fitted to experimental data on HgI_2 photoconductive detector to obtain the carrier ranges ($\mu\tau$) in poly-HgI_2. The model provides a very good fit to the experimental data.

5. DETECTIVE QUANTUM EFFICIENCY

5.1 Introduction

The detective quantum efficiency (DQE) is considered as the appropriate metric of imaging performance for image detectors including direct conversion flat-panel diagnostic medical x-ray image detectors. Among various medical applications, fluoroscopy (real-time x-ray imaging) is the most challenging for this technology. The x-ray image in fluoroscopy is highly sensitive to added noise because of its low exposure rate. Recently, there has been an increased interest in investigating the imaging performances of direct conversion image detectors based on different potential x-ray photoconductors (e.g., *a*-Se, poly-HgI_2, and poly-CdZnTe) [53, 69, 71].

The incident x-ray photons are attenuated exponentially along the photoconductor thickness. Each x-ray photon can generate several hundreds or thousands of electron-hole pairs (EHPs) in the photoconductor. Some of the x-ray generated carriers are lost due to random deep trapping during their drift across the photoconductor, which creates *statistical fluctuations* in the collected charge. Ruzin and Nemirovsky [72] have presented a statistical model for the calculation of charge collection efficiency and the variance of the charge collection efficiency assuming an exponential absorption of radiation.

Recently, Mainprize *et al*. [73] applied a *cascaded linear system model* and showed the effects of incomplete charge collection on the DQE of direct conversion flat-panel detectors for a monoenergetic x-ray beam. They showed that poor charge collection efficiency leads to a lower DQE. In this thesis, the ideas in Ref. 73 is extended by

incorporating signal loss due to scattering events (Compton and Rayleigh scattering) and K-fluorescence escape and we apply the extended model to examine the DQE of a photoconductive x-ray detector.

After primary photons interaction, a fraction of the scattered and fluorescent x rays are escaped from the detector volume, which reduces the amount of energy absorption per attenuated x-ray photon in the photoconductor. This effect reduces the conversion gain and hence influences the DQE. However, the rest of scattered x rays are reabsorbed within the detector volume and contribute to the output signal. The K-fluorescent photons are the dominant secondary photons that are reabsorbed in the photoconductor [74, 75]. The average reabsorption probability of a K-fluorescent photon depends on the position where it is created, and thus leads to the conversion gain varying across the photoconductor. The present work examines the effects of charge carrier trapping (i.e. incomplete charge collection) on the zero spatial frequency detective quantum efficiency, i.e. DQE = DQE(f') at $f' = 0$, of a photoconductive detector by considering x-ray interaction depth dependent conversion gain and depth dependent charge collection efficiency in the cascaded linear system model. The DQE(0) of *a*-Se detectors for a fluoroscopic application is analysed in detail as a function of charge transport parameters and photoconductor thickness with varying amounts of electronic noise and exposure under (a) constant field, and (b) constant voltage operating conditions. The optimum photoconductor thickness for maximum possible DQE(0) is investigated as a function of x-ray exposure, electronic noise and bias voltage.

The DQE of an *a*-Se x-ray image detector for actual broad x-ray spectrum emitted from a typical x-ray tube is calculated. This DQE of a polyenergetic x-ray beam is also compared with the DQE of a monoenergetic x-ray beam having the same average photon energy and the validity of using average energy concept in x-ray detector modeling is examined.

The DQE(0) model is applied to a-Se, poly-HgI_2 and poly-CdZnTe detectors for fluoroscopic applications to study and compare their DQE(0) performances. The

DQE(0) model is applied to explain experimental DQE data on *a*-Se image detectors [76]. The theoretical model shows a very good agreement with experimental DQE vs. exposure characteristics.

5.2 DQE(0) Model

We consider an x-ray image detector in which a photoconductor has been sandwiched between two large area parallel plate electrodes and biased with a voltage *V* across the terminals to establish an electric field *F* as shown in figure 5.1. The x-ray generated electrons and holes are separated by the applied field, and drift with constant velocities to the opposite contacts.

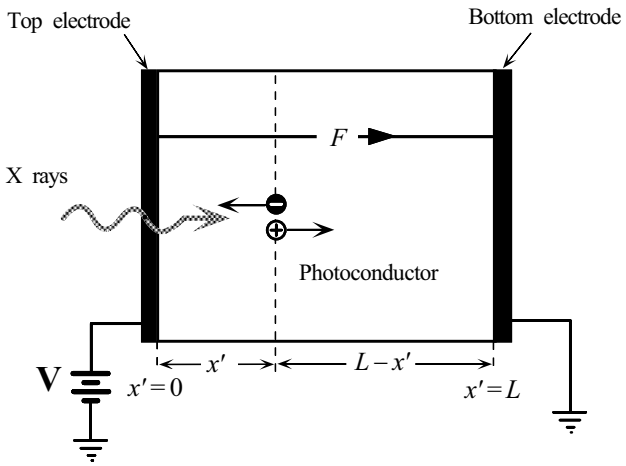

Figure 5.1 Schematic diagram representing a photoconductor sandwiched between two large area parallel plate electrodes used in the model. An electron and a hole are generated at *x′* and are drifting under the influence of the electric field *F*.

The DQE of an imaging detector is defined as

$$\mathrm{DQE} = \frac{\mathrm{SNR}_{\mathrm{out}}^2}{\mathrm{SNR}_{\mathrm{in}}^2}, \tag{5.1}$$

where $\mathrm{SNR}_{\mathrm{in}}$ and $\mathrm{SNR}_{\mathrm{out}}$ are the signal to noise ratio at the input and output stage of an x-ray image detector, respectively.

The x rays are attenuated exponentially across the photoconductor thickness. The probability density for an x-ray photon, that is attenuated within a detector, to interact at a distance x' from the top electrode is given by,

$$p_{x'}(E,x') = \begin{Bmatrix} \dfrac{\alpha e^{-\alpha x'}}{\eta}, 0 \le x' \le L \\ 0, \quad \text{elsewhere} \end{Bmatrix} \tag{5.2}$$

where E is the incident x-ray photon energy, $\alpha(E)$ and L are the linear attenuation coefficient and the thickness of the photoconductor, respectively. The x-ray photon energy dependent x-ray quantum efficiency $\eta(E)$ is given by,

$$\eta(E) = 1 - \mathrm{e}^{-\alpha(E)L} \tag{5.3}$$

For simplicity, we use a normalized distance coordinate x in this thesis where $x = x'/L$.

5.2.1 Linear system model

The signal and noise transfer through an x-ray image detector is a complex process. The cascaded linear-systems model has been used by various investigators to characterize the performance of many imaging systems in terms of signal-transfer and noise-transfer relationships [77, 78]. In the cascaded linear systems model an imaging system is described as cascades of simple and independent elementary stages. In most cases, the input and the output of each stage is a distribution of quanta. These quanta may be x-rays, light, or electrons. The linear system model for the calculation of DQE(0) of a photoconductive detector as shown in figure 5.1 consists of four stages: (1) x-ray attenuation, (2) the generation of charge carriers (conversion gain), (3) charge collection, (4) the addition of electronic noise. The flow chart shown in figure 5.2 illustrates these four separate stages and the signal and noise in different stages. Since the spatial correlations of signals and noise are not considered in this model, the DQE analysis in this work represents the zero spatial frequency detective quantum efficiency DQE ($f' = 0$). DQE(0) represents signal quality degradation due to the signal and noise transfer characteristics of the system without considering signal spreading.

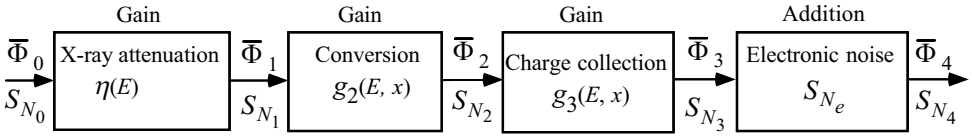

Figure 5.2 The block diagram shows the propagation of signal and noise power spectra through the four stages of an x-ray image detector. $x = x'/L$; normalized distance from the radiation-receiving electrode. E is the incident x-ray photon energy.

Each of the first three stages in Figure 5.2 is defined as a gain stage. For the gain stage i the output mean signal quanta per unit area and noise power spectrum (NPS) arising from incident x-ray photon interactions at each depth x from the radiation-receiving electrode are, respectively [73, 77, 78]

$$\overline{\Phi}_i(E,x) = \overline{g}_i(E,x)\overline{\Phi}_{i-1}(E,x) \tag{5.4}$$

$$S_{N_i}(E,x) = \overline{g}_i^2(E,x)S_{N_{i-1}}(E,x) + \sigma_{g_i}^2(E,x)\overline{\Phi}_{i-1}(E,x) \tag{5.5}$$

where E is the incident x-ray photon energy, $\overline{\Phi}_{i-1}(E,x)$ and $S_{N_{i-1}}(E,x)$ are the mean number of quanta and the NPS incident on stage i, respectively, and $\overline{g}_i(E,x)$ and $\sigma_{gi}^2(E, x)$ are the mean gain and variance of the gain of the ith stage. It is seen from the above equations that the stochastic amplification increases the noise associated with the quanta in two ways. First, the quantum noise is itself amplified (first term in equation 5.5), and second, noise associated with the stochastic nature of the amplifying mechanism is introduced into the output (second term in equation 5.5). The noise associated with the stochastic nature of the amplifying mechanism is proportional to the number of input quanta (An example supporting this is given in appendix B). Following the flow chart in figure 5.2, the mean gain and the variance of gain of each stage are determined as follows.

(1) X-ray attenuation

An x-ray quantum incident on this selection stage either interacts with the detector, probability $\bar{g}_1$, or does not, probability $(1-\bar{g}_1)$, where $\bar{g}_1$ is the quantum efficiency η of the detector. Therefore, this is a binary selection process [15]. According to the binomial theorem, the variance of η,

$$\sigma_{g1}^2 = \bar{g}_1(1-\bar{g}_1) = \eta(1-\eta) \tag{5.6}$$

(2) Conversion gain

The mean conversion gain $\bar{g}_2(E,x)$ of the second stage represents the mean number of free electron-hole pairs (EHPs) generated after the absorption of an x ray of energy E and interaction at x is

$$\bar{g}_2(E,x) = \frac{E_{ab}(E,x)}{W_{\pm}}, \tag{5.7}$$

where $W_{\pm}$ is the EHP creation energy of the photoconductor and $E_{ab}(E, x)$ is the average absorbed energy per x-ray photon of energy E and interaction at location x. The absorbed energy E_{ab} considering K-fluorescent photon reabsorption can be written as [79]

$$E_{ab}(E,x) = \frac{\alpha_{en}}{\alpha}E + f_{ph}(E)P_K Y_K [I_{K\alpha}E_{K\alpha}P_{r\alpha}(x) + I_{K\beta}E_{K\beta}P_{r\beta}(x)], \tag{5.8}$$

where, α_{en} is the energy absorption coefficient of the photoconductor, f_{ph} is the fraction of total attenuation that contributes to the photoelectric interaction, P_K is the fraction of photoelectric attenuation that results in K-shell interaction, Y_K is the K-shell fluorescent yield, $E_{K\alpha}$ and $E_{K\beta}$ are the energies of K_α and K_β fluorescent photons, $I_{K\alpha}$ and $I_{K\beta}$ are the relative frequencies of K_α and K_β production, and $P_{r\alpha}$ and $P_{r\beta}$ are the reabsorption probability of the K_α and K_β photons within the photoconductor thickness. The first term in equation (5.8) represents energy absorption contribution due to the primary photon absorption and the second term represents the energy absorption contribution due to the K-fluorescent photon reabsorption. In *a*-Se, $E_{K\alpha}$ (11.2 keV) and $E_{K\beta}$ (12.5

keV) are very close. For simplicity, the K_α and K_β x-rays are combined as the average K-line considering the relative production frequencies $I_{K\alpha}$ (0.865 for *a*-Se) and $I_{K\beta}$ (0.135 for *a*-Se) [80]. The reabsorption probability for average K- fluorescent photons is practically the same as that calculated when K_α and K_β are considered separately. Therefore, equation (5.8) can be written as

$$E_{ab}(E,x) = \frac{\alpha_{en}}{\alpha} E + f_{ph}(E) P_K Y_K \overline{E}_K P_r(x), \tag{5.9}$$

where $\overline{E}_K$ is the average energy of K-fluorescent photons and $P_r(x)$ is the reabsorption probability of a K-fluorescent photon within the photoconductor volume if it is created at a position x from the radiation receiving electrode (top electrode in figure 5.1). Note that some of the K-fluorescent photons may be reabsorbed at different points within the detector volume from the primary photon interaction point. This creates a lateral spreading of signal, which occurs before the conversion gain stage. But this spreading of signal does not affect the DQE(0) [81]. However, the scattered and fluorescent x rays that are escaping from the detector volume reduce the conversion gain, whose effect on the DQE(0) is studied in section 5.3.

The fluctuations in conversion gain are due to the statistical fluctuations of the number of carriers (EHPs) released per x-ray photon. If there is no K-fluorescence, the variance of the depth dependent conversion gain, $\sigma_{g_2}^2(E,x) = \bar{g}_2(E,x)$, assuming that the mean number of free EHP released per x-ray photon at x obeys a Poisson process. The K-fluorescence reabsorption leads to an additional statistical gain fluctuation. The effect of conversion gain fluctuation due to fluorescence reabsorption is maximum just above the K-edge (12.7 keV for *a*-Se) of the photoconductor and this effect decreases with increasing photon energy thereafter. This effect can be neglected when the K-edge of the photoconductor and the mean energy of the x-ray beam occur at widely different energies [82]. For fluoroscopic (70 kVp) and chest radiographic (120 kVp) applications, the mean energy of the x-ray beam is much higher than the K-edge of *a*-Se. Therefore, the effect of K-fluorescence on gain fluctuations can be neglected for fluoroscopic applications; and for simplicity we assume $\sigma_{g_2}^2(E,x) = \bar{g}_2(E,x)$.

(3) Charge collection

Suppose that an EHP is generated at x ($x = x'/L$) from the top electrode as shown in figure 5.1. Assuming a uniform electric field and neglecting carrier diffusion and bulk recombination, the average charge collection efficiency, $\bar{g}_3(x)$, at the electrodes from EHP generation at coordinate x can be described by the Hecht charge collection efficiency formula (equation 2.5) and is given by,

$$\bar{g}_3(x) = \tau_t\left(1 - \mathrm{e}^{-\frac{x}{\tau_t}}\right) + \tau_b\left(1 - \mathrm{e}^{-\frac{1-x}{\tau_b}}\right) \tag{5.10}$$

where $\tau_t = \mu_t \tau_t F/L$, $\tau_b = \mu_b \tau_b F/L$, μ is the drift mobility and τ' is the lifetime (deep trapping time) of the charge carriers. The subscript t and b refer to carrier types drifting to the top and bottom electrodes respectively; the top electrode receives the x-ray radiation. τ_t and τ_b are the shubwegs per unit thickness, or equivalently, carrier lifetimes per unit transit time. The schubweg ($\mu\tau' F$) is defined as the average distance a carrier drifts before becoming trapped. If the applied bias to the radiation-receiving electrode is positive, the subscript t represents electrons (e) and b represents holes (h).

The variance of charge collection due to random trapping for an EHP generation at x is given by [73],

$$\sigma_{g_3}^2(x) = \tau_t^2 + \tau_b^2 - \tau_t^2\,\mathrm{e}^{-\frac{2x}{\tau_t}} - \tau_b^2\,\mathrm{e}^{-\frac{2(1-x)}{\tau_b}} - 2\tau_t x\,\mathrm{e}^{-\frac{x}{\tau_t}} - 2\tau_b(1-x)\,\mathrm{e}^{-\frac{(1-x)}{\tau_b}} \tag{5.11}$$

(4) Addition of electronic noise

During image readout, the electronic noise power S_{N_e} associated with the TFTs and the external charge amplifiers will be added to the total noise power. The dominant sources of electronic noise are the TFT thermal noise (typical value is 600 e) and the amplifier noise (typical value is 1000-3000 e). Each of the component sources of noise is independent [83]. Therefore, the total noise power is the sum of the noise powers of

all the sources. Since the electronic noise generated from each pixel is independent from each other, the total output noise power, $S_{N_4} = S_{N_3} + S_{N_e}$, and the output signal of the detector, $\overline{\Phi}_4 = \overline{\Phi}_3$

5.2.2 DQE for monoenergetic x-ray beam

The noise in the number of x rays, or signal incident on the detector, is given by the *Poisson fluctuations*. If the mean incident x-ray fluence is $\overline{\Phi}_0$ photons per unit area, the input NPS in the number of x- rays incident on the detector is given by,

$$S_{\mathrm{N}_0} = \overline{\Phi}_0 . \tag{5.12}$$

Thus, the square of signal to noise ratio at the input,

$$\mathrm{SNR}_{\mathrm{in}}^2 = \overline{\Phi}_0 . \tag{5.13}$$

Applying equations (5.4) and (5.5) successively, the expected total signal at the output of the third stage is

$$\overline{\Phi}_3 = \eta\,\overline{\Phi}_0 \int_0^L \bar{g}_3(x')\bar{g}_2(x')p_{x'}(x')dx' = \frac{\overline{\Phi}_0}{\Delta}\int_0^1 \bar{g}_3(x)\bar{g}_2(x)\,\mathrm{e}^{-\frac{x}{\Delta}}\,dx \tag{5.14}$$

where, $\Delta = 1/\alpha L$, the attenuation depth per unit thickness. Similarly, the NPS at the output of the third stage is

$$S_{N_3} = \frac{\overline{\Phi}_0}{\Delta}\int_0^1 \left\{ \bar{g}_3^2(x)[\bar{g}_2(x)+1] + \sigma_{g_3}^2(x) \right\} \bar{g}_2(x)\,\mathrm{e}^{-\frac{x}{\Delta}}\,dx \tag{5.15}$$

Using equation (5.1), the DQE at the output of the detector is

$$\mathrm{DQE} = \frac{\overline{\Phi}_4^2 / S_{N4}}{\overline{\Phi}_0^2 / S_{N_0}} = \frac{\overline{\Phi}_3^2}{\overline{\Phi}_0\left(S_{N_3} + S_{N_e}\right)} \tag{5.16}$$

5.2.3 DQE for polyenergetic x-ray beam

If the incident x-ray fluence is $\Phi(E)$ photons per unit area per unit energy (at each photon energy E) of a polyenergetic x-ray beam, the mean input x-ray quanta $\overline{\Phi}_0$ per unit area can be calculated by integrating over the entire x-ray energy spectrum

$$\overline{\Phi}_0 = \int_{E_{\min}}^{E_{\max}} \Phi(E) dE \,, \tag{5.17}$$

where $E_{\min}$ and $E_{\max}$ are the minimum and the maximum photon energy of the x-ray spectrum, respectively. The input NPS,

$$S_{N_0} = \overline{\Phi}_0 = \int_{E_{\min}}^{E_{\max}} \Phi(E) dE \,. \tag{5.18}$$

Following the same procedure described above, the expected total signal and NPS at the output of third stage are,

$$\overline{\Phi}_3 = \int_{E_{\min}}^{E_{\max}} \frac{\Phi(E)}{\Delta(E)} \int_0^1 \overline{g}_3(x) \overline{g}_2(E,x) \, \mathrm{e}^{-\frac{x}{\Delta(E)}} \, dx dE \tag{5.19}$$

$$S_{N_3} = \int_{E_{\min}}^{E_{\max}} \frac{\Phi(E)}{\Delta(E)} \int_0^1 \left\{ \overline{g}_3^2(x) [\overline{g}_2(E,x) + 1] + \sigma_{g_3}^2(x) \right\} \overline{g}_2(E,x) \, \mathrm{e}^{-\frac{x}{\Delta(E)}} \, dx dE \tag{5.20}$$

The equation (16) is still applicable for the calculation of DQE provided that we consider the terms $\overline{\Phi}_0$, $\overline{\Phi}_3$ and S_{N_3} as appropriate for a polyenergetic x-ray beam and given by equations (5.17), (5.19) and (5.20).

5.3 Results and Discussions

The lateral dimensions of a flat-panel detector are much larger than L and assumed to be infinite. Therefore, the K-fluorescent x-rays may escape from the top or bottom surfaces only. The K-fluorescence reabsorption probability $P_r(x)$ in equation (5.9) is calculated using the method of Dance and Day [84]. For a monoenergetic x-ray beam, we calculate the expected signal $\overline{\Phi}_3$ and quantum noise S_3 at the output of the third

stage by performing a numerical integration of equations (5.14) and (5.15), whereas for a polyenergetic x-ray beam we perform a numerical integration of equations (5.19) and (5.20). We then calculate the DQE of the detector using equation (5.16).

5.3.1 DQE (0) of a-Se detectors

The DQE(0) performance of an *a*-Se direct conversion x-ray detector is examined for fluoroscopic (70 kVp) applications. We assume that the pixel area A = 150 μm × 150 μm. In flat-panel detectors, each 150 μm × 150 μm pixel is made of a thin film transistor (TFT), a storage capacitor and a collecting electrode having a geometrical fill factor of 65-80 %. It has been reported [65] in the literature that the effective fill factor (the effective fraction of pixel area used for image charge collection) of a selenium-based detector is close to 100 % due to electric field bending [85]. Therefore the full pixel area is used as the effective irradiation area per pixel. Unless otherwise stated in this section, the mobilities and lifetimes of carriers are taken as $\mu_h \approx 0.12$ cm^2/Vs, $\mu_e \approx 0.003$ cm^2/Vs, $\tau'_h \approx 50$ μs and $\tau'_e \approx 200$ μs.

The x-ray spectrum for a 70 kVp tungsten anode naked x-ray tube is taken from Ref. 20 and the corrections are made for the attenuations of 23.5 mm Al filtration (RQA5 beam quality of the IEC1267 standard). The average photon energy E_{av} is 52.1 keV for 70 kVp x-ray spectrum with 23.5 mm added Al filtration. Additive electronic noise, $N_e = \sqrt{S_{N_e}}$, for direct conversion flat-panel imaging sensors is typically in the range of 1000 to 3000 electrons (e) per pixel, where N_e is the rms electronic noise. Incident x-ray exposure (X) 0.2 μR to 10 μR is used in the calculation, where 1 μR is the mean exposure for fluoroscopic applications [3].

The electron-hole-pair creation energy $W_{\pm}$ in *a*-Se has a strong dependence on the electric field and weak dependence on the x-ray photon energy [21, 22]. The quantity $W_{\pm}$ decreases with increasing electric field and photon energy. The values of $W_{\pm}$ were taken from the work of Blevis, Hunt, and Rowlands [21] and depend on both the

electric field and photon energy (figure 5 and 6 of Ref. 21). For 52.1 keV x-ray photons, $W_{\pm} \approx 44$ eV at $F = 10$ V/μm. We have used the data for α, α_{en}, f_{ph}, P_k, Y_k and $\bar{E}_k$ from table 5.1. The density of *a*-Se is $\rho = 4.3$ g cm^{-3}.

Table 5.1. X-ray attenuation and K-fluorescence related parameters for *a*-Se

Average K fluorescence energy ($\bar{E}_k$)	11.375 keV	Ref. 80
K-shell contribution to photo-electric (P_k)	0.88	Ref. 33
K fluorescence yield (Y_k)	0.593	Ref. 86
α, α_{en} and f_{ph}		Ref. 33

Figure 5.3(a) shows the reabsorption probability $P_r(x)$ of a K-fluorescent photon as a function of normalized distance x for various detector (photoconductor layer) thicknesses. The reabsorption probability increases with increasing detector thickness. Obviously the reabsorption probability of a K-fluorescent photon is low if it is created at the edges of the detector as evident in figure 5.3 (a). Figure 5.3(b) shows the normalized absorbed energy (E_{ab}/E) of an incident x-ray as a function of normalized distance x for 52.1 keV incident x-ray photon energy. The normalized absorbed energy depends on the interaction depth in the photoconductor and increases with increasing detector thickness. We get a saturated E_{ab}/E of 0.917 at the center of thick detectors when $P_r(x) \approx 1$ (approximately no K-fluorescence escape). Therefore, in *a*-Se, about 8.3% of energy of incident x-ray photon is lost due to the other loss mechanisms (e.g., coherent and incoherent scattering), which is not negligible.

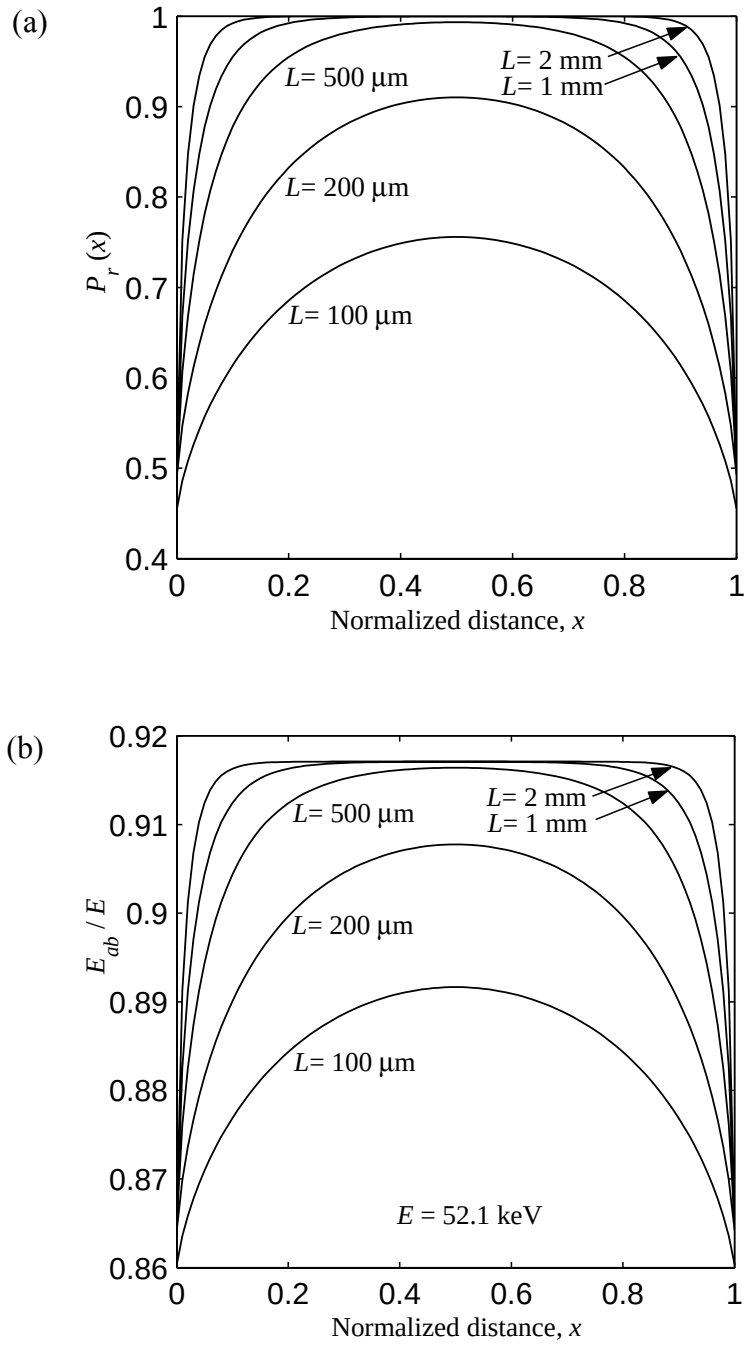

Figure 5.3 (a) The reabsorption probability $P_r(x)$ of a K-fluorescent photon as a function of normalized distance x for various detector thicknesses. (b) The normalized absorbed energy (E_{ab}/E) of an attenuated x-ray photon as a function of normalized distance x for 52.1 keV incident x-ray photon energy.

Figures 5.4(a) and 5.4(b) show the DQE as a function of detector thickness at a constant field (10 V/µm) operating condition for positive and negative bias respectively.

The *a*-Se detector is exposed to 1 μR exposure at an x-ray photon energy of 52.1 keV (monoenergetic beam), appropriate for fluoroscopy. The solid line represents the theoretical DQE using the model described above and the dotted line represents the theoretical DQE without considering the scattering events and fluorescence escape ($E_{ab} = E$) as described in Ref. 73. Without added electronic noise ($N_e = 0$), the two models predict almost the same DQE. But with electronic noise of 2000e, the previous model overestimates the DQE for fluoroscopic applications. At L = 1 mm, the previous model [Ref. 73] overestimates the DQE by 9.1% for positive bias and 10.7% for negative bias. As the conversion gain increases, the DQE improves inasmuch as the detector collects more charges and the relative effect of total additional noise is reduced.

The DQE for positive bias is higher than for negative bias as evident in figure 5.4. The mobility-lifetime product (carrier range) of holes in *a*-Se is longer than that of electrons as evident from typical values of mobilities and lifetimes of both carriers given above. Since the x-ray absorption is not uniform across the photoconductor, the charge collection is mainly controlled by the charges that have the same polarity as the bias on the radiation receiving electrode (top electrode); holes for positive bias and electrons for negative bias [67, 68]. The charge collection efficiency for positive bias is higher than for negative bias due to the higher carrier range ($\mu\tau$) of holes. Again, the noise associated with the random trapping mechanism increases with increasing trapping [72, 73]. Therefore, applying positive bias has advantages over negative bias in terms of higher charge collection efficiency as well as smaller effective noise associated with the stochastic charge collection mechanism. Thus higher charge collection efficiency and lower noise due to charge collection improves the DQE for positive bias.

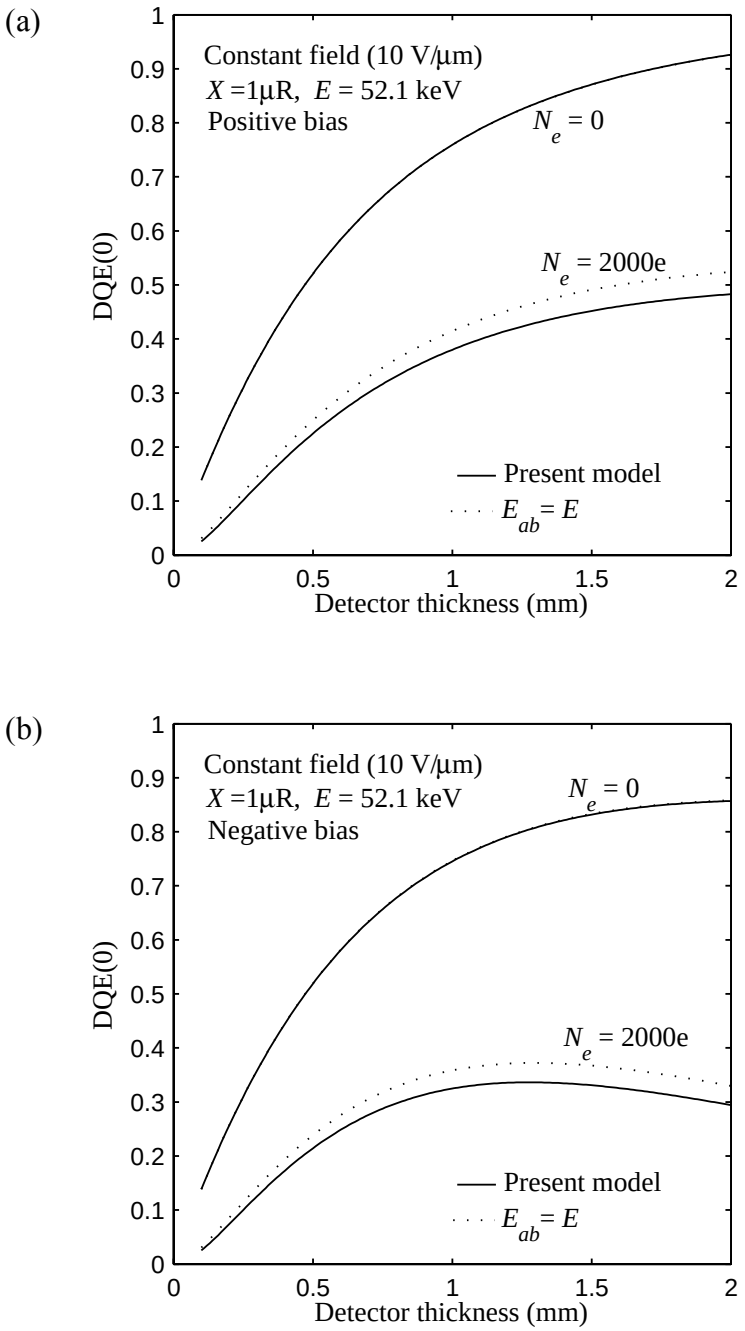

Figure 5.4 (a) DQE(0) versus detector thickness at a constant electric field of 10 V/μm for positive bias. (b) DQE(0) versus detector thickness at a constant electric field of 10 V/μm for negative bias. The *a*-Se detector is exposed to 1 μR exposure at an x-ray photon energy of 52.1 keV (monoenergetic beam). The solid line represents the theoretical DQE using present model and the dotted line represents the theoretical DQE without considering scattering and fluorescence events ($E_{ab} = E$) as described in Ref. 73.

The DQE decreases drastically for added electronic noise of 2000 e and also depends on the bias polarity as shown in figure 5.4. For N_e = 0, L = 1 mm and X = 1 μR, the DQE ≈ 0.759 for positive bias and 0.745 for negative bias, whereas for N_e = 2000e the DQE ≈ 0.381 (reduces by 49.9%) for positive bias and 0.325 (reduces by 56.4%) for negative bias. The quantum efficiency of this detector is 0.775 at x-ray photon energy of 52.1 keV.

Figure 5.5 shows the comparison of the quantum efficiency using the actual x-ray spectrum (70 kVp) and its average energy (52.1 keV) for positive bias. The average photon energy E_{av} is 52.12 keV for 70 kVp x-ray spectrum with 23.5 mm added Al filtration. There is no significant difference in the quantum efficiency [87].

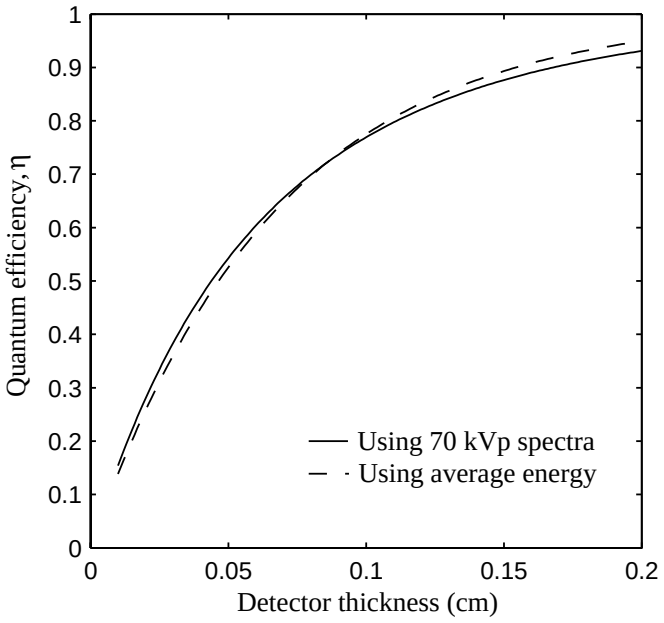

Figure 5.5 comparison of the quantum efficiency using the actual x-ray spectrum (70 kVp) and its average energy (52.1 keV) for positive bias.

Figures 5.6(a) and 5.6(b) exhibit the effect of electronic noise and charge collection on the DQE as a function of detector thickness for an *a*-Se detector operating at a constant bias of 10 kV and exposed to a monoenergetic (photon energy of 52.1 keV) and a polyenergetic (70 kVp) x-ray beams, respectively. X-ray exposure is 1 μR. The

average photon energy of the polyenergetic x-ray spectrum used in figure 5.6(b) is 52.1 keV. The wide difference in the photon energies of a polyenergetic x-ray beam creates additional signal fluctuations and hence decreases the DQE. For monoenergetic x-rays at L = 1 mm and N_e = 0, the DQE ≈ 0.759 for positive bias and 0.745 for negative bias, whereas for N_e = 2000 e, the DQE ≈ 0.381 for positive bias and 0.325 for negative bias. The decrease in DQE due to the broad x-ray spectrum at N_e = 0 is 2.2% for positive bias and 4% for negative bias, whereas at N_e = 2000 e, the decreases in DQE are 5.9% and 8.5% for positive and negative bias, respectively. The reduction in DQE for an x-ray spectrum will be increased with increasing width of the x-ray energy spectrum.

Under a constant bias, the electric field in the photoconductor decreases with the detector thickness, which further modifies the charge collection and conversion gain. The quantity $W_{\pm}$ increases with decreasing electric field. The conversion gain also decreases with increasing photoconductor thickness due to the increase of $W_{\pm}$ with decreasing field. There is an optimum detector thickness that maximizes the DQE for the case of added electronic noise as shown in figure 5.6. That means we obtain an optimum thickness that compromises between higher quantum efficiency (higher L), higher charge collection efficiency (smaller L), and higher conversion gain (smaller L at constant bias). The DQE peak changes with the levels of x-ray exposure. The effect of x-ray exposure (monoenergetic beam) on the DQE for a constant bias condition is shown in figure 5.7. The DQE strongly depends on x-ray exposure as illustrated in figure 5.7. As the x-ray exposure increases, the DQE improves inasmuch as a pixel receives more photons and the relative significance of electronic noise is reduced. The DQE peak also shifts towards the higher detector thickness with increasing x-ray exposure. The DQE of a detector should depend on the applied bias voltage. Therefore, it is instructive to calculate the optimum detector thickness as a function of bias voltage for various levels of exposure, which will be discussed below.

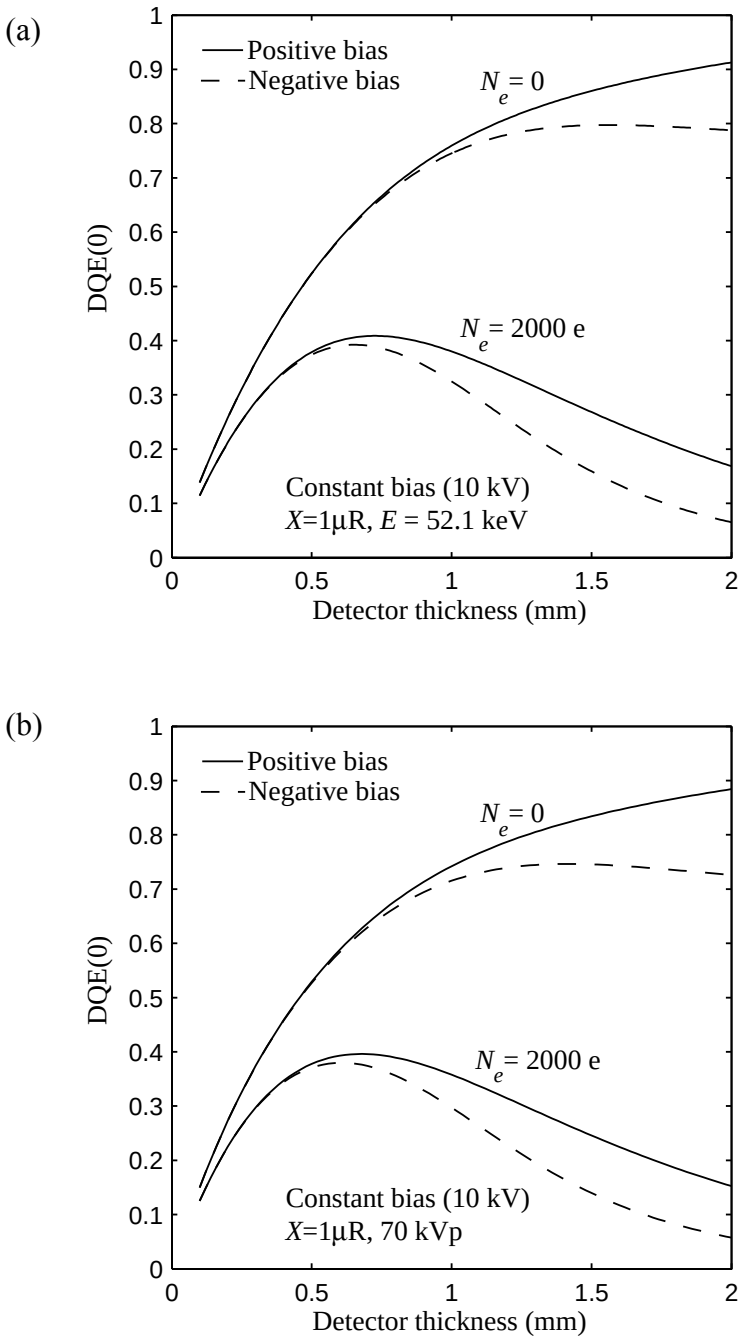

Figure 5.6 (a) DQE(0) versus detector thickness at a constant bias of 10 kV and for a monoenergetic x-ray beam of photon energy E = 52.1 keV. (b) DQE(0) versus detector thickness at a constant bias of 10 kV and for a 70 kVp polyenergetic x-ray spectrum with 23.5 mm Al filtration; average energy of 52.1 keV.

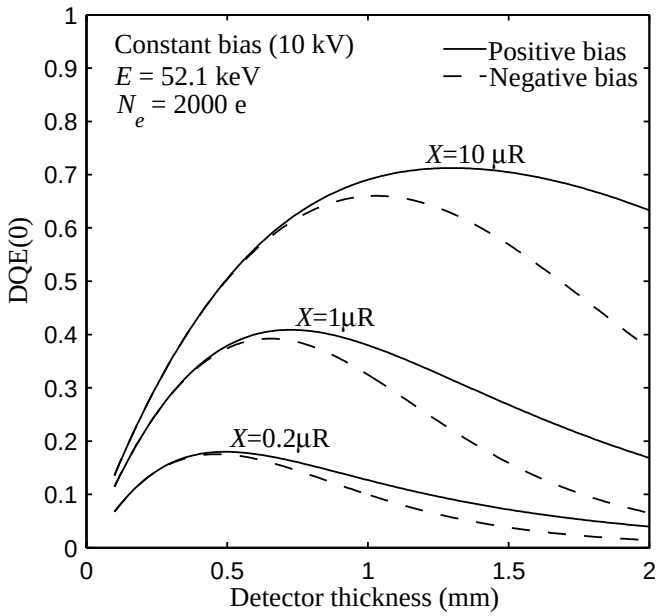

Figure 5.7 DQE(0) versus detector thickness for various levels of x-ray exposure (X) at a constant bias of 10 kV and for a monoenergetic x-ray beam of photon energy E = 52.1 keV.

The optimum detector thickness and the DQE at the optimum thickness (optimum DQE) as a function of bias voltage for various levels of x-ray exposure (monoenergetic beam) are shown in figures 5.8(a) and 5.8(b), respectively. Both the optimum detector thickness and the maximum obtainable DQE increase with increasing applied bias and x-ray exposure. Taking reasonable quantities, for example, $\mu_h \tau'_h = 6.0 \times 10^{-6}$ cm^2/V, $\mu_e \tau'_e = 6.0 \times 10^{-7}$ cm^2/V, N_e = 2000 e, E = 52.1 keV (monoenergetic beam), X = 1 μR and 10 kV bias, the optimum detector thickness for positive and negative bias are 727 μm (DQE = 0.409) and 654 μm (DQE = 0.392), respectively. The optimum detector thickness and corresponding DQE for x-ray spectrum with the same average photon energy will be slightly lower than for monoenergetic x rays. The optimum a-Se detector thickness obviously depends on a number of factors such as added electronic noise, x-ray exposure, applied bias (both magnitude and polarity) and transport properties (μ, τ') of charge carriers. However, the optimum a-Se detector thickness is in the range of ~ 700 μm (DQE ~ 0.4) for fluoroscopic applications (mean exposure is 1μR) and for reasonable quantities appropriate for *a*-Se detectors stated above.

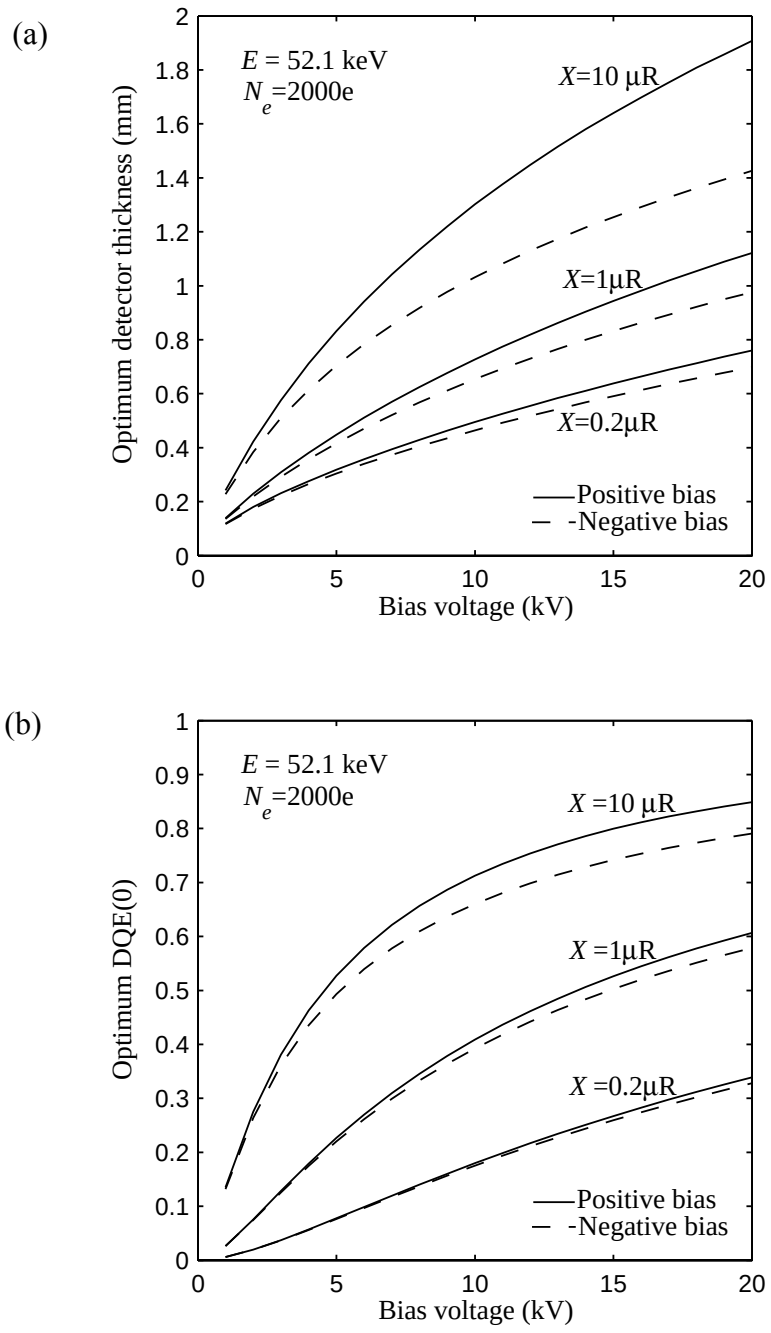

Figure 5.8 (a) Optimum detector thickness versus applied bias for various levels of x-ray exposure. E = 52.1 keV (monoenergetic x-ray beam). (b) Optimum DQE(0) versus applied bias for various levels of x-ray exposure.

Figure 5.9 shows a 3-D plot of the DQE versus L and N_e for a negatively biased (10 kV) *a*-Se detector and exposed to 1 μR at photon energy of 52.1 keV (monoenergetic

beam). For every level of electronic noise, there exists a DQE peak and the DQE peak shifts towards higher L, as N_e gets lower. The shape of DQE versus L and N_e plot for positive bias will be the same as for negative bias but shifts slightly towards higher DQE due to higher charge collection efficiency with positive bias. Figure 5.10 shows a 3-D plot of the DQE versus electronic noise (N_e) and x-ray exposure (X) for a negatively biased (10 kV) 1 mm thick *a*-Se detector and exposed to x rays of 52.1 keV photon energy (monoenergetic beam). It is clear from figure 5.10 that the DQE is severely reduced by electronic noise for low levels of exposure and the DQE does not depend on the x-ray exposure for no electronic noise.

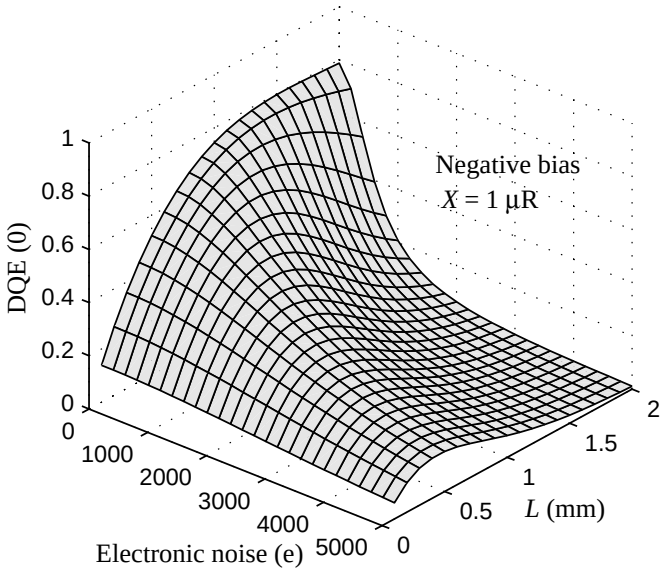

Figure 5.9 DQE(0) versus detector thickness (L) and electronic noise (N_e) for a negatively biased (10 kV) *a*-Se detector and exposed to 1 μR at photon energy of 52.1 keV (monoenergetic beam).

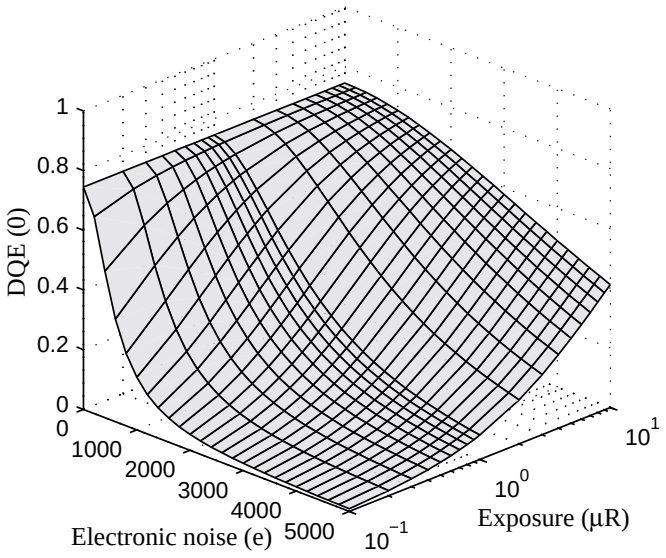

Figure 5.10 DQE(0) versus electronic noise (N_e) and x-ray exposure (X) for a negatively biased (10 kV) 1 mm thick *a*-Se detector and exposed to x rays of 52.1 keV photon energy (monoenergetic beam).

The charge collection efficiency and hence the DQE increases with increasing carrier lifetimes. Figures 5.11(a) and 5.11(b) show the DQE as a function of detector thickness for various levels of electron and hole lifetimes, respectively. The *a*-Se detector is exposed to 1 μR at photon energy of 52.1 keV (monoenergetic beam). Both electron and hole drift mobilities in *a*-Se are reasonably well defined so that $\mu\tau'$ products depend primarily on the carrier lifetimes [50]. In *a*-Se photoconductors, the electron lifetime (τ'_e) typically is in the range of 50-1000 μs whereas the hole lifetime (τ'_h) is in the range of 10-200 μs. It is clear from figures 5.11(a) and 5.11(b) that the DQE is much more dependent on electron lifetime than hole lifetime for negative bias, the opposite is true for positive bias. Full electron trapping, $\tau'_e = 0$ in figure 5.11(a), reduces the DQE by about 64.7% at L = 700 μm and 73.3% at L = 1000 μm whereas full hole trapping, $\tau'_h = 0$ in figure 5.11(b), reduces the DQE by about 43.3% at L = 700 μm and 43.7% at L = 1000 μm.

(a)

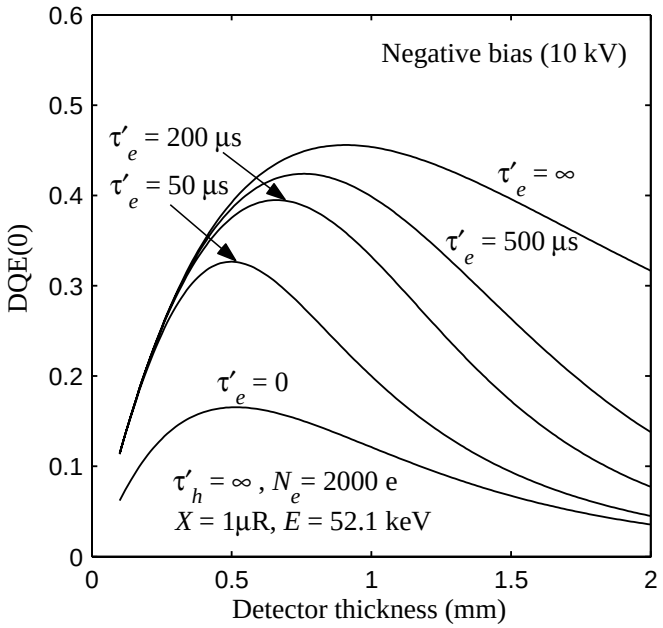

(b)

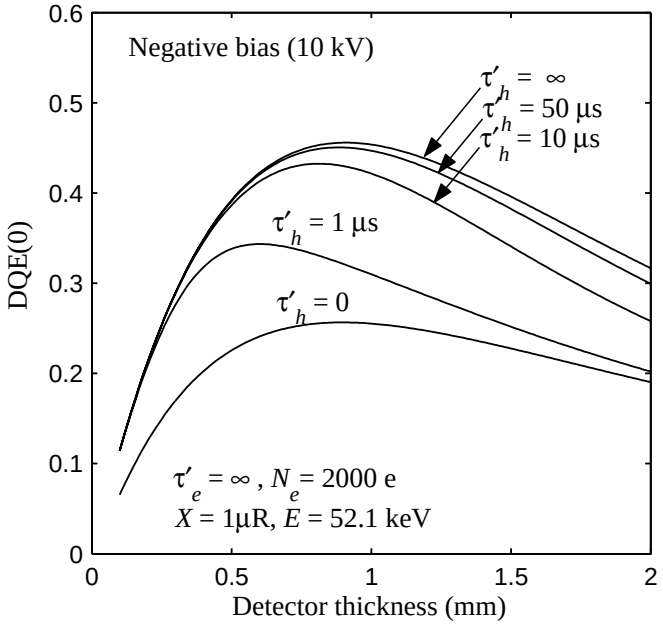

Figure 5.11 (a) DQE(0) versus detector thickness with no hole trapping (hole lifetime, $\tau'_h = \infty$) for various levels of electron lifetimes (τ'_e). E = 52.1 keV (monoenergetic x-ray beam). (b) DQE(0) versus detector thickness with no electron trapping ($\tau'_e = \infty$) for various levels of hole lifetimes (τ'_h).

The effect of carrier lifetimes on DQE is also illustrated in a more general 3-D plot of Figure 5.12. Figure 5.12 shows a 3-D plot of the DQE vs. τ_e and τ_h, electron and hole schubwegs per unit thickness, for a negatively biased 1000 μm thick *a*-Se detector operating at a constant field of 10 V/μm, and exposed to 1 μR at an energy of 52.1 keV (monoenergetic beam), appropriate for fluoroscopy. It is apparent that unless both the carrier schubwegs are greater than the thickness, the DQE is adversely affected by poor charge collection. The polarity of the carrier that is critical in controlling DQE is the same as the polarity of the radiation receiving electrode (negative in Fig. 5.12). One of the distinct advantages of *a*-Se as a photoconductor is that both electron and hole ranges ($\mu\tau'$ products) are such that $\mu\tau' F > L$ can be easily achieved while the dark current remains at a tolerable level. Further, these ranges can be controlled by appropriate alloying and doping *a*-Se [13]. The method used to generate the results in figure 5.12 is not unique to *a*-Se and can be easily extended to apply to other photoconductive detectors (*e.g.*, HgI_2) by appropriately modifying the material dependent parameters in DQE(0) model; however in all cases DQE decreases with decreasing τ_e and τ_h.

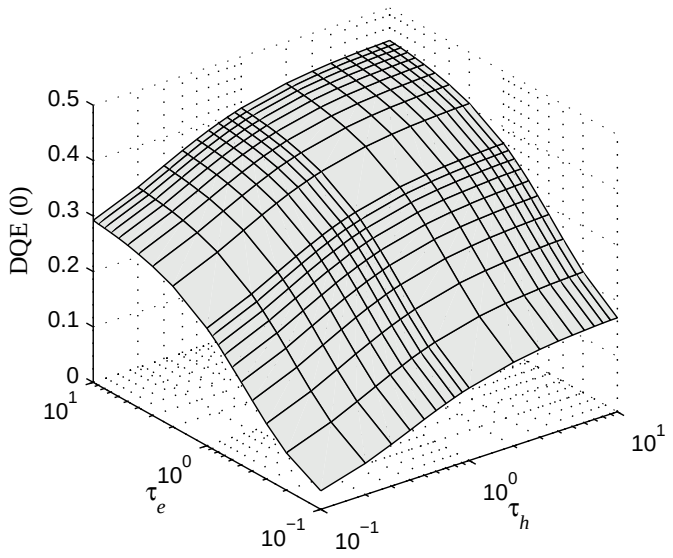

Figure 5.12 DQE(0) vs. electron and hole schubwegs per unit thickness τ_e and τ_h for an *a*-Se x-ray image detector biased negatively. L = 1000 μm; F = 10 V/μm; X = 1 μR; E = 52.1 keV.

Experimental values for the DQE(0) of a 1000 μm thick a-Se fluoroscopic detector exposed to 70 kVp x-rays and filtered by 23.5 mm Al, have been recently reported by Adachi *et al.* [88] and Tousignant *et al.* [89]. For a 1000 μm thick *a*-Se detector operating at a constant bias of 14 kV (negative), X = 1 μR and N_e = 1650 e (average electronic noise per pixel in 2 × 2 binning mode of operation), assuming $\mu_h \tau'_h = 7 \times 10^{-6}$ cm^2/V, $\mu_e \tau'_e = 7.2 \times 10^{-7}$ cm^2/V, we calculate the DQE = 0.508, which is very close to the experimental value of 0.5 reported by Adachi *et al* [88].

Figure 5.13 shows the DQE as a function of x-ray exposure for an *a*-Se fluoroscopic detector exposed to a 70 kVp x-ray spectrum with 23.5 mm Al filtration using N_e shown. The experimental data have been extracted from figure 7 of Ref. [89]. As apparent from figure 5.13, there is a very good agreement between the model and the experimental data. The best fit $\mu\tau'$ products of holes and electrons are $\mu_h \tau'_h = 7 \times 10^{-6}$ cm^2/V and $\mu_e \tau'_e = 7.2 \times 10^{-7}$ cm^2/V, which are very close to values measured for *a*-Se independently by transient photoconductivity interrupted field time-of-flight techniques.

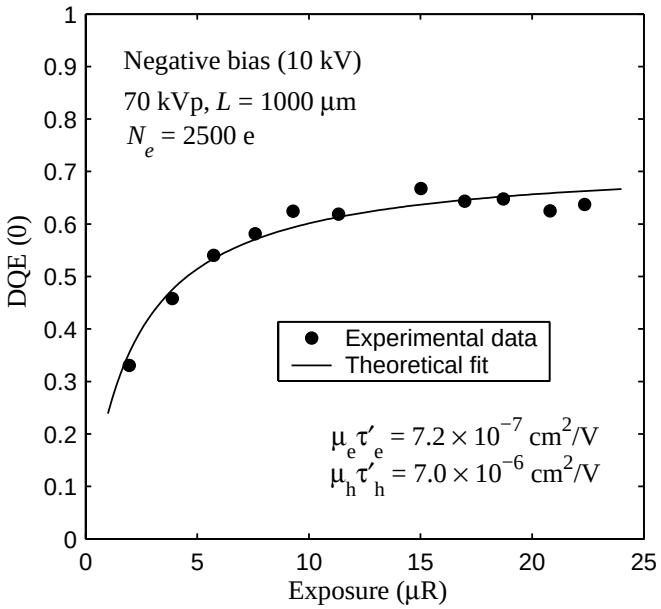

Figure 5.13 DQE(0) vs. exposure (X) for an a-Se x-ray image detector. Points are experimental data [Ref. 89] and the solid line is the theoretical fit to the experimental data for a 70 kVp x-ray spectrum with 23.5 mm Al filtration, and the best fit $\mu_h \tau'_h$ and $\mu_e \tau'_e$ are shown in the figure.

5.3.2 Comparison of DQE(0) of different photoconductive detectors

The DQE(0) model is applied to a-Se, poly-HgI_2 and poly-CdZnTe detectors for fluoroscopic applications to study and compare their DQE(0) performances. We assume that the pixel area, A = 200 μm × 200 μm and effective fill factor is 1.0 for all types of detectors. The average incident x-ray photon energy (E) is 60 keV and the additive electronic noise (N_e) is assumed to be 2000e per pixel.

Figure 5.14 shows the DQE(0) as a function of x-ray exposure for *a*-Se, HgI_2, and CdZnTe detectors for a 60 keV monoenergetic x-ray beam. The x-ray exposure (X) is varied from 0.1 μR to 10 μR, which is the range of x-ray exposure for fluoroscopic applications. The following transport and operating parameters are used in figure 5.14: for *a*-Se detectors, L = 1000 μm, F = 10 V/μm, $W_{\pm} \approx 43$ eV, $\mu_e \tau_e' = 10^{-6}$ cm^2/V and $\mu_h \tau_h' = 10^{-5}$ cm^2/V; for HgI_2 detectors, L = 260 μm, F = 0.5 V/μm, $W_{\pm}$ = 5 eV, $\mu_e \tau_e' = 6 \times 10^{-6}$ cm^2/V and $\mu_h \tau_h' = 10^{-7}$ cm^2/V; and for CdZnTe detectors, L = 270 μm, F = 0.25

V/μm, $W_{\pm}$ = 5 eV, $\mu_e \tau_e'$ = 2 ×10^{-4} cm^2/V and $\mu_h \tau_h'$ = 3 ×10^{-6} cm^2/V. The radiation-receiving electrode is biased positively for a-Se detectors and negatively for HgI_2 and CdZnTe detectors. The normalized attenuation depth $\Delta \approx 0.98$ is for all types of the detectors. The quantum efficiency, $\eta = 1 - \exp(-1/\Delta) \approx 0.64$, is the maximum achievable DQE(0) if all the liberated charges are collected. The DQE for the CdZnTe detector is relatively unchanged over the whole exposure range. This is due to a large conversion gain (low $W_{\pm}$) and high charge collection efficiency (good transport properties). The DQE for a-Se detectors is small at low exposures because of its relatively low conversion gain and is controlled by the added electronic noise. As the x-ray exposure increases, each pixel receives more photons. The relative contribution of electronic noise to total noise becomes less important and thus the DQE increases. The DQE(0) reaches almost a constant value when the x-ray exposure increases and is limited by the quantum noise (and hence by the charge collection efficiency) thereafter as evident in figure 5.14. The DQE for HgI_2 detectors is relatively small even at higher exposures because of its low charge collection efficiency. The charge collection efficiency can be improved by increasing the electric field. However, increasing the electric field also increases the dark current dramatically in both HgI_2 and CdZnTe detectors. An electric field as high as 20 V/μm is achievable in a-Se detectors keeping the dark current within an acceptable level for x-ray imaging [11]. The charge collection efficiency of a-Se detectors is relatively high because of the high applied fields that are needed to obtain a reasonable $W_{\pm}$.

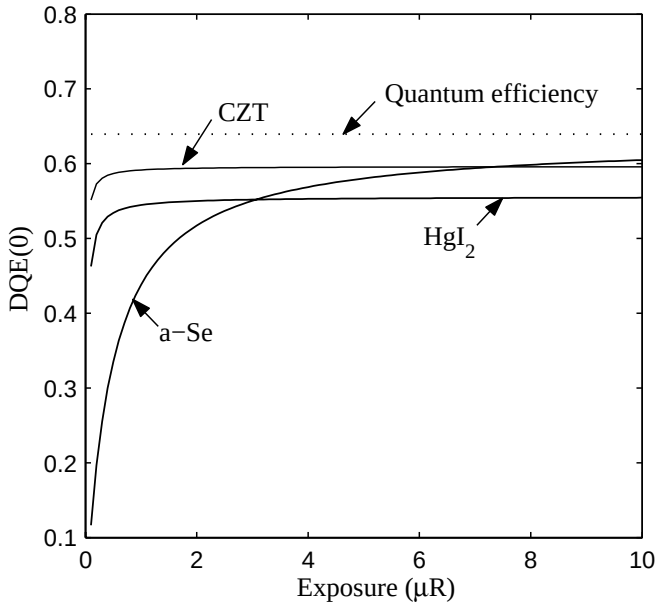

Figure 5.14 DQE(0) versus x-ray exposure for *a*-Se, poly-HgI_2, and poly-CdZnTe detectors and for a 60 keV monoenergetic x-ray beam. The electronic noise is 2000e per pixel. The electric field is assumed to be 10 V/μm for a-Se, 0.5 V/μm for HgI_2 and 0.25 V/μm for CdZnTe.

Figures 5.15 (a), (b) and (c) show 3-D plots of the DQE(0) versus L and N_e for *a*-Se, poly-HgI_2, and poly-CdZnTe detectors respectively, exposed to 1 μR (average exposure in fluoroscopic applications) at a photon energy of 60 keV (monoenergetic beam). The DQE(0) performance for a-Se detectors in Figure 5.15(a) is examined under a constant positive bias voltage of 10 kV as determined by the practical limitations in sensor electronics. On the other hand, the DQE(0) performances for HgI_2, and CdZnTe detectors in Figures 5.15 (b) and (c) are examined under a constant electric field of 0.5 V/μm for HgI_2 and 0.25 V/μm for CdZnTe as determined by the practical limitations in dark current. The bias polarity and mobility-lifetime products for each type of detector in Figure 5.15 are the same as in figure 5.14.

(a)

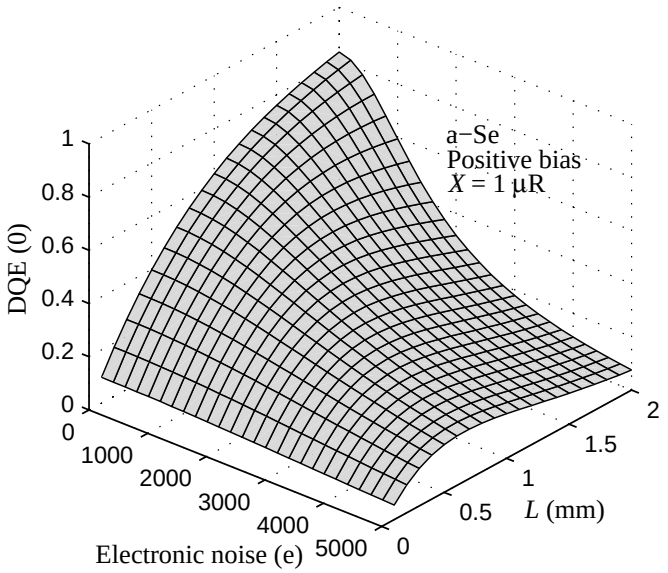
a−Se
Positive bias
X = 1 μR
DQE (0)
0
0.2
0.4
0.6
0.8
1
0
1000
2000
3000
4000
5000
Electronic noise (e)
0
0.5
1
1.5
2
L (mm)

(b)

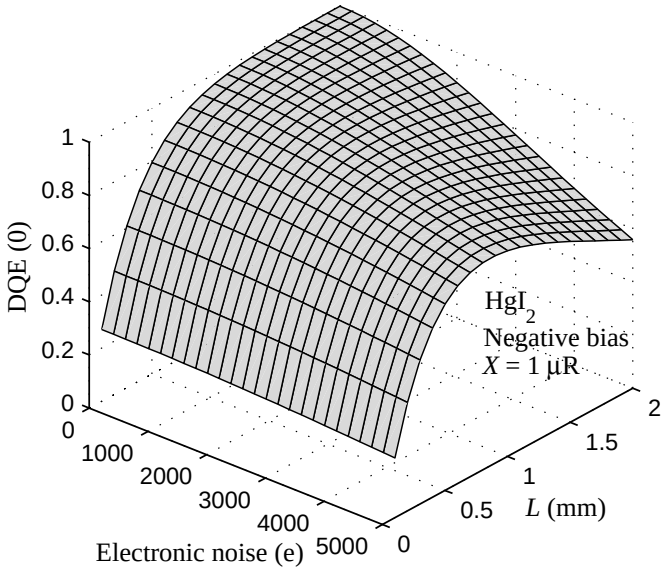
HgI2
Negative bias
X = 1 μR
DQE (0)
0
0.2
0.4
0.6
0.8
1
0
1000
2000
3000
4000
5000
Electronic noise (e)
0
0.5
1
1.5
2
L (mm)

(c)

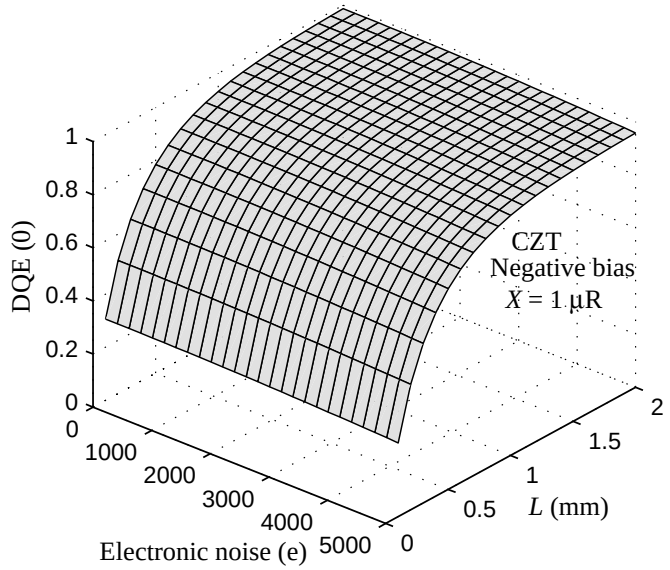

Figure 5.15 DQE(0) versus detector thickness (L) and electronic noise (N_e) for (a) *a*-Se, (b) HgI_2, and (c) CdZnTe detectors and for a 60 keV monoenergetic x-ray beam. The a-Se detector is operating under a constant voltage of 10 kV and, HgI_2 and CdZnTe detectors are operating under a constant electric field of 0.5 V/μm and 0.25 V/μm, respectively.

Under a constant bias *a*-Se detector, the electric field in the photoconductor decreases with the detector thickness, which further modifies the charge collection and conversion gain. The conversion gain also decreases with increasing photoconductor thickness due to the increase of $W_{\pm}$ with decreasing field. For a-Se detectors, there is an optimum detector thickness that maximizes the DQE for reasonable amounts of added electronic noise (e.g., 1000e or higher) as shown in Figure 5.15(a). Thus we obtain an optimum thickness that compromises between higher quantum efficiency (higher L), higher charge collection efficiency (smaller L), and higher conversion gain (smaller L at constant bias). The DQE peak shifts towards higher L, as N_e gets lower.

There exists a DQE peak for HgI_2 detectors and the DQE peak shifts towards higher L, as N_e gets lower as shown in Figure 5.15(b). The DQE for HgI_2 detectors does not continue to improve with higher photoconductor thickness because of low charge collection efficiency. Thus, there is an optimum thickness that compromises between

higher quantum efficiency (higher L), higher charge collection efficiency (smaller L). The DQE for the CdZnTe detector increases with increasing detector thickness and is relatively unchanged with varying electronic noise because of its large conversion gain (low $W_{\pm}$) and high charge collection efficiency. Therefore the DQE for the CdZnTe detector is only controlled by its quantum efficiency. It is apparent from Figures 5.15(a), (b) and (c) that both high conversion gain and high charge collection efficiency are required to improve the DQE performance of an x-ray image detector [90]. The conversion gain depends on $W_{\pm}$, which is a material property of the photoconductor. The charge collection efficiency can be improved by increasing the field and improving the mobility-lifetime products of the carriers. There is a practical limitation on increasing electric field imposed by the dark current. The mobility-lifetime products may vary dramatically from sample to sample, depending on processing techniques, impurities and crystal defects.

5.4 Summary

A cascaded linear system model that includes incomplete charge collection and x-ray interaction depth dependent conversion gain and charge collection stages has been considered for the calculation of the DQE(0) of a direct conversion x-ray image detector. Using this model, the DQE(0) of *a*-Se detectors for fluoroscopic applications has been examined in detail as a function of charge transport parameters and detector thickness under different operating conditions (electronic noise, x-ray exposure, bias voltage and polarity). We have found an *optimum photoconductor thickness* that maximizes the DQE(0) under a constant voltage operation. The optimum thickness increases with increasing x-ray exposure, bias voltage and charge collection efficiency, and decreasing added electronic noise. For reasonable quantities mentioned in this work that are appropriate for *a*-Se detectors and fluoroscopic applications, the optimum *a*-Se thickness is ~ 700 μm and the corresponding DQE is ~ 0.4. It was shown that DQE depends sensitively on the charge transport properties ($\mu\tau'$) of the photoconductors and hence the charge collection efficiency. With the radiation receiving electrode negatively biased, the DQE is much more dependent on electron lifetime than hole lifetime. The

DQE(0) of *a*-Se detector is higher for positive bias than for negative bias. The results suggest that the DQE can be improved by ensuring that the carrier with the higher mobility-lifetime product is drifted towards the bottom electrode. The DQE generally does not continue to improve with greater photoconductor thickness because of charge transport and trapping effects. The DQE of polyenergetic x-ray beam is slightly lower than monoenergetic x-ray beam with the same average photon energy. It is shown that the scattering events and fluorescence escape reduce the DQE(0) through the reduction of the conversion gain. This reduction of the DQE(0) depends on the operating conditions and transport properties of a-Se. The DQE(0) model is applied to explain experimental DQE data on a-Se image detectors and the model shows a very good agreement with experimental DQE data. The DQE(0) model is applied to three potential photoconductive x-ray image detectors (a-Se, poly-HgI_2 and poly-CdZnTe) for fluoroscopic applications considering their practical operating conditions. It is found that, in addition to high quantum efficiency, both high conversion gain and high charge collection efficiency are required to improve the DQE performance of an x-ray image detector.

6. RESOLUTION OF FLAT-PANEL DETECTORS

6.1 Introduction

The direct conversion flat-panel detector geometry consists of a photoconductor layer sandwiched between two electrodes; the electrode at one side is a continuous metal plate and the electrode on the other side of the photoconductor is segmented into an array of individual square pixels of size $a' \times a'$ as shown in Figure 6.1 (a). There is a gap of negligible dimension between the pixel electrodes. Some of the x-ray generated carriers become captured by deep traps (from which there is no escape over the time scale of observation) in the bulk of the photoconductor during their drift across the photoconductor. Suppose that a carrier is trapped in the photoconductor above a particular (central) pixel electrode of a pixellated image sensor. This trapped carrier induces charges not only on the central pixel electrode but also on neighboring pixel electrodes as shown in Figure 6.1(b), and consequently there is a lateral spread of information and hence a loss of image resolution. In this thesis, the general effect of charge carrier trapping on the resolution of direct conversion flat-panel detectors is considered as explained below.

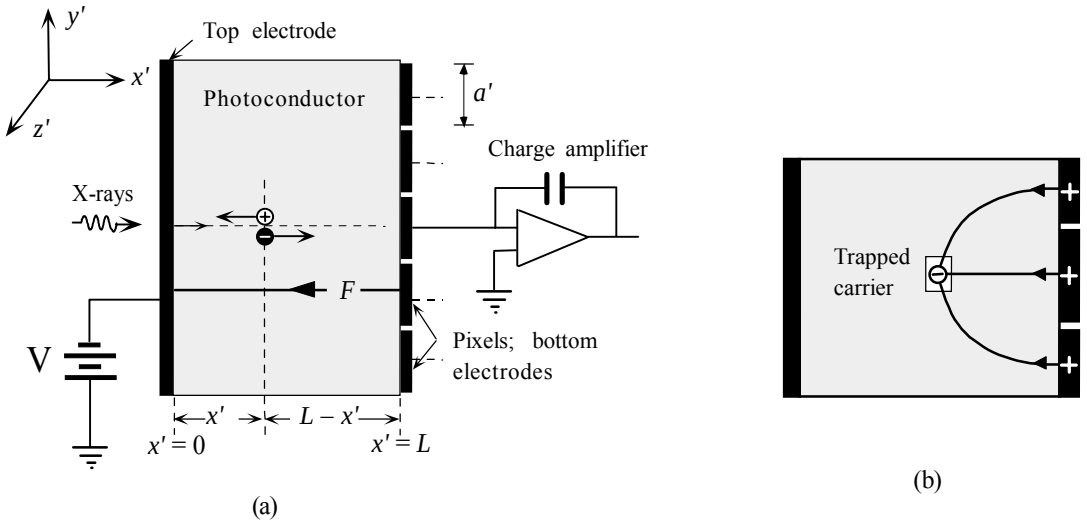

Figure 6.1 (a) A cross section of a direct conversion pixellated x-ray image detector. (b) Trapped carriers in the photoconductor induce charges not only on the central pixel electrode but also on neighboring pixel electrodes, spread the information and hence reduce spatial resolution.

The study of spatial resolution characteristics of an imaging detector is an important metric of examining the quality of images that it produces. The spatial resolution of an imaging device or a system is described in terms of the modulation transfer function (MTF), which is the relative response of the system as a function spatial frequency (see Section 2.6 for descriptions of MTF). Que and Rowlands [91] have evaluated the intrinsic spatial resolution of *a*-Se based x-ray image detectors including K-fluorescent photon reabsorption and the range of primary electrons. Some of the K-fluorescent x-ray photons may be reabsorbed at different points within the detector volume from the primary x-ray photon interaction point. This creates a lateral spreading of signal and a loss of resolution. Later, Zhao and Rowlands [81] have formulated the MTF due to carrier trapping at a fixed surface (parallel to the pixel plane) near the electrodes. Recently, Kasap *et al.* [14, 92] have discussed several causes for the loss of resolution in photoconductive detectors including the loss of resolution due to bulk trapping. In this thesis, an analytical expression of MTF due to distributed carrier trapping in the bulk of the photoconductor is derived using the trapped charge distribution across the photoconductor. The analytical expressions of trapped charge distributions are derived by solving the continuity equation for both types of carriers. The MTF of

photoconductive x-ray detectors is studied for (a) different levels of carrier trapping of both carrier types (electrons and holes) and (b) different values of x-ray absorption depths. To maintain generality, the calculations are given in normalized coordinates to enable the results to be applied to different photoconductive x-ray image detectors. The MTF model is applied to polycrystalline CdZnTe (CZT) detectors and is fitted to recently published experimental results.

6.2 MTF Model

The basic principle of a direct conversion flat panel pixel detector is schematically illustrated in Figure 6.1(a). A photoconductor layer has been sandwiched between two electrodes. A current integrating amplifier is connected to each pixel electrode and measures the collected charge by integrating the induced x-ray photocurrent through the pixel electrode (the integration time is longer than the exposure time). The lateral dimension of the photoconductor slab is much greater than the detector thickness L. The continuous electrode (top electrode) is biased with a voltage V to establish an electric field F in the photoconductor. It is assumed in Figure 6.1 that this electrode is biased negatively. The electric field lines very close to the pixellated electrodes bend slightly. Therefore the electric field remains relatively uniform provided the device is operated in the *small signal* condition. In this case, the carrier transport remains essentially one-dimensional. The x-ray generated carriers follow the straight electric field lines and either reach the electrodes or become trapped in the photoconductor. The diffusion of carriers is negligible compared with their drift because of high applied field across the photoconductor. Also, the loss of carriers by deep trapping is more significant than bulk recombination. We assign a constant drift mobility μ and a single deep trapping time (lifetime) τ to each type of carriers (holes and electrons) since the interrupted field time-of-flight measurements indicate a single deep trapping time for both types of carriers [50].

The incident x rays are attenuated exponentially across the photoconductor thickness and generate electron hole pair (EHP) concentration that follows the x-ray

photon absorption profile. The initial carrier concentration across the photoconductor for a short x-ray pulse is given by,

$$c_t'(x',0) = c_b'(x',0) = B\exp(-\alpha x'), \tag{6.1}$$

where α is the linear attenuation coefficient of the photoconductor, c_t' and c_b' are the carrier concentrations for the charge carriers drifting towards the top and the bottom electrodes respectively, and B is the carrier concentration at location $x'= 0$ and time, $t' = 0$. The subscript t and b refer to carrier types drifting towards the top and bottom electrodes respectively; the top electrode receives the x-ray radiation. If the applied bias to the radiation-receiving electrode is negative, the subscript t represents holes (h) and b represents electrons (e).

For simplicity, we use the normalized distance coordinates x, y and z, where $x = x'/L$, $y = y'/L$ and $z = z'/L$ to yield the normalized attenuation depth, $\Delta = 1/\alpha L$, the normalized pixel aperture width, $a = a'/L$ and normalized spatial frequency, $f = f'L$, in which f' is the actual spatial frequency. The *geometric* pixel aperture width in flat panel detector is smaller than the pixel pitch (center-to-center spacing between two pixels). However, it is shown that the effective fill factor (the effective fraction of pixel area used for image charge collection) of a photoconductive flat panel detector is close to unity [85, 93]. Therefore, the *effective* pixel aperture width is virtually identical to the pixel pitch. The time coordinate is normalized with respect to the transit time t_0 ($t_0 = L/\mu F$) for each species of carriers. Therefore, the normalized time coordinate $t = t'/t_0$ and normalized carrier lifetime, $\tau = \tau'/t_0 = \mu\tau F/L$. The normalized carrier lifetime is also called the normalized schubweg (schubweg / photoconductor thickness). Charge carrier concentrations are normalized with respect to the total initial collectable EHP generation in the photoconductor as if the total initial EHP is uniformly distributed over the sample volume. Therefore, the normalized carrier concentration, $c = c'/c_0$, where

$$c_0 = \frac{1}{L}\int_0^L B\, e^{-\alpha x'} dx' = B\Delta\left(1 - e^{-1/\Delta}\right) \tag{6.2}$$

6.2.1 Spatial trapped charge distributions

Considering the assumptions mentioned above and using the normalized coordinates, the continuity equation for the carriers drifting towards the bottom electrode is given by

$$\frac{\partial c_b}{\partial t} = -\frac{\partial c_b}{\partial x} - \frac{c_b}{\tau_b} \ , \tag{6.3}$$

where $\tau_b = \mu_b \tau'_b F/L$. The solution of equation (6.3) is a drifting carrier distribution that is given by, [68]

$$\begin{aligned} c_b(x,t) &= \frac{1}{\Delta\eta}\exp[-(x-t)/\Delta]\exp(-t/\tau_b) \ ; \ t < x < 1 \\ c_b(x,t) &= 0 \, ; \ x < t \text{ and } x > 1 \end{aligned} \tag{6.4}$$

where, $\eta = 1 - \exp(-1/\Delta)$; quantum efficiency of the detector. The trapping of charge carriers at any point occurs as long as free carriers exist there provided that we ignore trap saturation effects for small signal case (it is likely that some trap saturation cannot be totally ignored for large signals, e.g., see Kasap *et al*. [94]). Assuming no trapped charge carriers in the photoconductor just before an x-ray exposure, the normalized final trapped carrier distribution for the carriers that drift towards the bottom electrodes is given by [60, 95]

$$c_{b_t}(x) = \int_{t=0}^{t=x} \frac{c_b(x,t)}{\tau_b} dt \, , \tag{6.5}$$

Which gives,

$$c_{b_t}(x) = \frac{\left(e^{-x/\Delta} - e^{-x/\tau_b}\right)}{\Delta\eta\left(1 - \tau_b/\Delta\right)} \ ; 0 < x < 1 \tag{6.6}$$

where the sub-subscript *t* on *c* refers to trapped carriers. Similarly, the trapped carrier distribution for the carriers that drift towards the top electrode is

$$c_{t_t}(x) = \frac{\left[e^{-x/\Delta} - e^{-(1-x)/\tau_t} e^{-1/\Delta}\right]}{\Delta\eta(1+\tau_t/\Delta)} \; ; 0 < x < 1, \tag{6.7}$$

where $\tau_t = \mu_t \tau'_t F/L$. The normalized net space charge concentration distribution (i.e. normalized space charge density) across the photoconductor is

$$q_t(x) = \left[c_{b_t}(x) - c_{t_t}(x)\right]. \tag{6.8}$$

The polarity of the carriers that move towards the bottom electrode is considered as positive in equation (6.8). The normalized mean number of carriers that reach the pixel electrode is

$$\overline{Q}_b = \int_0^1 \frac{e^{-x/\Delta}}{\Delta\eta} dx - \int_0^1 c_{b_t}(x) dx = \frac{\tau_b\left(e^{-\frac{1}{\Delta}} - e^{-\frac{1}{\tau_b}}\right)}{\eta\Delta(1-\tau_b/\Delta)}. \tag{6.9}$$

6.2.2 Modulation transfer function

If the effective spacing between pixels is negligible compared to pixel dimensions, the detector geometry is just like a parallel plate configuration from the electrostatic point of view, except that the currents through individual pixels are integrated separately. The induced charge density at the pixel plane (y–z plane at x = 1) due to a point charge at (x, y, z) in the photoconductor can be conveniently calculated by constructing an infinite series of image charges [96, 97]. The line spread function (LSF) along y axis at the pixel plane is calculated by considering induced charges along y axis due to distributed bulk trapped charges in xz plane at y = 0 as shown in Figure 6.2. The LSF is given by [60],

$$L(y) = \frac{1}{2\pi} \int_0^1 \int_{-\infty}^{\infty} \sum_{k=-\infty}^{\infty} \frac{q_t(x)(1-x+2k)}{\left[(1-x+2k)^2 + y^2 + z^2\right]^{3/2}} dz dx + \overline{Q}_b \delta(y), \tag{6.10}$$

where k is an integer.

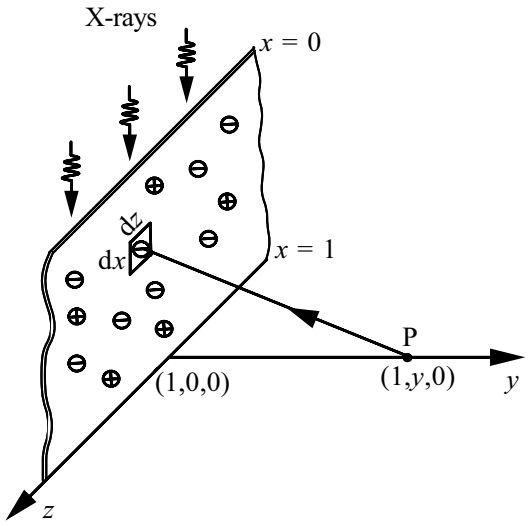

Figure 6.2 A schematic diagram for calculating LSF. The induced charge density at point P due to distributed bulk trapping in *xz* plane (at $y = 0$) is calculated, where P is an arbitrary point along the *y* axis.

The Fourier transform of $L(y)$ is (see Appendix C),

$$G(f) = \frac{(\tau_b + \tau_t)\left(\omega\,\mathrm{cosech}\omega - \mathrm{e}^{-\frac{1}{\Delta}}\,\omega\coth\omega - \Delta^{-1}\mathrm{e}^{-\frac{1}{\Delta}}\right)}{\eta\Delta^2(1-\tau_b/\Delta)(1+\tau_t/\Delta)\left(\Delta^{-2}-\omega^2\right)} - \frac{\left(\omega\,\mathrm{cosech}\omega - \mathrm{e}^{-\frac{1}{\tau_b}}\,\omega\coth\omega - \tau_b^{-1}\mathrm{e}^{-\frac{1}{\tau_b}}\right)}{\eta\Delta(1-\tau_b/\Delta)\left(\tau_b^{-2}-\omega^2\right)}$$

$$+ \frac{\left(\mathrm{e}^{-\frac{1}{\Delta}-\frac{1}{\tau_t}}\,\omega\,\mathrm{cosech}\omega - \mathrm{e}^{-\frac{1}{\Delta}}\,\omega\coth\omega + \tau_t^{-1}\mathrm{e}^{-\frac{1}{\Delta}}\right)}{\eta\Delta(1+\tau_t/\Delta)\left(\tau_t^{-2}-\omega^2\right)} + \frac{\tau_b\left(\mathrm{e}^{-\frac{1}{\Delta}} - \mathrm{e}^{-\frac{1}{\tau_b}}\right)}{\eta\Delta(1-\tau_b/\Delta)} \qquad (6.11)$$

where $\omega = 2\pi f$. The expression for $G(f = 0)$ is

$$G(0) = \frac{(\tau_b + \tau_t)\left(1 - \mathrm{e}^{-\frac{1}{\Delta}} - \Delta^{-1}\mathrm{e}^{-\frac{1}{\Delta}}\right)}{\eta(1-\tau_b/\Delta)(1+\tau_t/\Delta)} - \frac{\tau_b\left(\tau_b - \mathrm{e}^{-\frac{1}{\tau_b}} - \tau_b\mathrm{e}^{-\frac{1}{\tau_b}}\right)}{\eta\Delta(1-\tau_b/\Delta)}$$

$$+\frac{\tau_t\left(\tau_t\, e^{-\frac{1}{\Delta}-\frac{1}{\tau_t}}+e^{-\frac{1}{\Delta}}-\tau_t e^{-\frac{1}{\Delta}}\right)}{\eta\Delta\left(1+\tau_t/\Delta\right)}+\frac{\tau_b\left(e^{-\frac{1}{\Delta}}-e^{-\frac{1}{\tau_b}}\right)}{\eta\Delta\left(1-\tau_b/\Delta\right)} \tag{6.12}$$

The MTF is unity at zero spatial frequency. Therefore, the MTF due to bulk trapping is

$$\mathrm{MTF}_{\mathrm{trap}}(f)=\frac{G(f)}{G(0)} \tag{6.13}$$

6.3 Results and Discussions

6.3.1 Trapped charge distributions

Equations (6.6) and (6.7) are used to examine the distributions of trapped electron and hole concentrations across the photoconductor as a function of operating conditions (*e.g. F* and energy spectrum), detector thickness *L*, material properties; carrier ranges ($\mu\tau'$) and attenuation coefficient.

Figures 6.3 (a) and 6.3(b) show the trapped carrier distributions as a function of normalized distance *x* from the radiation receiving electrode for different levels of trapping at Δ = 0.25 with negative bias. The solid lines represent trapped electron distributions and the dashed lines represent trapped hole distributions. The trapped electron concentration versus distance has a maximum that moves to lower *x* as τ_e (τ_b in Figures 6.3 (a) and 6.3(b)) gets shorter. Electrons exist for a longer period at larger *x*, which gives higher electron trapping. The initial charge carrier concentration is not uniform throughout the thickness of the photoconductor but decreases exponentially with increasing *x*. If the electrons are trapped, electron density decreases gradually during their drift through the photoconductor, which leads to a lower trapping rate at higher *x*. Thus there is an optimum distance that compromises between longer trapping period (higher *x*) and higher trapping rate (lower *x*). The peak trap concentration for the

carriers (electrons in Figure 6.3 (a)) that move towards the pixel electrode occurs at a distance, x_{max}, from the top electrode, where

$$x_{max} = \begin{cases} \dfrac{\Delta \tau_b \ln\left(\frac{\Delta}{\tau_b}\right)}{\Delta - \tau_b}; & \text{if } \dfrac{\tau_b}{1 + \tau_b \ln \tau_b} \le \dfrac{\Delta}{1 + \Delta \ln \Delta} \\ 1 \quad ; & \text{otherwise} \end{cases} \tag{6.14}$$

The trapped hole concentration is maximum at the radiation receiving side and decreases with x. It is due to the fact that the holes exist for a longer period at lower x. The trapped carrier distribution becomes more linear as Δ increases (compare $\Delta = 0.25$ and 1 in figure 6.3) and as absorption becomes more uniform. Thus for a very large Δ (almost uniform x-ray interaction), the trapped electron concentration increases linearly with x and the trapped hole concentration decreases linearly with x. If the applied bias to the radiation-receiving electrode is positive, the solid lines and the dashed lines in Figure 6.3 (a) & 6.3(b) must represent trapped hole distributions and trapped electron distributions, respectively.

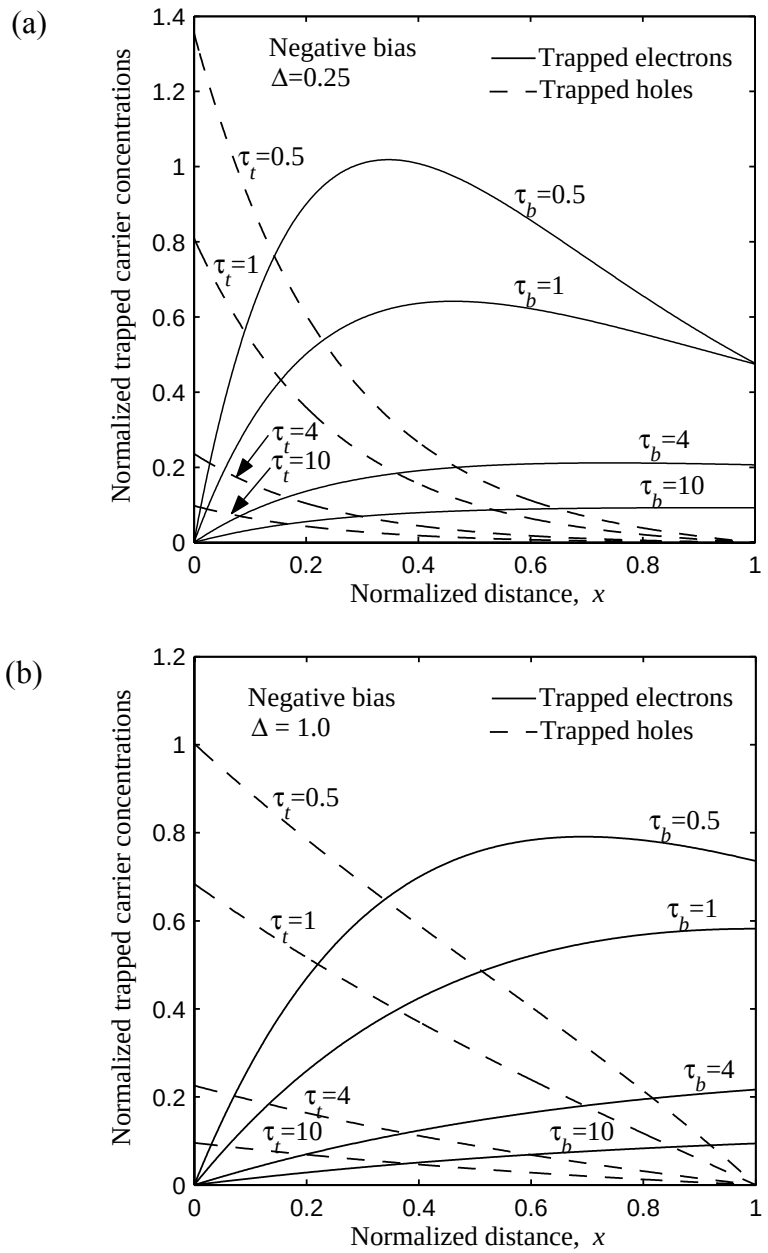

Figure 6.3 (a) The trapped carrier distributions versus normalized distance x from the radiation-receiving electrode for different levels of trapping at $\Delta = 0.25$ with negative bias. (b) The trapped carrier distributions versus normalized distance x from the radiation-receiving electrode for different levels of trapping at $\Delta = 1.0$ with negative bias. The solid lines represent trapped electron distributions and the dashed lines represent trapped hole distributions.

6.3.2 Modulation transfer function

If x rays are incident at a particular pixel, the radiation-receiving pixel and also the neighboring pixels collect charges due to carrier trapping effects. The polarity of collected charges in the neighboring pixels compared to that in the radiation-receiving pixel depends on the rate of trapping of both types of carriers. For $\tau_t = \infty$ and for various levels of τ_b, the polarity of collected charges in the surrounding pixels is the same as that in the radiation-receiving pixel. On the other hand, the polarity of collected charges in the surrounding pixels is the opposite of that in the radiation-receiving pixel for $\tau_b = \infty$ and for various levels of τ_t as described in the literature [95, 98] (see also section 7.3.3).

The signal spreading in terms of the MTF due to carrier trapping (MTF_{trap}) is studied by using equations (6.11), (6.12) and (6.13). Figure 6.4 (a) shows the MTF_{trap} versus normalized spatial frequency with no trapping of carriers that drift towards the top electrode ($\tau_t = \infty$) and various levels of trapping of the other type of carriers (τ_b) for $\Delta = 0.5$. For example, with negative applied bias to the radiation-receiving electrode, all the holes are collected but electrons suffer various degrees of trapping as represented by the values of τ_b. As expected, the effects of carrier trapping on MTF increases with increasing the rate of carrier trapping (decreasing τ_b) as shown in Figure 6.4 (a). If there is no trapping of both the carriers (τ_t, $\tau_b = \infty$), the MTF_{trap}, as expected, is unity for all spatial frequencies which is evident from Figure 6.4. The high carrier trapping can severely affect the MTF of the detector. For example, taking $a = 0.2$, full trapping of carriers that drift towards the bottom electrode, $\tau_b = 0$, reduces MTF_{trap} to 0.068 at Nyquist frequency ($f = f_{ny}$) of $MTF_{trap}(0)$.

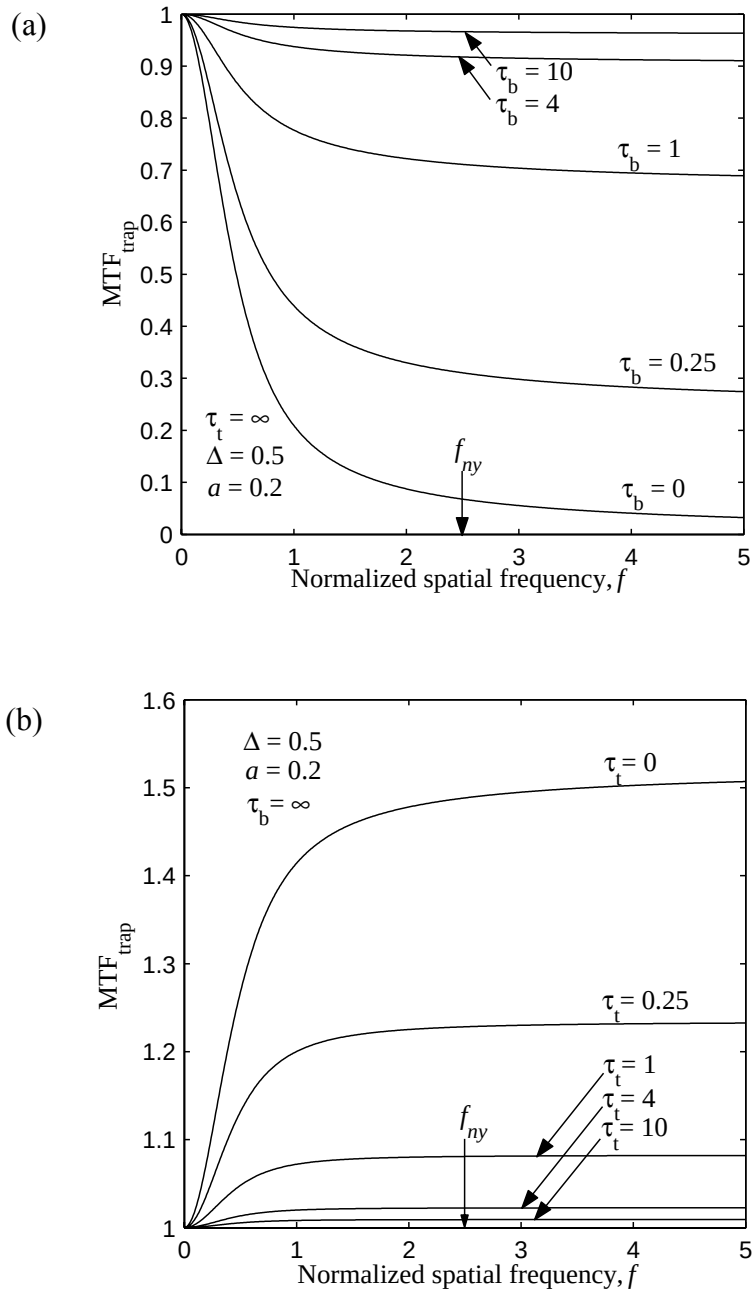

Figure 6.4 (a) MTF_{trap} versus normalized spatial frequency with $\tau_t = \infty$ for various levels of τ_b and for $\Delta = 0.5$. (b) MTF_{trap} versus normalized spatial frequency with $\tau_b = \infty$ for various levels of τ_t and for $\Delta = 0.5$. f_{ny} is the normalized Nyquist frequency for $a = 0.2$.

Figure 6.4 (b) shows the MTF_{trap} versus normalized spatial frequency with $\tau_b = \infty$ for various levels of τ_t and for $\Delta = 0.5$ (in this case, with negative bias, all electrons are

collected and holes suffer various degrees of trapping as represented by the values of τ_t). The MTF_{trap} increases with increasing spatial frequency, which is the opposite of the case shown in Figure 6.4(a). The reason is that the polarity of collected charges in the surrounding pixels is the opposite of that in the radiation-receiving pixel in this case. The image system can be described as a cascade of several stages and the overall MTF of image system is the product of the MTF of all the individual stages. It is instructive to examine the presampling MTF of the detector to get the effect of MTF_{trap} on the overall MTF of the system. For simplicity, we assume that the presampling MTF is the product of MTF_{trap} and the aperture function (a *sinc* function).

Figures 6.5 (a) and 6.5(b) show the effect of the MTF_{trap} on the presampling MTF of a pixellated detector. The range of normalized spatial frequencies (*f*) shown in Figure 6.5 is from zero to twice the normalized Nyquist frequency. Increase of trapping for the carriers that move towards the pixel electrodes reduces high frequency signals of its presampling MTF as shown in Figure 6.5 (a). On the contrary, increase of trapping for the carriers that move towards the top electrodes reduces low frequency signals and relatively enhances high frequency signals of its the presampling MTF as shown in Figure 6.5(b). Therefore, this effect enhances fine structure contrast and subdues broad area contrast of x-ray images [99]. Note that the presampling MTF is equal to the aperture function for no trapping of both the carriers (τ_t, $\tau_b = \infty$).

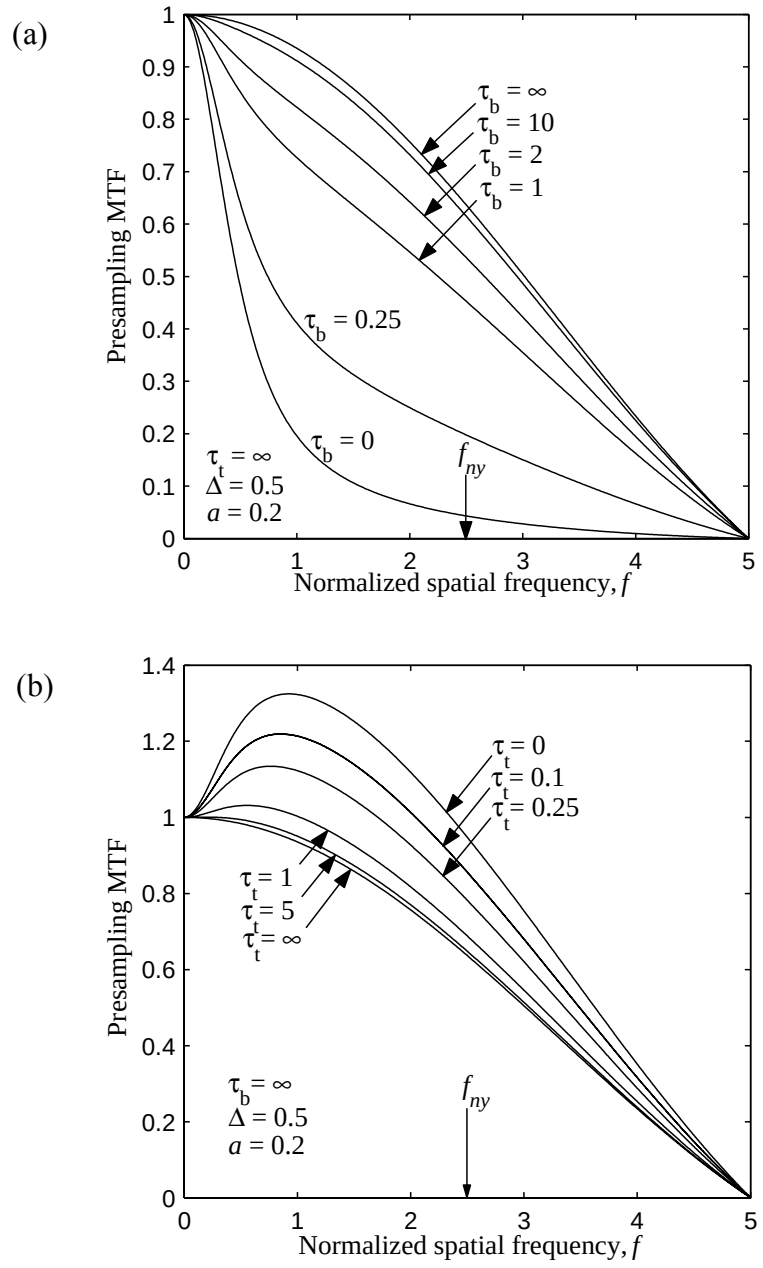

Figure 6.5 (a) Presampling MTF versus normalized spatial frequency with $\tau_t = \infty$ for various levels of τ_b including bulk charge carrier trapping. (b) Presampling MTF versus normalized spatial frequency with $\tau_b = \infty$ for various levels of τ_t including bulk trapping.

The effect of normalized absorption depth on the MTF_{trap} is shown in Figures 6.6 (a) and 6.6(b). The effect of trapping on MTF for the carriers that move towards the pixel electrodes decreases with increasing Δ as shown in Figure 6.6(a). On the other hand, the

effect of trapping on MTF for the carriers that move to the top electrode increases with increasing Δ as shown in Figure 6.6(b).

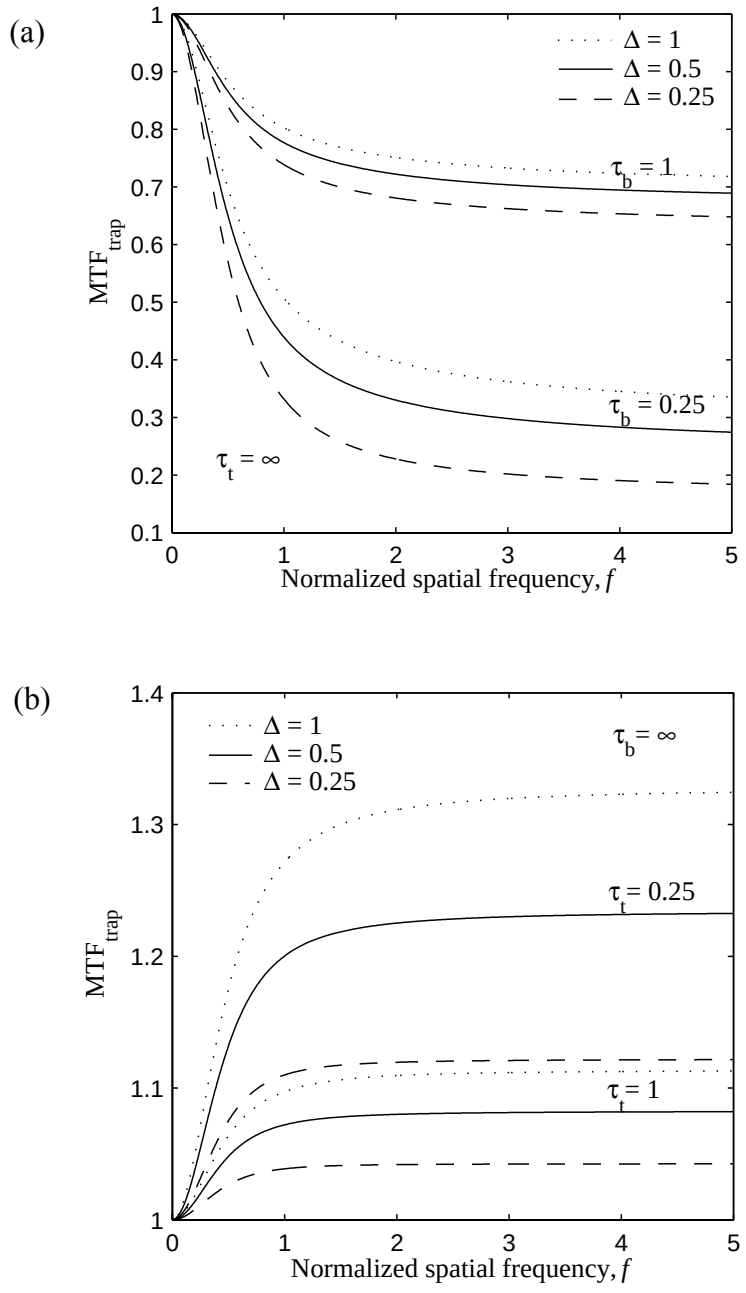

Figure 6.6 (a) MTF_{trap} versus normalized spatial frequency with $\tau_t = \infty$ for finite τ_b and for various values of Δ. (b) MTF_{trap} versus normalized spatial frequency with $\tau_b = \infty$ for finite τ_t and for various values of Δ.

The MTF model is fitted to recently published experimental data on polycrystalline CZT x-ray detector [100]. Figure 6.7 shows the MTF of a 300 μm thick positively biased CZT detector exposed to an 80 kVp x-ray beam with 26mm-Al filtration. The operating electric field is 0.25 V/μm and pixel pitch is 150 μm. The Nyquist frequency is 3.3 lp/mm. The experimental data have been extracted from Figure 10 of Ref. [100]. As apparent from figure 6.7, there is a very good agreement between the model and the experimental data. The best fit $\mu\tau'$ products of electrons and holes are $\mu_e\tau'_e = 2.4 \times 10^{-4}$ cm^2/V and $\mu_h\tau'_h = 3.2 \times 10^{-6}$ cm^2/V, which are very close to $\mu\tau'$ values reported in the literature [57, 59]. It is instructive to comment that Mainprize *et al*. [59] reported a value of $\mu_e\tau'_e \approx 2.4 \times 10^{-4}$ cm^2/V for polycrystalline CZT by modeling the charge collection efficiency (not MTF), which is a remarkable agreement with our value for $\mu_e\tau'_e$ from MTF modeling even though the two samples are different. Although we have applied the charge carrier trapping-limited MTF model to the CZT sensors, the model can also be applied to other photoconductive (e.g., a-Se and HgI_2) panel x-ray image detectors.

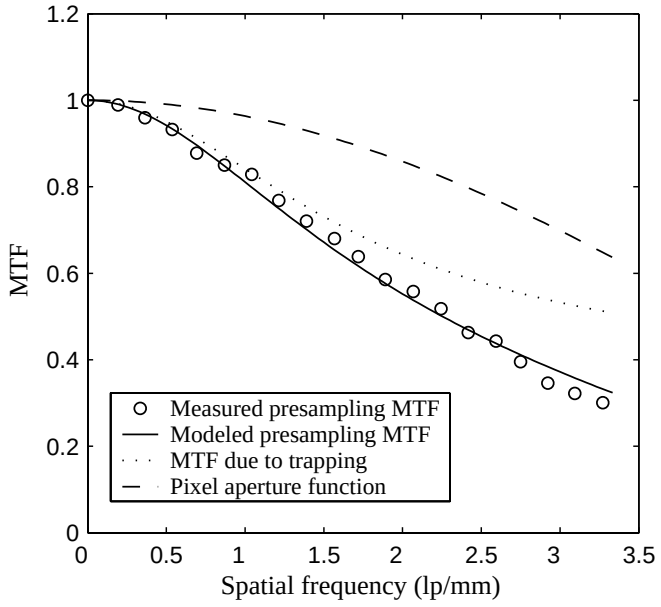

Figure 6.7 Measured presampling MTF of a polycrystalline CdZnTe detector in comparison with modeled results, which included blurring due to charge carrier trapping in the bulk of the photoconductor. The detector thickness is 300 μm and pixel pitch is 150 μm. [Measured data have been extracted from Figure 10 of Ref. 100]

6.4 Summary

An analytical expression of MTF due to distributed carrier trapping in the bulk of the photoconductor has been derived using the trapped charge distribution across the photoconductor. The analytical expressions for trapped charge distributions in an x-ray photoconductor have also been derived. The MTF of photoconductive x-ray detectors have been studied for (a) different levels of carrier trapping and (b) different values of x-ray absorption depths. To maintain generality, the calculations are given in normalized coordinates to enable the results to be applied to different photoconductive x-ray image detectors. Trapping of the carriers that move towards the pixel electrodes degrades the MTF performance, whereas trapping of the other type of carriers improves the sharpness of the x-ray image. The MTF model is applied to polycrystalline CdZnTe x-ray image detectors and is fitted to recently published experimental results. The theoretical model shows a very good agreement with the measured data with $\mu_e \tau'_e = 2.4 \times 10^{-4}$ cm^2/V and $\mu_h \tau'_h = 3.2 \times 10^{-6}$ cm^2/V, which are very close to $\mu\tau'$ values reported in the literature.

7. X-RAY SENSITIVITY OF PIXELLATED DETECTORS

7.1 Introduction

The direct conversion flat-panel detector geometry consists of a photoconductor layer sandwiched between two electrodes; the electrode at one side is a continuous metal plate and the electrode on the other side of the photoconductor is segmented into an array of individual square pixels of size $a' \times a'$ as shown in Figure 7.1. There is a gap of negligible dimension between the pixel electrodes. If x rays are incident over a particular pixel volume of a pixellated detector, the radiation-receiving pixel and also the neighboring pixels collect charges due to carrier trapping effects. The collected charge at the radiation-receiving pixel is the desired signal and contributes to sensitivity. The x-ray sensitivity of a pixellated detector is defined as the collected charge per unit area per unit exposure of radiation for a pixel that is assumed to receive the radiation. The x-ray sensitivity is influenced by the pixel size in addition to the photoconductor properties, operating conditions and the detector thickness.

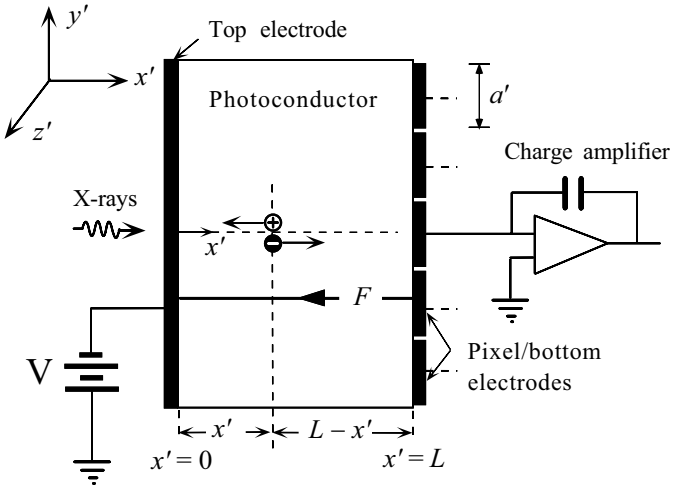

Figure 7.1 A cross section of a direct conversion pixellated x-ray image detector. An electron and a hole are generated at x' and are drifting under the influence of the electric field F. The center of the central pixel electrode is at $x' = L$, $y' = 0$ and $z' = 0$.

The method for calculating collected charge (or sensitivity) described in Chapter 4 applies to a large area unsegmented planar x-ray detector (small pixel effects are excluded) [67, 68]. In this chapter, the charge collection and absorption-limited x-ray sensitivity of a pixellated detector (e.g. flat panel detector) is considered by incorporating charge carrier trapping and small pixel effects [101]. The charge collection and absorption-limited normalized x-ray sensitivity of a direct conversion pixellated x-ray detector operating in the presence of deep trapping of charge carriers is calculated by two approaches: (i) use of the Shockley-Ramo theorem and the weighting potential of the individual pixel, and (ii) use of the final trapped charge distributions across the photoconductor and the weighting potential of the individual pixel. An analytical expression for calculating weighting potential of square pixels is also developed. The normalized sensitivity of a direct conversion pixellated x-ray detector is analyzed as a function of pixel size for various levels of both types of carrier trappings (electrons and holes). To maintain generality, the calculations are given in normalized coordinates and parameters to enable the results to be applied to different photoconductive pixellated x-ray detectors. For example, the sensitivity model is applied to a-Se, poly-HgI_2 and poly-CZT detectors for fluoroscopic and chest

radiographic applications to examine the x-ray sensitivity over the range of the operating electric fields and mobility-lifetime products.

7.2 Sensitivity Model for Pixellated Detectors

The basic structure of a direct conversion flat panel pixel detector is schematically shown in Figure 7.1. A photoconductor layer has been sandwiched between two electrodes. The lateral dimension of the photoconductor slab is much greater than the photoconductor thickness L. A current integrating amplifier is connected to each pixel electrode and measures the collected charge by integrating the induced x-ray photocurrent through the pixel electrode (the integration time is longer than the exposure time). The continuous electrode (top electrode) is biased with a voltage V to establish an electric field F in the photoconductor. The applied bias voltage to this electrode may be positive or negative. It is assumed in Figure 7.1 that this electrode is biased negatively. The electric field lines very close to the pixellated electrodes bend slightly. Therefore the electric field remains relatively uniform provided the device is operated in the *small signal* condition. In this case, the carrier transport remains essentially one-dimensional. The x-ray generated carriers (electrons and holes) follow the straight electric field lines and either reach the electrodes or become trapped in the photoconductor. The diffusion of carriers is negligible compared with their drift because of high applied field across the photoconductor. Also, the loss of carriers by deep trapping is more significant than bulk recombination. We assign a constant drift mobility μ and a single deep trapping time (lifetime) τ to each type of carriers (holes and electrons) since the interrupted field time-of-flight measurements indicate a single deep trapping time for both types of carriers [50].

The x rays are attenuated exponentially across the photoconductor thickness and generate electron hole pair (EHP) concentration that follows the x-ray photon absorption profile. The probability density for an x-ray photon, that is attenuated within a detector, to interact at a distance x' from the top electrode is given by,

$$p_{x'}(x') = \begin{Bmatrix} \dfrac{\alpha e^{-\alpha x'}}{\eta}, 0 \le x' \le L \\ 0, \quad \text{elsewhere} \end{Bmatrix} \tag{7.1}$$

where $\alpha(E)$ is the linear attenuation coefficient of the photoconductor, E is the incident x-ray photon energy, and $\eta(E)$ is the quantum efficiency of the detector. The x-ray photon energy dependent x-ray quantum efficiency $\eta(E)$ is given by,

$$\eta(E) = 1 - \mathrm{e}^{-\alpha(E)L} \tag{7.2}$$

The initial carrier concentration across the photoconductor for a short x-ray pulse is given by,

$$c_t'(x',0) = c_b'(x',0) = B\exp(-\alpha x'), \tag{7.3}$$

where α is the linear attenuation coefficient of the photoconductor, c_t' and c_b' are the carrier concentrations for the charge carriers drifting towards the top and the bottom electrodes respectively, and B is the carrier concentration at location $x' = 0$ and time, $t' = 0$. The subscript t and b refer to carrier types drifting towards the top and bottom electrodes respectively; the top electrode receives the x-ray radiation. If the applied bias to the radiation-receiving electrode is negative, the subscript t represents holes (h) and b represents electrons (e).

For simplicity, we use the normalized distance coordinates x, y and z, where $x = x'/L$, $y = y'/L$ and $z = z'/L$ to yield the normalized attenuation depth, $\Delta = 1/\alpha L$ and the normalized pixel aperture width, $a = a'/L$. The time coordinate is normalized with respect to the transit time t_0 ($t_0 = L/\mu F$) for each species of carriers. Therefore, the normalized time coordinate $t = t'/t_0$ and normalized carrier lifetime, $\tau = \tau'/t_0 = \mu\tau F/L$. The normalized carrier lifetime is also called the normalized schubweg (schubweg / thickness). Schubweg ($\mu\tau F$) is the mean distance a carrier traverses before being captured by a deep trap (from which there is no escape over the time scale of observation). Charge carrier concentrations are normalized with respect to the total initial collectable EHP generation in the photoconductor as if the total initial EHP is

uniformly distributed over the sample volume. Therefore, the normalized carrier concentration, $c = c'/c_0$, where

$$c_0 = \frac{1}{L}\int_0^L B\, e^{-\alpha x'} dx' = B\Delta\left(1 - e^{-1/\Delta}\right) \tag{7.4}$$

The pixel aperture width in a flat panel detector is smaller than the pixel pitch (center-to-center spacing between two pixels). However, it is shown that the effective fill factor (the effective fraction of pixel area used for image charge collection) of a photoconductive flat panel detector is close to unity [93]. In this thesis, we consider that the pixel aperture width is virtually identical to the pixel pitch. Therefore, the detector geometry is just like a parallel plate configuration from an electrostatic point of view, except that the currents through individual pixels are integrated separately.

7.2.1 Weighting potential of square pixel electrodes

The Shockley-Ramo theorem [28, 29] provides a convenient way to calculate the induced charges at different pixels due to the motion of charge carriers in the detector based on the weighting potential of individual pixels. Using Green's reciprocation theorem, the induced charge on a pixel j by a positive unit charge at x is equal to the weighting potential, $V_{wj}(x)$, of that pixel. The induced charge density at the pixel plane (y–z plane at x = 1) due to a point charge at x can be conveniently calculated by constructing an infinite series of image charges [96, 97]. The induced charge on any pixel is the integration of charge density over the pixel area. Thus the weighting potential of a square pixel j for x-ray interaction at (x, y, z) is given by [95, 102]

$$V_{wj}(x,y,z) = \frac{1}{2\pi}\int_{z_{1j}}^{z_{2j}}\int_{y_{1j}}^{y_{2j}} \sum_{k=-\infty}^{\infty} \frac{(1-x+2k)}{\left[(1-x+2k)^2 + (y'-y)^2 + (z'-z)^2\right]^{3/2}} dy'dz' \tag{7.5}$$

Which gives,

$$V_{wj}(x,y,z)=\frac{1}{2\pi}\sum_{k=-\infty}^{k=\infty}\left[\arctan\frac{\beta_2\gamma_2}{(1-x+2k)\sqrt{(1-x+2k)^2+\beta_2^2+\gamma_2^2}}\right.$$
$$-\arctan\frac{\beta_2\gamma_1}{(1-x+2k)\sqrt{(1-x+2k)^2+\beta_2^2+\gamma_1^2}}$$
$$-\arctan\frac{\beta_1\gamma_2}{(1-x+2k)\sqrt{(1-x+2k)^2+\beta_1^2+\gamma_2^2}} \quad , \qquad (7.6)$$
$$\left.+\arctan\frac{\beta_1\gamma_1}{(1-x+2k)\sqrt{(1-x+2k)^2+\beta_1^2+\gamma_1^2}}\right]$$

where k is an integer, $\beta_1 = y_{1j} - y$, $\beta_2 = y_{2j} - y$, $\gamma_1 = z_{1j} - z$ and $\gamma_2 = z_{2j} - z$. The area of a square pixel j in y–z plane is defined by the y coordinate from y_{1j} to y_{2j} and the z coordinate from z_{1j} to z_{2j}. The above expression of weighting potential is applicable provided the gap between the pixels is negligibly small. The weighting potential of a large area single-element detector is equivalent to an infinite-size pixel of the pixellated detectors, which is simply a linear function of depth x from 0 to 1. But the weighting potential profile across the detector is no longer linear for a finite size pixel of the pixellated detectors as evident from equation (7.6).

7.2.2 Charge collections in different pixels

If x rays are incident over a particular pixel volume of a pixellated detector, the radiation-receiving pixel and also the neighboring pixels collect charges due to carrier trapping effects. In this thesis, two techniques are presented for calculating the collected charges at the pixels. One approach uses the Ramo-Shockley theorem and the weighting potential of the individual pixel. The other technique is based on the calculation of the induced charges on the pixels due to the final trapped charges in the photoconductor.

A. Solution using the Shockley-Ramo theorem

Brunett *et al*. [103] have calculated the collected charge of a detector by dividing the detector thickness into a large number of small segments. Note that Brunett *et al*. did not neglect trapping but accounted for trapping at the end of each segment. The calculations of charge collection in this thesis follow the technique described by Brunett *et al*. except that we also introduce the charge collection efficiency in each segment rather than assuming full charge collection in a very narrow segment. We calculate the mean charge collection taking into account that the x-ray photon absorption profile across the photoconductor thickness is exponential.

The normalized uniform step size, $\Delta x = 1/N$, where N is number of spatial divisions. Then the discrete point $x = x_i \Delta x$, where x_i is an integer varies from 0 to N. The slope of weighting potential profile is considered as constant within each step and thus the weighting field is approximately constant. After an EHP generation at x due to x-ray interaction, one type of carrier drifts towards the bottom electrode and the other type of carrier drifts towards the top electrode. Both types of carrier drift produce currents of the same polarity at any electrode. Therefore, the collected charge at any electrode is the sum of the contributions of both types of carrier transports. The contributions of collected charges at a pixel j for an EHP generation at x are [102]

$$Q_j(x)_b = \sum_{m=x_i}^{N-1} \frac{\tau_b}{\Delta x}[1-\exp(-\Delta x/\tau_b)]\exp[-(m-x_i)\Delta t/\tau_b][V_{wj}(m+1) - V_{wj}(m)],\ 0 \le x_i \le N-1 \tag{7.7a}$$

$$Q_j(x)_t = \sum_{m=1}^{x_i} \frac{\tau_t}{\Delta x}[1-\exp(-\Delta x/\tau_t)]\exp[-(x_i-m)\Delta t/\tau_t][V_{wj}(m) - V_{wj}(m-1)],\ 1 \le x_i \le N \tag{7.7b}$$

where, $\tau_t = \mu_t \tau'_t F/L$, $\tau_b = \mu_b \tau'_b F/L$. Δt is the normalized transit time to move a carrier across the normalized distance Δx. The net collected charge,

$$Q_j(x) = Q_j(x)_t + Q_j(x)_b. \tag{7.8}$$

For a large area single-element detector the weighting potential $V_w(x) = x$ and substituting this in equations (7.6) and (7.7), the collected charge for an EHP generation at x (from equation (7.8)), is

$$Q(x) = \tau_t \left(1 - \mathrm{e}^{-\frac{x}{\tau_t}} \right) + \tau_b \left(1 - \mathrm{e}^{-\frac{1-x}{\tau_b}} \right) \tag{7.9}$$

Equation (7.9) is the well-known Hecht charge collection equation (section 2.2), which describes the mean collected charge for a large area single-element detector and for an EHP generation at x.

The average normalized collected charge (charge collection efficiency) $\overline{Q}_j$ at a pixel j for an exponential x-ray absorption profile across the photoconductor thickness is

$$\overline{Q}_j = \int_0^1 Q_j(x) P_x(x) dx = \frac{1}{\Delta\eta} \int_0^1 Q_j(x) \mathrm{e}^{-\frac{x}{\Delta}} dx \tag{7.10}$$

Thus, the normalized mean collected charge at the central pixel ($j = 0$) for exponential x-ray interaction at (y, z) is given by

$$\overline{Q}_0(y,z) = \int_0^1 Q_0(x,y,z) P_x(x) dx = \frac{1}{\Delta\eta} \int_0^1 Q_0(x,y,z) \mathrm{e}^{-\frac{x}{\Delta}} dx \tag{7.11}$$

B. Solution using the final trapped charge distribution

Assuming no trapped charge carriers in the photoconductor just before an x-ray exposure, the normalized final trapped carrier distributions for the carriers that drift towards the bottom and top electrodes are given respectively by [60, 95]

$$c_{b_t}(x) = \frac{\left(e^{-x/\Delta} - e^{-x/\tau_b}\right)}{\Delta\eta\left(1-\tau_b/\Delta\right)} \; ; 0 < x < 1 \tag{7.12}$$

$$c_{t_t}(x) = \frac{\left[e^{-x/\Delta} - e^{-(1-x)/\tau_t} e^{-1/\Delta}\right]}{\Delta\eta\left(1+\tau_t/\Delta\right)} \; ; 0 < x < 1, \tag{7.13}$$

where the sub-subscript t on c refers to trapped carriers. The normalized net space charge concentration distribution (i.e. normalized space charge density) across the photoconductor is

$$q_t(x) = \left[c_{b_t}(x) - c_{t_t}(x)\right]. \tag{7.14}$$

The polarity of the carriers that move towards the bottom electrode is considered as positive in equation (7.14). The normalized mean number of carriers that reach the pixel electrode is

$$\overline{Q_b} = \int_0^1 \frac{e^{-x/\Delta}}{\Delta\eta} dx - \int_0^1 c_{b_t}(x) dx = \frac{\tau_b\left(e^{-\frac{1}{\Delta}} - e^{-\frac{1}{\tau_b}}\right)}{\eta\Delta\left(1-\tau_b/\Delta\right)}. \tag{7.15}$$

After x-ray interaction a charge profile is created in the photoconductor and it induces charges of opposite sign on the pixel electrodes. As the charge carriers drift, the induced surface charges on the electrodes change. These induced charges on the pixel electrodes are balanced by the transfer of charges between the pixel electrodes and the external circuit. The integration of these transferred charges is called the *collected charge*. Thus the sign of collected charge is the opposite of the induced charge. If a charge carrier reaches at a particular pixel electrode, it contributes to the full charge collection for that pixel and the neighboring pixels receive no signal. Therefore, the total collected charge at a pixel is equal to the induced charges (with opposite sign) on

the pixel due to the final trapped charges, plus the amount of charge carriers that reach the pixel electrode. The normalized mean collected charge at the central pixel ($j = 0$) for exponential x-ray interaction at (y, z), if the point (y, z) is within the boundary of the central pixel ($j = 0$), is [90, 95]

$$\overline{Q}_0(y,z) = \int_0^1 q_t(x) V_{w0}(x,y,z)dx + \overline{Q}_b \tag{7.16a}$$

Otherwise, $\overline{Q}_0(y,z) = \int_0^1 q_t(x) V_{w0}(x,y,z)dx$ (7.16b)

7.2.3 Average x-ray sensitivity

The normalized sensitivity is calculated by considering uniform x-ray radiation over the entire area of a particular pixel (e.g. center pixel in Fig. 2) as shown in Fig. 2. The normalized mean collected charge at the central pixel ($j = 0$) for exponential x-ray interaction at (y, z) can be calculated by the equation (7.11) or (7.16a). The point (y, z) represents the point of x-ray interaction in the detector plane and the mean collected charge $\overline{Q}_0(y,z)$ depends on this point of x-ray interaction. The normalized average collected charge at the pixel that receives radiation is [102]

$$\langle Q_0 \rangle = \frac{1}{a^2} \int_{-\frac{a}{2}}^{\frac{a}{2}} \int_{-\frac{a}{2}}^{\frac{a}{2}} \overline{Q}_0(y,z)dydz \; ; -a/2 \le y,z \le a/2 \tag{7.17}$$

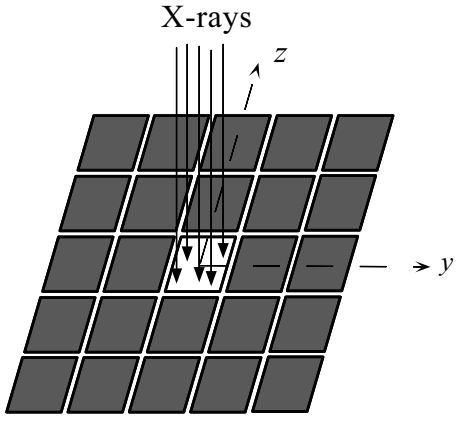

Figure 7.2 A two-dimensional array of pixel electrodes. X-rays are incident uniformly over the central pixel.

The normalized average collected charge represents the *charge collection efficiency* since the collected charge is normalized by the maximum collected charge per unit area that would arise if all the liberated carriers are collected. Therefore, the normalized sensitivity s is the product of the normalized collected charge Q and the quantum efficiency η. The normalized sensitivity is [102]

$$s(\tau_t, \tau_b, \Delta, a) = \langle Q_0 \rangle = \frac{\eta}{a^2} \int_{-\frac{a}{2}}^{\frac{a}{2}} \int_{-\frac{a}{2}}^{\frac{a}{2}} \overline{Q_0}(y,z)\, dydz \; ; -a/2 \le y, z \le a/2 \qquad (7.18)$$

It should be emphasized that this normalized sensitivity represents the x-ray sensitivity to x-rays that are incident only on the pixel of interest. The normalized sensitivity can be used to examine the sensitivity of various photoconductive pixellated detectors as a function of operating conditions (*e.g.*, electric field and incident x-ray photon energy), detector thickness, pixel size or material properties; carrier ranges ($\mu\tau$'s) and attenuation coefficients. Stated differently, the sensitivity of a pixellated detector is closely controlled by Δ, τ_t and τ_b as well as the normalized pixel size a.

7.3 Results and Discussions

7.3.1 Weighting potential

The weighting potentials of different pixels for different points of x-ray interactions have been calculated using equation (7.6). One thousand image charges is considered in the calculation, i.e., k = 500. Figure 7.3 (a) & (b) show the weighting potentials of the central pixel (V_{w0}) and the next neighboring pixel (V_{w1}) as a function of interaction position x for various normalized pixel widths and for x-ray interaction occurring along the center of the central pixel as it has been done by others previously [103]. For small pixels, the weighting potential V_{w0} rises very slowly until very close to the pixel electrodes (near-field region); then rises upwards sharply. On the other hand, the weighting potential V_{w0} is almost linear for large pixels, $a >> 1$, (e.g., $a = 4$ curve in Figure 7.3 a) as shown in Figure 7.3 (a). The later case is equivalent to the case of a single-element detector. The weighting potentials of neighboring pixels are zero at both

ends of the detector as shown in Figure 7.3 (b). The nonlinearity of the weighting potential of the next neighboring pixel V_{w1} increases with decreasing normalized pixel width a.

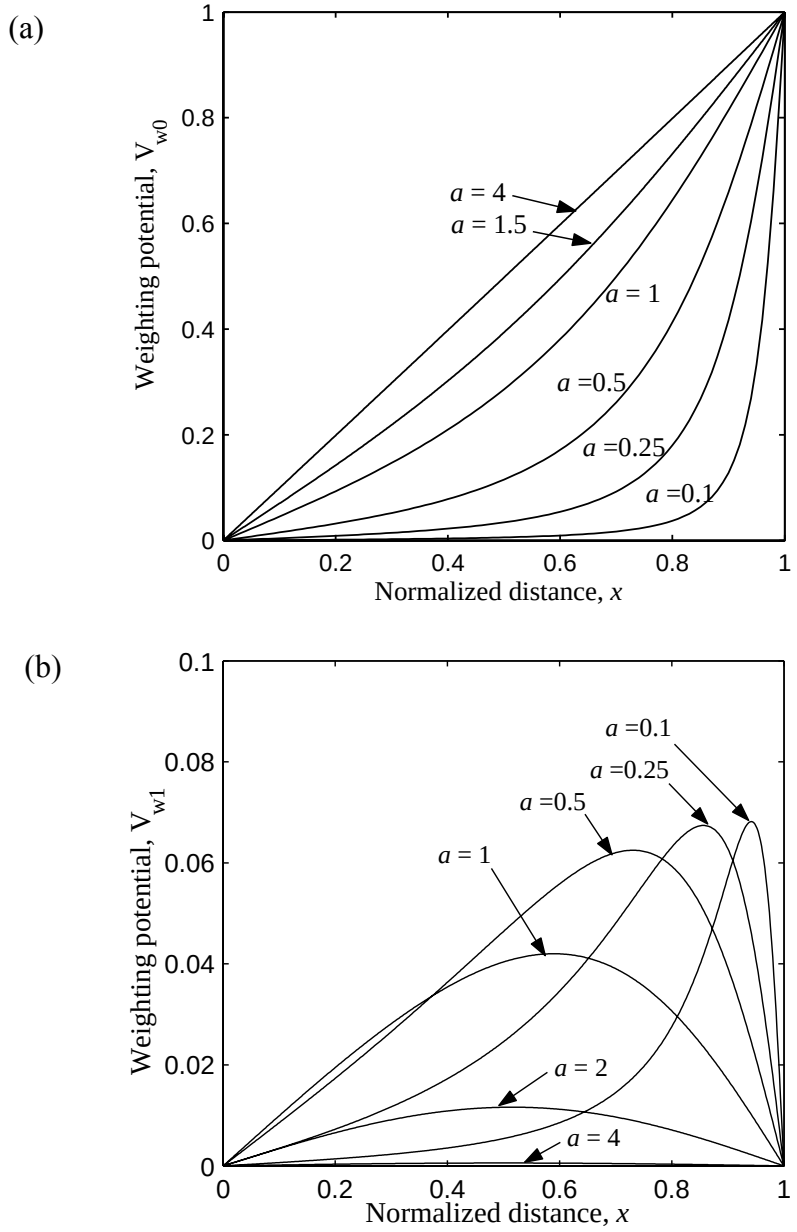

Figure 7.3 (a) Weighting potentials (V_{w0}) of the central pixel as a function of normalized distance x from the radiation-receiving electrode for x-ray interaction occurring along the center of the central pixel. (b) Weighting potentials of the next neighboring pixel (V_{w1}) versus normalized distance x for x-ray interaction occurring along the center of the central pixel.

7.2.2 Average x-ray sensitivity

The normalized sensitivity has been calculated by using equation (7.18). The effects of the normalized attenuation depth on the sensitivity have been studied in details in chapter 4 (see also Refs. 67 and 68). Figures 7.4(a) and (b) show the individual carrier contributions to the normalized sensitivity (s_t and s_b) versus normalized pixel width, a, for various levels of trapping and for $\Delta = 0.5$. s_t and s_b are the individual carrier contributions to the normalized sensitivity due to the carrier drifts towards the top and the bottom electrodes, respectively. s_t decreases with decreasing normalized pixel width. Since the weighting potential curve for small pixels is very steep in the near-field region and almost flat in the other part of the detector thickness (Figure 7.3), the carrier's drift through the small near-field region can produce almost full signal strength in the external circuit and the motion of charge carriers outside of this region induces very little signal. The extent of near field region decreases with decreasing pixel width. A very small fraction of carriers move through the near-field region for the carriers that move towards the top electrode. Therefore, the induced signals due to the carrier drift towards the top electrode decreases with decreasing normalized pixel width and so does s_t. The sensitivity obviously decreases with increasing amounts of trapping as evident in Figure 7.4(a).

Without carrier trapping and for small pixels, all the carriers that drift towards the bottom electrode pass through the near field region. Therefore, the relative fraction of the total normalized sensitivity, s_b, contributed by the charges that drift towards the bottom electrode increases with decreasing pixel width and the other type of carrier contribution becomes less important. Notice that s_b increases with decreasing pixel width for weak trapping but it decreases with decreasing pixel width under heavy trapping. The initial carrier profile is exponential across the photoconductor thickness. Most of the carriers are being trapped before reaching the near field region under heavy trapping for very small pixel detectors. Thus s_b for very small pixel detectors is also small under heavy trapping.

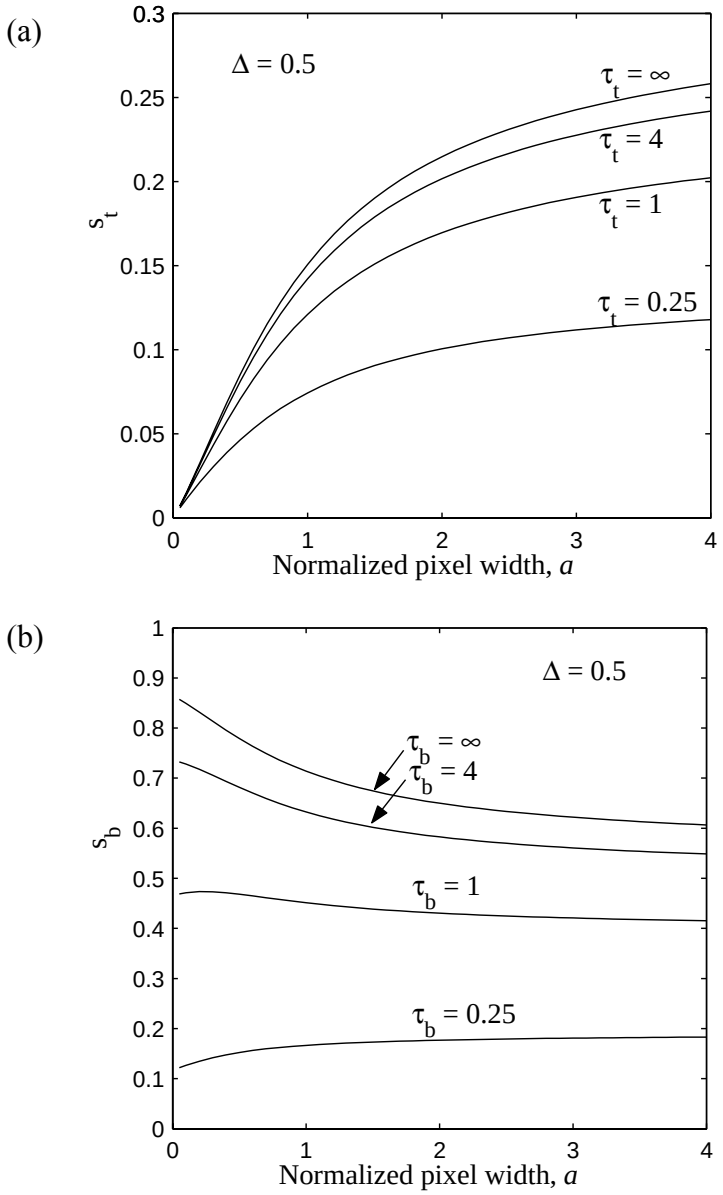

Figure 7.4 (a) Normalized sensitivity due to transport of the carriers that drift towards the top electrode, s_t, versus normalized pixel width for various levels of carrier trapping (finite τ_t). (b) Normalized sensitivity due to transport of the carriers that drift towards the bottom electrode, s_b, versus normalized pixel width for various levels of carrier trapping (finite τ_b). The normalized absorption depth, $\Delta = 0.5$.

It is instructive to examine the dependence of the total normalized sensitivity on the normalized pixel width, which is discussed below. Figure 7.5 (a) shows the normalized sensitivity versus pixel width with no trapping of carriers that drift towards the top

electrode ($\tau_t = \infty$) and various levels of trapping of the other type of carriers (finite τ_b) for $\Delta = 0.5$. If there is no trapping of both the carriers (τ_t, $\tau_b = \infty$), the normalized sensitivity is constant which is equal to the quantum efficiency of the detector; there is no variation with the pixel size as shown in Figure 7.5. The normalized sensitivity decreases with decreasing pixel width for finite carrier trapping (finite τ_b). Figure 7.5 (b) shows the normalized sensitivity versus pixel width with no trapping of carriers that move towards the pixel electrode ($\tau_b = \infty$) and various levels of trapping of the other type of carriers (finite τ_t). The normalized sensitivity increases with decreasing pixel width for finite carrier trapping of the carriers that drift towards the top electrode (finite τ_t); this type of trapping has almost no effect for very small pixel detectors. Some of the potential photoconductors (e.g. *a*-Se, CdZnTe and HgI_2) for x-ray image detectors have asymmetric transport properties (mobility-lifetime product) for electrons and holes. Therefore, having smaller pixels is advantageous in terms of higher sensitivity by ensuring that the carriers with the lower mobility-lifetime product are drifted towards the top electrode.

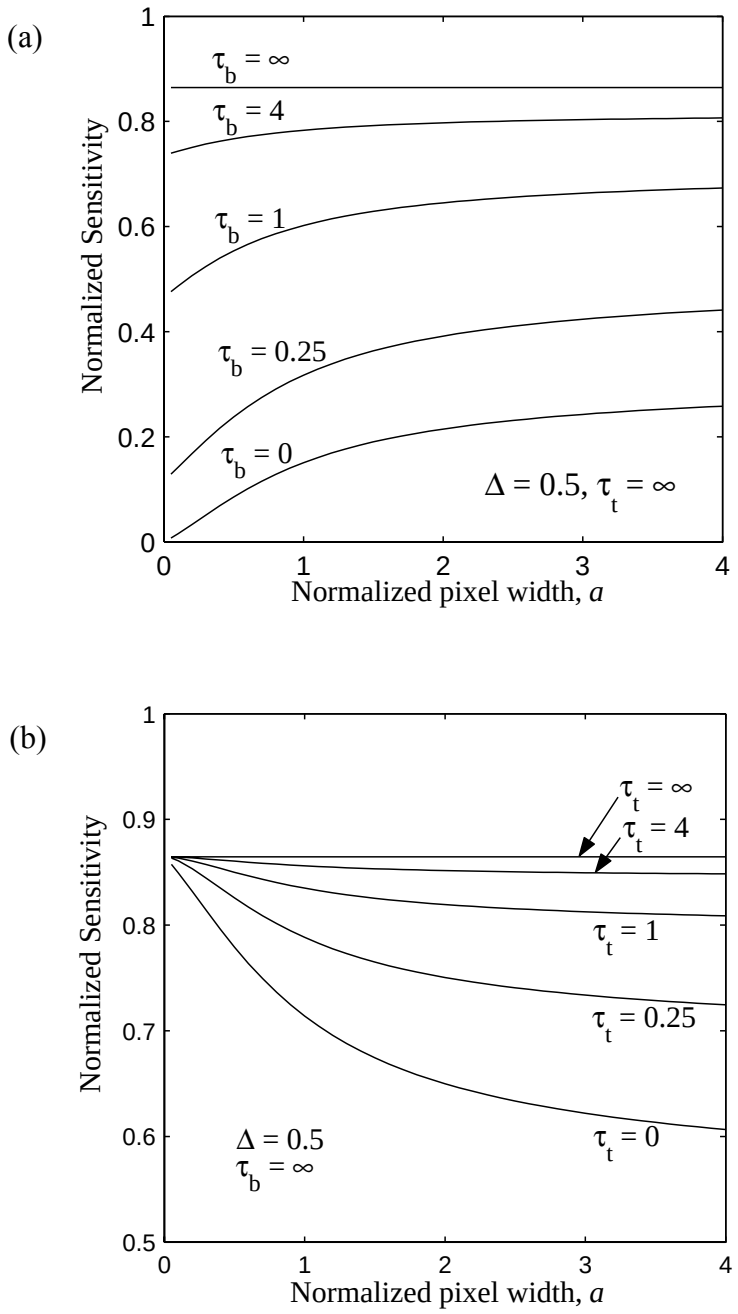

Figure 7.5 (a) Normalized sensitivity versus pixel width with no trapping of carriers that drift towards the top electrode ($\tau_t = \infty$) and various levels of trapping of the other type of carriers (finite τ_b). (b) Normalized sensitivity versus pixel width with no trapping of carriers that drift towards the bottom electrode ($\tau_b = \infty$) and various levels of trapping of the other type of carriers (finite τ_t). The normalized absorption depth, $\Delta = 0.5$.

The sensitivity model is applied to a-Se detectors for fluoroscopic and chest radiographic applications. Figure 7.6 shows the normalized sensitivity as a function of normalized pixel width for both positive and negative bias. Taking E = 60 keV, F = 10 V/μm, $\mu_e\tau_e' \approx 10^{-6}$ cm^2/V, $\mu_h\tau_h' \approx 10^{-5}$ cm^2/V, Δ = .976, τ_e = 1 and τ_h = 10. The sensitivity for positive bias increases with decreasing pixel width whereas the sensitivity for negative bias decreases with decreasing pixel width. The normalized sensitivity reaches its saturation value for very large pixels, which are equivalent to the results for a single-element planar detector as in chapter 4. The normalized pixel width varies from 0.1 to 1.0 in actual pixellated x-ray image detectors. For example, taking a' = 200 μm, a = 0.2; the normalized sensitivities are 0.605 for positive bias and 0.403 for negative bias, whereas for a single-element detector the sensitivities are 0.563 for positive bias and 0.528 for negative bias. Note that the sensitivity is improved slightly at positive bias but deteriorated significantly at negative bias because of the combined effects of small pixel and charge carrier trapping. Since electrons have a lower carrier range than holes in *a*-Se, positive bias is more advantageous over negative bias for *a*-Se based pixellated detectors. It should be strongly emphasized that the expected sensitivity estimated in this chapter represents the x-ray sensitivity to x-rays that are incident only on the pixel of interest. The induced charge on the pixel of interest by charge carriers liberated over neighboring pixels is undesired charge and can, in a sense, slightly negate the sensitivity improvement that smaller pixels seems to provide. (A more detailed and rigorous analysis would consider the sensitivity as a function of spatial frequencies making up the signal.)

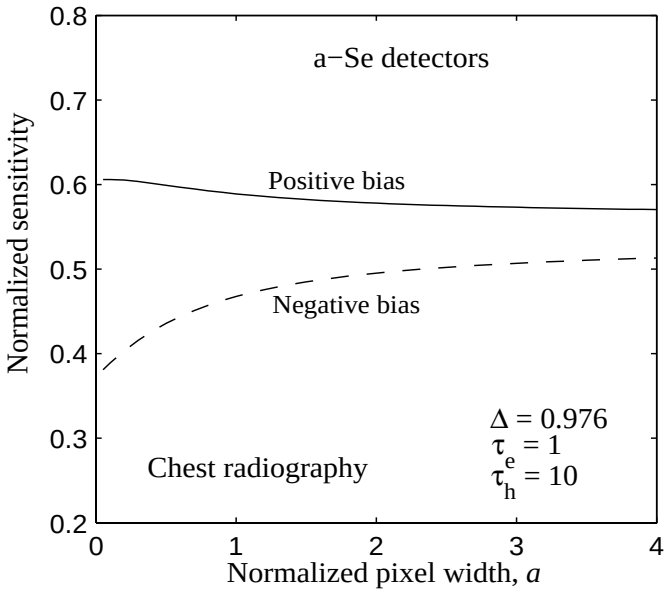

Figure 7.6 Normalized sensitivity of a-Se based pixellated detectors versus normalized pixel width.

The sensitivity model is also applied to *a*-Se, poly-HgI_2 and poly-$Cd_{.95}Zn_{.05}Te$ pixellated detectors (e.g., flat-panel detector) for fluoroscopic and chest radiographic applications to examine the x-ray sensitivity over the range of the operating electric fields and mobility-lifetime products. We have taken $a' = 200$ μm for all of the detector types. For *a*-Se detectors, $L = 1000$ μm, $F = 1 - 20$ V/μm, $\mu_e\tau_e' = 10^{-7} - 10^{-6}$ cm^2/V and $\mu_h\tau_h' = 10^{-6} - 10^{-5}$ cm^2/V (table 3.1); therefore, a = 0.2, $\tau_e = 0.01 - 2$ and $\tau_h = 0.1 - 20$. For HgI_2 detectors, $L = 260$ μm, $F = 0.1 - 1.0$ V/μm, $\mu_e\tau_e' = 6 \times 10^{-6} - 6 \times 10^{-5}$ cm^2/V and $\mu_h\tau_h' = 7 \times 10^{-8} - 7 \times 10^{-7}$ cm^2/V (table 3.1); therefore, $a = 0.77$, $\tau_e = 0.1 - 20$ and $\tau_h = 0.001 - 0.2$. For CdZnTe detectors, $L = 270$ μm, $F = 0.1 - .5$ V/μm, $\mu_e\tau_e' = 10^{-4} - 10^{-3}$ cm^2/V and $\mu_h\tau_h' = 10^{-6} - 10^{-5}$ cm^2/V (table 3.1); therefore, $a = 0.74$, $\tau_e = 1 - 100$ and $\tau_h = 0.01 - 1$. The average energy of incident x rays is 60 keV and the normalized absorption depth, $\Delta \approx 0.98$ for all of the detector types. The quantum efficiency, $\eta = 1 - \exp(-1/\Delta) \approx 0.64$.

Both positive and negative biases to the radiation-receiving electrode are used in a-Se and CdZnTe detectors, and only negative bias is used in HgI_2 detectors. Figure 7.7

(a) and (b) show three-dimensional plots of the normalized sensitivity of an *a*-Se detector as a function of τ_e and τ_h for positive and negative biases respectively. The x-ray sensitivity has a very little dependence on the charge carriers that have the opposite polarity to the bias on the radiation-receiving electrode. The normalized sensitivity with positive bias is better than that with negative bias as evident from Figures 7.7 (a) and (b). The normalized sensitivity with negative bias is quite sensitive to the normalized electron lifetime (τ_e). Figures 7.7 (c) and (d) show three-dimensional plots of the normalized sensitivity as a function of τ_e and τ_h for HgI_2 and CdZnTe detectors, respectively. The normalized x-ray sensitivity of CdZnTe detector is relatively constant over the whole range of operation. It is clear from Figures 7.7 (a), (b), (c) and (d) that the normalized carrier lifetimes (τ_e and τ_h) have significant effect on the x-ray sensitivity. It should be mentioned that the maximum normalized sensitivity is less than unity for a finite detector thickness because not all the radiation interacts in the photoconductor layer. The maximum normalized sensitivity is equal to the quantum efficiency of the detector (in this case, maximum $s = 0.64$).

(a)

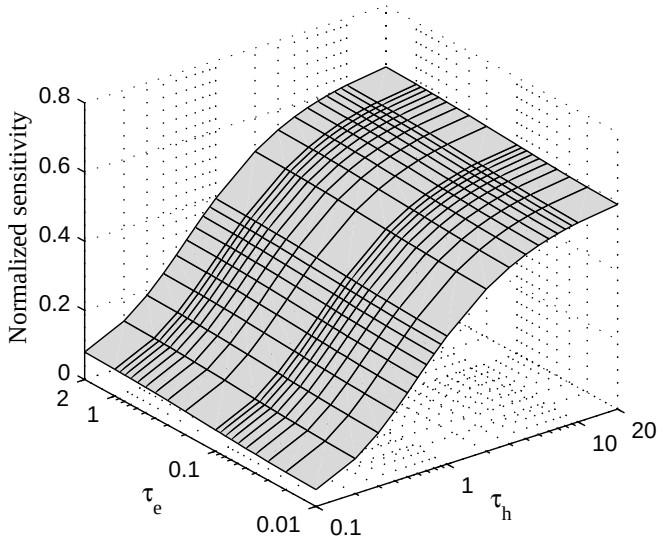

(b)

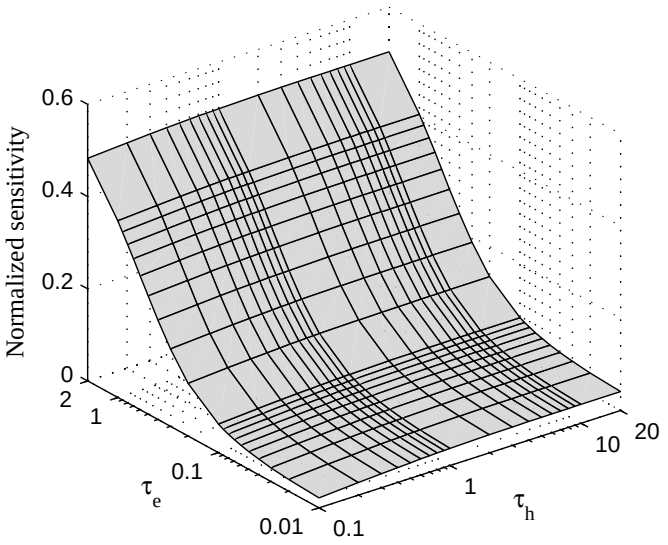
Normalized sensitivity
0.6
0.4
0.2
0
2
1
0.1
0.01
τe
0.1
1
10
20
τh

(c)

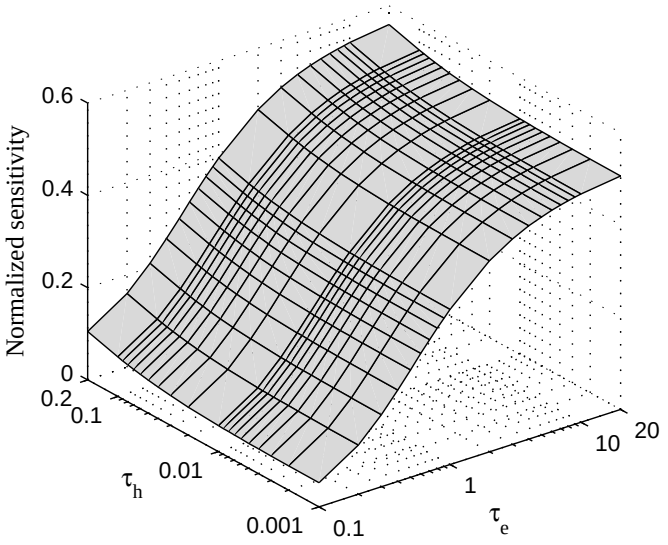
Normalized sensitivity
0.6
0.4
0.2
0
0.2
0.1
0.01
0.001
τh
0.1
1
10
20
τe

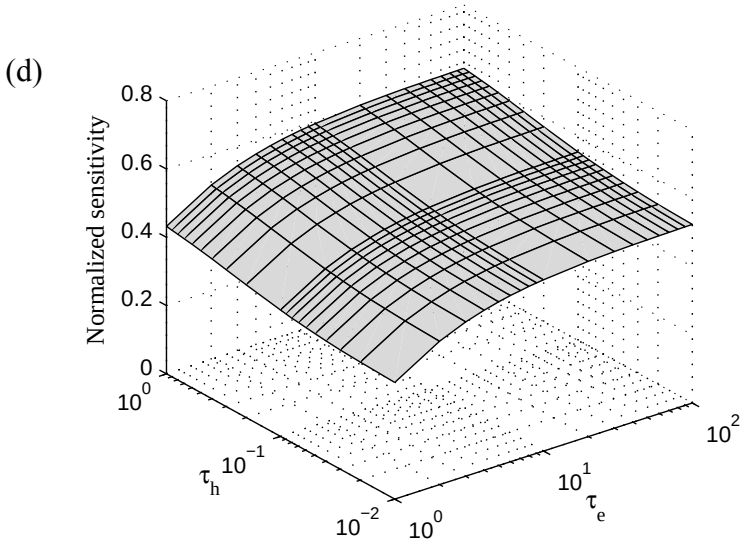

Figure 7.7 Normalized x-ray sensitivity versus τ_e and τ_h for *a*-Se, HgI_2 and CdZnTe fluoroscopic and chest radiographic detectors: (a) positively biased *a*-Se detector, (b) negatively biased *a*-Se detector, (c) negatively biased HgI_2 detector, and (d) negatively biased CdZnTe detector. Pixel pitch = 200 μm and $\Delta \approx 0.98$. Normalized pixel pitch is 0.2 for a-Se detectors, 0.77 for HgI_2 detectors and 0.74 for CdZnTe detectors.

7.3.3 Charge collections in different pixels

To study the induced signal in different pixels due to carrier trapping we first consider the x-ray interaction along the center of a pixel and calculate the collected charges in the corresponding pixel and also in the neighboring pixels using equation (7.11) or (7.16). The collected charges in the neighboring pixels are normalized with respect to the collected charge of the center pixel. The distance from the center of one pixel to the nearest neighbor pixel along any lateral axis, say *y* in Figure 7.8, is approximately equal to the pixel pitch since the gap between the pixels is negligible. The collected charges in different pixels are symmetrical about the center pixel that receives x-ray radiation along its center. We, therefore, consider the charge collection along any lateral direction, say positive *y* in Figure 7.8.

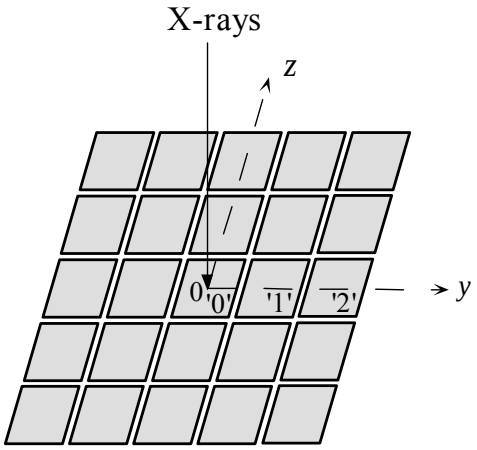

Figure 7.8 A two-dimensional array of pixel electrodes. The center of the central pixel electrode is at $x = 1$, $y = 0$ and $z = 0$, and the central pixel is marked as '0' pixel. The adjacent pixels of the central pixel along positive y direction are marked as '1', '2', etc.

Figures 7.9 (a) and (b) show the normalized collected charges in the center pixel and the neighboring pixels as a function of the normalized lateral distance from the x-ray interaction point. Stated differently, filled squares in Figures 7.9 (a) and (b) represent the collected charges at various pixels as a function of the normalized lateral distance of the center of pixels from the x-ray interaction point. Figure 7.9 (a) shows the charges in the pixels as a function of normalized lateral distance from the x-ray interaction point with $\tau_t = \infty$ for various levels of τ_b and for $a = 0.25$. For example, with negative applied bias to the radiation-receiving electrode, all the holes are collected but electrons suffer various degrees of trapping as represented by the values of τ_b. As expected, the signal spreading increases with increasing carrier trapping.

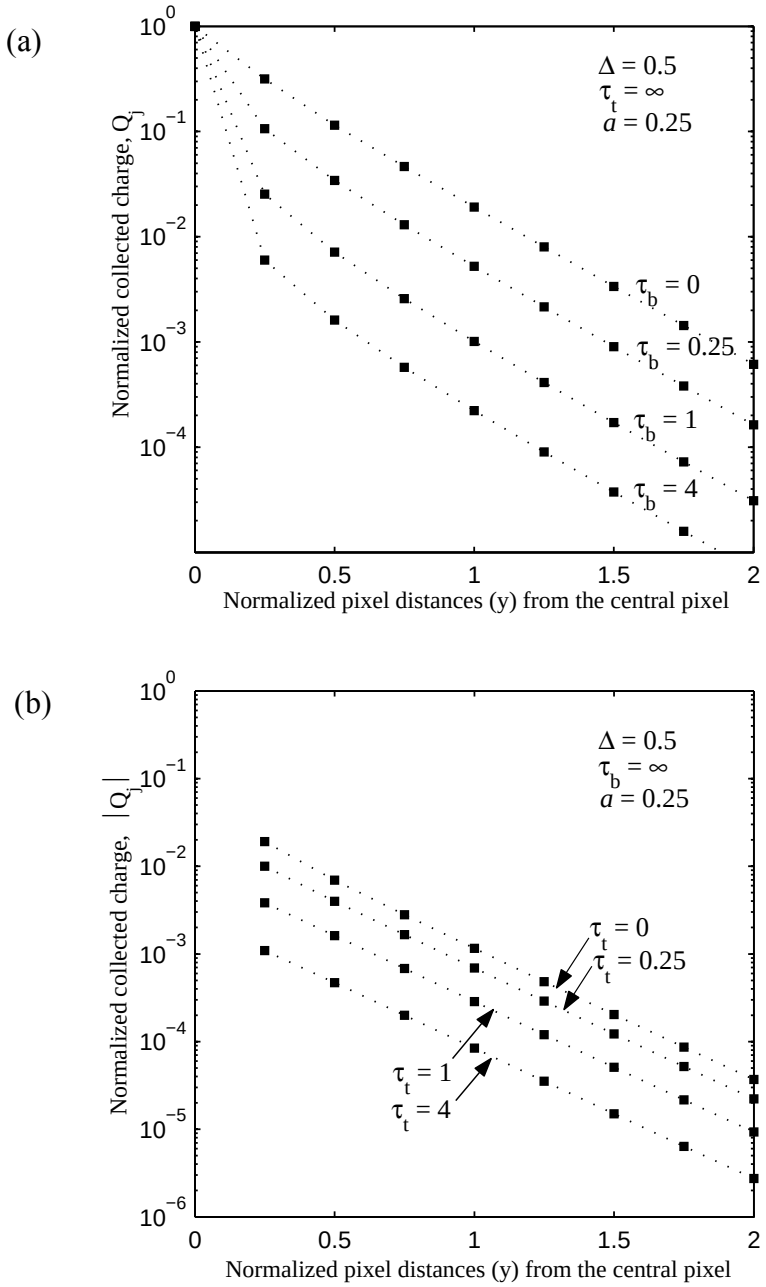

Figure 7.9 (a) Normalized collected charges in the pixels as a function of normalized lateral distance from the x-ray interaction point with $\tau_t = \infty$ for various levels of τ_b. (b) Normalized collected charges in the neighboring pixels as a function of normalized lateral distance from the x-ray interaction point with $\tau_b = \infty$ for various levels of τ_t. Note that the polarity of collected charges in the neighboring pixels in (b) is opposite of that in the central pixel.

Figure 7.9 (b) shows the charges in the neighboring pixels as a function of normalized distance from the x-ray interaction point with $\tau_b = \infty$ for various levels of τ_t and for $a = 0.25$ (in this case, all electrons are collected and holes suffer various degrees of trapping as represented by the values of τ_t). Note that the polarity of the collected charges in the neighboring pixels in Figure 7.9 (b) is the opposite of that in the central pixel. In a single element detector, the current through the top electrode must be equal to the current through the bottom electrode. In the pixellated detector, the sum of the currents through all the pixels is equal to the current through the top electrode. It is seen from Figure 7.5 (b) (the same case as in Figure 7.9 (b)) that the sensitivity of the small pixel detectors is higher than that of the infinite-size pixel detector (equivalent to a single-element detector). This result indicates that the collected charge through the center electrode is higher than through the top electrode. Therefore, the polarity of collected charges at the neighboring pixels must be the opposite (shown negative charges in Figure 7.9 (b)) of that at the central pixel.

It is evident from Figures 7.9 (a) & (b) that the effects of carrier trapping on signal spreading for the carriers drifting towards the bottom electrode is much more important than the other type of carriers. That means, the signal spreading mostly depends on the trapped charges that have the same polarity as the bias on the radiation-receiving electrode; electrons for negative bias and holes for positive bias. For example, with negative bias, the signal in the first neighbor pixel is 31.6 % of that in the central pixel for full electron trapping ($\tau_e = 0$), whereas for full hole trapping ($\tau_h = 0$), the signal in the first neighbor pixel is only 2 % (negative) of that in the central pixel.

7.4 Summary

The x-ray sensitivity of a direct conversion pixellated x-ray image detector in the presence of deep trapping of charge carriers has been studied. The analytical expressions for the weighting potentials of square pixels have been derived by

considering negligibly small gaps between the pixels and constructing an infinite series of image charges. To maintain generality, the calculations are given in normalized coordinates to enable the results to be applied to different photoconductive pixellated detectors. For $\tau_t = \infty$ and for various levels of τ_b, the polarity of collected charges in the surrounding pixels is the same as that in the radiation-receiving pixel. On the other hand, the polarity of collected charges in the surrounding pixels is the opposite of that in the radiation-receiving pixel for $\tau_b = \infty$ and for various levels of τ_t. The normalized sensitivity of pixellated x-ray detectors mainly depend on the transport properties (mobility and lifetime product) of charges that move towards the pixel electrodes and the extent of dependence increases with decreasing normalized pixel width. The x-ray sensitivity of smaller pixels may be higher or lower than that of larger pixels depending on the rate of electron and hole trapping and the bias polarity. Having smaller pixels is advantageous in terms of higher sensitivity by ensuring that the carrier with the higher mobility-lifetime product is drifted towards the pixel electrodes. The calculations have been applied to fluoroscopic and chest radiographic type pixellated detectors using a-Se, HgI_2 and CdZnTe as x-ray photoconductors.

8. RECOMBINATION AND GHOSTING IN A-SE DETECTORS

8.1 Introduction

The small signal models of x-ray sensitivity, MTF and DQE described in previous chapters provide reasonable fits to the experimental data obtained on *a*-Se, poly-HgI_2 and poly-CdZnTe photoconductive detectors. In previous analyses the recombination between x-ray photogenerated electrons and holes (i.e., bimolecular recombination) has been neglected. The bulk recombination between drifting holes and electrons is proportional to the product of the concentration of holes and electrons, and typically it is very small provided the carrier generation rate is not too high. However, this bimolecular recombination has very adverse effect on charge collection at very high carrier generation regime; because the collected charge exhibits a square root dependence on the x-ray intensity in the recombination-limited regime of detector operation. Therefore, one must include the recombination effects on charge collection for large signal case. Obviously, the effects of recombination on the charge collection efficiency depend upon the rate of carrier generation in the photoconductor layer and hence on the x-ray intensity. It is also reported in the literature that high intensity x rays can create new deep trap centers in the bulk of a-Se [104], which reduces the carrier lifetimes and hence reduces the charge collection.

Recent experiments on a-Se detectors indicate that the x-ray sensitivity of an a-Se x-ray image detector deceases in subsequent exposures [23, 24]. It should be noted that this sensitivity changes in a-Se have been found to be reversible; over the course of approximately two days resting the initial sensitivity of the a-Se layer was restored. The study of ghosting (change in the x-ray sensitivity of the x-ray image detector as a result

of previous exposure to radiation) mechanisms in amorphous selenium-based flat panel x-ray image detectors is currently considered as a topical research area since the exact origins of ghosting have not been resolved. Although the amount of ghosting is not significantly large, its study is still of interest for an accurate characterization of the detector. The bulk carrier trapping has the following effects. (i) Some of the trapped charges in the photoconductor due to previous exposure act as a charge capture center for opposite charge carriers. The trapped charge may recombine with subsequently generated oppositely charged carriers. The recombination cross-section is much higher than the trapping cross-section, reduces effective carrier lifetime [105] and thus reduces the charge collection efficiency in subsequent exposures. (ii) The trapped carrier concentrations become relatively large after a few consecutive x-ray exposures. These trapped charges modify the electric field distribution across the photoconductor, change the conversion gain and hence modify the new carrier generation in subsequent exposures. Therefore, the x-ray sensitivity in subsequent exposures is modified. It is also reported in the literature that x-ray exposure can create new meta-stable deep trap centers in the bulk of a-Se [25, 26, 27], which reduces the carrier lifetimes and hence reduces the sensitivity. The characteristic detrapping times for trapped holes and electrons in a-Se are in the order of several minutes and hours, respectively. Therefore, a considerable amount of hole detrapping is expected during an experimental study of ghosting.

In previous analyses [106], the dependence of the x-ray sensitivity of a-Se based x-ray image detectors on repeated x-ray exposures are studied by considering deep trapping of charge carriers, trapped charges due to previous exposures, trap filling effects, recombination between trapped and drifting carriers, space charge effects and electric field dependent electron-hole pair creation energy. It was illustrated that the relative x-ray sensitivity decreases with increasing cumulative x-ray exposure but the model failed somewhat to match quantitatively with experimental results. In this chapter, we have extended our model by incorporating x-ray induced new deep trap center generation, and detrapping of trapped carriers with time.

The objectives of this chapter are as follows:

(1) Study of the effects of bimolecular recombination on charge collection efficiency of an x-ray image detector as a function of the charge carrier generation rate. This analysis will show the upper limit of small signal operation (up to a level of carrier generation rate, the bimolecular recombination plays practically no role) and how the bimolecular recombination affects the charge collection efficiency. The rate of carrier generation can be related to x-ray exposure depending on the material properties of the photoconductor used in the x-ray detector. The effects of carrier generation rate (or the x-ray exposure rate) on the charge collection efficiency are examined by considering bimolecular recombination and x-ray induced new trap center generation. The numerical results are also compared with experimental data. The comparison of the model against the experimental data reveals a quantitative explanation of the mechanisms that cause signal nonlinearity as a function of exposure rate.

(2) Study of the relative sensitivity (ghosting) as a function of cumulative x-ray exposure for different levels of trapping and different detector operating conditions (applied bias and photon energy) by considering all the effects mentioned above. The theoretical model is compared with experimental results. The comparison of the model against the experimental data reveals a quantitative explanation of the mechanisms that cause ghosting.

The continuity equations for holes and electrons, trapping rate equations, and the Poisson's equation across the photoconductor for a step x-ray exposure are simultaneously solved by the finite difference method. The numerical results are compared with Monte Carlo simulations of carrier transport [107] and yield almost identical results. The ghosting and large signal models are applied to a-Se detectors.

8.2 Theoretical Model

We consider an x-ray image detector in which a photoconductor has been sandwiched between two large area parallel plate electrodes and biased with a voltage V across the terminals to establish an electric field in the photoconductor as shown in figure 8.1. The diffusion of carriers is negligible compared with their drift because of the high applied field across the photoconductor. We assign a constant drift mobility μ and a single deep trapping time (lifetime) τ' to each type of carrier (holes and electrons). Defining $p'(x', t')$ as the free hole concentration, $n'(x', t')$ as the free electron concentration, $p'_t(x', t')$ as the trapped hole concentration and $n'_t(x', t')$ as the trapped electron concentration at point x' at time t', the following physical equations thus hold.

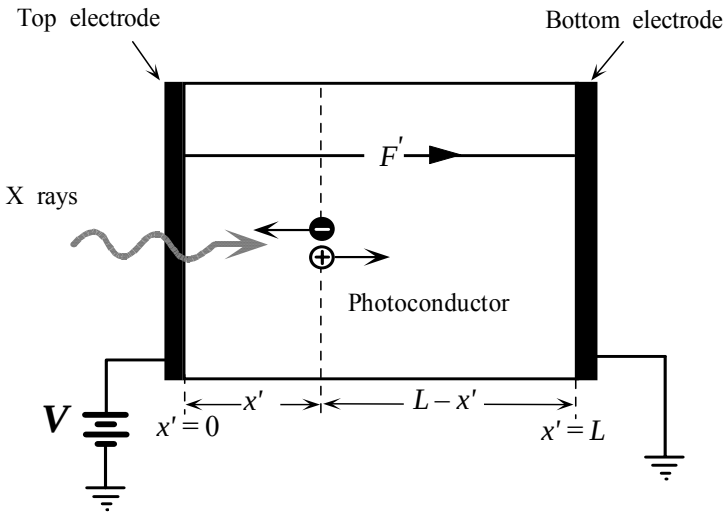

Figure 8.1 Schematic diagram representing a photoconductor sandwiched between two large area parallel plate electrodes used in the model. An electron and a hole are generated at x' and are drifting under the influence of the electric field F'.

(a) The electron and hole continuity equations for positive bias applied to the radiation-receiving electrode are,

$$\frac{\partial n'}{\partial t'} = \mu_e \frac{\partial (n'F')}{\partial x'} - \frac{n'}{\tau'_e} - C_r n'p' - C_e n'p'_t + g(x',t')\mathrm{e}^{-\alpha x'} \tag{8.1}$$

$$\frac{\partial p'}{\partial t'} = -\mu_h \frac{\partial (p'F')}{\partial x'} - \frac{p'}{\tau_h'} - C_r p'n' - C_h p'n_t' + g(x',t')\mathrm{e}^{-\alpha x'} \tag{8.2}$$

where $F'(x', t')$ is the electric field in the photoconductor, $g(x', t')$ is the electron hole pair generation rate, α is the linear attenuation coefficient of the photoconductor, C_r is the bimolecular recombination coefficient between free electrons and holes, C_e is the capture coefficient between free electrons and trapped holes, and C_h is the capture coefficient between free holes and trapped electrons. The subscripts *e* and *h* represent electrons and holes respectively. For an a-Se photoconductor, a recombination-type capture process follows the *Langevin recombination* mechanism [108, 109] and thus $C_r = e(\mu_h+\mu_e)/\varepsilon$, $C_h = e\mu_h/\varepsilon$ and $C_e = e\mu_e/\varepsilon$, where *e* is the elementary charge and ε (= $\varepsilon_0\varepsilon_r$) is the permittivity of the photoconductor.

(b) The detailed balance or the rate equations for deep trapping are

$$\frac{\partial n_t'}{\partial t'} = \frac{n'}{\tau_e'} - C_h p'n_t' \tag{8.3}$$

$$\frac{\partial p_t'}{\partial t'} = \frac{p'}{\tau_h'} - C_e n'p_t' \tag{8.4}$$

(c) The Poisson equation

$$\frac{\partial F'}{\partial x'} = \frac{e}{\varepsilon}\left(p' + p_t' - n' - n_t'\right) \tag{8.5}$$

Considering the trap filling effect and x-ray induced meta-stable deep trap center generation, the trapping times for electrons and holes are, respectively [110, 111],

$$\tau_e' = \frac{\tau_{0e}'}{1 + \left(N_{Xe} - n_t\right)/N_{0e}} \tag{8.6}$$

and $$\tau_h' = \frac{\tau_{0h}'}{1 + \left(N_{Xh} - p_t\right)/N_{0h}}. \tag{8.7}$$

where N_X is the concentration of x-ray induced deep trap centers, N_0 is the concentration of initial deep trap centers, and τ'_0 is the initial carrier trapping time. The concentration of x-ray induced deep trap centers depend on the photoconductor material, the irradiation energy and the amount of exposure. The x-ray induced deep trap center generation kinetics is taken to be a first rate equation so that [112]

$$N_{Xe}(x', X) = N_{se}\left(1 - e^{-X/D}\right)e^{-\alpha x'} \tag{8.8}$$

$$N_{Xh}(x', X) = N_{sh}\left(1 - e^{-X/D}\right)e^{-\alpha x'} \tag{8.9}$$

Where N_s is the saturation value of the x-ray induced deep trap centers, D is an irradiation energy dependent constant, and X is the amount of cumulative exposure. The value of D is large compared to typical exposures in medical x-ray imaging and thus the new deep trap center generation is almost proportional to the cumulative x-ray exposure.

It can be assumed that only a certain fraction f of trapped charges act as recombination centers for oppositely charged drifting carriers [112]. For all practical purposes, this assumption is equivalent to assuming that there are two types of deep traps: (I) neutral when empty and charged when a carrier is trapped, (II) charged when empty and neutral when a carrier is trapped. Obviously the latter would participate in the recombination process. Stated differently, effective recombination coefficients fC_h and fC_e can be assigned. It is well known that the a-Se structure has valance alternation pair (Se_3^+ and Se_1^-) type defects and must also have seemingly "neutral" trap centers. These trap centers can also interconvert [113].

For simplicity, we use the normalized distance coordinate x, where $x = x'/L$, and the normalized absorption depth, $\Delta = 1/\alpha L$. The time coordinate is normalized with respect to the transit time of electrons t_e ($t_e = L/\mu_e F_0$, where $F_0 = V/L$, t_e is the longest transit time). Therefore, the normalized time coordinate $t = t'/t_e$, and normalized carrier lifetimes, $\tau_e = \mu_e \tau'_e F_0/L$ and $\tau_h = \mu_h \tau'_h F_0/L$. The normalized electric field, $F = F'/F_0$. Charge carrier concentrations are normalized with respect to the total photogenerated

charge per unit area, Q_0 (electrons / m^2) in the photoconductor as if the total charge is uniformly distributed over the sample volume.

Let g_0 be the EHP generation rate under a uniform electric field of F_0. Then, the total collectable EHP generated in the photoconductor layer per m^2 is given by [106]

$$Q_0 = p_0 L = \int_0^T \int_0^L g_0 e^{-\alpha x'} dx' dt' = \frac{g_0 T \eta}{\alpha} = \frac{5.45 \times 10^{17} X \eta}{(\alpha_{\text{air}} / \rho_{\text{air}}) W_0} \left(\frac{E_{\text{ab}}}{E} \right) \tag{8.10}$$

where T is the exposure time, η is the quantum efficiency of the detector, E_{ab} is the average absorbed energy per x-ray photon of energy E, X is the exposure (X is in roentgens), W_0 is the EHP creation energy (W_0 is in eV) of the photoconductor at an electric field of F_0 and for an incident photon energy of E, α_{air} and ρ_{air} are the energy absorption coefficient and the density of air respectively ($\alpha_{\text{air}}/\rho_{\text{air}}$ is in cm^2 g^{-1}). Equations (8.1) – (8.5) can now be recast into the dimensionless forms [110, 111]:

$$\frac{\partial n}{\partial t} = \frac{\partial (nF)}{\partial x} - \frac{n}{\tau_e} - c_R np - f c_0 n p_t + K e^{-\frac{x}{\Delta}} \tag{8.11}$$

$$\frac{\partial p}{\partial t} = -r_\mu \frac{\partial (pF)}{\partial x} - r_\mu \frac{p}{\tau_h} - c_R pn - f c_0 r_\mu p n_t + K e^{-\frac{x}{\Delta}} \tag{8.12}$$

$$\frac{\partial n_t}{\partial t} = \frac{n}{\tau_e} - f c_0 r_\mu p n_t \tag{8.13}$$

$$\frac{\partial p_t}{\partial t} = r_\mu \frac{p}{\tau_h} - f c_0 n p_t \tag{8.14}$$

$$\frac{\partial F}{\partial x} = c_0 \left[p + p_t - n - n_t \right] \tag{8.15}$$

where $r_\mu = \mu_h/\mu_e$, $c_0 = eQ_0/\varepsilon F_0$, $c_R = c_0(1 + r_\mu)$, $n = n'/p_0$, $p = p'/p_0$, $n_t = n'_t/p_0$, $p_t = p'_t/p_0$, and $K(x,t) = \{t_e W_0\}/\{T\eta\Delta\ W(x,t)\}$. The ratio $W_0/W(x,t) = g(x,t)/g_0$. $W(x,t)$ is the electron hole pair creation energy at the instantaneous electric field $F(x,t)$.

The equations (8.11)–(8.15) are a nonlinearly coupled partial differential equations. Theses nondimensionalized coupled equations are simultaneously solved by the finite difference method (the solution technique is given in Appendix D). To solve the above equations, the initial and boundary conditions must be defined. The necessary initial conditions before any exposure are

$$p(x,0)=0,\quad n(x,0)=0,\quad p_t(x,0)=0,\quad n_t(x,0)=0,\quad \text{and } F(x,0)=1 \tag{8.16}$$

The boundary condition for electric field is given by

$$\int_0^1 F(x,t)dx = 1 \tag{8.17}$$

After EHP generation due to an x-ray exposure, one type of carrier drifts towards the radiation-receiving electrode (top electrode) and the other type of carrier drifts towards the other electrode (bottom electrode). For positive bias, electrons move towards the radiation-receiving electrode and holes move towards the bottom electrode. Therefore, just after (or shortly after) x-ray exposure, the free hole concentration at x = 0 and the free electron concentration at x = 1 are zero since the carriers would have started drift.

The total normalized current density is given by [28, 114],

$$j(t)=\int_0^1 F(x,t)\left[n(x,t)+r_\mu\, p(x,t)\right]dx \tag{8.18}$$

The integration of current over time period of interest is the normalized collected charge or charge collection efficiency. The product of the normalized collected charge and the quantum efficiency represents the normalized x-ray sensitivity.

In ghosting measurement experiments, a series of x-ray exposures is applied to the detector and the average x-ray sensitivity of each x-ray exposure is measured. There is a

time gap of few minutes (typically 1 to 5 minutes) between two successive x-ray exposures. Therefore, a considerable amount of hole detrapping is expected during an experimental study of ghosting. The hole detrapping probability within time t_{off} for a carrier with detrapping time τ_{dh} is $[1-\exp(-t_{off}/\tau_{dh})]$. The density of trapped carriers before each test measurement is the density of trapped carriers after previous exposure with adjustment due to detrapping.

8.3 Results and Discussions

8.3.1 Effects of large signals on charge collection

A very short x-ray beam is considered to examine the effects of large signal on charge collection. The trapped charge carrier concentrations are negligibly small compared to the concentrations of moving carriers and thus trap saturation effect can also be neglected [94]. The charge carrier generation in a-Se photoconductors depends on the electric field. However, the charge carrier generation occurs within very short time and thus it occurs before changing the electric field distribution across the photoconductor layer due to the separation of electrons and holes. Therefore, charge carrier trapping and the recombination between drifting carriers play dominant roles on charge collection efficiency at high intensity short pulse x-ray excitation.

Figure 8.2 shows the effect of recombination between drifting carriers on charge collection efficiency in a-Se detectors as a function of the rate of total photogenerated charge carriers, q_0 (EHPs/m^2/s). Charge carrier trapping is neglected in Figure 8.2. The exposure time, T = 5 μs, E = 60 keV (e.g., chest radiographic applications), L = 1 mm, F_0 = 10 V/um and thus Δ = 0.98. The mobilities of carriers are taken as $\mu_h \approx 0.12$ cm^2/Vs and $\mu_e \approx 0.003$ cm^2/Vs, and thus transit time of electrons, t_e = 0.33 ms. The dotted and dashed curves represent positively and negatively biased a-Se detectors, respectively. The solid line represents numerical results considering uniform electric field at positive bias and the points represent numerical results considering uniform

electric field at negative bias. In all cases, the recombination plays practically no role up to the total carrier generation rate of 10^{18} EHPs/m^2-s. At large values of q_0, the charge collection efficiency gradually decreases with increasing q_0 and approaches almost zero at q_0 larger than 10^{24} EHPs/m^2-s. Thus the recombination has a very adverse effect on charge collection in the high carrier generation regime. The effect of recombination between drifting carriers on charge collection efficiency does not depend on the bias polarity considering uniform electric field since the two representing curves overlapped each other as shown in figure 8.2. In case of considering uniform electric field, the carrier transport is independent of the electric field and the total losses of carriers due to the recombination are the same in both bias conditions. Therefore, the charge collection efficiency considering only bimolecular recombination is independent of bias polarity under uniform electric field.

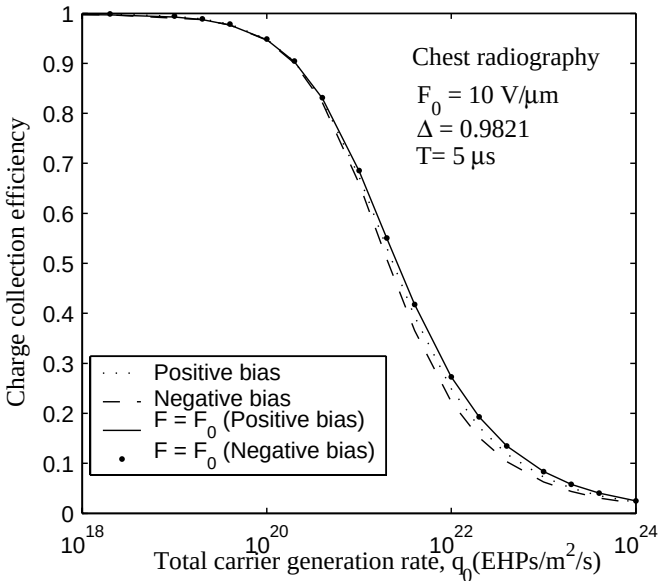

Figure 8.2 Charge collection efficiency versus total carrier generation rate, q_0 (EHPs/m^2/s). The dotted and dashed curves represent positively and negatively biased a-Se detectors, respectively. The solid line represents numerical results considering uniform electric field at positive bias and the points represent numerical results considering uniform electric field at negative bias.

The charge collection efficiency at positive bias is slightly lower than at the uniform electric field case, and is slightly higher than at negative bias in the large signal regime of operation. The electric field distributions across the photoconductor for positive and negative bias conditions are shown in figure 8.3(a) and 8.3(b), respectively. The total carrier generation rate q_0 of 10^{22} EHPs/m^2-s is considered in figure 8.3, when the charge collection efficiency is less than 0.3. All parameters in figure 8.3 are the same as in figure 8.2. It is evident from figure 8.3 that the instantaneous electric field distributions change widely during the travel of the carriers towards the electrodes. However, the change in charge collection efficiency based on the change in electric field distributions is not so significant provided the magnitude of applied electric field (F_0) is unchanged. The effect of recombination on charge collection strongly depends on the applied electric field strength, which will be discussed below.

(a)

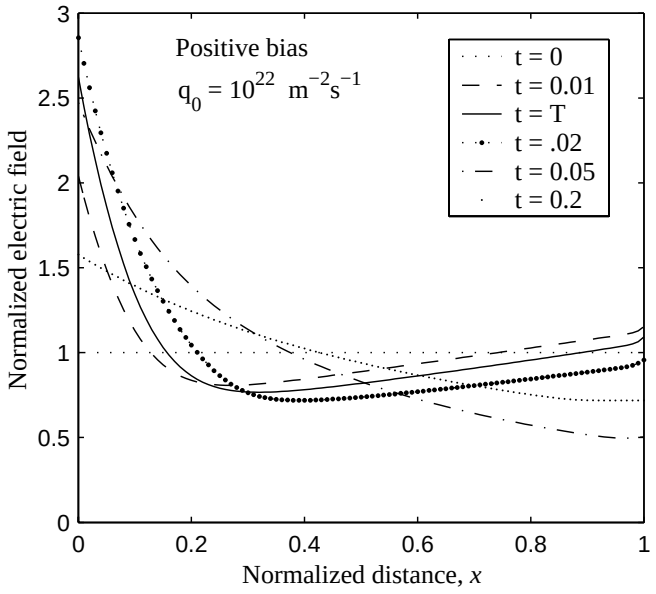

(b)

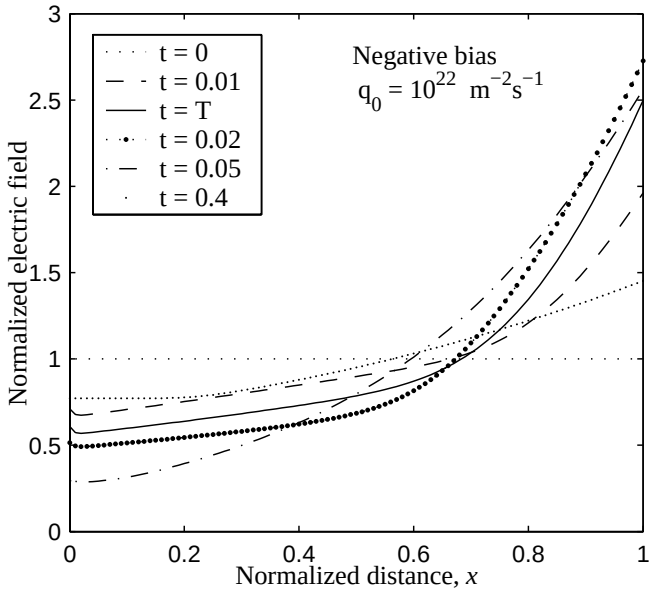

Figure 8.3 Normalized electric fields versus normalized distance from the radiation-receiving electrode for a total photogenerated charge carriers, $q_0 = 10^{22}$ EHPs/m^2-s for chest radiographic applications. (a) Positively biased a-Se detectors (b) Negatively biased a-Se detectors.

Figure 8.4 shows the effect of recombination between drifting carriers on charge collection efficiency in a-Se detectors as a function of the rate of total photogenerated charge carriers for mammographic and chest radiographic applications. For mammographic applications, E = 20 keV, L = 0.2 mm, F_0 = 10 V/μm and Δ = 0.24. The solid lines represent numerical results and the closed circles represent Monte Carlo simulation results [115]. Both methods give almost identical results. The effect of recombination on charge collection is more pronounced in the chest radiographic detectors because of longer carrier transit time. Recombination takes place for a longer time because holes stay for a longer time (since the photoconductor thickness is higher) in the photoconductor layer in chest radiographic detectors. Holes move almost 40 times faster than electrons in a-Se and the bimolecular recombination occurs as long as holes exist in the photoconductor layer.

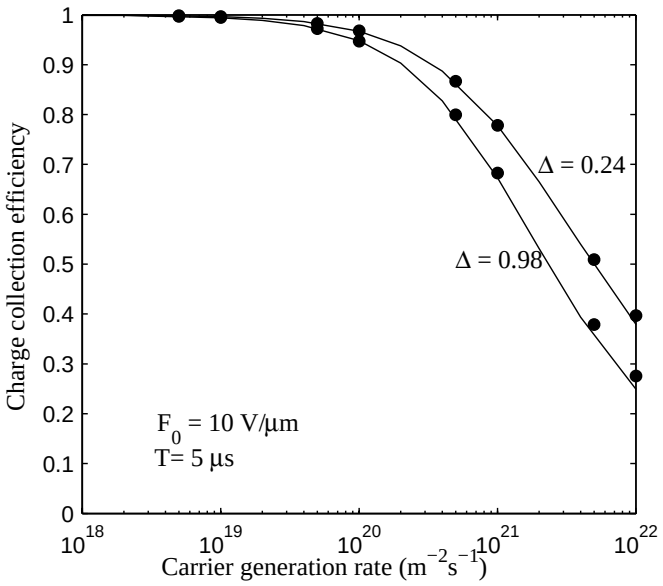

Figure 8.4 Charge collection efficiency versus total carrier generation rate, q_0 (EHPs/m^2/s) mammographic and chest radiographic applications. $\Delta \approx 0.24$ and 0.98 for mammographic and chest radiographic detectors, respectively. The solid lines represent numerical results and the closed circles represent Monte Carlo simulation results [115].

The extent of the effect of recombination on charge collection obviously depends on the applied electric field. Figure 8.5 shows the effect of recombination on charge collection efficiency in positively biased chest radiographic a-Se detectors as a function of the rate of total photogenerated charge carriers q_0 for various levels of applied electric field. The effect of recombination is higher at lower applied electric fields. Charge carriers stay longer in the photoconductor layer at a lower field and thus the loss of carriers due to recombination is also higher.

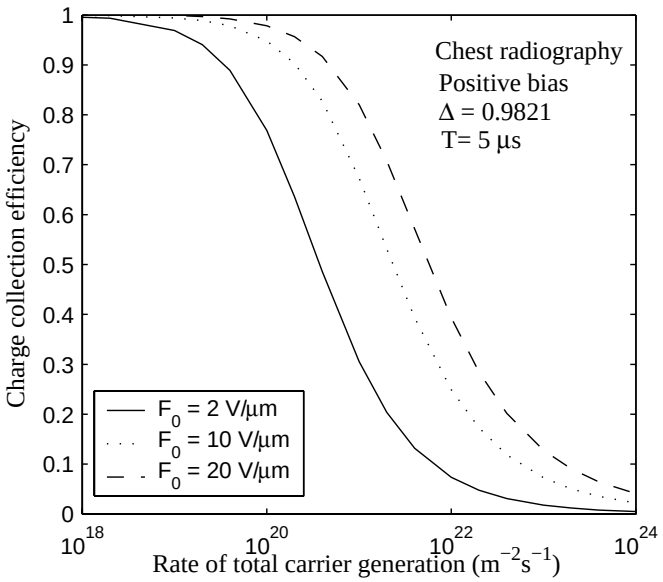

Figure 8.5 Charge collection efficiency versus rate of total photogenerated charge carriers, q_0 (EHPs/m^2/s) for various levels of applied electric field.

The effects of recombination in a-Se x-ray image detectors for mammographic and chest radiographic applications has been examined. Figures 8.6 (a) and 8.6 (b) show the effects of recombination on charge collection efficiency as a function of exposure rates for chest radiographic and mammographic applications, respectively. For chest radiographic a-Se detectors, the recombination has practically no role on charge collection up to the exposure rate of 100 mR/ms. The average exposure for chest radiographic applications is 0.3 mR. If the minimum exposure time is 1 ms, the maximum exposure rate is 0.3 mR/ms. Therefore, the recombination has no effect for chest radiographic applications. Although, the applied electric field has a significant effect on charge collection efficiency versus total carrier generation rate characteristics (figure 8.5), it has little effect on charge collection efficiency versus exposure rate characteristics in a-Se detectors. The effect of recombination on charge collection efficiency for the same amount of charge carriers depends strongly on the applied electric field. However, a less number of collectable charge carriers are generated in a-Se detectors at low electric fields because of higher $W_{\pm}$ at low fields, and thus one can expect less recombination. For mammographic a-Se detectors, the recombination has practically no role on charge collection up to the exposure rate of 1000 mR/ms. The

average exposure for mammograhic applications is 12 mR. If the minimum exposure time is 1 ms, the maximum exposure rate is 12 mR/ms. Therefore, the recombination has practically no effect for mammographic applications too. However, some other factors (e.g., x-ray induced new trap centers) may have significant effect on charge collection in the regime of high exposure, which will be examined below.

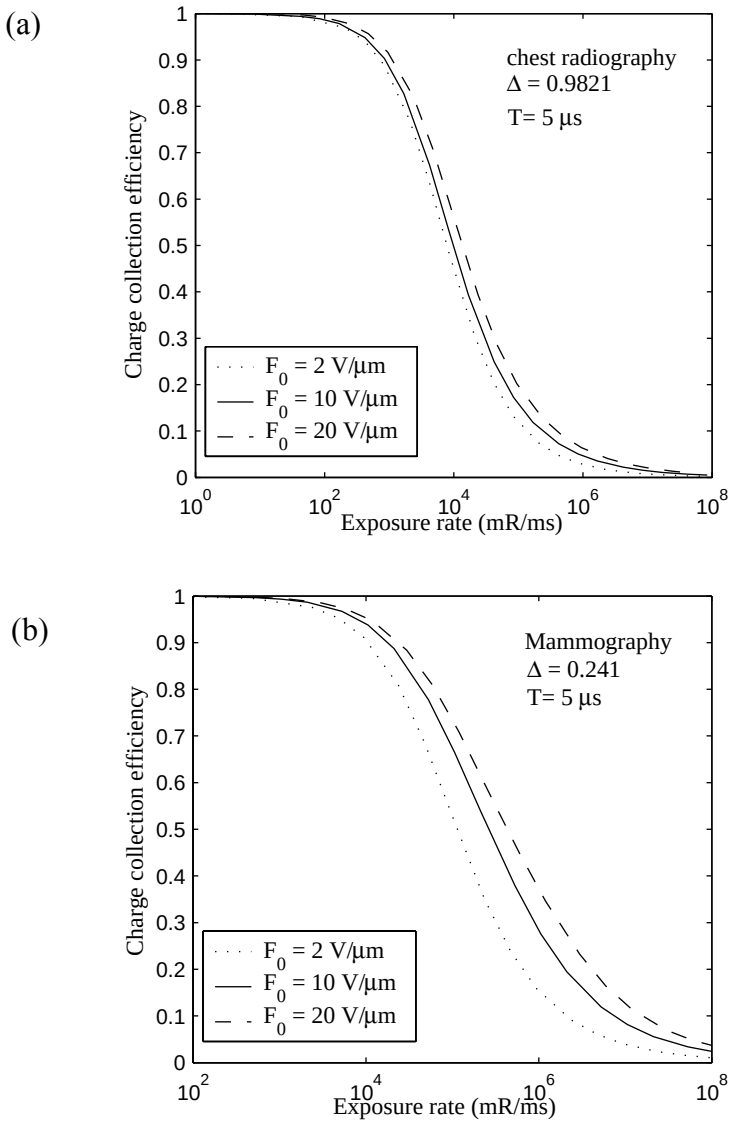

Figure 8.6 Charge collection efficiency versus exposure rate for various levels of applied electric field. (a) a-Se detectors for chest radiographic applications, and (b) a-Se detectors for mammographic detectors.

The model is fitted to experimental data on collected charge versus charge generation rate characteristics of a-Se detectors for tomotherapy applications. Figure 8.7 shows the collected charge as a function of exposure (mGy) per x-ray pulse. Note that 1 mGy ≈ 0.114 R. The average photon energy, E = 2 MeV, F_0 = 5 V/μm, L = 1 mm, T = 3.66 μs and the active radiation receiving area of the detector, A = 37 μm × 37 μm. The mobilities and lifetimes of carriers are taken as $\mu_h \approx 0.13$ cm^2/Vs, $\mu_e \approx 0.003$ cm^2/Vs, $\tau'_{0h} \approx 10.8$ μs and $\tau'_{0e} \approx 310$ μs. The normalized absorption depth $\Delta \approx 58$ and therefore, the x-ray absorption is almost uniform across the photoconductor thickness. In Figure 8.7, the open circle represents the experimental data, the dotted line is the linear curve through small signals, the dashed line represents collected charge considering the recombination between drifting carriers only, the dash-dotted line represents collected charge considering the recombination between oppositely charged both drifting and the trapped carriers, and the solid line represents the collected charge considering the recombination between oppositely charged both drifting and the trapped carriers and x-ray induced new trap center generation. The experimental data is received from Ref. 116. The recombination between the drifting and oppositely charged trapped carriers has a little effect on charge collection as evident from the difference between the dashed line and the dash-dotted line in Figure 8.7. The numerical result considering recombination between both drifting and trapped carriers and x-ray induced new deep trap center generation has a very good agreement with experimental data. The x-ray induced new trap centers is considered as proportional to the x-ray intensity and hence to the charge generation rate. As evident from figure 8.7, the recombination between drifting carriers and the x-ray induced new trap center generation are mainly responsible for the nonlinearity in charge collection versus charge generation rate characteristics in a-Se detectors. However, we need experimental results at diagnostic x-ray photon energies to get the rate of new trap center generation in a-Se detectors for diagnostic medical x-ray imaging applications.

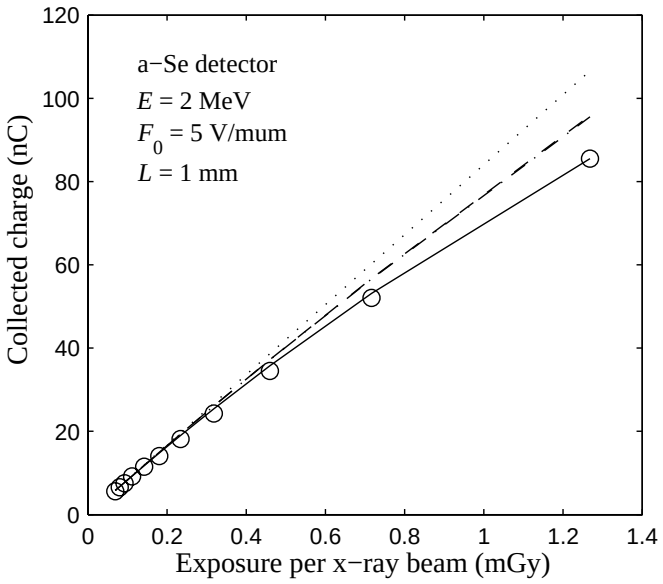

Figure 8.7 Collected charge versus charge generation rate in a-Se detectors. The open circle represents the experimental data, the dotted line is the linear curve through small signals, the dashed line represents collected charge considering the recombination between drifting carriers only, the dash-dotted line represents collected charge considering the recombination between oppositely charged both drifting and trapped carriers, and the solid line represents the collected charge considering the recombination between both drifting and trapped carriers and x-ray induced new trap center generation. The experimental data is received from Ref. 116.

8.3.2 Ghosting in a-Se detectors

The instantaneous electric field, free and trapped carrier distributions are obtained by numerically solving the equations (8.11) – (8.15) with the initial and the boundary conditions. The numerical technique used is the finite-difference method. The relative x-ray sensitivity is calculated as a function of cumulative x-ray exposure or dose. The relative x-ray sensitivity is obtained by normalizing the sensitivity by the expected sensitivity before any x-ray exposure [67, 68]. The amount of EHP generation from a fixed exposure is calculated using equation (8.10).

The ghosting model is fitted to the experimental data to obtain a quantitative explanation of the mechanisms that cause ghosting. Figure 8.8 (a) shows the relative x-ray sensitivity as a function of cumulative exposure for a positively biased a-Se

detector. The average photon energy E_{av} is 55 keV for an 80 kVp applied x-ray spectrum with 23.5 mm Al filtration. The applied electric field, F_0 = 3 V/μm, L = 498 μm, and thus Δ = 1.56. The hole detrapping time τ_{dh} = 5 minutes and $N_0 = 5 \times 10^{18}$ m^{-3} for both holes and electrons are assumed in the calculations. The interval between two exposures is 2 minutes and the exposure time is 250 ms. The mobility-lifetimes of carriers are $\mu_h \tau'_{0h} \approx 3.5 \times 10^{-6}$ cm^2/V, $\mu_e \tau'_{0e} \approx 2.2 \times 10^{-6}$ cm^2/V (experimentally measured values [110]). For simplicity, we consider the ratio $E_{ab}/E \approx \alpha_{en}/\alpha \approx 0.81$. The closed circles in figure 8.8 (a) represents experimental data [110]. The dashed line represents numerical results considering only recombination (f = 1.0), the dash-dotted line represents numerical results considering recombination (f = 1.0) and field dependent charge carrier generation, the dotted line represents numerical results considering effective recombination (f = 0.3) and field dependent charge carrier generation, and the solid line represents numerical results considering effective recombination (f = 0.3) and field dependent charge carrier generation and x-ray induced new trap center generation. Considering only recombination with f = 1.0, the relative sensitivity decreases very sharply and quickly reaches a saturation value due to a balance between two processes: the rate at which new carriers are trapped and the rate at which trapped carriers are removed by recombination with oppositely charged free carriers. The relative sensitivity improves a bit incorporating field dependent carrier generation mechanism with recombination (f = 1.0) but the shape of sensitivity reduction curve remains almost the same. The experimental data shows a continuous reduction of sensitivity with exposure (at least up to the exposure of 0.6 R). To fit the initial trends of experimental data an *effective* recombination coefficient has been used. The numerical result (dotted line) by changing f from 1.0 to 0.3 still shows a saturation value and fails to match the experimental data. The numerical results considering effective recombination (f = 0.3) and field dependent charge carrier generation and x-ray induced new trap center generation (solid line) agree well with experimental data. The fitted values of N_{se}, N_{sh} and D are 2×10^{19} m^{-3}, 3.2×10^{19} m^{-3} and 2 R, respectively. The unequal x-ray induced new trap centers for electrons and holes have been reported by Schiebel *et al* [26].

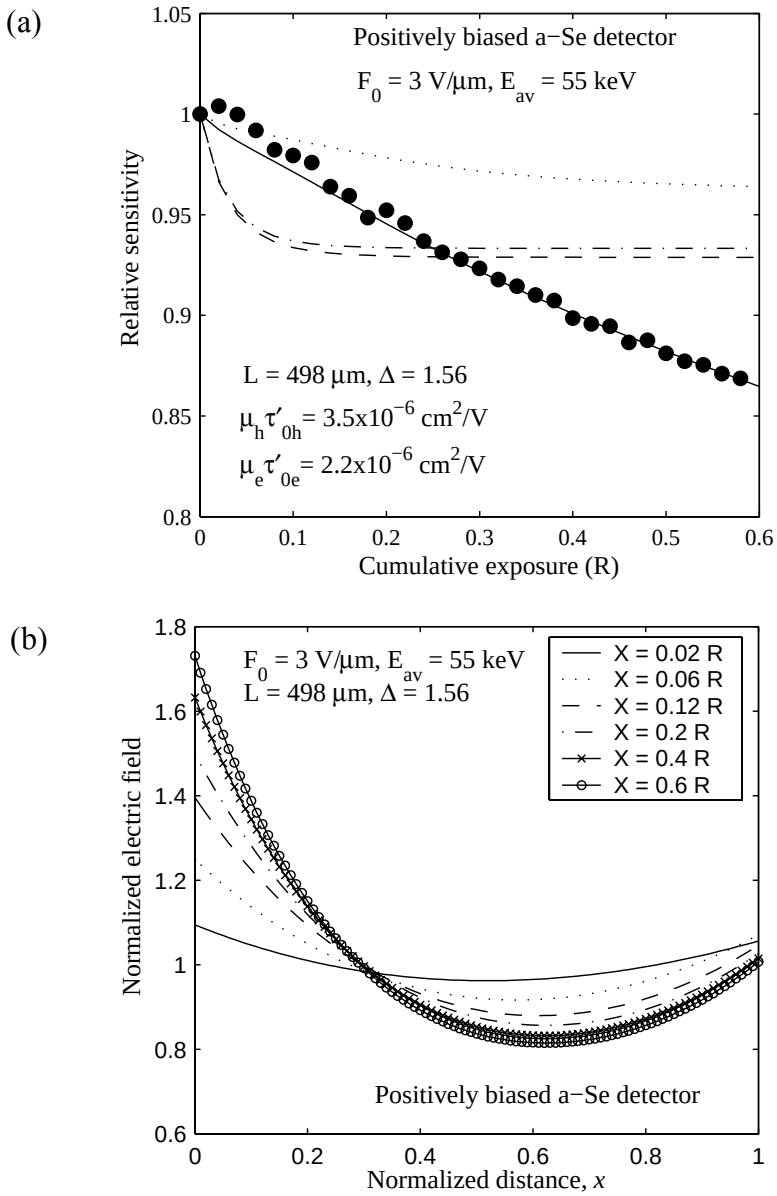

Figure 8.8 (a) Relative x-ray sensitivity versus cumulative exposure for a positively biased a-Se detector. The dashed line represents numerical results considering only recombination (f = 1.0), the dash-dotted line represents numerical results considering recombination (f = 1.0) and field dependent charge carrier generation, the dotted line represents numerical results considering recombination (f = 0.3) and field dependent charge carrier generation, and the solid line represents numerical results considering recombination (f = 0.3) and field dependent charge carrier generation and x-ray induced new trap center generation. (b) The electric distributions across the photoconductor for the conditions of solid line in (a).

The experimental data show a little increase in sensitivity during second exposure and thus there is a little discrepancy between the theoretical results and the experimental data in the initial part of the sensitivity versus cumulative exposure curves. The probable reason is the increase of dark current due to x-ray exposure at positive bias and mixing of dark current with x-ray photocurrent, which increases the collected charge (or sensitivity). An order of magnitude increase of dark current due to x-ray exposure at positive bias has been reported by Fogal et al. [117]. The maximum discrepancy between the experimental data and the theoretical results is 1.3 %, which corresponds to an increase of dark current of 0.45 nA/cm^2. This increase of dark current is comparable with the usual dark current in a-Se detectors [64].

Figure 8.8 (b) shows the electric field distributions across the photoconductor for different cumulative x-ray exposures. The electric field distributions in figure 8.8 represent the conditions of solid line in figure 8.8 (a). The electric field at the radiation-receiving electrode increases with increasing cumulative exposure. The electric field distributions reach a steady value after a large cumulative exposure. Since the x-ray absorption profile is exponential across the photoconductor, it is expected that the total EHP generation is somewhat greater under positive bias because most of the x-ray photons are absorbed in the high field region. Consequently, the sensitivity increases a bit with exposure, which is the cause of the little difference between dashed and dash-dotted lines in figure 8.8 (a).

Figure 8.9 (a) shows the relative x-ray sensitivity as a function of cumulative exposure for a negatively biased a-Se detector. The average photon energy E_{av} is 55 keV for an 80 kVp applied x-ray spectrum with 23.5 Al filtration. The applied electric field, F_0 = 6 V/μm, L = 1 mm, and thus Δ = 0.78. The hole detrapping time τ_{dh} = 8 minutes and N_0 = 3 × 10^{18} m^{-3} for both holes and electrons are assumed in the calculations. The interval between two exposures is 2 minutes. The mobility-lifetimes of carriers are $\mu_h\tau'_{0h} \approx 5.7 \times 10^{-6}$ cm^2/V, $\mu_e\tau'_{0e} \approx 5.2 \times 10^{-6}$ cm^2/V (experimentally measured values [111]). For simplicity, we consider the ratio $E_{ab}/E \approx \alpha_{en}/\alpha \approx 0.81$. The closed circles in figure 8.8 (a) represents experimental data [111]. The dashed line

represents numerical results considering only recombination (f = 1.0), the dash-dotted line represents numerical results considering recombination (f = 1.0) and field dependent charge carrier generation, the dotted line represents numerical results considering effective recombination (f = 0.35) and field dependent charge carrier generation, and the solid line represents numerical results considering effective recombination (f = 0.35) and field dependent charge carrier generation and x-ray induced new trap center generation. Similar to the negative bias case, the relative sensitivity decreases very sharply considering only recombination with f = 1.0 and quickly reaches a saturation value. The relative sensitivity deteriorates further incorporating field dependent carrier generation mechanism with recombination (f = 1.0) but the shape of sensitivity reduction curve remains almost the same. The numerical result (dotted line) by changing f from 1.0 to 0.35 still shows a tendency towards a saturation value and fails to match the experimental data. The numerical results considering effective recombination (f = 0.35) and field dependent charge carrier generation and x-ray induced new trap center generation (solid line) agree well with experimental data. The fitted values of N_{se}, N_{sh} and D are 2.7 $\times 10^{19}$ m^{-3}, 3.6 $\times$ 10^{19} m^{-3} and 1.5 R, respectively.

Figure 8.9 (b) shows the electric field distributions across the photoconductor for different cumulative x-ray exposures, which correspond to the solid line in figure 8.9 (a). The electric field at the bottom electrode increases with increasing cumulative exposure. Since the x-ray absorption profile is exponential across the photoconductor, it is expected that the total EHP generation is less under negative bias because most of the x-ray photons are absorbed in the low field region. Consequently, the sensitivity decreases with exposure, which is the cause of the difference between dashed and dash-dotted lines in figure 8.8 (a).

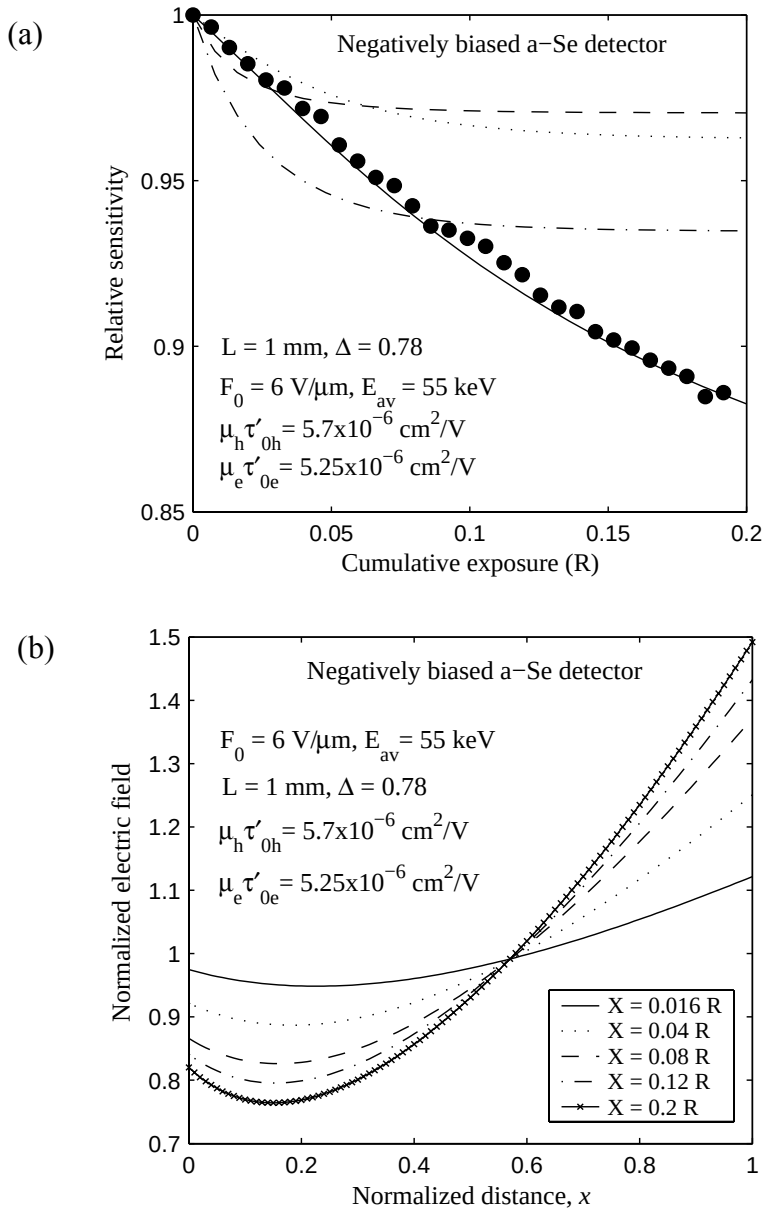

Figure 8.9 (a) Relative x-ray sensitivity versus cumulative exposure for a negatively biased a-Se detector. The dashed line represents numerical results considering only recombination (f = 1.0), the dash-dotted line represents numerical results considering recombination (f = 1.0) and field dependent charge carrier generation, the dotted line represents numerical results considering recombination (f = 0.35) and field dependent charge carrier generation, and the solid line represents numerical results considering recombination (f = 0.35) and field dependent charge carrier generation and x-ray induced new trap center generation. (b) The electric distributions across the photoconductor for the conditions of solid line in (a).

The factor f decreases slightly with increasing N_0 or trapped charge concentrations. For example, if N_0 is changed from 3×10^{18} m^{-3} to 10^{19} m^{-3} in figure 8.9 (a), the fitted value of f is then 0.15. It is likely that charge carriers injected into the sample by the dark current will neutralize some of the trapped charges and the actual amount of trapped charges in biased a-Se samples be reduced with time. An order of magnitude increase of dark current due to x-ray exposure at positive bias has been reported by Fogal et al [117]. However, the exact physics of dark current behavior during exposures and field variations in a-Se detectors is still unknown.

The effect of x-ray induced new trap centers on ghosting is larger at positive bias than at negative bias. Because, the x-ray induced hole traps are higher than that of electron traps, and the sensitivity mainly depends on the transport properties of the charges that have the same polarity as the bias; holes for positive bias and electrons for negative bias. The field dependent carrier generation mechanism has less effect on ghosting at positive bias but has a very adverse effect on ghosting at negative bias. In fact, ghosting at negative bias largely depends on the field dependent carrier generation mechanism in subsequent exposure, whereas ghosting at positive bias largely depends on carrier recombination and the x-ray induced new deep trap center generation. In both bias conditions, the amount of ghosting strongly depends on the applied electric field and carrier lifetimes, which will be discussed below.

Figure 8.10 (a) shows the relative sensitivity of a positively biased a-Se detector as a function of cumulative x-ray exposure for different applied electric fields. All parameters in figure 8.10 (a) are the same as in solid curve in figure 8.8 (a). Figure 8.10 (b) shows the relative sensitivity of a negatively biased a-Se detector as a function of cumulative x-ray exposure for different applied electric fields. All parameters in figure 8.10 (b) are the same as in solid curve in figure 8.9 (a). The circles represent experimental data [110, 111]. The triangles represent Monte Carlo simulation results [110, 111] and the solid lines represent numerical results. The fitted value of the factor f varies from 0.3 to 0.4 for the field variation from 3 V/μm to 10 V/μm, the physics of this small variation is unknown. Monte Carlo simulation results are almost identical to

the numerical results and the theoretical results match well with the experimental data. The amount of ghosting increases with decreasing applied electric field because of higher carrier trapping at lower applied electric field.

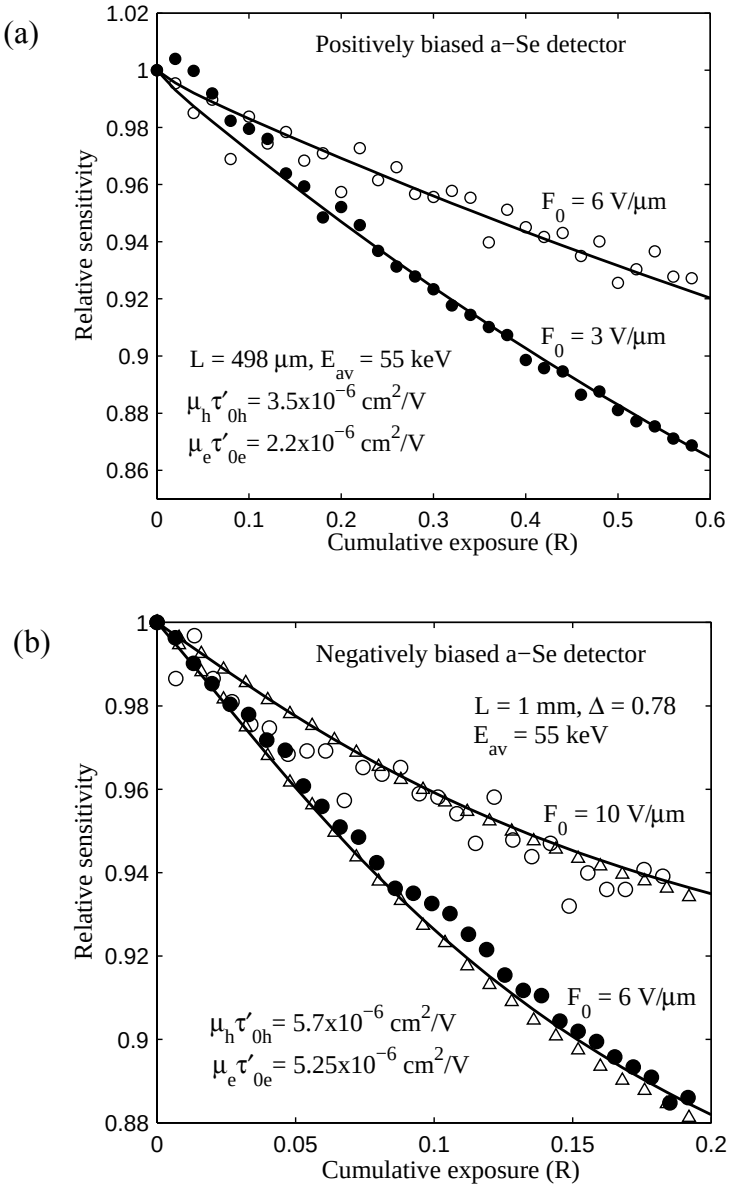

Figure 8.10 Relative x-ray sensitivity versus cumulative x-ray exposure for a (a) positively and (b) negatively biased a-Se detector for different applied electric fields. The circles represent experimental data [110, 111]. The triangles represent Monte Carlo simulation results [110, 111] and the solid lines represent numerical results.

The effect of mobility lifetime products on ghosting is shown in figure 8.11. The mobility-lifetimes of holes and electrons for (a) solid, (b) dashed, (c) dotted, and (d) dash-dotted curves are: (a) $\mu_h\tau'_{0h} \approx 3.5 \times 10^{-6}$ cm^2/V, $\mu_e\tau'_{0e} \approx 2.2 \times 10^{-6}$ cm^2/V; (b) $\mu_h\tau'_{0h} \approx 1.75 \times 10^{-6}$ cm^2/V, $\mu_e\tau'_{0e} \approx 2.2 \times 10^{-6}$ cm^2/V; (c) $\mu_h\tau'_{0h} \approx 3.5 \times 10^{-6}$ cm^2/V, $\mu_e\tau'_{0e} \approx 1.1 \times 10^{-6}$ cm^2/V; and (d) $\mu_h\tau'_{0h} \approx 1.75 \times 10^{-6}$ cm^2/V, $\mu_e\tau'_{0e} \approx 1.1 \times 10^{-6}$ cm^2/V. All other parameters in figure 8.11 are the same as in solid line in figure 8.8 (a). The amount of ghosting at positive bias increases with decreasing lifetime of holes. However, the relative sensitivity increases initially with decreasing electron lifetime. The concentration of trapped electrons at the radiation-receiving electrode side increases with decreasing electron lifetime, which increases the electric field and enhances total carrier generation in subsequent exposures. Consequently the amount of ghosting is improved slightly. However, this effect depends critically on a combination of factors such as the electron and hole lifetimes, applied electric field and Δ.

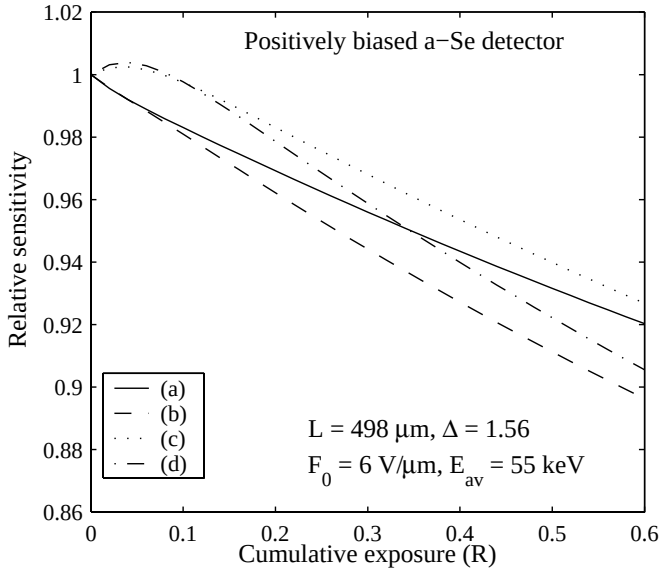

Figure 8.11 Relative x-ray sensitivity versus cumulative exposure for a positively biased a-Se detector, and for different carrier lifetimes. The mobility-lifetimes of holes and electrons for different curves are: (a) $\mu_h\tau'_{0h} \approx 3.5 \times 10^{-6}$ cm^2/V, $\mu_e\tau'_{0e} \approx 2.2 \times 10^{-6}$ cm^2/V, (b) $\mu_h\tau'_{0h} \approx 1.75 \times 10^{-6}$ cm^2/V, $\mu_e\tau'_{0e} \approx 2.2 \times 10^{-6}$ cm^2/V, (c) $\mu_h\tau'_{0h} \approx 3.5 \times 10^{-6}$ cm^2/V, $\mu_e\tau'_{0e} \approx 1.1 \times 10^{-6}$ cm^2/V, and (d) $\mu_h\tau'_{0h} \approx 1.75 \times 10^{-6}$ cm^2/V, $\mu_e\tau'_{0e} \approx 1.1 \times 10^{-6}$ cm^2/V. All other parameters in this figure are the same as in Figure 8.8.

Figure 8.12 shows the comparison of the amount of ghosting in an a-Se detector between positive and negative bias conditions for an applied electric field of 6 V/μm. All simulation parameters in figure 8.12 are the same as in solid curve in figure 8.8 (a). The amount of ghosting at negative bias is higher than at positive bias for the same a-Se detector. As mentioned before, the x-ray sensitivity at negative bias deteriorates in subsequent exposure because of less carrier generation as a result of field dependent carrier generation mechanism in a-Se detectors. Therefore, the polarity of applied bias to the radiation-receiving electrode has a significant effect on ghosting in a-Se detectors. However, the quantitative difference in ghosting performance between the positive and negative biases depends on the carrier transport properties, applied electric field and Δ. The difference increases with decreasing carrier lifetimes, applied field, and Δ.

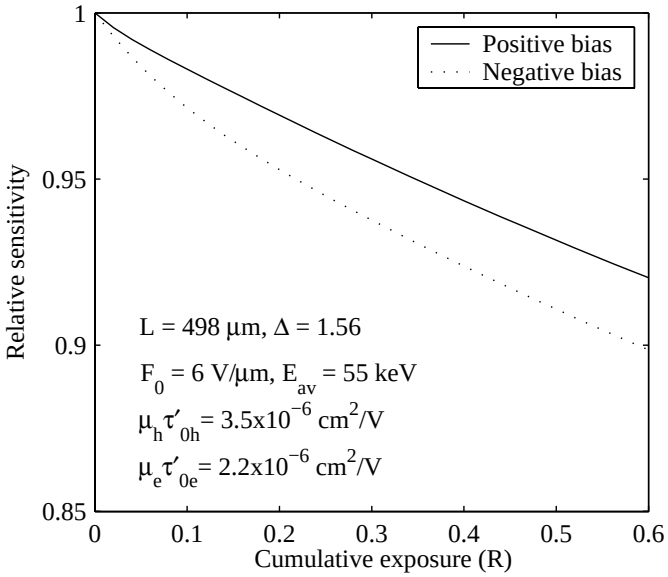

Figure 8.12 Relative x-ray sensitivity versus cumulative exposure for both positively and negatively biased a-Se detector. All other parameters in this figure are the same as in figure 8.8.

It is worth noting that this sensitivity changes in a-Se have been found to be reversible; over the course of approximately two days resting, the initial sensitivity of the a-Se layer was restored. It is expected that almost all trapped carriers will be released in two days. Again, the x-ray induced new trap centers should be meta-stable in nature; these may be stable for hours but anneal away within days. The exact physics and chemistry of these meta-stable traps are still unknown.

8.4 Summary

A numerical model for studying the effects of large signals on charge collection efficiency has been described. The effects of large signals include bimolecular recombination between drifting charge carriers, nonuniform electric fields across the photoconductor, and the high intensity x-ray induced new deep trap center generation. It has been shown that the recombination plays practically no role on charge collection in a-Se detectors up to the total carrier generation rate q_0 of 10^{18} EHPs/m^2-s. At large values of q_0, the charge collection efficiency gradually decreases with increasing q_0 and approaches almost zero at q_0 larger than 10^{24} EHPs/m^2-s. The bimolecular recombination between drifting carriers has practically no effect on charge collection in a-Se detectors for medical digital x-ray imaging applications. The recombination between oppositely charged carriers and the high intensity x-ray induced new deep trap center generation are mainly responsible for the nonlinearity in charge collection versus charge generation rate characteristics in a-Se detectors for tomotherapy applications. However, we need rigorous experimental study to quantify the high intensity x-ray induced new deep trap center generation in a-Se detectors for medical diagnostic x-ray imaging.

A model for calculating the dependence of the x-ray sensitivity of a-Se based x-ray image detectors on repeated x-ray exposures and exposure history has been described. The model considers deep trapping of charge carriers, trapped charges due to previous exposures, trap filling effects, recombination between drifting and trapped carriers,

space charge effects, electric field dependent charge carrier generation, x-ray induced new deep trap center generation, and detrapping of trapped carriers with time. The electric field distribution across the photoconductor varies widely depending on operating conditions and exposure history. The relative sensitivity decreases with increasing cumulative x-ray exposure. The sensitivity reduction at negative bias is greater than at positive bias. The amount of ghosting in a-Se detectors increases with decreasing applied electric field. The comparison of the model with the experimental data reveals that the recombination between trapped and the oppositely charged drifting carriers, electric field dependent charge carrier generation and x-ray induced new deep trap centers are mainly responsible for the sensitivity reduction in biased a-Se- based x-ray detectors. We expect that the ghosting phenomenon may also be present in other photoconductive (e.g., HgI_2, CdZnTe, PbO and PbI_2) detectors though it has not yet been measured.

The continuity equations for holes and electrons, trapping rate equations, and the Poisson's equation across the photoconductor for a step x-ray exposure are simultaneously solved by the finite difference method. The numerical results have been compared with Monte Carlo simulations of carrier transport and yield almost identical results.

9. SUMMARY, CONCLUSIONS AND FUTURE WORKS

9.1 Introduction

In this thesis the models for calculating the x-ray sensitivity, detective quantum efficiency, modulation transfer function and ghosting of a direct conversion flat-panel x-ray image detector have been developed by considering the combined effects of charge transport properties of the photoconductor, detector operating conditions, and the detector geometry and design. The modeling work has examined how the imaging characteristics such as x-ray sensitivity, detective quantum efficiency, resolution in terms of modulation transfer function and ghosting depend on charge transport properties (e.g., carrier trapping and recombination) of the photoconductor, operating conditions (e.g., bias voltage and polarity), and the detector geometry (detector thickness and pixel size). The modeling works in this thesis are based on the physics of the individual phenomena and the systematic solution of the fundamental physical equations in the photoconductor layer: (1) semiconductor continuity equation (2) Poisson's equation (3) trapping rate equations. The general approach of this project has been to develop models in normalized coordinates to describe different photoconductive x-ray image detectors. These models have been applied to different photoconductive detectors (e.g., a-Se, poly-HgI_2 and ploy-CdZnTe) for diagnostic medical x-ray imaging applications (e.g., mammography and chest radiography) and compared their performances. The theoretical results have been compared to experimental data obtained on a-Se, poly-HgI_2 and ploy-CdZnTe detectors. The theoretical models show a very good agreement with the experimental data.

The quantitative analyses presented in thesis have identified the important factors that limit the detector performances, which can ultimately lead to the reduction of

patient exposure/dose consistent with better diagnosis for the different imaging modalities. The imaging characteristics depend critically on the photoconductor's charge transport properties and the detector structure, *i.e*., the size of the pixel and the thickness of the photoconductor. It has been shown that detector structure is just as important to the overall performance of the detector as the material properties of the photoconductor itself. In Chapter 3, the charge transport, material and imaging detector properties (e.g., dark current and image lag) of some of the potential photoconductors have also been critically discussed and compared with the properties of an ideal photoconductor for direct conversion x-ray image detectors. The original contributions and findings of the research presented in this thesis are summarized in the following sections.

9.2 X-ray Sensitivity

A normalized model of the x-ray sensitivity of a photoconductor sandwiched between two parallel plate electrodes (a detector) operating under a constant electric field has been developed by analytically solving the *continuity equation* for both holes and electrons, and considering the drift of electrons and holes in the presence of deep traps. A generalized expression for charge carrier transport and absorption-limited normalized sensitivity of an x-ray detector has been derived in terms normalized parameters Δ, τ_e and τ_h. We have obtained the three-dimensional universal sensitivity curves which allow x-ray sensitivity of any potential photoconductive detector to be determined from τ_t, τ_b and Δ. It has been shown that the carrier schubwegs have to be several times greater, and the absorption depth δ (=1/α) has to be at least two times smaller than the photoconductor thickness L for achieving sufficient sensitivity. The normalized sensitivity equation has been applied to stabilized *a*-Se, poly-CdZnTe and poly-HgI_2 detectors considering their practical operating conditions. It has been found that the sensitivity is mainly controlled by the transport properties of the charges that have the same polarity as the bias on the radiation receiving electrode; holes for positive bias and electrons for negative bias. Therefore, positive bias is the preferred choice for a-Se detectors and negative bias is for poly-HgI_2 and poly-CdZnTe detectors as shown

in table 4.1. The x-ray sensitivity is also strongly influenced by Δ. The sensitivity model has been fitted to experimental data on HgI_2 photoconductive detector to obtain the carrier ranges ($\mu\tau'$) in poly-HgI_2. The model provides a very good fit to the experimental data.

We have also developed a model for calculating the charge collection and absorption-limited normalized x-ray sensitivity of a pixellated detector (e.g., flat panel detector) by incorporating charge carrier trapping and small pixel effects. The analytical expressions for the weighting potentials of square pixels have been derived by considering negligibly small gaps between the pixels and constructing an infinite series of image charges. For $\tau_t = \infty$ and for various levels of τ_b, the polarity of collected charges in the surrounding pixels is the same as that in the radiation-receiving pixel. On the other hand, the polarity of collected charges in the surrounding pixels is the opposite of that in the radiation-receiving pixel for $\tau_b = \infty$ and for various levels of τ_t. τ_t and τ_b are the normalized carrier lifetimes for the carriers that move towards the top and bottom electrodes, respectively. The normalized sensitivity of pixellated x-ray detectors mainly depend on the transport properties (mobility and lifetime product) of charges that move towards the pixel electrodes and the extent of dependence increases with decreasing normalized pixel width. The x-ray sensitivity of smaller pixels may be higher or lower than that of larger pixels depending on the rate of electron and hole trapping and the bias polarity. Having smaller pixels is advantageous in terms of higher sensitivity by ensuring that the carrier with the higher mobility-lifetime product is drifted towards the pixel electrodes. The model calculations have been applied to fluoroscopic and chest radiographic type pixellated detectors using a-Se, HgI_2 and CdZnTe as x-ray photoconductors.

9.3 Detective Quantum Efficiency

A cascaded linear system model that includes incomplete charge collection and x-ray interaction depth dependent conversion gain and charge collection stages has been developed for the calculation of the DQE(0) of a direct conversion x-ray image detector.

Using this model, the DQE(0) of *a*-Se for fluoroscopic applications has been examined in detail as a function of charge transport parameters and detector thickness under different operating conditions (electronic noise, x-ray exposure, bias voltage and polarity). We have found an *optimum photoconductor thickness* that maximizes the DQE(0) under a constant voltage operation. The optimum thickness increases with increasing x-ray exposure, bias voltage and charge collection efficiency, and decreasing added electronic noise. For reasonable quantities mentioned in this work that are appropriate for *a*-Se detectors and fluoroscopic applications, the optimum *a*-Se thickness is ~ 700 μm and the corresponding DQE is ~ 0.4. With the radiation receiving electrode negatively biased, the DQE is much more dependent on electron lifetime than hole lifetime. The DQE(0) of *a*-Se detector is higher for positive bias than for negative bias because of higher range of holes than electrons in a-Se. The results suggest that the DQE can be improved by ensuring that the carrier with the higher mobility-lifetime product is drifted towards the bottom electrode. The DQE generally does not continue to improve with greater photoconductor thickness because of charge transport and trapping effects. The DQE of polyenergetic x-ray beam is slightly lower than monoenergetic x-ray beam with the same average photon energy. It has been shown that the scattering events and fluorescence escape reduce the DQE(0) through the reduction of the conversion gain. This reduction of the DQE(0) depends on the operating conditions and transport properties of a-Se. The DQE(0) model is applied to explain experimental DQE data on a-Se image detectors and the model shows a very good agreement with experimental DQE data. The DQE(0) model is also applied to three potential photoconductive x-ray image detectors (a-Se, poly-HgI_2 and poly-CdZnTe) for fluoroscopic applications considering their practical operating conditions. It has been found that, in addition to high quantum efficiency, both high conversion gain and high charge collection efficiency are required to improve the DQE performance of an x-ray image detector.

9.4 Modulation Transfer Function

An analytical expression of MTF due to distributed carrier trapping in the bulk of the photoconductor has been derived using the trapped charge distribution across the photoconductor. The analytical expressions for trapped charge distributions in an x-ray photoconductor have also been derived. The MTF of photoconductive x-ray detectors have been studied for (a) different levels of carrier trapping and (b) different values of x-ray absorption depths. Trapping of the carriers that move towards the pixel electrodes degrades the MTF performance, whereas trapping of the other type of carriers improves the sharpness of the x-ray image. The MTF model is applied to polycrystalline CdZnTe x-ray image detectors and is fitted to recently published experimental results. The theoretical model shows a very good agreement with the measured data with $\mu_e \tau'_e = 2.4 \times 10^{-4}$ cm^2/V and $\mu_h \tau'_h = 3.2 \times 10^{-6}$ cm^2/V, which are very close to $\mu\tau'$ values reported in the literature.

9.5 Recombination and Ghosting

A numerical model for studying the effects of large signals on charge collection efficiency has been described. The effects of large signals include bimolecular recombination between drifting charge carriers, nonuniform electric field across the photoconductor, and the high intensity x-ray induced new deep trap center generation. It has been shown that the recombination plays practically no role on charge collection in a-Se detectors up to the total carrier generation rate q_0 of 10^{18} EHPs/m^2-s. At large values of q_0, the charge collection efficiency gradually decreases with increasing q_0 and approaches almost zero at q_0 larger than 10^{24} EHPs/m^2-s. For chest radiographic a-Se detectors, the recombination has practically no role on charge collection up to the exposure rate of 100 mR/ms that is much higher than the average exposure for chest radiographic applications (average exposure is 0.3 mR and the exposure time is in the order of ms). Again, for mammographic a-Se detectors, the recombination has practically no role on charge collection up to the exposure rate of 1000 mR/ms that is also much higher than the average exposure for mammographic applications (average

exposure is 12 mR and the exposure time is in the order of ms). Therefore, the bimolecular recombination between drifting carriers has practically no effect on charge collection in a-Se detectors for diagnostic medical x-ray imaging applications. The recombination between oppositely charged carriers and the high intensity x-ray induced new deep trap center generation are mainly responsible for the nonlinearity in charge collection versus charge generation rate characteristics in a-Se detectors for tomotherapy applications. However, we need rigorous experimental study to quantify the high intensity x-ray induced new deep trap center generation in a-Se detectors for medical diagnostic x-ray imaging.

A model for calculating the dependence of the x-ray sensitivity of a-Se based x-ray image detectors on repeated x-ray exposures and exposure history has been described. The model considers deep trapping of charge carriers, trapped charges due to previous exposures, trap filling effects, recombination between drifting and oppositely charged trapped carriers, space charge effects, electric field dependent charge carrier generation, x-ray induced new deep trap center generation, and detrapping of trapped carriers with time. The electric field distribution across the photoconductor varies widely depending on operating conditions and exposure history. The relative sensitivity decreases with increasing cumulative x-ray exposure. The sensitivity reduction at negative bias is greater than at positive bias. The amount of ghosting in a-Se detectors increases with decreasing applied electric field. The comparison of the model with the experimental data reveals that the recombination between trapped and the oppositely charged drifting carriers, electric field dependent charge carrier generation and x-ray induced new deep trap centers are mainly responsible for the sensitivity reduction in biased a-Se- based x-ray detectors. We expect that the ghosting phenomenon may also be present in other photoconductive (e.g., HgI_2, CdZnTe, PbO and PbI_2) detectors though it has not yet been measured.

9.6 Suggestions for Future Works

It has been found that having smaller pixels is advantageous in terms of higher sensitivity by ensuring that the carriers with the lower mobility-lifetime product are drifted towards the top electrode. However, the expected sensitivity estimated in this thesis represents the x-ray sensitivity to x-rays that are incident only on the pixel of interest. The induced charge on the pixel of interest by charge carriers liberated over neighboring pixels is undesired charge and can, in a sense, slightly negate the sensitivity improvement that smaller pixels seems to provide. The sensitivity model for pixellated detector described in chapter 7 can be improved by incorporating the induced charge on the pixel of interest by charge carriers liberated over neighboring pixels. In other word, a more detailed and rigorous analysis would consider the sensitivity as a function of spatial frequencies making up the signal.

The effects of charge carrier trapping on DQE(0) and MTF(f) have been studied in chapter 5 and 6, respectively. The loss of resolution due to charge carrier trapping has a significant effect on DQE(f). The DQE(0) model described in this thesis can be extended to calculate DQE(f) by incorporating the loss of resolution due to charge carrier trapping, MTF(f), in the recently developed cascaded linear system model.

The MTF model described in chapter 6 is valid for a single and low x-ray exposure case. For the repeated x-ray exposure case, the trapped charge distributions across the photoconductor layer can be different from the single exposure case, and so does the MTF. The MTF model of this thesis can be extended for repeated exposure case by determining the trapped charge distributions under extended exposures.

It has been found that the bimolecular recombination between drifting carriers has practically no effect on charge collection in a-Se detectors for diagnostic medical digital x-ray imaging applications. However, recent experiments show nonlinearity in charge collection versus charge generation rate characteristics in a-Se detectors at MeV range incident x-ray beam, which can not be described by the bimolecular recombination

mechanism alone. The possible mechanism for this signal nonlinearity is the x-ray induced new deep trap center generation due to the interaction of high intensity x-ray beam with the a-Se layer. However, we need experimental results at diagnostic x-ray photon energies to confirm the rate of new trap center generation due to high intensity x-ray beam for diagnostic (at keV x-ray photon energies) medical x-ray imaging applications. The large signal model can also be applied to other photoconductive detectors, for example, HgI_2 and CdZnTe detectors.

It has been found that only a certain fraction f of trapped charges act as recombination centers for oppositely charged drifting carriers. Stated differently, effective recombination coefficients fC_h and fC_e can be assigned. However, its physics is not clearly understood. A systematic research is necessary to investigate the physics behind the effective recombination coefficients that are less than the coefficients described by Langevin recombination mechanism. The ghosting model described in this thesis can also be applied to other photoconductive detectors, for example, HgI_2 and CdZnTe detectors, based on the availability of the experimental data.

Appendix A- X-ray Photon Fluence

Consider an x-ray beam incident on unit area. If Ψ is the energy fluence (energy per unit area) and X is the exposure, then the energy absorbed by the medium from the beam is (considering the energy absorbed in air by 1 R exposure is 0.00876 J/kg) [32],

$$\Psi\left(\alpha_{air}/\rho_{air}\right) = 0.00876\times10^{-3}\,X \quad \text{J/gm}, \tag{A.1}$$

Thus, $$\Psi = \frac{0.00876\times10^{-3}\,X}{\left(\alpha_{air}/\rho_{air}\right)} \quad \text{J/cm}^2 = \frac{5.45\times10^{13}\,X}{\left(\alpha_{air}/\rho_{air}\right)} \quad \text{eV/cm}^2, \tag{A.2}$$

where α_{air}/ρ_{air} is in cm^2/gm. Therefore, the x-ray photon fluence Φ_0 is given by

$$\Phi_0 = \frac{5.45\times10^{13}\,X}{\left(\alpha_{air}/\rho_{air}\right)E} \quad \text{Photons/cm}^2 \tag{A.3}$$

The x-ray photon fluence per unit exposure versus x-ray photon energy is shown in Figure A.1. The x-ray fluence per mR is energy dependent because the mass energy absorption coefficient (α_{air}/ρ_{air}) for air is energy dependent.

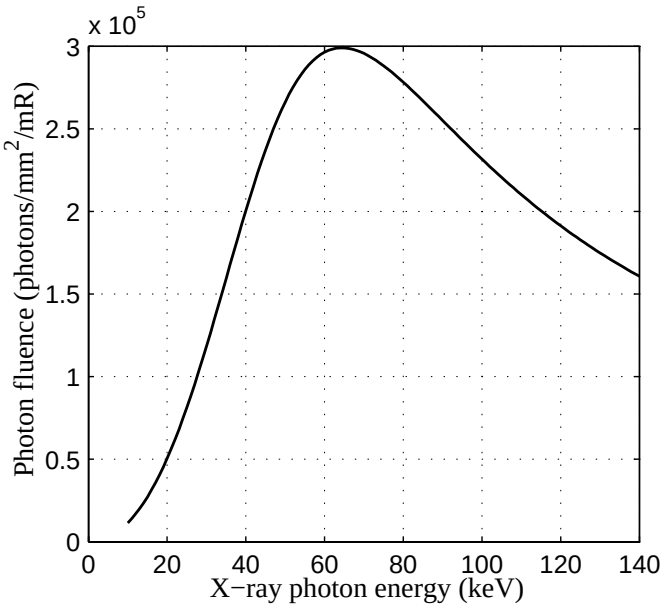

Figure A.1 The x-ray photon fluence (photons/mm^2) per unit exposure (mR) versus x-ray photon energy for diagnostic x-ray imaging.

Appendix B- Gain Fluctuation Noise

Let us consider a stochastic gain stage *i*, whose possible gains are 3, 4 and 5. Thus the average gain, $\bar{g}_i$ = 4 and the variance of gain, σ_{gi}^2 = 2/3. The number of input quanta (e.g., x rays) $\overline{\Phi}_{i-1}$ is varied from 1 to 3, and the output quanta (e.g., optical photons or EHPs) and its variation are shown in table B.1. It is evident from table B.1 that the variance of output quanta due to gain fluctuation is always equal to $\sigma_{gi}^2 \overline{\Phi}_{i-1}$, i.e., proportional to the average input quanta.

Table B.1 Gain fluctuation noise

Input quanta, $\overline{\Phi}_{i-1}$	Possible outcomes		Average output quanta, $\overline{\Phi}_i$	Variance of output quanta
	Output quanta Φ_i	probability		
1	3 4 5	1/3 1/3 1/3	4 ($=\bar{g}_i \overline{\Phi}_{i-1}$)	2/3 ($=\sigma_{gi}^2 \overline{\Phi}_{i-1}$)
2	6 7 8 9 10	1/9 2/9 3/9 2/9 1/9	8 ($=\bar{g}_i \overline{\Phi}_{i-1}$)	4/3 ($=\sigma_{gi}^2 \overline{\Phi}_{i-1}$)
3	9 10 11 12 13 14 15	1/27 3/27 6/27 7/27 6/27 3/27 1/27	12 ($=\bar{g}_i \overline{\Phi}_{i-1}$)	6/3 ($=\sigma_{gi}^2 \overline{\Phi}_{i-1}$)

Appendix C- Fourier Transform

The Fourier transform of equation (6.10) is given by

$$G(f)=\frac{1}{2\pi}\int_{-\infty}^{\infty}\int_{0}^{1}\int_{-\infty}^{\infty}\sum_{k=-\infty}^{\infty}\frac{q_t(x)(1-x+2k)}{\left[(1-x+2k)^2+y^2+z^2\right]^{3/2}}\mathrm{e}^{-j2\pi fy}\mathrm{d}z\mathrm{d}x\mathrm{d}y+\overline{Q}_b \qquad \text{(C.1)}$$

Changing the order of integrations the equation (C.1) becomes

$$G(f)=\frac{1}{2\pi}\int_{0}^{1}q_t(x)\sum_{k=-\infty}^{\infty}\int_{-\infty}^{\infty}\mathrm{e}^{-j2\pi fy}\int_{-\infty}^{\infty}\frac{(1-x+2k)}{\left[(1-x+2k)^2+y^2+z^2\right]^{3/2}}\mathrm{d}z\mathrm{d}y\mathrm{d}x+\overline{Q}_b$$

$$=\int_{0}^{1}q_t(x)\frac{\sinh(2\pi fx)}{\sinh(2\pi f)}\mathrm{d}x+\overline{Q}_b\ . \qquad \text{(C.2)}$$

Substituting the expression of $q_t(x)$ in equation (C.2) and performing the above integration, we obtain the equation (6.11) for $G(f)$.

Appendix D- Finite Difference Method

One of the widely used numerical techniques to solve partial differential equation is the finite-difference method. It proceeds by replacing the derivatives in the equation by finite differences and involves an initial discretization of domain.

Suppose we are interested in solving equations (8.11) – (8.15) over the space interval $0 < x < 1$, and the time interval $0 < t < 1$. For example, we compute a numerical solution by estimating $p(t,x)$ over a uniform grid consisting of m +1 values of t and n +1 values of x as shown in Figure D.1. Let Δt and Δx denote the step sizes of the variables t and x, respectively.

$$\Delta t = \frac{1}{m} \quad and \quad \Delta x = \frac{1}{n} \tag{D.1}$$

To simplify the final equations, let t_k and x_j denote the values of t and x at the grid points. That is,

$$t_k = k\Delta t \ , \ 0 \le k \le m \tag{D.2a}$$

$$x_j = j\Delta x \ , \ 0 \le j \le n \tag{D.2b}$$

Let p_j^k denote the computed value of $p(t_k,x_j)$. We need initial and boundary condition to get unique solution to the problem. The initial and boundary conditions for $p(t,x)$ are:

$$p(0,x) = 0, \ 0 < x < 1 \tag{D.3a}$$

$$p(t,0) = 0, \ t > 0 \tag{D.3b}$$

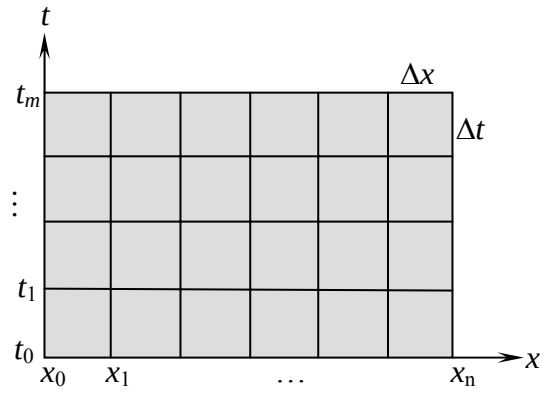

Figure D.1 Grid used to obtain a numerical solution to the equations (8.11) – (8.15).

There are several finite difference methods. Each method has some advantages and disadvantages in terms of stability, convergence and required time for calculation. The implicit *backward Euler method* is used to solve partial differential equations in this thesis since it is unconditionally stable [118, 119]. In backward Euler method, the difference approximation is taken from its value from an earlier time, i.e., the difference approximation is evaluated at t_{k+1} rather than t_k. Thus,

$$\frac{\partial p\left(t_{k+1}, x_j\right)}{\partial t} = \frac{p_j^{k+1} - p_j^k}{\Delta t} \tag{D.4a}$$

$$\frac{\partial pF\left(t_{k+1}, x_j\right)}{\partial x} = \frac{p_j^{k+1}F_j^{k+1} - p_{j-1}^{k+1}F_{j-1}^{k+1}}{\Delta x} \tag{D.4b}$$

Using t_{k+1} as the reference time in place of t_k has the effect of making the Euler approximation of $\partial p/\partial t$ in (D.4a) a backward difference. Substituting (D.4) into (8.12) we get,

$$\begin{aligned}\frac{p_j^{k+1} - p_j^k}{\Delta t} = &-r_\mu \frac{p_j^{k+1}F_j^{k+1} - p_{j-1}^{k+1}F_{j-1}^{k+1}}{\Delta x} - r_\mu \frac{p_j^{k+1}}{\tau_{hj}^{k+1}} - c_R p_j^{k+1} n_j^{k+1} \\ &- fc_0 r_\mu p_j^{k+1} n_{tj}^{k+1} + K_j^k e^{-x_j/\Delta}\end{aligned} \tag{D.5}$$

or, $$p_j^{k+1} A_h = \frac{p_j^k}{\Delta t} + r_\mu \frac{p_{j-1}^{k+1} F_{j-1}^{k+1}}{\Delta x} + K_j^k e^{-x_j/\Delta} \tag{D.6}$$

Where, $$A_h = \frac{1}{\Delta t} + \frac{r_\mu F_j^{k+1}}{\Delta x} + \frac{r_\mu}{\tau_{hj}^{k+1}} + c_R n_j^{k+1} + f c_0 r_\mu n_{tj}^{k+1} \tag{D.7}$$

Or, $$A_h \approx \frac{1}{\Delta t} + \frac{r_\mu F_j^{k}}{\Delta x} + \frac{r_\mu}{\tau_{hj}^{k}} + c_R n_j^{k} + f c_0 r_\mu n_{tj}^{k} \tag{D.8}$$

For practical purposes, $\left|F_j^{k+1} - F_j^k\right|$, $\left|n_j^{k+1} - n_j^k\right|$, $\left|n_{tj}^{k+1} - n_{tj}^k\right|$ or $\left|\tau_{hj}^{k+1} - \tau_{hj}^k\right| << 1$, provided that the Δt is very small. Moreover, the value of Δt needs to be very small to get a reasonable accuracy for changing derivatives into finite differences. Specifically, n and p reach steady values very quickly. The value of Δt is taken as less than 2.5×10^{-4} in all calculations and so the equation (D.8) is justified for this Δt. Then, p_j^{k+1} can be calculated using equations (D.6) & (D.8) and the solution proceeds in space from left to right as in Figure D.1. Alternately, approximate values of n_j^{k+1}, n_{tj}^{k+1} and F_j^{k+1} can be calculated explicitly (forward Euler method) from all variables at t_k using equations (8.11), (8.13) & (8.15), and then p_j^{k+1} can be calculated using equations (D.6) & (D.7) [120, 121]. However, these two approaches give almost identical results for sufficiently small values of Δt.

Similarly, the value of n_j^{k+1} can be calculated using equations (8.11) by the following initial and boundary conditions,

$$n(0,x) = 0,\ 0 < x < 1 \tag{D.9a}$$

$$n(t,1) = 0,\ t > 0 \tag{D.9b}$$

Thus, the value of n_j^{k+1} is calculated from the following two linear algebraic equations and the solution proceeds in space from right to left as in Figure D.1.

$$n_j^{k+1} A_e = \frac{n_j^k}{\Delta t} + \frac{n_{j+1}^{k+1} F_{j+1}^{k+1}}{\Delta x} + K_j^k e^{-x_j/\Delta} \tag{D.10}$$

And, $$A_e \approx \frac{1}{\Delta t} + \frac{F_j^k}{\Delta x} + \frac{1}{\tau_{hj}^k} + c_R p_j^k + f c_0 p_{tj}^k \tag{D.11}$$

Then the values of p_{tj}^{k+1} and n_{tj}^{k+1} are calculated from p_j^{k+1} and n_j^{k+1} using the following two equations and the initial conditions in equation (8.16).

$$p_{tj}^{k+1}\left(\frac{1}{\Delta t} + f c_0 n_j^{k+1}\right) = \frac{p_{tj}^k}{\Delta t} + r_\mu \frac{p_j^{k+1}}{\tau_{hj}^k} \tag{D.12}$$

$$n_{tj}^{k+1}\left(\frac{1}{\Delta t} + f c_0 r_\mu p_j^{k+1}\right) = \frac{n_{tj}^k}{\Delta t} + \frac{n_j^{k+1}}{\tau_{ej}^k} \tag{D.13}$$

Then τ_{ej}^{k+1} and τ_{hj}^{k+1} are calculated from p_{tj}^{k+1} and n_{tj}^{k+1} using equations (8.6) and (8.7) in normalized coordinates. The electric field profile at t_{k+1} is calculated from the values of p_j^{k+1}, n_j^{k+1}, p_{tj}^{k+1} and n_{tj}^{k+1} using the equation (8.15) and the boundary condition described in equation (8.17). Thus,

$$F_0^{k+1} = 1 - \int_0^1 \{\int_0^x c_0 (p + p_t - n - n_t) dx\} dx \tag{D.14a}$$

And $$F_j^{k+1} = F_0^{k+1} + \int_0^{x_j} c_0 (p + p_t - n - n_t) dx \;;\; 1 \le \mathrm{j} \le \mathrm{n} \tag{D.14b}$$

The integration in equation (D.14) is numerically performed using the discrete values of p_j^{k+1}, n_j^{k+1}, p_{tj}^{k+1} and n_{tj}^{k+1}. Thus, the values of p_j^{k+1}, n_j^{k+1}, p_{tj}^{k+1}, n_{tj}^{k+1} and F_j^{k+1} are obtained simultaneously at time t_{k+1} by numerically solving the equations (8.11) to (8.15). Then the same calculations are repeated for the next time step. The

calculations were repeated for different step sizes to check the convergence and accuracy. The space step size $\Delta x = 10^{-2}$ is sufficiently small for getting a reasonable accuracy. The time step size Δt was varied from 2.5×10^{-4} to 2.5×10^{-5} and did not get any noticeable change in the numerical results. Therefore, the time step size $\Delta t = 2.5 \times 10^{-4}$ is assumed to be sufficiently small for getting a reasonable accuracy. The above formulations are valid for positive bias. The same procedure can be applied for negative bias case, provided all the continuity and rate equations are changed accordingly.

10. REFERENCES

[1] J. A. Rowlands and S. O. Kasap, "Amorphous semiconductors usher in digital x-ray imaging," *Physics Today*, **50**, pp. 24-30, (1997), and references therein.

[2] M. J. Yaffe and J. A. Rowlands, "X-ray detectors for digital radiology," *Phys. Med. Biol.*, **42**, pp. 1-39, (1997).

[3] J. A. Rowlands and J. Yorkston, "Flat panel detectors for digital radiography" in *Handbook of Medical Imaging Vol.* 1, edited by J. Beutel, H. L. Kundel and R. L. Van Metter (SPIE Press, Washington, 2000), Ch. 4 and references therein.

[4] V. N. Cooper III, T. Oshiro, C. H. Cagnon, L. W. Bassett, T. M. McLeod-Stockmann, N. V. Bezrukiy, "Evaluation of detector dynamic range in the x-ray exposure domain in mammography: A comparison between film-screen and flat panel detector systems," *Med. Phys.*, **30**, pp. 2614-2621, (2003).

[5] D. C. Hunt, O. Tousignant, and J. A. Rowlands, "Evaluation of the imaging properties of an amorphous selenium-based flat panel detector for digital fluoroscopy," *Med. Phys.*, **31**, pp. 1166-1175, (2004).

[6] S. O. Kasap and J. A. Rowlands, "Direct-conversion flat panel X-ray image detectors," *IEE Proc.-CDS*, **149**, pp. 85-96, (2002).

[7] L. E. Antonuk, J. M. Boudry, Y. El-Mohri, W. Huang, J. H. Siewerdsen, J. Yorkston, and R. A. Street, "Large area, flat-panel, amorphous silicon imagers," *Proc. SPIE – Int. Soc. Opt. Eng.*, **2432,** pp. 216-227, (1995).

[8] J. Chabbal, C. Chaussat, T. Ducourant, L. Fritsch, J. Michaïlos, V. Spinnler, G. Vieux, M. Arques, G. Halm, M. Hoheisel, H. Horbaschek, R. Schulz, and M. Spahn, "Amorphous silicon x-ray image sensor," *Proc. SPIE – Int. Soc. Opt. Eng.*, **2708,** pp. 499-510, (1996).

[9] E. Samei, and M. J. Flynn, "An experimental comparison of detector performance for direct and indirect digital radiography systems," *Med. Phys.*, **30**, pp. 608-622, (2003).

[10] R. S. Saunders Jr., E. Samei, and C. Hoeschen, "Impact of resolution and noise characteristics of digital radiographic detectors on the detectability of Lung nodules," *Med. Phys.*, **31**, pp. 1603-1613, (2004).

[11] B. Polischuk, Z. Shukri, A. Legros, and H. Rougeot, "Selenium direct converter structure for static and dynamic x-ray detection in medical imaging," *Proc. SPIE*, **3336**, pp. 494-504, (1998).

[12] S. O. Kasap and J. A. Rowlands, "X-ray photoconductors and stabilized a-Se for direct conversion digital flat panel x-ray image detectors," in *Optoelectronics & Photonics: Principles and Practices*, S.O. Kasap, (Prentice-Hall, Upper Saddle River, New Jersey, 2001), (in CDROM).

[13] S. O. Kasap, "Photoreceptors: the selenium alloys," in *HandBook of Imaging Materials*, edited by A. S. Diamond (Marcel Dekker, New York, 1991), p. 329-372.

[14] S. O. Kasap and J. A. Rowlands, "Direct-conversion flat panel x-ray image sensors for digital radiography," *Proc. IEEE*, **90**, pp. 591-604, (2002).

[15] A. Zuck, M. Schieber, O. Khakhan, and Z. Burshtein, "Near single-crystal electrical properties of polycrystalline HgI_2 produced by physical vapor deposition," *IEEE Trans. Nucl. Sci.*, **50**, pp. 991-997, (2003).

[16] S. Tokuda, H. Kishihara, S. Adachi, and T. Sato, "Improvement of the temporal response and output uniformity of polycrystalline CdZnTe films for high sensitivity X-ray imaging," *Proc. SPIE*, **5030**, pp. 861-870, (2003).

[17] R. A. Street, S. E. Ready, K. Van Schuylenbergh, J. Ho, J. B. Boyec, P. Nylen, K. Shah, L. Melekhov, and H. Hermon, "Comparison of PbI_2 and HgI_2 for direct detection active matrix x-ray image sensors," *J. Appl. Phys.*, **91**, pp. 3345-3355, (2002).

[18] S. Tokuda, H. Kishihara, S. Adachi, and T. Sato, "Preparation and characterization of polycrystalline CdZnTe films for large area, high sensitivity X-ray detectors: review," *J. Mat. Sci.*: *Mat. Elec.*, **15**, pp. 1-8, (2004).

[19] M. Simon, R. A. Ford, A. R. Franklin, S. P. Grabowski, B. Mensor, G. Much, A. Nascetti, M. Overdick, M. J. Powell, and D. U. Wiechert, "PbO as direct conversion x-ray detector material," *Proc. SPIE*, **5368**, pp. 188-199, (2004).

[20] J. M. Boone, "X-ray production, interaction, and detection in diagnostic imaging," in *Handbook of Medical Imaging Vol.* 1, edited by J. Beutel, H. L. Kundel and R. L. Van Metter (SPIE Press, Washington, 2000), Ch. 1 and references therein.

[21] I. M. Blevis, D. C. Hunt, and J. A. Rowlands, "Measurement of X-ray photogeneration in amorphous selenium," *J. Appl. Phys.*, **85**, pp. 7958-7963, (1999).

[22] M. F. Stone, W. Zhao, B. V. Jacak, P. O'Conner, B. Yu, and P. Rehak, "The x-ray sensitivity of amorphous selenium for mammography," *Med. Phys.*, **29**, pp. 319-324, (2002).

[23] S. Steciw, T. Stanescu, S. Rathee, and B.G. Fallone, "Sensitivity reduction in biased amorphous selenium photoconductors," *J. Phys. D: Appl. Phys*., **35**, pp. 2716-2722, (2002).

[24] W. Zhao, G. DeCrescenzo, and J. A. Rowlands, "Investigation of lag and ghosting in amorphous selenium flat-panel x-ray detectors," *Proc. SPIE*, **4682**, pp. 9-20, (2002).

[25] S. O. Kasap, V. Aiyah, A. Baillie, and A. G. Leiga, "X-ray induced hole trapping in electroradiographic plates," *J. Appl. Phys.*, **69**, pp. 7087-7096, 1991.

[26] U. Schiebel, T. Buckremer, G. Frings, and P. Quadfling, "Deep trapping and recombination in a-Se:As X-ray sensitive photoreceptors," *J. Non-Cryst. Solids*, **115,** pp. 216-218, (1989).

[27] M. Abkowitz and R. C. Enck, "Photoenhanced metastable deep trapping in amorphous chalcogenides near room temperature," *Phys. Rev. B*, **27**, pp. 7402-7411, (1983).

[28] W. Shockley, "Currents to conductors induced by a moving point charge," *J. Appl. Phys.*, **9**, pp. 635-636, (1938).

[29] S. Ramo, "Current induced by electron motion," *Proc. IRE*, **27**, pp. 584-585, (1939).

[30] Z. He, "Review of the Shockley-Ramo theorem and its application in semiconductor gamma-ray detectors," *Nucl. Instr. Meth. Phys. Res. A*, **463**, pp. 250-267, (2001).

[31] S. O. Kasap, "*Optoelectronics and photonics: Principles and practices*," (Prentice-Hall, Upper Saddle River, New Jersey, 2001), chapter 5.

[32] H. E. Johns and J. R. Cunningham, "*The physics of radiology*," fourth edition (Springfield, IL: Charges C Thomas, 1983). Chs. 5 and 7.

[33] http://physics.nist.gov/PhysRefData/

[34] C. A. Klein, "Bandgap dependence and related features of radiation ionization energies in semiconductors," *J. Appl. Phys*., **39**, pp. 2029-2038, (1968).

[35] G. F. Knoll, "*Radiation Detection and Measurement*," third edition (John Wiley and Sons, New York, 2000). Ch. 11.

[36] W. Que and J. A. Rowlands, "X-ray photogeneration in amorphous selenium: Geminate versus columnar recombination," *Phys. Rev.*, **B51**, pp. 10500–10507, (1995).

[37] G. Belev and S. O. Kasap, "Amorphous selenium as an x-ray photoconductor," *J. Non-Cryst. Solids*, **345 & 346,** pp. 484-488, (2004).

[38] D. C. Hunt, "Imaging performance of amorphous selenium flat-panel detector for digital fluoroscopy," *SPIE Medical Imaging conference presentation*, San Diego, (2003).

[39] S. O. Kasap, "*Principles of electronic materials and devices*," 2nd edition (McGraw-Hill, New York, 2002), chapter 1.

[40] M. Nesdoly, "X-ray sensitivity and x-ray induced charge transport changes in stabilized a-Se films," Ph.D. thesis, Electrical Engineering, University of Saskatchewan, Saskatoon, Canada, (2000).

[41] M. Kastner and D. Adler, "Valence-alternation model for localized gap states in lone-pair semiconductors," *Phys. Rev. Letts.*, **37**, pp. 1504-1507, (1976).

[42] A. V. Kolobov, H. Oyanagi, A. Roy, and K. Tanaka, "A nanometer scale mechanism for the reversible photostructural change in amorphous chalcogenides," *J. Non-crystalline Solids*, **232-234**, pp. 80-85, (1998).

[43] S. O. Kasap and C. Juhasz, "Time-of-flight drift mobility measurements on chlorine doped amorphous selenium films," *J. Phys. D: Applied Physics*, **33**, pp. 703-720, (1985).

[44] H.-Z. Song, G. J. Adriaenssens, E. V. Emelianova, and V. I. Arkhipov, "Distribution of gap states in amorphous selenium thin films," *Phys. Rev. B.*, **59**, pp. 10607-10613, (1999).

[45] S. O. Kasap, K. V. Koughia, B. Fogal, G. Belev, and R. E. Johanson, "The influence of deposition conditions and alloying on the electronic properties of amorphous selenium," *Semiconductors*, **14**, pp. 816-821, (2003).

[46] K. Koughia, Z. Shakoor, S. O. Kasap, and J. M. Marshall, "Density of localized electronic states in a-Se from electron time-of-flight photocurrent measurements," J. Appl. Phys., **97**, 033706 (2005).

[47] S. O. Kasap, V. Aiyah, B. Polischuk, A. Bhattacharyya, and Z. Liang, "Deep-trapping kinematics of charge carriers in amorphous semiconductors: A theoretical and experimental study," *Phys. Rev. B*, **43**, pp. 6691-6705, (1991).

[48] M. Abkowitz, "Density of states in a-Se from combined analysis of xerographic potentials and transient transport data," *Philosophical Magazine Letters* **58**, pp. 53–57 (1988).

[49] S. O. Kasap, **M. Zahangir Kabir**, and J. A. Rowlands, "Recent advances in X-ray photoconductors for direct conversion X-ray image sensors," *Current Applied Physics*,- in press.

[50] S. O. Kasap, "X-ray sensitivity of photoconductors: application to stabilized *a*-Se," *J. Phys. D: Applied Physics*, **33**, pp. 2853-2865, (2000).

[51] E. Fourkal, M. Lachaine, and B. G. Fallone, "Signal formation in amorphous-Se-based x-ray detectors," *Physical Rev.* **B 63**, 195204 (2001).

[52] D. Mah, J.A. Rowlands, and J.A. Rawlinson, "Sensitivity of amorphous selenium to x rays from 40 kVp to 18 MV: Measurements and implications for portal imaging," *Med. Phys.*, **25**, pp. 444-456, (1998).

[53] M. Choquette, Y. Demers, Z. Shukri, O. Tousignant, K. Aoki, M. Honda, A. Takahashi, and A. Tsukamoto, "Performance of a real time selenium based x-ray detector for fluoroscopy," *Proc. SPIE*, **4320**, pp. 501-508, (2001).

[54] G. Zentai, L. Partain, R. Pavlyuchkova, C. Proano, B. N. Breen, A. Taieb, O. Dagan, M. Schieber, H. Gilboa, and J. Thomas, "Mercuric iodide medical imagers for low exposure radiography and fluoroscopy," *Proc. SPIE*, **5368**, pp. 200-210, (2004).

[55] M. Schieber, A. Zuck, M. Braiman, J. Nissenbaum, R. Turchetta, W. Dulinski, D. Husson, and J.L. Riester, "Novel mercuric iodide polycrystalline nuclear particle counters," *IEEE trans. Nuc. Sci.* **NS-44**, pp. 2571-2575, (1997).

[56] R. C. Whited and L. van den Berg, "Native defect compensation in HgI_2 crystals," *IEEE trans. Nuc. Sci.* **NS-24**, 165 (1977).

[57] Y. Eisen and A. Shor, "CdTe and CdZnTe room-temperature x-ray and Gamma ray detectors and imaging systems," *Mat. Res. Soc. Symp. Proc.*, **487**, pp. 129-144, (1997).

[58] A. Ruzin and Y. Nemirovsky, "Methodology for evaluation of mobility-lifetime product by spectroscopy measurements in CdZnTe spectrometers," *J. Appl. Phys.*, **82**, pp. 4166-4171, (1997).

[59] J. G. Mainprize, N. L. Ford, S. Yin, E. E. Gordon, W. J. Hamilton, T. O. Tümer, and M. J. Yaffe, "A CdZnTe slot-scanned detector for digital mammography," *Med. Phys.*, **29,** 2767-2781, (2002).

[60] **M. Zahangir Kabir** and S. O. Kasap, "Modulation transfer function of photoconductive x-ray image detectors: effects of charge carrier trapping," *J. Phys. D*: *Appl. Phys.*, vol. **36**, pp. 2352-2358, (2003).

[61] G. Zentai, L. Partain, R. Pavlyuchkova, C. Proano, G. Virshup, L. Melekhov, A. Zuck, B. N. Breen, O. Dagan, A. Vilensky, M. Schieber, H. Gilboa, P. Bennet, K. Shah, Y. Dmitriev, and J. Thomas, "Mercuric iodide and lead iodide x-ray detectors for radiographic and fluoroscopic medical imaging," *Proc. SPIE*, **5030**, pp. 77-91, (2003).

[62] R. A. Street, S. E. Ready, F. Lemmi, K. S. Shah, P. Bennett, and Y. Dmitriyev, "Electronic transport in polycrystalline PbI_2 films," *J. Appl. Phys.*, **86**, pp. 2660-2667, (1999).

[63] A. Brauers, and U. Schiebel, "X-ray image sensor," *US Patent*, 5729021, (1998)

[64] **M. Zahangir Kabir**, S. O. Kasap, and J. A. Rowlands, "Photoconductors for x-ray image sensors," in *The Springer Handbook of Electronic and Optoelectronic Materials*, Eds: S. O. Kasap and P. Capper, Springer 2005 (in press).

[65] M. Choquette, H. Rougeot, J. P. Martin, L. Laperrier, Z. Shukri and B. Polischuk, "Direct selenium x-ray detector for fluoroscopy, R&F, and radiography," *Proc. SPIE*, **3977**, pp. 128-136 (2000).

[66] Y. Nemirovsky, A. Ruzin, G. Asa, and J. Gorelik, "Study of the charge collection efficiency of CdZnTe radiation detectors," *J. Electron. Mater.*, **25**, pp. 1221-1231, (1996).

[67] **M. Zahangir Kabir** and S. O. Kasap, "Charge collection and absorption-limited sensitivity of x-ray photoconductors: Applications to a-Se and HgI_2," *Appl. Phys. Lett.*, **80**, pp. 1664-1666, (2002).

[68] **M. Zahangir Kabir** and S. O. Kasap, "Sensitivity of x-ray photoconductors: Charge trapping and absorption-limited universal sensitivity curves," *J. Vac. Sci. Tech. A*, **20**, pp. 1082-1086, (2002).

[69] R.A. Street, M. Mulato, M. Schieber, H. Hermon, K. Shah, P. Bennet, Y. Dmitriyev, J. Ho, R. Lau, E. Meerson, S.E. Ready, B. Reisman, Y. Sado, K. Vanschuylenbergh, A. Vilensky, and A. Zuck, "Comparative study of PbI_2 and

HgI_2 as direct detector materials for high resolution x-ray image sensors," *Proc. SPIE*, **4320**, pp. 1-12, (2001).

[70] M. Schieber, A. Zuck, M. Braiman, L. Melekhov, J. Nissenbaum, R. Turchetta, W. Dulinski, D. Husson, J.L. Riester, T.E. Schlesinger, J. Toney, S. Sanguinetti, M. Montalti, and M. Guzzi, "Towards imaging with polycrystalline mercuric iodide semiconductor detectors," *Mat. Res. Soc. Symp. Proc.*, **487**, pp. 329-337, (1998).

[71] S. Tokuda, S. Adachi, T. Sato, T. Yoshimuta, H. Nagata, K. Uehara, Y. Izumi, O. Teranuma, and S. Yamada, "Experimental evaluation of a novel CdZnTe flat-panel x-ray detector for digital radiography and fluoroscopy," *Proc. SPIE* **4320**, pp. 140-147, (2001).

[72] A. Ruzin and Y. Nemirovsky, "Statistical models for charge collection efficiency and variance in semiconductor spectrometers," *J. Appl. Phys.* **82**, pp. 2754-2758, (1997).

[73] J. G., Mainprize, D. C. Hunt, and M. J. Yaffe, "Direct conversion detectors: the effect of incomplete charge collection on detective quantum efficiency," *Med. Phys.*, **29**, pp. 976-990, (2002).

[74] S. M. Seltzer, "Calculation of photon mass energy-transfer and mass energy-absorption coefficients," *Radiat. Res.* **136,** pp. 147-170, (1993).

[75] H. P. Chan and K. Doi, "Energy and angular dependence of x-ray absorption and its effect on radiographic response in screen-film systems," *Phys. Med. Biol.* **28**, pp. 565-579, (1983).

[76] S. O. Kasap, **M. Zahangir Kabir,** J. A. Rowlands, O. Tousignant, J. Leboeuf, L. Laperrière, and Y. Demers, "Dependence of the detective quantum efficiency of photoconductive x-ray detectors on charge transport parameters and exposure: applications to a-Se," *Appl. Phys. Lett.*, **81**, pp. 3482-3484, (2002).

[77] M. Rabbani, R. Shaw and R. Van Metter, "Detective quantum efficiency of imaging systems with amplifying and scattering mechanisms," *J. Opt. Soc. Am. A* **4**, pp. 895-901, (1987).

[78] I. A. Cunningham, "Applied linear-systems theory," in *Handbook of Medical Imaging*, **Vol. 1**, Ed: J. Beutel, H.L. Kundel and R.L. Van Metter, (SPIE Press, Washington, 2000), Ch.2 and references therein.

[79] **M. Zahangir Kabir** and S. O. Kasap, "DQE of photoconductive x-ray image detectors: application to a-Se," *J. Phys. D*: *Appl. Phys.*, **35**, pp. 2735-2743, (2002).

[80] E. Storm and H. I. Israel, "Photon cross sections from 1 keV to 100 MeV for elements $Z = 1$ to $Z = 100$," *Nuclear Data Tables* **A7,** pp. 565-681, (1970).

[81] W. Zhao and J. A. Rowlands, "Digital radiology using active matrix readout of amorphous selenium: theoretical analysis of detective quantum efficiency," *Med. Phys.* **24**, pp. 1819-1833, (1997).

[82] I. M. Blevis, D. C. Hunt, and J. A. Rowlands, "X-ray imaging using amorphous selenium: Determination of Swank factor by pulse height spectroscopy," *Med. Phys.* **25,** pp. 638-641, (1998).

[83] W. Zhao and J.A. Rowlands, "X-ray imaging using amorphous selenium: Feasibility of a flat panel self-scanned detector for digital radiology," *Med. Phys.* **22**, pp. 1595-1604, (1995).

[84] D. R. Dance and G. Y. Day, "Escape probabilities for fluorescent x-rays," *Phys. Med. Biol.* **30,** pp. 259-262, (1985).

[85] G. Pang, W. Zhao and J.A. Rowlands, "Digital radiology using active matrix readout of amorphous selenium: geometric and effective fill factors," *Med. Phys.* **25**, pp. 1636-1646, (1998).

[86] G. W. C. Kaye and T. H. Laby, "*Tables of Physical and Chemical Constants*," 16th ed. (Longman, London, U.K., 1985), p. 388.

[87] **M. Zahangir Kabir** and S. O. Kasap, "Dependence of the DQE of photoconductive X-ray detectors on charge transport and trapping," *Proc. SPIE – Int. Soc. Opt. Eng.*, **4682**, pp. 42-52, (2002).

[88] S. Adachi, S. Hirasawa, M. Takahashi, H. Okada, Y. Yamane, and S. Yamada, "Noise properties of a Se-based flat-panel x-ray detector with CMOS readout integrated circuits," *SPIE Proc.* **4682,** pp. 580-591, (2002).

[89] O. Tousignant, M. Choquette, Y. Demers, L. Laperrière, J. Leboeuf, M. Honda, M. Nishiki, A. Takahashi, and A. Tsukamoto, "Progress report on the performance of real time selenium flat panel detectors for direct x-ray imaging," *SPIE Proc.* **4682,** pp. 503-510, (2002).

[90] **M. Zahangir Kabir**, S.O. Kasap, W. Zhao, and J.A. Rowlands, "Direct conversion x-ray sensors: Sensitivity, DQE & MTF", *IEE Proc.–CDS*: Special Issue on Amorphous and Microcrystalline Semiconductors, **150**, pp. 258-266, (2003).

[91] W. Que and J. A. Rowlands, "X-ray imaging using amorphous selenium: Inherent spatial resolution," *Med. Phys.* **22,** pp. 365-374, (1995).

[92] S. O. Kasap, J. Rowlands, B. Fogal, **M. Zahangir Kabir**, G. Belev, S. O'Leary, B. Polischuk and R. E. Johanson, "Progress in the science and technology of direct conversion a-Se X-ray sensors," *J. Non-cryst. Solids* **299-302**, pp. 988-992, (2002).

[93] D. C. Hunt, O. Tousignant, Y. Demers, L. Laperrière, and J. A. Rowlands, "Imaging performance of amorphous selenium flat panel detector for digital fluoroscopy," *Proc. SPIE*, **5030,** pp. 226-234, (2003).

[94] S. O. Kasap, D. Brinkhurst, and C. Haugen, "Modelling of photoinduced discharge of photoreceptors under pulsed photoexcitation: small and large signal xerographic time-of-flight analysis," *J. Phys. D: Appl. Phys.* **33,** pp. 449-463, (2000).

[95] **M. Zahangir Kabir** and S. O. Kasap, "Charge transport and trapping-limited sensitivity and resolution of pixellated x-ray image detectors," *Proc. SPIE – Int. Soc. Opt. Eng.*, **5030**, pp. 26-38, (2003).

[96] L.-A. Hamel and S. Paquet, "Charge transport and signal generation in CdTe pixel detectors," *Nucl. Instr. Meth. Phys. Res.* **A 380**, pp. 238-240, (1996).

[97] O. D. Kellogg, "*Foundations of Potential Theory*," (Ungar, New York, 1929), p. 230-232.

[98] J. D. Eskin, H. H. Barrett, and H. B. Barber, "Signals induced in semiconductor gamma-ray imaging detectors," *J. Appl. Phys.* **85**, pp. 647-659, (1999).

[99] M. A. Kriss, C. N. Nelson, and F. C. Eisen, "Modulation transfer function in photographic systems containing development adjacency effects," *Photogr. Sci. Eng.* **18,** pp.131-138, (1974).

[100] S. Tokuda, H. Kishihara, S. Adachi, T. Sato, Y. Izumi, O. Teranuma, Y. Yamane, and S. Yamada, "Large area deposition of a poly-crystalline CdZnTe film and its applicability to x-ray panel detectors with superior sensitivity," *Proc. SPIE* **4682**, pp. 30-41, (2002).

[101] H. H. Barrett, J. D. Eskin, and H. B. Barber, "Charge transport in arrays of semiconductor gamma-ray detectors," *Phy. Rev. Lett.* **75**, pp. 156-159, (1995).

[102] **M. Zahangir Kabir** and S. O. Kasap, "Charge collection and absorption-limited x-ray sensitivity of pixellated x-ray detectors," *J. Vac. Sci. Tech. A*, vol. **22**, pp. 975-980, (2004).

[103] B. A. Brunett, J. M. Van Scyoc, R. B. James, and T. E. Schlesinger, "CdZnTe pixel array detectors and implications for producing large volume gamma-ray spectrometers," *J. Appl. Phys.* **86**, 3926-3933, (1999).

[104] V. L. Averyanov, A. V. Kolobov, B. T. Kolomiets, and V. M. Lyubin, "A model of photostructural changes in chalcogenide vitreous semiconductors: experimental results," *J. Non-crystalline Solids*, **45**, pp. 343-353, (1981).

[105] B. Fogal, **M. Zahangir Kabir,** R. E. Johanson, S. K. O'Leary and S. O. Kasap, "X-ray induced recombination effects in a-Se based x-ray photoconductors used in direct conversion x-ray sensors," *J. Vac. Sci. Tech. A*, **22**, pp. 1005-1009, (2004).

[106] **M. Zahangir Kabir,** M. Yunus, and S. O. Kasap, "Dependence of x-ray sensitivity of direct conversion x-ray detectors on x-ray exposure and exposure history," *Proc. SPIE – Int. Soc. Opt. Eng.*, **5368,** pp. 170-176, (2004).

[107] M. Yunus, "Monte Carlo modeling of the sensitivity of x-ray photoconductors," M. Sc. thesis, Electrical Engineering, University of Saskatchewan, Saskatoon, Canada (2005).

[108] C. Haugen and S. O. Kasap, "Langevin recombination of drifting electrons and holes in stabilized a-Se (Cl-doped a-Se: 0.3% As)," *Philosophical Magazine*, **71**, pp. 91-96, (1995).

[109] S. O. Kasap, B. Fogal, **M. Zahangir Kabir**, R. E. Johanson, S. K. O'Leary and S. O. Kasap, "Recombination of drifting holes with trapped electrons in stabilized a-Se photoconductors: Langevin recombination," *Appl. Phys. Lett.*, **84**, pp. 1991-1993, (2004).

[110] **M. Zahangir Kabir,** M. Yunus, S. O. Kasap, O. Tousignant, H. Mani, and P. Gauthier, "Ghosting mechanisms in a-Se based direct conversion x-ray image sensors," *Proc. SPIE – Int. Soc. Opt. Eng.*, **5745,** pp. 223-231 (2005).

[111] **M. Zahangir Kabir,** M. Yunus, S. O. Kasap, O. Tousignant, H. Mani, and P. Gauthier, "Sensitivity of stabilized a-Se based x-ray photoconductors," *Current Applied Physics*,- to be published.

[112] M. Yunus, **M. Zahangir Kabir,** and S. O. Kasap, "Sensitivity reduction mechanisms in amorphous selenium photoconductive x-ray image detectors," *Appl. Phys. Lett.*, **85**, pp. 6430-6432, (2004).

[113] R. A. Street, "Recombination in amorphous semiconductors," *Phys. Rev.* **B 17,** pp. 3984-3995, (1978).

[114] A. E. Iverson and D. L. smith, "Mathematical modeling of photoconductor transient response," *IEEE Trans. Electron Devices*, **ED-34**, pp. 2098-2107, (1987).

[115] **M. Zahangir Kabir,** M. Yunus, and S. O. Kasap, "The effects of large signals on charge collection in photoconductive x-ray image detectors," *Proc. IEEE Canadian Conference on Electrical and Computer Engineering,* pp. 197-199, (2005).

[116] A. W. Rau, L. Bakueva, and J. A. Rowlands, "The x-ray time of flight method for investigation of ghosting in amorphous selenium based flat panel medical x-ray imagers," *Med. Phys.*,- to be published (data used with permission of Andreas Rau).

[117] B. Fogal, R. E. Johanson, G. Belev, S. O'Leary, and S. O. Kasap, "X-ray induced effects in stabilized a-Se x-ray photoconductors," *J. Non-crystalline Solids*, **299-302**, pp. 993-997, (2002).

[118] R. J. Schilling and S. L. Harris, "Applied numerical methods for engineers using MATLAB and C," (Pacific Grove, California, Brooks/Cole, 2000), ch. 9.

[119] G. Strang, "*Introduction to Applied Mathematics*," (Wellesley, MA: Wellesley-Cambridge, 1986) ch. 6.

[120] G. E. Forsythe and W. R. Wasow, "*Finite-difference methods for partial differential equations*," (John Wiley & sons, Inc., New York, USA, 1960), p. 141-143.

[121] J. Crank and P. Nicolson, "A practical method for numerical evaluation of solutions of partial differential equations of the heat-conduction type," *Advances in Computational Mathematics,* **6**, pp. 207-226, (1996).